Modeling the diffraction-limited images of interacting emitters and plasmonic nanoantennas

Harrison Jay Goldwyn

A dissertation
submitted in partial fulfillment of the
requirements for the degree of

Doctor of Philosophy

University of Washington

2020

Reading Committee:

David J. Masiello, Chair

Anne B. McCoy

Cody W. Schlenker

Program Authorized to Offer Degree:
Chemistry

University of Washington

Abstract

Modeling the diffraction-limited images of interacting emitters and plasmonic nanoantennas

Harrison Jay Goldwyn

Chair of the Supervisory Committee:
Professor David J. Masiello
Chemistry

The combination of optical microscopy and nanoscale antennas has great potential, but numerous complexities must first be understood. In this dissertation I use simple mathematical models of plasmonic nanoantennas interacting with their environment together with models of the diffraction limited imaging process occurring in a modern microscope to solve previously open questions in the literature. The two major stories are (1) resolving the mislocalization of molecules in plasmon-enhanced super-resolution fluorescence microscopy and (2) unification of past photothermal imaging theories and generalizing the formalism to resonant phenomena.

TABLE OF CONTENTS

ACKNOWLEDGMENTS

I thank my advisor Professor David J. Masiello and other committee members Professor Anne B. McCoy, Professor Cody W. Schlenker, and Professor Peter J. Pauzauskie. Thank you Anne and Cody for volunteering to serve on my reading committee as well. Anne has been in the audience for many of the presentations I gave throughout graduate school and often offered clear questions and broad perspective. I am thankful to Anne for always pushing me to make experimentally testable predictions. I am grateful to Cody was always supportive of my tendency to distract his graduate students and even more supportive of our collaboration. I am grateful to Peter for his enthusiasm for my work and dissertation.

As an advisor, David made sure I worked harder for this PhD than I had before, but he also convinced me it was worth doing. I am grateful that he talked me into coming to graduate school. But David also respected of my hesitance and I am thankful for that. He let me loose to study whatever I pleased for the first year, until it was clear I needed some structure. Only when I was ready to hear it did he step in and teach me the organizational skills it takes to make scientific progress. I am also grateful for Davids high standards for clear communication. When it came time to give my first exam talk, preparation was a team effort, and that didn't change until I could do it on my one. I will carry the value of communication into my next journey, scientific or otherwise. Throughout my graduate school career David allowed me to pursue mostly what I was interested in. It was a gift to experience research in this idealized sense, studying problems simply because they were interesting, which did work out in my favor. Lastly, I am grateful to David for his honestly. Although my own anxieties have often led me to dread authority, I trusted that when David was disappointed in me he would tell me (because he did). This allowed my self-critical mind

to accept praise when I deserved it, and he did give it.

With regard to the value of clear communication and scientific rigor, I can't ignore my other major mentor figures in the group. Charles Cherqui patiently honed my story telling through listening to many of my early talks. Charles also had a large influence on the supportive culture in the group that I deeply value. He also pioneered the reductionist approach that David's group has since overwhelmingly adopted. This skillset has made the group excellent explainers, a fun niche to play in collaborations. Thank you, Charles. There are many others from the group that deserve my thanks. Nick Bigelow was my first mentor during my undergraduate internship in the group. His excitement for science was contagious. I am grateful that since the end of his time in the group, Niket Thakkar become a friend and mentor. I am grateful to have had Niket a few years ahead of me in life, because I find his experiences inspiring and his mindset very relatable. He has been a consistently kind ear to rely on. I am also grateful to have had Niket as a manager, when I interned at the Institute for Disease Modeling and hope to continue working with him. Niket leads by example, with consistent earnestness, creativity, and drive to understand, something I will be trying to emulate whenever I manage people in the future.

I am thankful that David challenged me to write my first paper under a time constraint, which came to teach me maybe the most important lesson I learned in graduate school. I had to ask for help. To get the paper done, I asked Jake Bunche and Kevin Smith to help me, and they devoted all of their working hours for months to do so. I am very proud of that paper as the first piece of science I pushed to publication, but even more proud that I did it with the help from these two friends. I thank you both for all the great conversations on runs, on coffee walks, or just hanging out in the office. Kevin and Jake have been both great collaborators and companions through the last 5 years, but also role models. They both approach their work with a committed passion. I have seen both of them display incredible discipline while working on projects that no one will ever see. They have both inspired me

to push for more rigor in my own pursuits. I am also deeply grateful to Kevin and Jake for their appreciation of Fano resonance related memes.

I am grateful to have worked beside Steven Quillin and Nick Montoni for the first few years of my Ph.D. Steve showed me how to be a serious researcher without taking myself too seriously. I'm grateful to Steve for our bus-ride chats about our scientific curiosities, which helped me develop an enthusiasm for what I don't yet understand. I am grateful Nick Montoni for much emotional support in troubling times, and the willingness to be silly in the good times. I also thank Nick for showing me that a scientist can be other things too, like a marathon runner and a politician.

Claire West and Elliot Beutler joined the group the year after me and I am grateful to have both struggled and succeeded alongside them. Claire and I stuck together early on as we shared UCSB alumni status and were both California transplants. I am grateful to Claire for her patience as I learned how to share my experiences productively and for consistently putting in the work to have a positive relationship as housemates, coworkers, and friends. Claire has also played a large role in maintaining the group as a community, something that I value sincerely. Elliot was always a source of joy, and I am grateful to him for all the times we would be in the office after hours talking nonsense in silly accents, facilitated for by his joy for life that was undisturbed by the trials and tribulations of graduate school.

Seeing Praise Anyanwu and Austin Nixon come up in the group next has been a treat. I am grateful to them both for sharing their genuine curiosity just as I started to get a little jaded. Siamak Khorasani also brought excitement to the group for both the science and my gymnastics practice, I am thankful for this. I have also had the pleasure of working alongside Zhongwei Hu, Xiang-Tian Kong, and Aniruddha Bhattacharya. I am grateful to Zhongwei for his willingness to do anything helpful for the group. Kong had a quiet dedication to science that inspired me to be more rigorous and Ronnies passion for science was a joy to work alongside.

I am grateful to all the great collaborators I have gotten to work with. I probably had a hundred hours of conversations with Curly Zuo from Julie Biteen's group between him approaching me after my ACS talk in New Orleans and us publishing our first paper together. These conversations were always fruitful and enjoyable as we explored and came to understand the many subtitles which never ended up written explicitly in a paper. Julie Biteen was also a pleasure to work with; I felt supported by Julie and saw her pursue research with curiosity and patience. I am also grateful to Kallie Willets and Stephan Link, who both supported my growth as a scientist in numerous ways. Between patiently lending outside perspective to my technical presentations to kindly correcting my conference etiquette, I have always felt under their wings and am grateful for Kallie and Stephans honest guidence.

Adjusting to the workload of graduate school was difficult for me, and I am thankful for those that stood by me. I am grateful to Robert Waite and Alan Zhan who I lived with for the first two years of graduate school. Both have told me when I made mistakes in the past and I trust them to do it again the next time I screw up. This is a quality I value in the people around me and I thank them for doing the honor. Along with putting up with my nonsense and having many fruitful discussions, Robert and Alan have both been at my side for many laughs, and I cherish these experiences. I am grateful to Jake Precht for many reasons. Jake was always willing to talk things out over tea, during a run, while climbing a rock, or on a ski lift. Jake never spares an opportunity to connect with people and has taught me a lot, including how to have confidence and still ask for help. I am grateful to Nicole Emahiser for teaching me what it means to take care of myself and to really care for other people. Nicole is honestly the most inspiring person I have ever met, and I hope to achieve the spiritual connections to the world and those around her that she had at 25 by the time I'm 75. Emily Rabe was also a massive support for me in this time and has become the best friend I have ever had, more on her later. I am also deeply thankful to Becca Best for supporting me through the first year and a half of grad school and setting me up with

many skills (most learned in the kitchen) that helped me succeed in a Ph.D program.

Especially in the first few years of graduate school, a helpful staple was afternoon hacky-sack with Andrew Francis, Ben Figueroa, Sam Barlow, and other less regular guests. Andrew has always been a source of joy and I am grateful to have gotten to spend time with him. Ben as well, they both were great examples of hard work and hard play, making the most of grad school while making the best time they could be having. Thanks for your example and friendship. I am grateful to Sam Barlow and Catherine Kauffman for being fantastic friends through the years. Sam offered me a combination of tough love and genuine praise that I had never heard from a peer before. I am grateful to Sam for somehow always knowing when I need to be told to stop being a baby. Sam is also impressively comfortable with who he is, and this continues to inspire me to come to terms with myself. On the off chance that I did not want to hear from Sam "how it be", Catherine was right there ready to build me up. Her care and support has meant a lot to me, especially because I have seen glimpses of her as a powerful teacher and brave musical artist. This pair of people is one of a kind.

I also need to thank the wonderful group of people I lived with for the last 3 years. Including significant others who were around about half the time, I am grateful to Alex Peek, Savanna Jensen, Alan Zhan, Katy Johnson, Claire West, Mike Wilensky, and Emily Rabe. Each of them contributed in unique ways to building a place I felt truly comfortable coming home too. This is not something I take for granted, and I am deeply grateful to all of you.

Other friends I have met while in graduate school and owe thanks for connections big and small are Julia Greenwald, Megan Gadzuk-Shea, Victor Lee, Jacob Ziegler, Trevor Johnston, Camille Houferak, Lucas Flagg, Mark Boyer, and many others I am forgetting in this moment. Cody Schlenker's group served as a second home to me. I am grateful to Danna Sulas for her positivity and openness, Jared Olsen for his silliness, Katie Corp for her caring demeanor as well as Tim Pollock, Emma Cave, Sarah Pristash, and Ryan Flores for all the good times. I

was also fortunate to spend lots of time outside with Ian Bloom, Andy Bondesson, Ashley Anderson, Kat Ryan and many others, having a blast destroying our bodies on rocks and mountains and healing our minds around campfires.

I am also grateful to my high school friends for amazingly staying connected over the past decade. Their commitment to supporting each other over the years has inspired me. They include Michelle Blemker, Edward Chen, Kenny Lee, Cutter White, Jacob Moore, Ian McQuillin, Geoff Wilkins, Mickey Kumar, Kevin Klein, Melinda Berge, Robert Waite, Chelsea Anderson, Patrick Hanafin, Zach Bunker, and others I'm likely forgetting. Each of you given me something unique and I am grateful for your friendship .

I owe a lot to Scott Shiebler at the UW Counseling center. I was quite depressed the first year or so of graduate school and Scott was crucial to getting me through this Ph.D. Among many things, Scott has showed me the path to understanding myself and even liking the person I am. I am extremely grateful to have spent a few years now in the men's therapy group run by Scott, a space dedicated to practicing discussing and feeling emotions with other men in the context that men are socialized to avoid such settings. Scott led this group as an example of an authority figure and expert in clinical psychology that was also a whole person with emotions, desires, and fears. Scott is a beautiful example of a man doing the most for this world, and has inspired a reorganization of my priorities to be forgiving and to lift up those around me. I also owe thanks to all the men I have had the pleasure of practicing these values with; I have learned many things and have lots of love for all of you.

Although I'll have trouble doing it justice, my family probably deserves the largest acknowledgment. There are likely two main reasons I became a scientist. First was my dad's childlike fascination with all things big and small. I feel like I can trace my life as a physicist back to my dad showing me the film *National Geographic: The Invisible World*. I am grateful for my dads curiosity and enthusiasm for weird ideas, and he has certainly shown me that one can be opinionated and open minded. I am grateful to my dad for teaching me

never to take life too seriously, because its really just one long prop comedy routine. But my mom is what made a career in science happen though. From sitting with me for hours while I sobbed at the thought of doing 15 minutes of homework, to fighting to get me into honors classes in middle school and then AP classes in high school, my mom always pushed me to succeed with kindness and quiet persistence. I still look up to her as an example of real independence, always taking care of herself and those around her, looking forward with a confidence that any problem can be solved. Thank you mom for the role model you are. I am also grateful to my sister Briar for growing into a great friend. I have learned a lot from Briar in the last decade and am grateful she forgave me for being a crap older brother when we were kids. I am thankful to Briar for always being generous with her own journey to self-understanding. She has helped me see myself clearly over and over again.

If I am a better person (and scientist) now than when I entered graduate school, then I must acknowledge Emily Rabe for much of that progress. Emily has gone from a great friend to an amazing partner in everything. Our time together is always stimulating, as she consistently holds me accountable to reasonable versions of my own unrealistic expectations... and basic tidiness. She has a talent for supporting me when I need it and gently nudging me when I veer off course. I completely trust her and turn to her whenever I need a second perspective on what is happening in my life. It's really quite a gift to be able to trust someone so completely. I am grateful she not only gives, but allows me to support her in return, as support of community is something I am continually learning from her. Not only is Emily the best emotional support I could ask for, but her intellect often surpasses me. Our conversations have revealed to me so much about how the world works. I have also had the privilege of working with her on science, a joyful celebration of our compatibility. Thank you, Emily for helping me be the best version of myself. Emily's family has also supported me throughout our relationship and I feel very loved, cared for, and respected by Mama and Papa Rabe.

DEDICATION

To all my teachers. But specifically Mom for teaching me how to get things done, Dad for teaching me how to wonder, Briar for teaching me how to listen, and Emily for teaching me how to be a part of a team.

Part I

OPTICS OF THE PLASMON RESONANCE

Optical microscopy has been our fundamental tool for exploring the small parts of the world since Hooke and Leeuwenhoek first glimpsed microorganisms in the 1600s [63]. This technique arouse first simply because we see optical light, but it's utility has endured major technological advancement. Modern non-optical techniques like X-ray and Electron microscopy achieve much higher resolution then their optical counterparts, and have since become common laboratory techniques [157, 35, 131]. But the noninvasive character of optical light provides the special ability to visualize the details of fragile living systems [119].

The biocompatibility of optical light relies on its relatively low energy, or long wavelength, which sets a fundamental limit on resolution. This limit can be understood by the fact that even point sources of light will appear as fuzzy spots of finite size through even the best microscope objective. The shape and size of this bright spot, called the point spread function (PSF) is characteristic to diffraction through a particular system of optics. The closest distance between two point sources such that their PSFs are discernible as distinct is called the diffraction limit. The expression for this limit is usually attributed to pioneering work by Abbe [1] and Rayleigh [130], and can be approximated as $\lambda/(2\text{NA})$, in terms of the wavelength of light (λ) and the numerical aperture of the microscope objective lens (NA). Attainable resolution is therefore near 200 nm for visible light ($\lambda = 550\text{nm}$) using a high-NA objective lens ($\text{NA} = 1.4$) [49]. Because of the diffraction limit, optical images of nanoscale objects are non-trivially related to their size and shape. In order to optically investigate the nanoscale, we need to employ some tricks. A strategy starts to appear when considering the fact that the diffraction limit is not a property of the system under study, but instead the optical system through which we are viewing. By coupling light into a nanoscale object capable of generating localized electromagnetic fields, like a capacitor or an antenna, we can effectivly bypass the diffraction limit.

It turns out that nanoscale antennas for visible light do exist. Plasmonic nanoparticles (objects supporting one or multiple localized surface plasmon resonances, LSPRs or simply plasmons) serve this role. Noble metal particles of 10–100s of nm is size support plasmon resonances in the visible spectrum [161]. With dimensions smaller then the diffraction limit

of resonant light, plasmonic nanoparticles and have become a window to the nanoscale. Just like the radio antennas we have on our cars, or the microwave antennas in our cellphones, plasmonic nanoparticles can send and receive signals in the form of electromagnetic radiation. In any of these cases, the antenna relies on a conductive material, usually metal, whose conduction electrons oscillate in response to electromagnetic field. For the macro-scale electronic devices we use on a daily basis, the signals are sent by driving the antenna's free charges into oscillation with a electronic circuit. Oscillating charges radiate in response to acceleration, which is fundamental feature of electrodynamics. Plasmonic nanoparticles radiate similarly. But instead of being circuit driven, plasmonic nanoparticles are often coupled to nanoscale emitters like fluorescent or Raman active molecules. This nearby emission source readily transfers energy to the nanoantenna, whose electrons are easily set into oscillation at the optical frequencies near it's natural resonance. The reverse is also true. Incoming radiation drives the plasmon resonance strongly. This confined charge oscillation produces large local electric fields, which will increase light-matter coupling to anything in proximity. In fact, the discovery of the antenna-like properties of plasmonic nanoparticles began with the observation of fantastic feats such as Raman spectroscopy enhanced up to a millionfold times what was expected [112], which opened up the entire field of Surface enhanced Raman Spectroscopy (SERS), eventually leading to even single molecule detection [89]. Despite this success, imaging the nanoscale with plasmonic antennas is not a trivial feat. As we will discuss in detail in the following chapters, combining the plasmonic antenna with an imaging system yields complexity greater then the sum of it's parts.

The history of the plasmon resonance as something useful lies in the discovery that for certain molecules adsorbed on particular metal surfaces a Raman spectrum is observed with intensity unexplainable by simple calculations considering the metal as a simple reflecting mirror With the effect eventually attributed to the plasmonic resonance of nanoscale features in a roughened metal surface [139], researchers began to explore fabrication of distinct plasmonic particles for better SERS active substrates [31]. These ideas were quickly translated to enhancement of other molecular optical processes like absorption, emission, and fluores-

cence. At the same time, nanoscale fabrication techniques were becoming more accessible, and measurements of single and aggregated plasmonic particles became more intricate.

This simultaneous development of plasmonic enhanced spectroscopy and spatially precise nanoengineering techniques to control ever more complicated fabrication revived the study of electrodynamic theory [112, 66, 149]. Once thought dead, seemingly esoteric topics very close to those studied by first year physics graduate students became cutting edge, experimentally testable research topics. In particular, unlike many quantum mechanical problems, numerical solutions of electrodynamics problems are usually quite tractable [92, 72, 53]. With the tools to actually test predictions both numerically and experimentally, the physics of plasmonic particles interacting with each other and their environment are prime for reduced order models that can reveal the origins of emergent phenomena [125, 127, 40, 110, 37, 98, 164].

A predominant method for simplifying electrodynamic models is to incorporate only a finite number of interacting multipoles [38] (often just dipoles). These models have had such success in part because modeling plasmon-enhances spectroscopies like Raman and fluorescence requires predicting only fundamental physical quantities of the system, such as the radiative decay rate of an excited molecule [117]. But in order to model the microscope image of emitting molecules coupled to a plasmonic antenna, we must take into account the distribution of electromagnetic radiation from the near-field into the far-field as well as the diffraction limited optics of image formation in the microscope. In order to bring simple yet predictive models of plasmon-emitter interactions from spectroscopy to imaging, a detailed model of the observable needs to be implemented.

This has been my pursuit of the last 5 years. I have sought to combine a simple model of diffraction limited imaging with similarity distilled mathematical descriptions of plasmonic antennas. Both plasmons and molecules take the form of electric dipoles, and the connection between dipolar interaction and their far-field interference effects explain real images of these complicated systems.

The combination of these two models provides us intuitive interpretation of plasmonic imaging in general, but in particular I present in this dissertation two concrete attempts

to resolve discrepancies of the past. The first, in Part II of this dissertation, is manifested in plasmon-enhanced single-molecule localization microscopy, a subfield of super-resolution fluorescence. In this case, the diffraction limited images of a coupled plasmonic antenna and fluorescence molecule were commonly observed localize towards the center of the antenna. But occasionally, interference effects seam to shift the image away from the antenna. I demonstrate how the relative infrequency of the second case is explained by the image and plasmon-emitter interaction model. The second, in Part III, manifests in the photothermal imaging of single plasmonic particles, a technique developed to optically detect absorbers. Two separate lineages of theoretical analysis seem to start with disparate assumptions for the mathematical description of the photothermal image. I develop a theory that combines the past approaches and explores the possible reasons why both were independently justified in their own contexts.

Before exploring the detailed implications of plasmon-enhanced imaging in those two cases, the remainder of Part I of this dissertation sets up the fundamental theory of diffraction limited imaging, and then the reduced order modeling of a plasmonic nanoparticle as an electric dipole oscillator. With the theory of imaging and interaction established, we move to the applications discussed above.

Chapter 1

INTRO TO IMAGING: SCALAR DIFFRACTION THEORY

The plasmon resonance is useful for its ability to effectivly break the diffraction limit. But how can this be in the diffraction limit is really a lower bound on the spatial confinement of light? In reality the diffraction limit is more a consequence of how we interact with light, sending it through lenses with finite dimension, then it is a fundamental property of light itself. In this chapter, we will explore this notion and develop a mathematical understanding of the diffraction limit. It is our goal to see how the diffraction limit, a lower bound on imaging length-scale, arises when attempting to focus light with a lens. We will start with the fundamental governing equations of electrodynamics, and build a theoretical understanding of imaging limitations. The theory presented here, known as scalar diffraction theory, does make some simplifying approximations at the outset. We will forgo these to some degree in the next chapter to derive a higher level theory for the image fields of dipole emitters under high numerical aperture microscope objectives. But in the meantime the simplifying assumptions presented here are adequate for our education.

Much of this derivation follows Goodman's excellent book, *Introduction to Fourier optics* [65], with the details and cometary my own.

1.1 Maxwell's equations

We start with the governing equations of electrodynamics. Outside of quantum mechanical effects for very small objects and gravitational effects for very large objects, most all of known physics can be derived from the following 4 equations. These are referred to as the

macroscopic Maxwell's equations,

$$\nabla \cdot \mathbf{D} = 4\pi\rho \qquad \nabla \times \mathbf{E} = -\frac{1}{c}\partial_t \mathbf{B} \tag{1.1}$$

$$\nabla \cdot \mathbf{B} = 0 \qquad \nabla \times \mathbf{H} = \frac{1}{c}\partial_t \mathbf{D} + \frac{4\pi}{c}\mathbf{J}\ , \tag{1.2}$$

relating the electric and magnetic fields $\mathbf{E}$ and $\mathbf{B}$, along with the displacement field $\mathbf{D}$ and the magnetizing field $\mathbf{H}$, to their sources. The latter two fields are macroscopic quantities that contain the effects of net material polarization, so that the so called free charge ρ and free current density $\mathbf{J}$ represent only macroscale quantities of interest.

In order to compensate for macroscopic polarization of matter, the fields $\mathbf{D}$ and $\mathbf{H}$ are related to material properties through the phenomenological constitutive relations, which harbor the material properties resulting from a macroscopic average over molecular scale polarizations.

$$\mathbf{D} = \epsilon\mathbf{E} \qquad \mathbf{H} = \frac{1}{\mu}\mathbf{B} \tag{1.3}$$

For our interest in light propagation, we will first consider isotropic space with no sources, $\{\mu, \epsilon\} \neq f(\mathbf{x})$, in which we can derive the wave equation,

$$\begin{aligned}
\nabla \times (\nabla \times \mathbf{E}) &= \nabla \times (-\frac{1}{c}\partial_t \mathbf{B}) \\
&= -\frac{1}{c}\partial_t \nabla \times \mathbf{B} \\
&= -\frac{\mu}{c}\partial_t \nabla \times \mathbf{H} \\
&= -\frac{\mu}{c^2}\partial_t^2 \mathbf{D} \\
&= -\frac{\mu\epsilon}{c^2}\partial_t^2 \mathbf{E} \\
\nabla(\nabla \cdot \mathbf{E}) - \nabla^2\mathbf{E} &= \\
\frac{1}{\epsilon}\nabla(\nabla \cdot \mathbf{D}) - \nabla^2\mathbf{E} &= \\
-\nabla^2\mathbf{E} &= \\
\nabla^2\mathbf{E} - \frac{\mu\epsilon}{c^2}\partial_t^2\mathbf{E} &= 0\ .
\end{aligned} \tag{1.4}$$

This of course has eigenstates of the form $\mathbf{E}_0 e^{-i(\omega t - \mathbf{k}\cdot\mathbf{x})}$, the electric field of a plane wave. But if we introduce some matter (like a microscope or other imaging optical device) and consider it to be describable by $\epsilon(\mathbf{x})$ and $\mu(\mathbf{x})$, a source term appears on the right hand side of the wave equation.

We will assume our microscope is not magnetic, and take $\mu \to 1$. Maxwell's equations then take the form

$$\nabla \cdot \mathbf{D} = 0 \qquad \nabla \times \mathbf{E} = -\frac{1}{c}\partial_t \mathbf{B} \tag{1.5}$$

$$\nabla \cdot \mathbf{B} = 0 \qquad \nabla \times \mathbf{B} = \frac{1}{c}\partial_t \mathbf{D} \tag{1.6}$$

and the wave equation becomes

$$\nabla^2 \mathbf{E} - \frac{\epsilon}{c^2}\partial_t^2 \mathbf{E} = \nabla\left(\epsilon \mathbf{E} \cdot \nabla\left(\frac{1}{\epsilon}\right)\right) . \tag{1.7}$$

This wave equation mixes the vector components of $\mathbf{E}$ anywhere where $\nabla\left(\frac{1}{\epsilon}\right) \neq 0$. This will of course be true at the interfaces between the lenses in our microscope and the air. But it turns out, we are able to make decent predictions even by neglecting the right hand side of Eq. (1.7). By doing so, we return to the homogeneous wave equation, in which the vector components of $\mathbf{E}$ are independent. It is this approximation that allows us to treat the electric field as a scalar, and how scalar diffraction theory gets its name. For more discussion on the limitations, see Goodman's text, Ref. [65]. Our goal hear will be to solve the wave equation around a finite sized lens. In abiding as much as possible to the scalar diffraction approximation, we will seek the focused fields at distanced many wavelengths from the lens, where our assumption is obviously broken

1.2 Helmhotz

As we often do in electrodynamics, it is convenient to solve our problem one frequency at a time. Since our problem is that of light propagation, we will first convert the wave equation to the frequency domain. We can do this by defining the Fourier transform and its inverse

as

$$\mathcal{F}[f(t)] = \tilde{f}(\omega) = \int \mathrm{d}t\, e^{i\omega t} f(t) \tag{1.8}$$

$$\mathcal{F}^{-1}[\tilde{f}(\omega)] = f(t) = \int \frac{\mathrm{d}\omega}{2\pi} e^{-i\omega t} \tilde{f}(\omega), \tag{1.9}$$

which for practical purposes, maps some function of a variable and its time derivatives $f(g, \partial_t^n g) \to f(\tilde{g}, (-i\omega)^n \tilde{g})$. The wave equation in free space transforms into the Helmhotz equation

$$\begin{aligned}
\mathcal{F}[\nabla^2 \mathbf{E} - \frac{n^2}{c^2}\partial_t^2 \mathbf{E} = 0] \\
\nabla^2 \tilde{\mathbf{E}} - \frac{n^2}{c^2}\mathcal{F}[\partial_t^2 \mathbf{E}] = 0 \\
\nabla^2 \tilde{\mathbf{E}} - \frac{n^2}{c^2}\int \mathrm{d}t\, e^{i\omega t}\partial_t^2 \mathbf{E} = 0 \\
\nabla^2 \tilde{\mathbf{E}} - \frac{n^2}{c^2}\left(\left[e^{-i\omega t}\partial_t \mathbf{E}\right]_{t=-\infty}^{+\infty} - \int \mathrm{d}t\, \partial_t e^{i\omega t}\partial_t \mathbf{E} \right) = 0 \\
\nabla^2 \tilde{\mathbf{E}} - \frac{n^2}{c^2}\left(\left[e^{-i\omega t}\partial_t \mathbf{E}\right]_{t=-\infty}^{+\infty} - \left[e^{-i\omega t}\mathbf{E}\right]_{t=-\infty}^{+\infty} + \int \mathrm{d}t\, \partial_t^2 e^{i\omega t}\mathbf{E} \right) = 0 \\
\nabla^2 \tilde{\mathbf{E}} - \frac{n^2}{c^2}(i\omega)^2 \tilde{\mathbf{E}} = 0 \\
\nabla^2 \tilde{\mathbf{E}} + \frac{n^2\omega^2}{c^2}\tilde{\mathbf{E}} = 0 \\
\nabla^2 \tilde{\mathbf{E}} + k^2 \tilde{\mathbf{E}} = 0.
\end{aligned} \tag{1.10}$$

The Helmholtz equation can be thought of as a linear diagonal operator $[\nabla^2 + k^2]$ acting on the field. It therefore leaves each scalar component of the field independent from each other. With sources, or a heterogeneous medium represented by $\epsilon(\mathbf{x})$, the field components are mixed by off-diagonal terms, as in the time domain. In continuing within the scalar diffraction limit, we can discuss the field components individually in terms of the historically relevant disturbance $u(\mathbf{x}, t)$ and its Fourier components $U(\mathbf{x}, \omega)$ satisfying the scalar Helmhotz equation,

$$\nabla^2 U + k^2 U = 0\,. \tag{1.11}$$

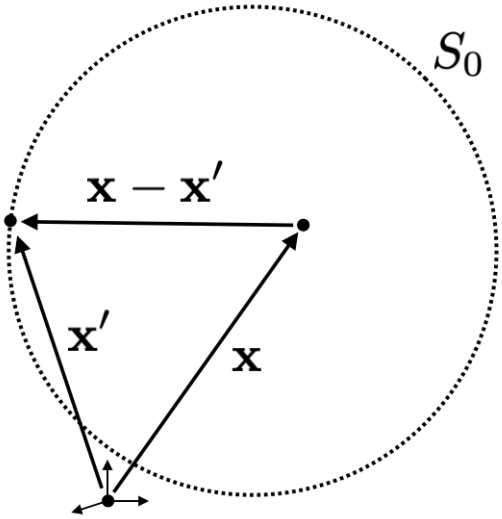

Figure 1.1: Integration surface for Greens Second Identity to relate the field at point $\mathbf{x}$ to the surface S_0.

This equation has the the (outward propagating) Green's function

$$G(\mathbf{x},\mathbf{x}') = \frac{e^{ik|\mathbf{x}-\mathbf{x}'|}}{4\pi|\mathbf{x}-\mathbf{x}'|} \tag{1.12}$$

where $U \in \{\tilde{E}_x, \tilde{E}_y, \tilde{E}_z\}$.

1.3 Green's second identity

In the context of light propagating through a lens, we are interested in solving for the focal fields as a function of the field incident upon the lens. This is can be accomplished by manipulating the fundamental theorem of calculus to arrive at

$$\int_V \mathrm{d}^3x' \left(U\nabla^2 G - G\nabla^2 U\right) = \int_{\delta V} \mathrm{d}^2x' \left(U\frac{\partial G}{\partial n} - G\frac{\partial U}{\partial n}\right) \tag{1.13}$$

where $\frac{\partial U}{\partial n} = \hat{n}\cdot\nabla U$ and $\hat{n}$ is the unit normal to the outer surface. Letting $G \to G(\mathbf{x},\mathbf{x}')$ be the Green's function in a region where $\mathbf{x} \neq \mathbf{x}'$ and U be the field disturbance also satisfying the Helmholtz equation, the left side of Eq. 1.13 cancels. The right side can then reduced with knowledge of G. Given $r \equiv |\mathbf{x}-\mathbf{x}'|$

$$\frac{\partial G}{\partial n} = \left(ik - \frac{1}{r}\right)\frac{e^{ikr}}{r}\hat{n}\cdot\hat{r} \tag{1.14}$$

and then

$$0 = \int_{\delta V} \mathrm{d}^2x \left[U \frac{\partial G}{\partial n} - G \frac{\partial U}{\partial n} \right] \tag{1.15}$$

$$= \int_{\delta V} \mathrm{d}^2x \left[U \left(ik - \frac{1}{r} \right) \hat{n} \cdot \hat{r} - \frac{\partial U}{\partial n} \right] \frac{e^{ikr}}{r} \tag{1.16}$$

This expression can be used to relate the field on the surface S' by taking $S = \delta V = S' + S_\epsilon$ equal to the bounding surfaces of the volume V minus some small spherical volume around the point x_0 with radius ε. Eq. 1.15 then results in the expression

$$\begin{aligned}
0 &= \int_{S'} \mathrm{d}^2x \left[U \left(ik - \frac{1}{r} \right) \hat{n} \cdot \hat{r} - \frac{\partial U}{\partial n} \right] \frac{e^{ikr}}{r} + \int_{S_\epsilon} \mathrm{d}^2x \left[U \left(ik - \frac{1}{r} \right) \hat{n} \cdot \hat{r} - \frac{\partial U}{\partial n} \right] \frac{e^{ikr}}{r} \\
&= \int_{S'} \mathrm{d}^2x \cdots + \lim_{\epsilon \to 0} 4\pi\epsilon^2 \frac{e^{ik\epsilon}}{\epsilon} \left[U(\mathbf{x}_0) \left(ik - \frac{1}{\epsilon} \right) (-1) - \left. \frac{\partial U}{\partial n} \right|_{\mathbf{x}=\mathbf{x}_0} \right] \\
&= \int_{S'} \mathrm{d}^2x \cdots + \lim_{\epsilon \to 0} 4\pi e^{ik\epsilon} \left[-U(\mathbf{x}_0) \left(ik\epsilon - 1 \right) - \epsilon \left. \frac{\partial U}{\partial n} \right|_{\mathbf{x}=\mathbf{x}_0} \right] \\
&= \int_{S'} \mathrm{d}^2x \cdots + 4\pi U(\mathbf{x}_0) \ ,
\end{aligned}$$

so

$$U(\mathbf{x}_0) = -\frac{1}{4\pi} \int_{S'} \mathrm{d}^2x \left[U \left(ik - \frac{1}{r} \right) \hat{n} \cdot \hat{r} - \frac{\partial U}{\partial n} \right] \frac{e^{ikr}}{r} \ . \tag{1.17}$$

and in general,

$$0 = \int_{S_0 + S_\varepsilon} \mathrm{d}^2x' \left[U \frac{\partial G}{\partial n} - G \frac{\partial U}{\partial n} \right] \ . \tag{1.18}$$

The small surface S_ε containing the observation point can be integrated in the limit where $\varepsilon \to 0$,

$$\begin{aligned}
\lim_{\varepsilon \to 0} \int_{S_\varepsilon} \mathrm{d}^2x' \left[U \frac{\partial G}{\partial n} - G \frac{\partial U}{\partial n} \right] &= \lim_{\varepsilon \to 0} \int_{\delta V} \mathrm{d}^2x' \left[U \left(ik - \frac{1}{r} \right) \hat{n} \cdot \hat{r} - \frac{\partial U}{\partial n} \right] \frac{e^{ikr}}{r} \\
&= \lim_{\varepsilon \to 0} 4\pi\varepsilon^2 \left[U(\mathbf{x}) \left(ik - \frac{1}{\varepsilon} \right) (-1) + \left. \frac{\partial U}{\partial r} \right|_{\mathbf{x}} \right] \frac{e^{ik\varepsilon}}{\varepsilon} \\
&= \lim_{\varepsilon \to 0} 4\pi \left[U(\mathbf{x}) \left(1 - ik\varepsilon \right) + \varepsilon \left. \frac{\partial U}{\partial r} \right|_{\mathbf{x}} \right] e^{ik\varepsilon} \\
&= 4\pi U(\mathbf{x})
\end{aligned}$$

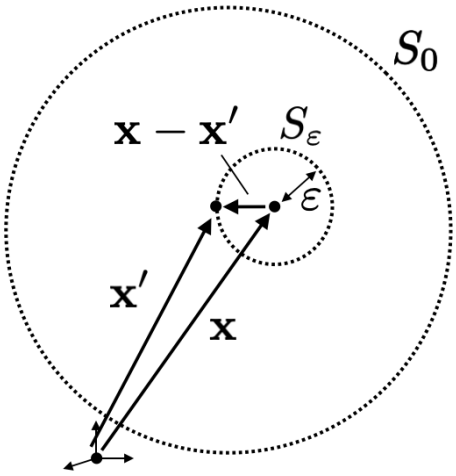

Figure 1.2: Integration surfaces for manipulating Greens Second Identity to relate the field at point $\mathbf{x}$ to the surface S_0 with exclusion of a small volume around the observation point.

and the field at point $\mathbf{x}$ can therefore be defined by just the integral over the surface S_0,

$$U(\mathbf{x}) = -\frac{1}{4\pi}\int_{S_0} \mathrm{d}^2x' \left[U\frac{\partial G}{\partial n} - G\frac{\partial U}{\partial n}\right] . \tag{1.19}$$

1.4 Kirchoff's diffraction integral

Kirchoff's formula for diffraction through an aperture relies on taking Eq. 1.17 and splitting the surface into two pieces

$$U(\mathbf{x}_0) = -\frac{1}{4\pi}\int_{S_p+S_R} \mathrm{d}^2x \left[U\left(ik - \frac{1}{r}\right)\hat{n}\cdot\hat{r} - \frac{\partial U}{\partial n}\right]\frac{e^{ikr}}{r} \tag{1.20}$$

If S_R is a spherical surface of radius R and we take the limit as $r \to \infty$, $\hat{n}\cdot\hat{r} = 1$ and

$$\begin{aligned}
\lim_{R\to\infty}\int_{S_R}[\cdots] &= \frac{-1}{4\pi}\lim_{R\to\infty}\int_{S_R}\mathrm{d}^2x\left[U\left(ik-\frac{1}{R}\right) - \frac{\partial U}{\partial r}\right]\frac{e^{ikR}}{R} \\
&= \frac{-1}{4\pi}\lim_{R\to\infty}\int_{S_R}R^2\mathrm{d}^2\Omega\left[U\left(ik-\frac{1}{R}\right) - \frac{\partial U}{\partial r}\right]\frac{e^{ikR}}{R} \\
&= \frac{-1}{4\pi}\int_{S_R}\mathrm{d}^2\Omega\lim_{R\to\infty}R\left[Uik - \frac{\partial U}{\partial r}\right]e^{ikR},
\end{aligned}$$

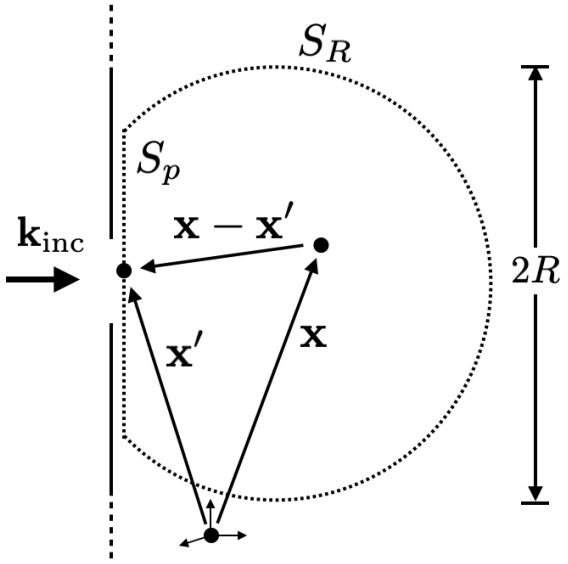

Figure 1.3: Splitting the integration surface S_0 into a spherical portion S_R and a planar portion along the aperture S_p.

which does tend to 0 if the Sommerfield radiation condition for U

$$\lim_{R\to\infty} R\left[Uik - \frac{\partial U}{\partial r}\right] = 0 \tag{1.21}$$

is satisfied for any value of the solid angle Ω.

This result reduces the surface S_p to a plane with infinite extend. We have arrived at a relationship for the field at some point $\mathbf{x}$ beyond this plane in terms of an integral over its value and first derivative on the plane S_p. If S_p is taken to be the plane $z = 0$ and the point $\mathbf{x}$ lies in the half space $z > 0$, then

$$U(\mathbf{x}) = \frac{1}{4\pi}\int_{-\infty}^{\infty} \mathrm{d}y' \int_{-\infty}^{\infty} \mathrm{d}x' \left[U(\mathbf{x}')\left(\frac{1}{r} - ik\right)\hat{z}\cdot\hat{r} - \frac{\partial}{\partial z}U(\mathbf{x}')\right]\frac{e^{ikr}}{r} \tag{1.22}$$

where $r \equiv |\mathbf{x} - \mathbf{x}'|$. But of course most of the plane S_p is the opaque screen, and we expect light to propagate through only a small portion. We will therefore make two simplifying assumptions. First, in the geometric shadow of the screen, we assume the field and its derivative are both zero. Second, inside the aperture, the field and its derivative are assumed

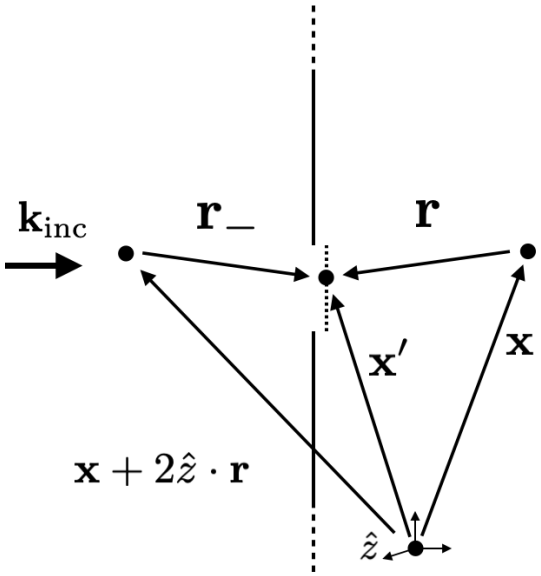

Figure 1.4: Incorporation of the image Green's function into Kirchoff's diffraction integral to send the derivative term to zero.

equal to the incident field as it would have been undisturbed without the presence of the screen. These two approximations break the electromagnetic boundary conditions, but in a similar spirit to original assumption of a scalar theory, so we will accept them.

Rayleigh-Sommerfeld modification

We can further simplify Kirchoff's integral without approximation by superimposing two forms of the Green's function. Taking

$$G \to G_- = \frac{1}{2}\left(\frac{e^{ikr}}{r} - \frac{e^{ikr_-}}{r_-}\right) \tag{1.23}$$

where $r_- \equiv |\mathbf{x} + 2\hat{z} \cdot \mathbf{r} - \mathbf{x}'|$ we now satisfy the relations

$$G_-(\mathbf{x}, \mathbf{x}' \in \text{Ap.}) = 0 \qquad \text{but} \qquad \left.\frac{\partial G_-}{\partial z}\right|_{\mathbf{x}' \in \text{Ap.}} = \frac{\partial G}{\partial z}\,. \tag{1.24}$$

This simplified the integral relation for the field, leaving us

$$\begin{aligned} U(\mathbf{x}) &= \frac{-1}{4\pi}\int_{\text{Ap.}} \mathrm{d}^2x' U \frac{\partial G}{\partial n} \\ &= \frac{-1}{4\pi}\int_{\text{Ap.}} \mathrm{d}^2x' U(\mathbf{x}')\hat{z}\cdot\hat{r}\left(ik-\frac{1}{r}\right)\frac{e^{ikr}}{r} \\ &\approx \frac{-ik}{4\pi}\int_{\text{Ap.}} \mathrm{d}^2x' U(\mathbf{x}')\hat{z}\cdot\hat{r}\frac{e^{ikr}}{r} \\ &\approx \frac{1}{i\lambda}\int_{\text{Ap.}} \mathrm{d}^2x' U(\mathbf{x}')\frac{e^{ikr}}{r}. \end{aligned} \tag{1.25}$$

But in interest of computing the field U, it will be useful to further apply the paraxial approximation to an expantion of r. Let the coordinate origin be placed inside the aperture. It then follows that r can be defined in cylindrical coordinates as

$$\begin{aligned} r &= ((x-x')^2+(y-y')^2+z^2)^{1/2} \\ &= (\rho^2+z^2)^{1/2} \\ &= z((\rho/z)^2+1)^{1/2} \end{aligned} \tag{1.26}$$

if the observation point is far from the aperture in z but not ρ, this paraxial approximation facilitates truncation of the expansion

$$r = z\left(1+\frac{1}{2}\frac{\rho^2}{z^2}-\frac{1}{8}\frac{\rho^4}{z^4}+\mathcal{O}(\tfrac{\rho^6}{z^6})\right). \tag{1.27}$$

Keeping only the the first two terms in the exponential and the first in the denominator,

$$\begin{aligned} U(\mathbf{x}) &= \frac{1}{i\lambda}\int_{\text{Ap.}} \mathrm{d}^2x' U(\mathbf{x}')\frac{e^{ik(z+\frac{1}{2}\frac{\rho^2}{z})}}{z}. \\ &= \frac{e^{ikz}}{i\lambda z}\int_{\text{Ap.}} \mathrm{d}^2x' U(\mathbf{x}')e^{ik\frac{\rho^2}{2z}}. \\ &= \frac{e^{ikz}}{i\lambda z}\int_{\text{Ap.}} \mathrm{d}^2x' U(\mathbf{x}')e^{i\frac{k}{2z}[(x-x')^2+(y-y')^2]}\,, \end{aligned} \tag{1.28}$$

which is the final form of the diffraction integral we will use for calculation.

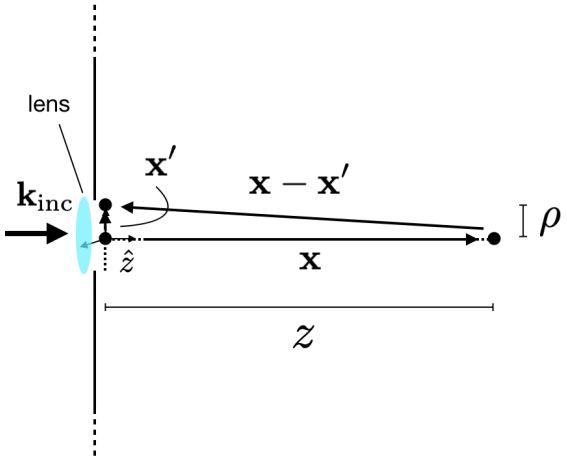

Figure 1.5: Introduction of the lens into the aperture, with observation point now complicit with the paraxial approximation, $\rho \ll z$.

1.5 Lens as a phase transformation

By completing out model of diffraction affects from light passing through the aperture, we are finished with most of the complexity. The last step is to introduce the lens into the aperture, accounting for refraction of the incident light toward the focal spot. Relying briefly on some intuition from geometric optics, consider a lens so thin that some ray entering with coordinates (x, y) exits at approximately the same coordinate, translating negligibly within the lens. If the lens has some thickness $\Delta(x, y)$, maximum thickness $\Delta_0(x, y)$ and constant refractive index n, the effect of the lens on this ray can be described by the phase delay

$$\phi(x, y) = kn\Delta(x, y) + k(\Delta_0 - \Delta(x, y)). \tag{1.29}$$

But for our purposes, we can consider a perfect lens, which will transform an incident plane $U_i(x, y, z = 0_-) = U_0$ into the spherical wave $U_0 e^{-ik(x^2+y^2+(z-z_f)^2)^{1/2}}$ converging onto the focal point $(0, 0, z_f)$.

Plugging this expression for the focused incident field into our diffraction integral,

$$U(\mathbf{x}) = \frac{e^{ikz}}{i\lambda z} \int_{\text{Ap.}} \mathrm{d}^2x' U_0 e^{-ik(x'^2+y'^2+z_f^2)^{1/2}} e^{i\frac{k}{2z}[(x-x')^2+(y-y')^2]} \tag{1.30}$$

which can be reduced by the same paraxial approximation as before since we are interested in observing the field in the focal plane, in which case $z = z_f$.

$$\begin{aligned} U(\mathbf{x}) &= \frac{e^{ikz_f}}{i\lambda z}\int_{\text{Ap.}} \mathrm{d}^2x' U_0 e^{-ikz_f} e^{-i\frac{k}{2z_f}[x'^2+y'^2]} e^{i\frac{k}{2z_f}[(x-x')^2+(y-y')^2]} \\ &= \frac{1}{i\lambda z}\int_{\text{Ap.}} \mathrm{d}^2x' U_0 e^{-i\frac{k}{2z_f}[x'^2+y'^2]} e^{i\frac{k}{2z_f}[x^2+x'^2-2xx'+y^2+y'^2-2yy']} \\ &= \frac{1}{i\lambda z}\int_{\text{Ap.}} \mathrm{d}^2x' U_0 e^{i\frac{k}{2z_f}[x^2-2xx'+y^2-2yy']} \\ &= \frac{e^{i\frac{k\rho^2}{2z_f}}}{i\lambda z}\int_{\text{Ap.}} \mathrm{d}^2x' U_0 e^{i\frac{k}{2z_f}[-2xx'-2yy']}, \end{aligned} \tag{1.31}$$

which is integrable over a circular aperture of radius a, or is at least expressible as a cylindrical Bessel. In cylindrical coordinates we may write,

$$\begin{aligned} \int_{\text{Ap.}} \mathrm{d}^2x' U_0 e^{-i\frac{k}{z_f}[(xx'+yy')]} &= U_0\int_0^a \mathrm{d}\rho'\,\rho'\int_0^{2\pi}\mathrm{d}\phi'\, e^{-i\frac{k}{z_f}[\boldsymbol{\rho}\cdot\boldsymbol{\rho}']} \\ &= U_0\int_0^a \mathrm{d}\rho'\,\rho'\int_0^{2\pi}\mathrm{d}\phi'\,\sin\phi' e^{-i\frac{k}{z_f}\rho\rho'\cos\phi'} \\ &= U_0\int_0^a \mathrm{d}\rho'\,\rho' 2\pi J_0(\tfrac{k\rho\rho'}{z}). \end{aligned} \tag{1.32}$$

We can then use the identity

$$\int_0^a \mathrm{d}\rho'\,\rho' J_0(\alpha\rho')\alpha\rho' = aJ_1(\alpha a)\ , \tag{1.33}$$

which in our case specifically becomes,

$$\int_0^a \mathrm{d}\rho'\,\rho' J_0(\tfrac{k\rho\rho'}{z}) = J_1(\tfrac{k\rho a}{z_f})\frac{z_f}{k\rho}a\ . \tag{1.34}$$

The field in the focal plane can be reduced to

$$\begin{aligned} U(x,y,z_f) &= \frac{e^{i\frac{k\rho^2}{2z_f}}}{i\lambda z_f}2\pi U_0 J_1(\tfrac{k\rho a}{z_f})\frac{z_f}{k\rho}a \\ &= \frac{e^{i\frac{k\rho^2}{2z_f}}}{i}kU_0 J_1(\tfrac{k\rho a}{z_f})\frac{1}{k\rho}a \\ &= -ie^{i\frac{k\rho^2}{2z_f}}U_0 J_1(\tfrac{k\rho a}{z_f})\tfrac{a}{\rho} \end{aligned} \tag{1.35}$$

With the focal plane field defined, the problem is solved. We have defined the field in the focus on an ideal lens, which will be peaked with finite width. The only thing left to do is to consider the intensity that we would detect on a camera. The imaged intensity is proportional to the field squared,

$$|U(\rho, z_f)|^2 = |U_0|^2 J_1^2(\tfrac{k\rho a}{z_f})\tfrac{a^2}{\rho^2} \,, \tag{1.36}$$

which is peaked at the origin and falls to zero with the cylindrical Bessel function.

This model has been constructed not for the image of some object, but simply the focus of plane wave light by a lens. regardless, the finite size of the focal spot is simply a consequence of finite size of the aperture. We will therefore use this result to define the resolution limit of an idealized microscope. The diffraction limit is typically defined as the minimum distance between two emitters such that their two independent diffraction limited spots can be distinguished. Assuming this would coincide with the first emitter located at the first minimum of second image, then the diffraction limited resolution is equal to the first zero of Eq. (1.36). Taking the first zero of $J_1(\frac{k\rho a}{z_f})$ to be ρ_0,

$$\rho_0 = \frac{1.29\lambda z_f}{2a} \approx \frac{\lambda}{2\mathrm{NA}} \quad \blacksquare \,, \tag{1.37}$$

where we have introduced the numerical aperture $\mathrm{NA} \equiv a/z_f$, defined trigonometrically by the lens radius and focal distance. This last expression justifies the commonly quoted diffraction limit, defined by the wavelength and numerical aperture. It is simply a consequence of focusing light through a finite sized aperture. It is reasonable to consider that with an infinitely large lens (aka no aperture), we would be able to focus to an infinitely small point. This is exactly the case in terms of our simplified model here, which suggests the diffraction limit is a consequence of information lost by collection only some of the light emitted by some object. It is reminiscent of the uncertainty relations characteristic of wave mechanics.

Chapter 2

IMAGE FIELD OF A ELECTRIC DIPOLE

The techniques presented for imaging in the scalar diffraction theory do generalize for a fully vectorial theory. The math gets more complicated and is therefore less transparent, so we will forgo the derivation of the diffraction integral, and instead apply it to obtain an analytical form for the diffraction limited image of a radiating electric dipole.

Following the methods section of reference [64], we will calculate the focused and diffracted fields of dipole emitter using the Debye-Wolf integral [163], which provides an accurate model of the fields produced by diffraction-limited optical systems with the large numerical apertures common in single-molecule fluorescence imaging [50]. For an idealized infinity-corrected microscope, the field composing the image can be constructed by first computing the refraction at the objective lens, and then focusing at a top lens into image space where the light is subject to diffraction.

As outlined in Ref. [71], both the objective and top lens are considered spherical refracting surfaces with focal lengths f' and f respectively. The objective is defined by the spherical coordinates $(r' = f', \zeta', \xi')$ relative to the focal point in objective space, where the physical dipole will be located. If we assume that the objective lens lies far enough from any light emitting object that only far-fields need be considered, the focusing of the field can be calculated with geometric optics. It is this scattered+focused field $\mathbf{E}^{\text{foc}}$ that is propagated through an aperture to calculate diffraction effects. The top lens is treated as a portion of the reference sphere defined by the spherical coordinates $(r = f, \zeta, \xi)$ relative to the focal point in image space. The focused+diffracted image field is defined by the following integral across the top lens aperture,

$$\mathbf{E}(\rho, \varphi, z) = -\frac{ikfe^{ikf}}{2\pi} \int_0^{\zeta_m} d\zeta \sin\zeta \int_0^{2\pi} d\xi \, \mathbf{E}^{\text{foc}}(r = f, \zeta, \xi) e^{ik[\rho \sin\zeta \cos(\varphi - \xi) + (z-h)\cos\zeta]}. \quad (2.1)$$

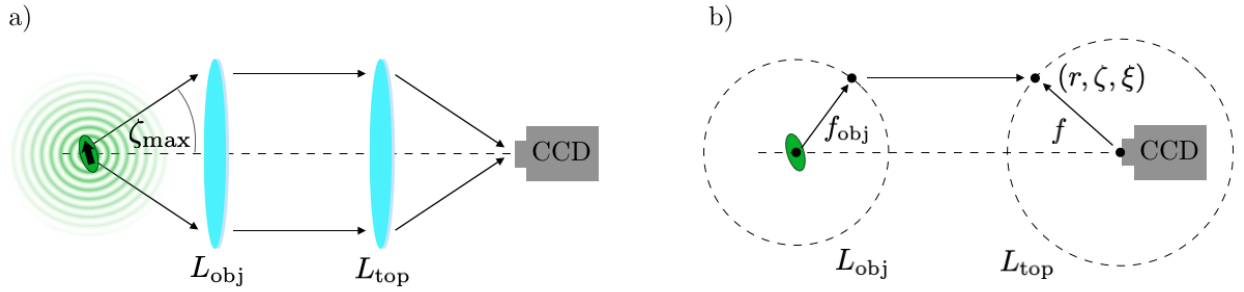

Figure 2.1: (a) Diagram of the infinity corrected microscope as modeled, with object and top lenses defining the aperture size, and therefore the collection angle $\zeta_{\max}$. (b) Diagram of the idealized spherical refracting surfaces of focal length f_{obj} and f, and the image space spherical coordinates.

The term $e^{ik(z-h)\cos\zeta}$ describes defocusing and defines the focal plane at $z = h$. The rotational symmetry of the lens/aperture allows analytic solution of the azimuthal ξ integral, leaving the polar integral over cylindrical Bessel functions. The polar integral is often evaluated numerically, but for the case of a oscillating electric dipole we can compute the integrals, leading to an analytic form in good agreement with full-wave electrodynamics simulation and numerical computation of the integral.

2.1 Dipole aligned in focal plane

Let's start with a dipole moment $\mathbf{p} = \hat{\mathbf{p}}|p|e^{-i\omega t} = \hat{\mathbf{e}}_x|p|e^{-i\omega t}$ where $\mathbf{e}_x$ is perpendicular to the optical axis. This dipole will generate the radiation zone field

$$\mathbf{E}^{\text{scat}}(\mathbf{x}) = |p|\frac{k^2}{r}e^{i(kr-\omega t+\phi)}[\hat{\mathbf{p}} - \mathbf{n}(\mathbf{n}\cdot\hat{\mathbf{p}})]. \tag{2.2}$$

Converting to the object space spherical coordinates (r', ζ', ξ'), we note that

$$\mathbf{n} = \begin{pmatrix} \sin\zeta'\cos\xi' \\ \sin\zeta'\sin\xi' \\ \cos\zeta' \end{pmatrix} \tag{2.3}$$

in the implied basis $\hat{\mathbf{e}}_x = (1, 0, 0)$. Taking the harmonic time dependence as implicit from this point forward, the scattered field can be written

$$\mathbf{E}^{\text{scat}}(r', \zeta', \xi') = |p|\frac{k^2}{r'}e^{ikr'}\begin{pmatrix} 1 - \sin^2\zeta'\cos^2\xi' \\ -\sin^2\zeta'\cos\xi'\sin\xi' \\ -\cos\zeta'\sin\zeta'\cos\xi' \end{pmatrix}. \tag{2.4}$$

Calculation can be simplified by assuming negligible radiated field perpendicular to the radial propagation axis. To do this, we decompose the scattered dipole field into angular components $\mathbf{E}^{\text{scat}}(r' = f', \zeta', \xi') = E_r'\hat{\mathbf{r}}' + E_{\zeta'}\hat{\boldsymbol{\zeta}}' + E_{\xi'}\hat{\boldsymbol{\xi}}'$ and drop $E_{r'}$. Representing the spherical unit vectors in a Cartesian basis, we take

$$\mathbf{E}^{\text{scat}}(r' = f', \zeta', \xi') = E_{\zeta'}\begin{pmatrix} \cos\zeta'\cos\xi' \\ \cos\zeta'\sin\xi' \\ -\sin\zeta' \end{pmatrix} + E_{\xi'}\begin{pmatrix} -\sin\xi' \\ \cos\xi' \\ 0 \end{pmatrix} \tag{2.5}$$

where

$$E_{\zeta'}\left(|p|\frac{k^2}{f'}e^{ikf'}\right)^{-1} = \hat{\boldsymbol{\zeta}}' \cdot \begin{pmatrix} 1 - \sin^2\zeta'\cos^2\xi' \\ -\sin^2\zeta'\cos\xi'\sin\xi' \\ -\cos\zeta'\sin\zeta'\cos\xi' \end{pmatrix} \tag{2.6}$$

$$= (1 - \sin^2\zeta'\cos^2\xi')(\cos\zeta'\cos\xi') \tag{2.7}$$
$$+ (-\sin^2\zeta'\cos\xi'\sin\xi')(\cos\zeta'\sin\xi')$$
$$+ (-\cos\zeta'\sin\zeta'\cos\xi')(-\sin\zeta')$$

$$= (1 - \underbrace{\sin^2\zeta'\cos^2\xi' + \sin^2\zeta'\sin^2\xi'}_{\sin^2\zeta'})(\cos\zeta'\cos\xi') \tag{2.8}$$
$$+ (-\cos\zeta'\sin\zeta'\cos\xi')(-\sin\zeta')$$

$$= \cos^2\zeta'\cos\zeta'\cos\xi' + \sin^2\zeta'\cos\zeta'\cos\xi' \tag{2.9}$$

$$= \cos\zeta'\cos\xi' \tag{2.10}$$

and

$$E_{\xi'}\left(|p|\frac{k^2}{f'}e^{ikf'}\right)^{-1} = \hat{\boldsymbol{\xi}}' \cdot \begin{pmatrix} 1-\sin^2\zeta'\cos^2\xi' \\ -\sin^2\zeta'\cos\xi'\sin\xi' \\ -\cos\zeta'\sin\zeta'\cos\xi' \end{pmatrix} \tag{2.11}$$

$$= (1-\sin^2\zeta'\cos^2\xi')(-\sin\xi') \tag{2.12}$$
$$+ (-\sin^2\zeta'\cos\xi'\sin\xi')(\cos\xi')$$

$$= \sin\xi'(\sin^2\zeta'\cos^2\xi' - 1 - \sin^2\zeta'\cos^2\xi') \tag{2.13}$$

$$= -\sin\xi' \tag{2.14}$$

For the purpose of integration, it will be useful to sort the scattered field at the objective into ζ and ξ components,

$$\mathbf{E}^{\text{scat}}(r'=f',\zeta',\xi') = |p|\frac{k^2}{f'}e^{ikf'}\left[\cos\zeta'\cos\xi'\begin{pmatrix}\cos\zeta'\cos\xi'\\ \cos\zeta'\sin\xi'\\ -\sin\zeta'\end{pmatrix} - \sin\xi'\begin{pmatrix}-\sin\xi'\\ \cos\xi'\\ 0\end{pmatrix}\right] \tag{2.15}$$

$$= |p|\frac{k^2}{f'}e^{ikf'}\left[\begin{pmatrix}\cos^2\zeta'\\ \cos^2\zeta'\\ -\cos\zeta'\sin\zeta'\end{pmatrix}\begin{pmatrix}\cos^2\xi'\\ \cos\xi'\sin\xi'\\ \cos\xi'\end{pmatrix} + \begin{pmatrix}\sin^2\xi'\\ -\sin\xi'\cos\xi'\\ 0\end{pmatrix}\right] \tag{2.16}$$

The focused field at the top lens is simply related to the scattered field at the objective by the relation

$$\mathbf{E}^{\text{foc}}(r=f,\zeta,\xi) = \sqrt{\frac{\cos\zeta}{\cos\zeta'}}\mathbf{E}^{\text{scat}}(r'=f',\zeta',\xi') \tag{2.17}$$

because only components transverse to the refractive surfaces remain. The two polar angles ζ and ζ' are defined by the geometry in figure Fig. 2.1 (b), $\sin\zeta = (f'/f)\sin\zeta'$ and the azimuthal angles satisfy $\xi = \pi - \xi'$ to establish both coordinate systems as right handed.

We can now write the integral for the focused+diffracted field with all integration variable dependence made explicit,

$$\mathbf{E}(\rho,\varphi,z) = -\frac{ikfe^{ikf}}{2\pi}\frac{|p|k^2}{f'}e^{ikf'}\int_0^{\zeta_m} d\zeta \sin\zeta\sqrt{\frac{\cos\zeta}{\cos\zeta'}}e^{ik(z-h)\cos\zeta}$$
$$\int_0^{2\pi} d\xi \left[\begin{pmatrix}\cos^2\zeta\\ \cos^2\zeta\\ -\cos\zeta\sin\zeta\end{pmatrix}\begin{pmatrix}\cos^2\xi\\ -\cos\xi\sin\xi\\ \cos\xi\end{pmatrix} + \begin{pmatrix}\sin^2\xi\\ \sin\xi\cos\xi\\ 0\end{pmatrix}\right] e^{ik\rho\sin\zeta\cos(\varphi-\xi)}. \quad (2.18)$$

where we have utilized the trigonometric identities[1],

$$\cos^2(\pi-\xi) = \cos^2\xi, \quad (2.19)$$
$$\sin^2(\pi-\xi) = \sin^2\xi, \quad (2.20)$$
$$-\sin(\pi-\xi)\cos(\pi-\xi) = \sin\xi\cos\xi. \quad (2.21)$$

To obtain a simple closed form for the image fields, the numerical aperture is fixed at NA = 1 and the magnification the magnification is also set by, $f/f' = 1$. The effect of magnification can be restored mathematically by choosing a small, high-resolution image detection plane [67], but the choice of numerical aperture is a compromise. Under these conditions, Eq. 2.18 can be simplified to

$$\mathbf{E}(\rho,\varphi,z) = -\frac{ik^3|p|e^{i2kf}}{2\pi}\int_0^{\zeta_m} d\zeta \sin\zeta e^{ik(z-h)\cos\zeta}$$
$$\left[\begin{pmatrix}\cos^2\zeta\\ \cos^2\zeta\\ -\cos\zeta\sin\zeta\end{pmatrix}\int_0^{2\pi} d\xi \begin{pmatrix}\cos^2\xi\\ -\cos\xi\sin\xi\\ \cos\xi\end{pmatrix} e^{ik\rho\sin\zeta\cos(\varphi-\xi)}\right.$$
$$\left. + \int_0^{2\pi} d\xi \begin{pmatrix}\sin^2\xi\\ \sin\xi\cos\xi\\ 0\end{pmatrix} e^{ik\rho\sin\zeta\cos(\varphi-\xi)}\right], \quad (2.22)$$

[1]Note that these identities flip the sign of the y component relative to what I have in Chapter 5. If I remember correctly this sign flip can also be attributed the the matching of focal space and objective space spherical coordinates, and I believe the expression here is more accurate.

which can be integrated in ξ. Performing each integral separately, note that each term component splits into the following two integrals by relation $\cos(\varphi - \xi) = \cos\varphi\cos\xi + \sin\varphi\sin\xi$.

$$\int_0^{2\pi} d\xi\ \sin^2\xi e^{ik\rho\sin\zeta\cos(\varphi-\xi)} = 2\pi\left(\frac{J_1(k\rho\sin\zeta)}{k\rho\sin\zeta}\cos(2\varphi) + J_0(k\rho\sin\zeta)\sin^2\varphi\right), \quad (2.23)$$

$$\int_0^{2\pi} d\xi\ \cos^2\xi e^{ik\rho\sin\zeta\cos(\varphi-\xi)} = 2\pi\left(-\frac{J_1(k\rho\sin\zeta)}{k\rho\sin\zeta}\cos(2\varphi) + J_0(k\rho\sin\zeta)\cos^2\varphi\right), \quad (2.24)$$

$$\int_0^{2\pi} d\xi\ \sin\xi\cos\xi e^{ik\rho\sin\zeta\cos(\varphi-\xi)} = -2\pi J_2(k\rho\sin\zeta)\cos\varphi\sin\varphi, \quad (2.25)$$

$$\int_0^{2\pi} d\xi\ \sin\xi e^{ik\rho\sin\zeta\cos(\varphi-\xi)} = 2i\pi J_1(k\rho\sin\zeta)\sin\varphi, \quad (2.26)$$

$$\int_0^{2\pi} d\xi\ \cos\xi e^{ik\rho\sin\zeta\cos(\varphi-\xi)} = 2i\pi J_1(k\rho\sin\zeta)\cos\varphi, \quad (2.27)$$

and we can write the focused+diffracted field with only one integral remaining,

$$\mathbf{E}(\rho,\varphi,z) = -\frac{ik^3|p|e^{i2kf}}{2\pi}\int_0^{\zeta_m} \tilde{d\zeta}\sin\zeta e^{ik(z-h)\cos\zeta} \\ 2\pi\left[\begin{pmatrix}\cos^2\zeta\\ \cos^2\zeta\\ -\cos\zeta\sin\zeta\end{pmatrix}\begin{pmatrix}J_0(k\rho\sin\zeta)\cos^2\varphi - \frac{J_1(k\rho\sin\zeta)}{k\rho\sin\zeta}\cos(2\varphi)\\ J_2(k\rho\sin\zeta)\cos\varphi\sin\varphi\\ iJ_1(k\rho\sin\zeta)\cos\varphi\end{pmatrix}\right. \\ \left. + \begin{pmatrix}J_0(k\rho\sin\zeta)\sin^2\varphi + \frac{J_1(k\rho\sin\zeta)}{k\rho\sin\zeta}\cos(2\varphi)\\ -J_2(k\rho\sin\zeta)\cos\varphi\sin\varphi\\ 0\end{pmatrix}\right]. \quad (2.28)$$

A failed attempt at NA generalization

Here, we will take a brief interlude to discuss a failed attempt at generalizing the numerical aperture based on a paper (I think) I once read and then was never able to find again. Don't worry, we will return to the relative simplicity of NA = 1 shortly, but I think this would be a great project for a mathematically inclined future graduate student because I think it is possible and will be useful. To compute the integral analytically for arbitrary numerical aperture, we take $\zeta \to \frac{2\zeta_m}{\pi}\tilde{\zeta}$ so that the integration in $\tilde{\zeta}$ runs from 0 to $\pi/2$ with differential

$\mathrm{d}\tilde{\zeta} = \mathrm{d}\zeta \frac{\pi/2}{\zeta_m}$.

$$\mathbf{E}(\rho,\varphi,z) = -\frac{ik^3|p|e^{i2kf}}{2\pi}\int_0^{\frac{\pi}{2}} \mathrm{d}\tilde{\zeta}\frac{2\zeta_m}{\pi}\sin[\tfrac{2\zeta_m}{\pi}\tilde{\zeta}]e^{ik(z-h)\cos[\frac{2\zeta_m}{\pi}\tilde{\zeta}]}$$
$$2\pi\left[\begin{pmatrix}\cos^2[\frac{2\zeta_m}{\pi}\tilde{\zeta}]\\ \cos^2[\frac{2\zeta_m}{\pi}\tilde{\zeta}]\\ -\cos[\frac{2\zeta_m}{\pi}\tilde{\zeta}]\sin[\frac{2\zeta_m}{\pi}\tilde{\zeta}]\end{pmatrix}\begin{pmatrix}J_0(k\rho\sin[\frac{2\zeta_m}{\pi}\tilde{\zeta}])\cos^2\varphi - \frac{J_1(k\rho\sin[\frac{2\zeta_m}{\pi}\tilde{\zeta}])}{k\rho\sin[\frac{2\zeta_m}{\pi}\tilde{\zeta}]}\cos(2\varphi)\\ J_2(k\rho\sin[\frac{2\zeta_m}{\pi}\tilde{\zeta}])\cos\varphi\sin\varphi\\ iJ_1(k\rho\sin[\frac{2\zeta_m}{\pi}\tilde{\zeta}])\cos\varphi\end{pmatrix}\right.$$
$$\left. + \begin{pmatrix}J_0(k\rho\sin[\frac{2\zeta_m}{\pi}\tilde{\zeta}])\sin^2\varphi + \frac{J_1(k\rho\sin[\frac{2\zeta_m}{\pi}\tilde{\zeta}])}{k\rho\sin[\frac{2\zeta_m}{\pi}\tilde{\zeta}]}\cos(2\varphi)\\ -J_2(k\rho\sin[\frac{2\zeta_m}{\pi}\tilde{\zeta}])\cos\varphi\sin\varphi\\ 0\end{pmatrix}\right]. \quad (2.29)$$

We can then take the substitution $\beth = \frac{1}{\sin\zeta_m}\sin(\frac{2\zeta_m}{\pi}\tilde{\zeta})$ and $\mathrm{d}\beth = \frac{2\zeta_m/\pi}{\sin\zeta_m}\cos(\frac{2\zeta_m}{\pi}\tilde{\zeta})\mathrm{d}\tilde{\zeta}$. The differential element can be converted by the relation

$$\mathrm{d}\tilde{\zeta} = \mathrm{d}\beth\frac{1}{\cos(\frac{2\zeta_m}{\pi}\tilde{\zeta})}\frac{\pi\sin\zeta_m}{2\zeta_m} = \frac{\mathrm{d}\beth}{(1-\sin^2\zeta_m\beth^2)^{1/2}}\frac{\pi\sin\zeta_m}{2\zeta_m} \quad (2.30)$$

which is not going to lead to integrable expressions, dangit.

Back to safety

So here we retreat to $\zeta_m \to \pi/2$ or equivalently the numerical aperture to 1. Under this approximation $\tilde{\zeta} = \zeta$ and the integration variables transform as

$$\sin\left(\frac{2\zeta_m}{\pi}\zeta\right) \to \sin(\zeta) \to \beth \quad (2.31)$$
$$\cos(\zeta) \to (1-\beth^2)^{1/2} \quad (2.32)$$
$$\mathrm{d}\zeta \to \frac{\mathrm{d}\beth}{(1-\beth^2)^{1/2}} \quad (2.33)$$

The integral can then be written in terms of Bessel functions.

$$\begin{aligned}
\mathbf{E}(\rho,\varphi,z) = & -\frac{ik^3|p|e^{i2kf}}{2\pi}\int_0^1 \mathrm{d}\beth \frac{\beth}{(1-\beth^2)^{1/2}} e^{ik(z-h)\sqrt{1-\beth^2}} \\
& 2\pi\left[\begin{pmatrix} 1-\beth^2 \\ 1-\beth^2 \\ -\sqrt{1-\beth^2}\beth \end{pmatrix}\begin{pmatrix} J_0(k\rho\beth)\cos^2\varphi - \frac{J_1(k\rho\beth)}{k\rho\beth}\cos(2\varphi) \\ J_2(k\rho\beth)\cos\varphi\sin\varphi \\ iJ_1(k\rho\beth)\cos\varphi \end{pmatrix}\right. \\
& \left. + \begin{pmatrix} J_0(k\rho\beth)\sin^2\varphi + \frac{J_1(k\rho\beth)}{k\rho\beth}\cos(2\varphi) \\ -J_2(k\rho\beth)\cos\varphi\sin\varphi \\ 0 \end{pmatrix}\right] \qquad (2.34) \\
= & -ik^3|p|e^{i2kf}\sin\zeta_m \int_0^1 \mathrm{d}\beth \frac{\beth}{(1-\beth^2)^{1/2}} e^{ik(z-h)\sqrt{1-\beth^2}} \\
& \begin{pmatrix} J_0(k\rho\beth)[1-\beth^2\cos^2\varphi] + \beth\frac{J_1(k\rho\beth)}{k\rho}\cos(2\varphi) \\ -\beth^2 J_2(k\rho\beth)\cos\varphi\sin\varphi \\ -i\beth\sqrt{1-\beth^2}J_1(k\rho\beth)\cos\varphi \end{pmatrix} \qquad (2.35) \\
= & -ik^3|p|e^{i2kf}\sin\zeta_m \int_0^1 e^{ik(z-h)\sqrt{1-\beth^2}} \\
& \begin{pmatrix} J_0(k\rho\beth)\frac{\beth[1-\beth^2\cos^2\varphi]}{(1-\beth^2)^{1/2}} + \frac{\beth^2}{(1-\beth^2)^{1/2}}\frac{J_1(k\rho\beth)}{k\rho}\cos(2\varphi) \\ \frac{-\beth^3}{(1-\beth^2)^{1/2}}J_2(k\rho\beth)\cos\varphi\sin\varphi \\ -i\beth^2 J_1(k\rho\beth)\cos\varphi \end{pmatrix}. \qquad (2.36)
\end{aligned}$$

Evaluating the diffracted field in the focal plane defined by $z = h$, the remaining phase in the integrand disappears and the integrals can be evaluated using the following,

$$\int_0^1 \mathrm{d}\beth \frac{\beth}{(1-\beth^2)^{1/2}} J_0(k\rho\beth) = \frac{\sin(k\rho)}{k\rho} \qquad (2.37)$$

$$-\int_0^1 \mathrm{d}\beth \frac{\beth^3}{(1-\beth^2)^{1/2}} J_0(k\rho\beth) = -\frac{k\rho\cos[k\rho] + (-1+k^2\rho^2)\sin[k\rho]}{k^3\rho^3} \qquad (2.38)$$

$$\int_0^1 \mathrm{d}\beth \frac{\beth^2}{(1-\beth^2)^{1/2}} \frac{J_1(k\rho\beth)}{k\rho} = \frac{-k\rho\cos[k\rho] + \sin[k\rho]}{k^2\rho^2} \qquad (2.39)$$

$$-\int_0^1 \mathrm{d}\beth \frac{\beth^3}{(1-\beth^2)^{1/2}} J_2(k\rho\beth) = \frac{3k\rho\cos[k\rho] + (-3+k^2\rho^2)\sin[k\rho]}{k^3\rho^3} \qquad (2.40)$$

$$-i\int_0^1 \mathrm{d}\beth\, \beth^2 J_1(k\rho\beth) = -\frac{iJ_2(k\rho)}{k\rho} \qquad (2.41)$$

$$\mathbf{E}(\rho,\varphi,z=h) = -ik^3|p|e^{i2kf}\int_0^1 \begin{pmatrix} J_0(k\rho\beth)\frac{\beth[1-\beth^2\cos^2\varphi]}{(1-\beth^2)^{1/2}} + \frac{\beth^2}{(1-\beth^2)^{1/2}}\frac{J_1(k\rho\beth)}{k\rho}\cos(2\varphi) \\ \frac{-\beth^3}{(1-\beth^2)^{1/2}}J_2(k\rho\beth)\cos\varphi\sin\varphi \\ -i\beth^2 J_1(k\rho\beth)\cos\varphi \end{pmatrix} \tag{2.42}$$

$$= -ik^3|p|e^{i2kf}\begin{pmatrix} \frac{\sin(k\rho)}{k\rho} - \left[\frac{\cos(k\rho)}{k^2\rho^2} - \frac{\sin(k\rho)}{k^3\rho^3} + \frac{\sin(k\rho)}{k\rho}\right]\cos^2\varphi - \left[\frac{\cos(k\rho)}{k^2\rho^2} - \frac{\sin(k\rho)}{k^3\rho^3}\right]\cos(2\varphi) \\ \frac{3k\rho\cos(k\rho)}{k^3\rho^3} + \frac{(-3+k^2\rho^2)\sin(k\rho)}{k^3\rho^3}\cos\varphi\sin\varphi \\ -i\frac{J_2(k\rho)}{k\rho}\cos\varphi \end{pmatrix} \tag{2.43}$$

$$= -ik^3|p|e^{i2kf}\begin{pmatrix} \frac{\sin(k\rho)}{k\rho}\left[1-\cos^2\varphi\right] - \left[\frac{\cos(k\rho)}{k^2\rho^2} - \frac{\sin(k\rho)}{k^3\rho^3}\right]\left[\cos(2\varphi)+\cos^2\varphi\right] \\ \frac{3k\rho\cos(k\rho)}{k^3\rho^3} + \frac{(-3+k^2\rho^2)\sin(k\rho)}{k^3\rho^3}\cos\varphi\sin\varphi \\ -i\frac{J_2(k\rho)}{k\rho}\cos\varphi \end{pmatrix} \tag{2.44}$$

$$= -ik^3|p|e^{i2kf}\begin{pmatrix} j_0(k\rho)\sin^2\varphi + \frac{j_1(k\rho)}{k\rho}\left[\cos(2\varphi)+\cos^2\varphi\right] \\ -j_2(k\rho)\cos\varphi\sin\varphi \\ -i\frac{J_2(k\rho)}{k\rho}\cos\varphi \end{pmatrix} \quad \blacksquare \tag{2.45}$$

which only differs by a sign (or term of complex modulus 1) from the result we have published.

The published result for the image field in the focal plane produced by a single dipole source with moment magnitude p_x located along the optical axis ($\hat{\mathbf{e}}_z$) and oriented in the $\hat{\mathbf{e}}_x$ direction is

$$\mathbf{E}^{\text{published}}_{p_x}(\rho,\varphi,z=h) = -ik^3e^{2ikf}p_x\begin{pmatrix} [\cos^2(\varphi)+\cos(2\varphi)]\frac{j_1(k\rho)}{k\rho} + \sin(\varphi)^2 j_0(k\rho) \\ \sin(\varphi)\cos(\varphi)j_2(k\rho) \\ -\cos(\varphi)\frac{J_2(k\rho)}{k\rho} \end{pmatrix}, \tag{2.46}$$

where the dipole moment points at an angle ψ relative to $\hat{\mathbf{e}}_x$.

To express the field of an arbitrarily oriented dipole, this expression must be rotated. For a dipole $\mathbf{p} = |p|(\cos\psi_p\hat{\mathbf{e}}_x + \sin\psi_p\hat{\mathbf{e}}_y)$ oriented in the focal plane at an angle ψ_p from the x-axis, the generalized image field can be written in terms of Eq. 2.46 as

$$\mathbf{E}^{\text{im}}(\rho,\varphi,z=h;\psi_p) = \mathbf{R}(\psi_p)\cdot\mathbf{E}^{\text{im}}_{p_x}(\rho,\varphi-\psi_p,z=h), \tag{2.47}$$

where the rotation matrix is defined by

$$\mathbf{R}(\psi) = \begin{pmatrix} \cos\psi & -\sin\psi & 0 \\ \sin\psi & \cos\psi & 0 \\ 0 & 0 & 1 \end{pmatrix} . \tag{2.48}$$

Dipole aligned along the optical axis

For a dipole oriented along the optical axis, $\mathbf{p} = |p|\hat{e}_z$ and the scattered dipole field can be written by taking Eq. 2.2 and plugging in the specific dipole orientation vector and observation unit in spherical coordinates,

$$\mathbf{E}^{\text{scat}}(r', \zeta', \xi') = |p|\frac{k^2}{r'}e^{ikr'}\left[\begin{pmatrix} 0 \\ 0 \\ 1 \end{pmatrix} - \begin{pmatrix} \sin\zeta'\cos\xi' \\ \sin\zeta'\sin\xi' \\ \cos\zeta' \end{pmatrix}\cos\zeta'\right] . \tag{2.49}$$

Following from Eq. 2.5, we define the transverse field components in spherical coordinates by vector multiplying the total field into the spherical unit vectors,

$$E_{\zeta'}\left(|p|\frac{k^2}{f'}e^{ikf'}\right)^{-1} = \begin{pmatrix} -\sin\zeta'\cos\xi'\cos\zeta' \\ -\sin\zeta'\sin\xi'\cos\zeta' \\ 1-\cos^2\zeta' \end{pmatrix} \cdot \begin{pmatrix} \cos\zeta'\cos\xi' \\ \cos\zeta'\sin\xi' \\ -\sin\zeta' \end{pmatrix} \tag{2.50}$$

$$= \sin\zeta'\left[-\cos^2\xi'\cos^2\zeta' - \sin^2\xi'\cos^2\zeta' + \sin^2\zeta'\right] \tag{2.51}$$

$$= \sin\zeta'\left[-\cos^2\zeta' - \sin^2\zeta'\right] \tag{2.52}$$

$$= -\sin\zeta' , \tag{2.53}$$

$$E_{\xi'}\left(|p|\frac{k^2}{f'}e^{ikf'}\right)^{-1} = \begin{pmatrix} -\sin\zeta'\cos\xi'\cos\zeta' \\ -\sin\zeta'\sin\xi'\cos\zeta' \\ 1-\cos^2\zeta' \end{pmatrix} \cdot \begin{pmatrix} -\sin\xi' \\ \cos\xi' \\ 0 \end{pmatrix} \tag{2.54}$$

$$= \sin\zeta'\left[\cancel{\cos\xi'\sin\xi'\cos\zeta'} - \cancel{\sin\xi'\cos\xi'\cos\zeta'}\right] \tag{2.55}$$

$$= 0 . \tag{2.56}$$

Plugging these components into the scattered field we arrive at

$$\mathbf{E}^{\text{scat}}(r'=f',\zeta',\xi') = |p|\frac{k^2}{f'}e^{ikf'}\sin\zeta'\begin{pmatrix}-\cos\zeta'\cos\xi'\\-\cos\zeta'\sin\xi'\\\sin\zeta'\end{pmatrix}. \tag{2.57}$$

This expression can now be related to the image space coordinates as in Eq. 2.17, the diffraction integral can be written,

$$\mathbf{E}(\rho,\varphi,z) = -\frac{ik^3e^{2ikf}}{2\pi}|p|\int_0^{\zeta_m} d\zeta\sin\zeta\sqrt{\frac{\cos\zeta}{\cos\zeta'}}e^{ik(z-h)\cos\zeta} \int_0^{2\pi} d\xi\ \sin\zeta\begin{pmatrix}\cos\zeta\cos\xi\\-\cos\zeta\sin\xi\\\sin\zeta\end{pmatrix}e^{ik\rho\sin\zeta\cos(\varphi-\xi)}. \tag{2.58}$$

where we have utilized the fact that

$$\sin\xi' = \sin\xi \tag{2.59}$$

$$\cos\xi' = -\cos\xi. \tag{2.60}$$

We can then take the ξ integrals using the relations defined in Eqs. 2.23-2.27 along with

$$\int_0^{2\pi} d\xi\, e^{ik\rho\sin\zeta\cos(\varphi-\xi)} = 2\pi J_0(k\rho\sin\zeta) \tag{2.61}$$

for the z component, yielding,

$$\mathbf{E}(\rho,\varphi,z) = -\frac{ik^3e^{2ikf}}{2\pi}|p|\int_0^{\zeta_m} d\zeta\sin^2\zeta e^{ik(z-h)\cos\zeta}\begin{pmatrix}2i\pi J_1(k\rho\sin\zeta)(\cos\zeta\cos\varphi)\\2i\pi J_1(k\rho\sin\zeta)(-\cos\zeta\sin\varphi)\\2\pi J_0(k\rho\sin\zeta)\sin\zeta\end{pmatrix}. \tag{2.62}$$

Making the variable substitution outlined in Eqs. 2.31-2.33,

$$\mathbf{E}(\rho,\varphi,z) = -\frac{ik^3e^{2ikf}}{2\pi}|p|\int_0^1 \frac{\mathrm{d}\beth}{(1-\beth^2)^{1/2}}\beth^2 e^{ik(z-h)(1-\beth^2)^{1/2}} \xrightarrow{z-h=0} \times \begin{pmatrix} 2i\pi J_1(k\rho\beth)(1-\beth^2)^{1/2}\cos\varphi \\ -2i\pi J_1(k\rho\beth)(1-\beth^2)^{1/2}\sin\varphi \\ 2\pi J_0(k\rho\beth)\beth \end{pmatrix}. \tag{2.63}$$

$$= -\frac{ik^3e^{2ikf}}{2\pi}|p|\int_0^1 \mathrm{d}\beth \begin{pmatrix} 2i\pi\beth^2 J_1(k\rho\beth)\cos\varphi \\ -2i\pi\beth^2 J_1(k\rho\beth)\sin\varphi \\ 2\pi J_0(k\rho\beth)\frac{\beth^3}{(1-\beth^2)^{1/2}} \end{pmatrix}. \tag{2.64}$$

Then using the integral relations in Eqs. 2.37-2.41, the image space fields can be written as

$$\mathbf{E}(\rho,\varphi,z) = -ik^3|p|e^{2ikf}\begin{pmatrix} i\frac{J_2(k\rho)}{k\rho}\cos\varphi \\ -i\frac{J_2(k\rho)}{k\rho}\sin\varphi \\ \frac{k\rho\cos[k\rho]+(-1+k^2\rho^2)\sin[k\rho]}{k^3\rho^3} \end{pmatrix}. \tag{2.65}$$

This final expression can be simplified in terms of spherical Bessel functions using the relations

$$\frac{\sin x}{x} = j_0(x) \tag{2.66}$$

$$-\frac{\cos x + x\sin x}{x^2} = y_1(x)\ , \tag{2.67}$$

yielding our fianl result for the z oriented dipole,

$$\mathbf{E}(\rho,\varphi,z) = -ik^3|p|e^{2ikf}\begin{pmatrix} i\frac{J_2(k\rho)}{k\rho}\cos\varphi \\ -i\frac{J_2(k\rho)}{k\rho}\sin\varphi \\ -y_1(k\rho)-\frac{j_0(k\rho)}{(k\rho)^2} \end{pmatrix}. \quad \blacksquare \tag{2.68}$$

Chapter 3

MODELING THE PLASMON RESONANCE AND ITS ELECTROMAGNETIC INTERACTION WITH A NEIGHBORING MOLECULE

In this chapter, we shift from modeling the far-field optics responsible for image formation and shift to the nanoscale. We will build the fundamental mathematical tools used in the rest of this dissertation for describing the plasmon resonance and it's interactions with emitters as well as it's environment. These interactions are considered dipolar, which is adequate for our purposes.

3.1 The plasmon resonance as an oscillating electric dipole: Modeling the linear polarizability

This section first outlines the derivation of the quasi-static polarizability from Ref. [25] and then modifies the expression for the modified long-wavelength approximation derived in Ref. [104] for better accuracy with particles on the 100 nm scale. The Drude model is then introduced and combined with the sphere polarizability to demonstrate correspondence between the formalism used here and the oscillator representation of the localized surface plasmon resonance.

Quasi-static polarizability of spherical and spheroidal particles

The polarizability of the nanorod is approximated by the analytic solution to Maxwell's equations on a prolate spheroid in the quasi-static limit. In this limit, Maxwell's equations, which govern electrodynamics, reduce to Poisson's equation for the electrostatic potential Φ.

In an isotropic linear medium defined by the relative electric permittivity ϵ,

$$\nabla^2\Phi = 4\pi\frac{\rho}{\epsilon} \tag{3.1}$$

in Gaussian (or CGS) units. To define the polarizability, we ask for the field induced by polarization of the particle given a spatially constant field. Placing particle is at the coordinate origin, we may define the incident field in spherical coordinates as:

$$\lim_{r\to\infty}\Phi = -E_0 r\cos\theta = -E_0 z. \tag{3.2}$$

In order to solve for the potential induced by this field, the free charge in Eq. (3.1) is $\rho = 0$ everywhere. The potential inside and outside the particle must obey the boundary conditions:

$$\Phi_{\text{in}}|_S = \Phi_{\text{out}}|_S, \qquad \epsilon\left.\frac{\mathrm{d}\Phi_{\text{in}}}{\mathrm{d}n}\right|_S = \epsilon_b\left.\frac{\mathrm{d}\Phi_{\text{out}}}{\mathrm{d}n}\right|_S, \tag{3.3}$$

at the surface of the particle. in terms of the coordinate normal to the surface defined by unit vector $\mathbf{n} = n\hat{n}$.

The above differential equation and boundary conditions can be solved analytically for the case of a perfectly spherical particle. If the sphere is assumed to have radius a, the potential inside and out can be shown to be:

$$\Phi_{\text{in}} = -\frac{3\epsilon_b}{\epsilon+2\epsilon_b}E_0 r\cos\theta, \tag{3.4}$$

$$\Phi_{\text{out}} = -E_0 r\cos\theta + a^3\frac{\epsilon-\epsilon_b}{\epsilon+2\epsilon_b}\frac{\cos\theta}{r^2}E_0, \tag{3.5}$$

by matching coefficients of the spherical harmonic expansion. The potential outside the sphere is found to be that of the incident field plus the potential of an ideal point dipole:

$$\Phi_p = \frac{p\cos\theta}{\epsilon_b r^2} = \frac{\mathbf{p}\cdot\mathbf{r}}{\epsilon_b r^3} \tag{3.6}$$

with dipole moment,

$$\mathbf{p} = a^3\frac{\epsilon-\epsilon_b}{\epsilon+2\epsilon_b}\mathbf{E}_0. \tag{3.7}$$

Defining the polarizability α to be the constant of proportionality between the incident field and the induced dipole,

$$\mathbf{p} = \alpha \mathbf{E}_0, \tag{3.8}$$

$$\alpha = a^3 \frac{\epsilon - \epsilon_b}{\epsilon + 2\epsilon_b}. \tag{3.9}$$

A similar but less transparent procedure leads to the polarizability of a prolate spheroid. In this case, the polarizability is not isotropic, and Eq. (3.8) must be written $\mathbf{p} = \boldsymbol{\alpha} \cdot \mathbf{E}$. The dyadic polarizability is diagonal in the Cartesian basis with unit vectors aligned with the prolate spheroid's principal axes. If the long semi-radius is aligned along $\hat{e}_x$,

$$\boldsymbol{\alpha}^{\mathrm{QS}} = \begin{pmatrix} \alpha_a^{\mathrm{QS}} & 0 & 0 \\ 0 & \alpha_b^{\mathrm{QS}} & 0 \\ 0 & 0 & \alpha_b^{\mathrm{QS}} \end{pmatrix} \tag{3.10}$$

where α_a is the polarizability along the long axis of the spheroid with semi-radius a and α_b is polarizability of the degenerate short axis with radius b. With total volume $V = \frac{4\pi}{3} a b^2$, the principal components of the polarizability are:

$$\alpha_i^{\mathrm{QS}} = \frac{V}{4\pi} \frac{\epsilon_r - 1}{1 + L_i(\epsilon_r - 1)}, \tag{3.11}$$

where $\epsilon_r \equiv \epsilon/\epsilon_b$. The geometric factors L_i are defined by,

$$L_a = \frac{1 - e^2}{e^3}(-1 + \frac{1}{2e} \ln \frac{1 + e}{1 - e}), \tag{3.12}$$

$$L_b = \frac{1 - L_a}{2}, \tag{3.13}$$

where $e^2 = 1 - \frac{a^2}{b^2}$ is the eccentricity.

Accounting for electromagnetic retardation: the modified long-wavelength approximation

The quasi-static approximation provides a good model for the plasmonic response of noble metal nanoparticles, but does not show quantitative agreement with experiment for metal particles larger than ~ 10 nm in size. For the highly symmetric particles like the spheroid, the

full electrodynamic optical response consistent with Maxwell's equations can be written in analytic form using a modified Mie theory. What results from this procedure are the scattered fields expressed as series expansions in vectorized spherical harmonics, which obscure the dynamics of the plasmon resonance. A compromise between the transparent quasistatic approximation and rigorous scattering theory can be had by expanding the Mie coefficient describing dipole scattering about small wavenumber k and obtaining corrections to the quasistatic result. In terms of the components of the quasi-static polarizability $\alpha^{\mathrm{QS}}(\omega)$ defined in Eq. 3.11, the polarizability in the modified long-wavelength approximation is obtained by expanding each Bessel function inside the Mie coefficient to third order in k:

$$\alpha_i^{\mathrm{ML}}(\omega)\frac{\alpha_i^{\mathrm{QS}}(\omega)}{1-\frac{k^2}{l_{E,i}}D_i\alpha_i^{\mathrm{QS}}(\omega)-i\frac{2k^3}{3}\alpha_i^{\mathrm{QS}}(\omega)}, \tag{3.14}$$

for incident light polarized along the ith principal axis of the spheroid. The newly introduced geometric factors D_i are shorthand for:

$$D_a=\frac{3}{4}\left(\frac{1+e^2}{1-e^2}L_a+1\right), \tag{3.15}$$

$$D_b=\left(\frac{3}{e}\operatorname{arctanh}e-D_a\right)\frac{a}{2b}. \tag{3.16}$$

Modeling the material: Drude model of the metal permittivity

While the polarizability is generated by the geometry of the particle, the permittivity or dielectric function $\epsilon(\omega)$ encodes the material's inherent frequency dependent optical response. The simplest model for $\epsilon(\omega)$ of a metal is related to Paul Drude's 1900 model of electrical conduction. Here, we follow the derivation in Jackson [80] that starts with a more general model for an insulating material. In this case the optically active electrons are considered bound, but we will later free each electron from it's respective nucleus to model the conduction electrons in a metal.

We start by describing the classical motion of a single electron with charge $-e$ harmonically bound to some atomic nucleus and under influence of an external electric field $\mathbf{E}$. In the long-wavelength approximation that we are accustomed to working in when dealing with

nanoparticles, the field will be treated as spatially independent and the electron will obey the equation of motion:

$$m[\ddot{\mathbf{x}} + \gamma\dot{\mathbf{x}} + \omega_0^2\mathbf{x}] = -e\mathbf{E}e^{-i\omega t}, \tag{3.17}$$

where γ quantifies the phenomenological damping which may be due to radiation, electron-nuclear scattering, or electron-electron scattering. If the incident field varies harmonically with frequency in time ω as $e^{-i\omega t}$, than the dipole contributed by one electron can be written:

$$\mathbf{p} = -e\mathbf{x} = \frac{e^2}{m}\frac{\mathbf{E}}{\omega_0^2 - \omega^2 - i\omega\gamma}. \tag{3.18}$$

If we then suppose that our material consists of N molecules/nuclei per unit volume each with Z electrons, each with their own binding frequency ω_j and damping γ_j, the dipole per molecule is defined:

$$\mathbf{p}_{\text{mol}} = \sum_j^Z \frac{e^2}{m}\frac{\mathbf{E}}{\omega_j^2 - \omega^2 - i\omega\gamma_j}. \tag{3.19}$$

Then the polarization density becomes,

$$\mathbf{P} = \frac{\mathbf{p}_{\text{mol}}}{V_{\text{mol}}} = N\sum_j^Z \frac{e^2}{m}\frac{\mathbf{E}}{\omega_j^2 - \omega^2 - i\omega\gamma_j}, \tag{3.20}$$

which is often written in terms of an oscillator strength f_j, characterizing the number of electrons per molecule with the same resonance frequency and damping.

The polarization density $\mathbf{P}$ is related to the permittivity ϵ through the susceptibility χ, which is the constant of proportionality between the electric field and induced polarization $\mathbf{P} = \chi\mathbf{E}$. The permittivity is defined as the constant of proportionality between the electric field and the displacement field, which arises in constructing the macroscopic Maxwell's equations, $\mathbf{D} = \epsilon\mathbf{E} = \mathbf{E} + 4\pi\mathbf{P}$. Combining these expressions allows us to define the electric permittivity:

$$\epsilon = 1 + 4\pi\chi \tag{3.21}$$

$$= 1 + 4\pi N\sum_j^Z \frac{e^2}{m}\frac{1}{\omega_j^2 - \omega^2 - i\omega\gamma_j}. \tag{3.22}$$

This *dielectric function* of frequency is simply a collection of Lorentz oscillators.

The Drude dielectric function is obtained by freeing the electrons from their respective nuclei, accomplished by taking their resonance frequencies $\omega_j \to 0$ and all $\gamma_j \to \gamma$ to represent the scattering rate of free electrons against the background nuclear lattice. Defining the plasma frequency $\omega_p \equiv \frac{NZe^2}{m\epsilon_0}$ to be the characteristic response of the free electron gas, the *Drude dielectric function* can be written:

$$\epsilon(\omega) = \epsilon_\infty - \frac{\omega_p^2}{\omega^2 + i\omega\gamma}, \tag{3.23}$$

where a phenomenological high frequency limit ϵ_∞ helps account for the low-energy tails of higher energy bound-electron excitations that are not explicitly modeled but do contribute slightly to the optical response of gold.

The plasmon as an oscillator

In discussing the plasmon resonance of metal nanoparticles, we often invoke the analogy between the collective electron oscillation and a mechanical oscillator. But this is more than just imagery. In this section we will derive the oscillator equations for the plasmon resonance and make clear the approximations required to get there.

We start with the quasi-static limit of the polarizability for a prolate spheroid in Eq. (3.11). Plugging in the Drude model dielectric function in Eq. (3.23), in Gaussian units:

$$\alpha_i = \frac{V}{4\pi} \frac{\epsilon_\infty - \frac{\omega_p^2}{\omega^2 + i\omega\gamma} - \epsilon_b}{1 + L_i \left[\epsilon_\infty - \frac{\omega_p^2}{\omega^2 + i\omega\gamma} - \epsilon_b\right]} \tag{3.24}$$

$$= \frac{V}{4\pi} \frac{(\epsilon_\infty - \epsilon_b)(\omega^2 + i\omega\gamma) - \omega_p^2}{(1 + L_i[\epsilon_\infty - \epsilon_b])(\omega^2 + i\omega\gamma) - L_i\omega_p^2} \tag{3.25}$$

$$= \frac{V}{4\pi} \frac{\frac{(\epsilon_\infty - \epsilon_b)(\omega^2 + i\omega\gamma)}{1 + L_i(\epsilon_\infty - \epsilon_b)} - \frac{\omega_p^2}{1 + L_i(\epsilon_\infty - \epsilon_b)}}{(\omega^2 + i\omega\gamma) - \frac{L_i\omega_p^2}{1 + L_i[\epsilon_\infty - \epsilon_b]}}. \tag{3.26}$$

Defining the plasmon resonance frequency $\omega_{i,0}^2 \equiv \frac{L_i\omega_p^2}{1 + L_i[\epsilon_\infty - \epsilon_b]}$, then the denominator charac-

teristic of an oscillator appears. Continuing to simplify the expression,

$$\alpha_i = \frac{V}{4\pi} \frac{\frac{(\epsilon_\infty - \epsilon_b)\left(\omega^2 + i\omega\gamma\right)}{1+L_i(\epsilon_\infty - \epsilon_b)} - \frac{\omega_{i,0}^2}{L_i}}{\omega^2 + i\omega\gamma - \omega_{i,0}^2} \tag{3.27}$$

$$= \frac{V}{4\pi} \frac{\frac{(\epsilon_\infty - \epsilon_b)\left(\omega^2 + i\omega\gamma - \omega_{i,0}^2\right)}{1+L_i(\epsilon_\infty - \epsilon_b)} - \frac{\omega_{i,0}^2}{L_i} + \frac{\omega_{i,0}^2(\epsilon_\infty - \epsilon_b)}{1+L_i(\epsilon_\infty - \epsilon_b)}}{\omega^2 + i\omega\gamma - \omega_{i,0}^2} \tag{3.28}$$

$$= \frac{V}{4\pi} \left[\frac{\epsilon_\infty - \epsilon_b}{1 + L_i(\epsilon_\infty - \epsilon_b)} + \frac{\omega_{i,0}^2 \left(\frac{1}{L_i} - \frac{(\epsilon_\infty - \epsilon_b)}{1+L_i(\epsilon_\infty - \epsilon_b)} \right)}{\omega_{i,0}^2 - \omega^2 - i\omega\gamma} \right] \tag{3.29}$$

$$= \frac{V}{4\pi} \left[\frac{\epsilon_\infty - \epsilon_b}{1 + L_i(\epsilon_\infty - \epsilon_b)} + \frac{\frac{\omega_{i,0}^2/L_i}{1+L_i(\epsilon_\infty - \epsilon_b)}}{\omega_{i,0}^2 - \omega^2 - i\omega\gamma} \right], \tag{3.30}$$

$$\equiv \alpha^{\text{static}} + \alpha_i^{\text{osc}}(\omega) \tag{3.31}$$

where we now have the polarizability decomposed into a frequency independent term plus the polarizability of a linear dipole oscillator:

$$\alpha_i^{\text{osc}}(\omega) = \frac{e^2/m_i}{\omega_0^2 - \omega^2 - i\omega\gamma}, \tag{3.32}$$

which we call the plasmon resonance. The dipole plasmon effective mass along the ith principal axis of the spheroid is defined by $m_i \equiv \frac{L_i}{\omega_{i,0}^2 V} 4\pi e^2 [1 + L_i(\epsilon_\infty - \epsilon_b)]$, which assumes the charge $-e$ of the effective massive oscillator but does contribute to observables. This charge only parameterizes a freedom in the ratio of driving force on mass. The oscillator polarizability matches that derived from the same Newton's equation that we started with to derive the Drude model, by taking Eq. (3.18) and dividing by the driving field $\mathbf{E}$.

The first term in Eq. (3.30) is termed the *static* piece of the polarizability and can be interpreted as an insulating particle with dielectric constant ϵ_∞ superimposed underneath the plasmonic electron gas. This dielectric response is due to the core electrons tightly bound to their nuclei. These electrons reside deep enough in the valence band to have only excitations at high energy relative to the plasmon resonance and therefore respond much faster than the collective behavior of the conduction electrons comprising the plasmon oscillator.

A similar procedure yields an oscillator model for the polarizability in the modified long-wavelength approximation.[1] First, ignoring the contribution from the static polarizability, Eq. (3.14) becomes:

$$\lim_{\alpha_{\rm stat}\to 0}\alpha_i^{\rm ML} = \frac{\alpha_i^{\rm osc}}{1-\frac{k^2}{l_{E,i}}D_i\alpha_i^{\rm osc}-i\frac{2k^3}{3}\alpha_i^{\rm osc}} \tag{3.33}$$

$$= \frac{e^2/m_i}{\omega_{i,0}^2-\omega^2-i\gamma\omega-\frac{\omega^2n^2}{l_{E,i}c^2}D_i\frac{e^2}{m_i}-i\frac{2e^2\omega^3n^3}{3m_ic^3}} \tag{3.34}$$

$$= \frac{e^2/m_i}{\omega_{i,0}^2-\omega^2\left(1+\frac{n^2e^2D_i}{l_{E,i}c^2m_i}\right)-i\omega\left(\gamma+\frac{2e^2\omega^2n^3}{3m_ic^3}\right)} \tag{3.35}$$

$$= \frac{\frac{e^2}{m_i}\frac{l_{E,i}c^2m_i}{l_{E,i}c^2m_i+n^2e^2D_i}}{\omega_{i,0}^2\frac{l_{E,i}c^2m_i}{l_{E,i}c^2m_i+n^2e^2D_i}-\omega^2-i\omega\left(\gamma+\frac{2e^2\omega^2n^3}{3m_ic^3}\right)\frac{l_{E,i}c^2m_i}{l_{E,i}c^2m_i+n^2e^2D_i}} \tag{3.36}$$

$$= \frac{e^2/\tilde{m}_i}{\tilde{\omega}_{i,0}^2-\omega^2-i\omega\left(\gamma_{i,\rm NR}+\gamma_{i,\rm R}\right)}, \tag{3.37}$$

with the following definitions:

$$\tilde{m}_i \equiv m_i+\frac{n^2e^2D_i}{l_{E,i}c^2} \tag{3.38}$$

$$\tilde{\omega}_{i,0} \equiv \omega_{i,0}\sqrt{\frac{m_i}{\tilde{m}_i}} \tag{3.39}$$

$$\gamma_{i,\rm NR} \equiv \gamma\frac{m_i}{\tilde{m}_i} \tag{3.40}$$

$$\gamma_{i,\rm R} \equiv \frac{2e^2n^3}{3\tilde{m}_ic^3}\omega^2. \tag{3.41}$$

MLWA with static polarizability

Note!: This section contains a mistake, but is left here because I believe correcting and completing it would be a good project for a new graduate student, and would be an interesting contribution to the field.

Including the static portion of the quasistatic polarizability does add additional frequency

[1]The representation of the MLWA polarizability as an oscillator without the static portion is due to Kevin C. Smith, unpublished.

dependence,

$$\alpha_i^{\mathrm{ML}}(\omega) = \frac{\alpha^{\mathrm{static}} + \alpha_i^{\mathrm{osc}}}{1 - \frac{k^2}{l_{E,i}} D_i(\alpha^{\mathrm{static}} + \alpha_i^{\mathrm{osc}}) - i\frac{2k^3}{3}(\alpha^{\mathrm{static}} + \alpha_i^{\mathrm{osc}})} \tag{3.42}$$

$$= \frac{\alpha^{\mathrm{static}}(\omega_0^2 - \omega^2 - i\omega\gamma)(m_i/\tilde{m}_i) + e^2/\tilde{m}_i}{\tilde{\omega}_{i,0}^2 - \omega^2 - i\omega(\gamma_{i,\mathrm{NR}} + \gamma_{i,\mathrm{R}})} \tag{3.43}$$

$$= \frac{\alpha^{\mathrm{static}}(\tilde{\omega}_{i,0}^2 - \omega^2 - i\omega\gamma_{i,\mathrm{NR}}) + e^2/\tilde{m}_i}{\tilde{\omega}_{i,0}^2 - \omega^2 - i\omega(\gamma_{i,\mathrm{NR}} + \gamma_{i,\mathrm{R}})} \tag{3.44}$$

$$= \frac{\alpha^{\mathrm{static}}}{1 - i\omega\frac{\gamma_{i,\mathrm{R}}}{\tilde{\omega}_{i,0}^2 - \omega^2 - i\omega\gamma_{i,\mathrm{NR}}}} + \frac{e^2/\tilde{m}_i}{\tilde{\omega}_{i,0}^2 - \omega^2 - i\omega\left(\gamma_{i,\mathrm{NR}} + \gamma_{i,\mathrm{R}}\right)}, \tag{3.45}$$

but this new first term can not obviously be mapped onto an oscillator equation of motion.

To understanding the newfound dynamic properties of the formerly static contribution to the polarizability from the high frequency limit of the Drude model, it is helpful to consider the absorption cross section $\sigma_{\mathrm{abs}} \propto \Im[\alpha]$. In the quasi-static approximation the α^{static} does not absorb. Taking the imaginary part of just the first term of Eq. (3.45), $\alpha_i^{\mathrm{ML}} = \alpha_{i,\mathrm{static}}^{\mathrm{ML}} + \alpha_{i,\mathrm{dynamic}}^{\mathrm{ML}}$, the static portion is explicitly:

$$\Im[\alpha_{i,\mathrm{static}}^{\mathrm{ML}}] = \alpha^{\mathrm{static}}\Im\left[\frac{\tilde{\omega}_{i,0}^2 - \omega^2 - i\omega\gamma_{i,\mathrm{NR}}}{\tilde{\omega}_{i,0}^2 - \omega^2 - i\omega\left(\gamma_{i,\mathrm{NR}} + \gamma_{i,\mathrm{R}}\right)}\right] \tag{3.46}$$

$$= \alpha^{\mathrm{static}}\Im\left[\frac{\left(\tilde{\omega}_{i,0}^2 - \omega^2 - i\omega\gamma_{i,\mathrm{NR}}\right)\left(\tilde{\omega}_{i,0}^2 - \omega^2 + i\omega\left(\gamma_{i,\mathrm{NR}} + \gamma_{i,\mathrm{R}}\right)\right)}{\left(\tilde{\omega}_{i,0}^2 - \omega^2\right)^2 + \omega^2\left(\gamma_{i,\mathrm{NR}} + \gamma_{i,\mathrm{R}}\right)^2}\right] \tag{3.47}$$

$$= \alpha^{\mathrm{static}}\frac{\left(\tilde{\omega}_{i,0}^2 - \omega^2\right)\omega\gamma_{i,\mathrm{R}}}{\left(\tilde{\omega}_{i,0}^2 - \omega^2\right)^2 + \omega^2\left(\gamma_{i,\mathrm{NR}} + \gamma_{i,\mathrm{R}}\right)^2}, \tag{3.48}$$

which looks just like the usual oscillator absorption multiplied by the resonance condition $\tilde{\omega}_{i,0}^2 - \omega^2$. Interestingly, this term goes to zero on resonance and what was the static polarizability in the

3.2 Two couped dipoles

Classical oscillating dipoles with interaction and radiation

To understand the relationship between mispolarization and the configuration-dependent interaction between a molecule and a plasmonic nanorod, we turn to a simple analytical

model of both the near-field interaction and far-field radiation. The fluorescence emission from the coupled molecule and nanorod is attributed to two electric dipoles interacting and radiating into the far field. For justification, it is well known that plasmonic nanoparticles behave as polarizable point dipoles in the long-wavelength limit. This condition holds even under excitation from a nearby molecule at separations outside the region of fluorescence quenching [7]. At a particular oscillator frequency, electric dipoles can be described as linearly proportional to the total field at their location excluding their own field. For the molecule's emissive transition dipole moment (labeled $\mathbf{p}_0$) and dipole plasmon induced in the nanoparticle (labeled $\mathbf{p}_1$), the dipole magnitudes, phases and orientations must satisfy the following coupled equations for the complex vectors:

$$\begin{cases} \mathbf{p}_0 = \boldsymbol{\alpha}_0 \left[\mathbf{E}_1(\mathbf{x}_0) + \mathbf{E}_F\right] \\ \mathbf{p}_1 = \boldsymbol{\alpha}_1 \mathbf{E}_0(\mathbf{x}_1) \end{cases} \tag{3.49}$$

where the dipoles, linear polarizabilities α_i, and fields are all evaluated at the frequency ω and the inner product is implied by neighboring tensors in boldface. The fields $\mathbf{E}_i(\mathbf{x}_j) = \mathbf{G}(\mathbf{x}_i, \mathbf{x}_j) \cdot \mathbf{p}_i$ are the classical oscillating dipole fields generated by the ith dipole at the location of the jth dipole defined in terms of the tensor:

$$\mathbf{G}(\mathbf{d}) = \left[\left(3\hat{d}\hat{d} - \mathbf{1}\right)\left(\frac{1}{d^3} - \frac{ik}{d^2}\right) - \left(\hat{d}\hat{d} - \mathbf{1}\right)\frac{k^2}{d}\right] e^{ikd}, \tag{3.50}$$

which relays the dipole field from the dipole location $\mathbf{x}_i$ to another point $\mathbf{x}_j$. The separation vector $\mathbf{d} = d\hat{d} = \mathbf{x}_1 - \mathbf{x}_0$ defines the separation between the molecule and centroid of the plasmonic nanorod. The fictitious harmonic field $\mathbf{E}_F = E_0 \hat{e}_x e^{-i\omega t}$ driving only the molecule dipole forces the dipoles to oscillate harmonically and represents the continuous population of the emissive state by absorption of the real excitation field and subsequent vibrational relaxation characteristic of fluorescence.

Since the coupled dipole equations are linear, both dipoles will oscillate at the frequency ω, which can be thought of as a single Fourier component of the coupled fluorescence emission spectrum. To simplify analysis, we will take ω to be the resonance maximum in the uncoupled

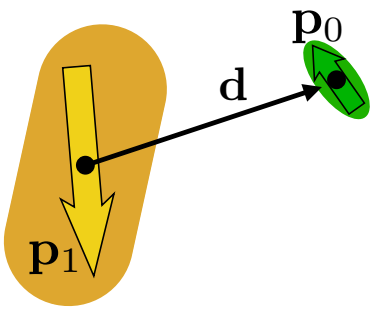

Figure 3.1: Diagram of two coupled dipoles and separation vector $\mathbf{d} = d\hat{d} = \mathbf{x}_1 - \mathbf{x}_0$.

molecules emission spectrum and will demonstrate that this single-color model approximates the character of the multicolor images collected experimentally. The governing dynamical equations for the dipole moments can then be solved to yield the dipole moments:

$$\begin{cases} \mathbf{p}_0 = \left[\mathbf{1} - \boldsymbol{\alpha}_1 \mathbf{G}(\mathbf{x}_1, \mathbf{x}_0)\boldsymbol{\alpha}_0 \mathbf{G}(\mathbf{x}_0, \mathbf{x}_1)\right]^{-1} \boldsymbol{\alpha}_0 \mathbf{E}_F \\ \mathbf{p}_1 = \boldsymbol{\alpha}_1 \mathbf{G}(\mathbf{x}_1, \mathbf{x}_0)\mathbf{p}_0 \end{cases} \tag{3.51}$$

and the indirectly driven plasmon dipole becomes,

$$\begin{aligned} \mathbf{p}_1 &= \boldsymbol{\alpha}_1 \mathbf{G}(\mathbf{x}_1, \mathbf{x}_0)\mathbf{p}_0 && (3.52)\\ &= \boldsymbol{\alpha}_1 \mathbf{G}(\mathbf{x}_1, \mathbf{x}_0)\boldsymbol{\alpha}_0[\mathbf{E}_F(\mathbf{x}_0) + \mathbf{E}_1(\mathbf{x}_0)] && (3.53)\\ &= \boldsymbol{\alpha}_1 \mathbf{G}(\mathbf{x}_1, \mathbf{x}_0)\boldsymbol{\alpha}_0[\mathbf{E}_F(\mathbf{x}_0) + \mathbf{G}(\mathbf{x}_0, \mathbf{x}_1)\mathbf{p}_1] && (3.54)\\ &= \boldsymbol{\alpha}_1\boldsymbol{\alpha}_1 \mathbf{G}(\mathbf{x}_1, \mathbf{x}_0)\boldsymbol{\alpha}_0 \mathbf{E}_F(\mathbf{x}_0) + \boldsymbol{\alpha}_1 \mathbf{G}(\mathbf{x}_1, \mathbf{x}_0)\boldsymbol{\alpha}_0 \mathbf{G}(\mathbf{x}_0, \mathbf{x}_1)\mathbf{p}_1 && (3.55)\\ &= \left(\mathbf{1} - \boldsymbol{\alpha}_1 \mathbf{G}(\mathbf{x}_1, \mathbf{x}_0)\boldsymbol{\alpha}_0 \mathbf{G}(\mathbf{x}_0, \mathbf{x}_1)\right)^{-1} \boldsymbol{\alpha}_1 \mathbf{G}(\mathbf{x}_1, \mathbf{x}_0)\boldsymbol{\alpha}_0 \mathbf{E}_F(\mathbf{x}_0). && (3.56) \end{aligned}$$

QED treatment of coupled dipoles

I am spent a significant amount of time trying and failing to come up with a semi-classical model of plasmon-molecule coupling that would preserve the simplicity of the classical coupled dipole approach while incorporating the spectral behavior of molecule (like what results from the displaced oscillator model in Appendinx 8).

One attempt I explored, but did not progress too far, started with a model proposed by Cui and Raymer [46] from which Mathew Pelton [97] used in the case of quantum dot-plasmon photoluminescence,

$$\mathrm{PL}(\omega-\omega_{pl}) = \frac{\gamma_{pl}}{\pi}\left|\frac{-ig_0}{(K/2+i\Delta/2-i\Omega)^2+g^2}\right|^2 \tag{3.57}$$

where $\hbar g$ is the quantum dot - plasmon interaction energy, $g = \sqrt{g_0^2+(\Delta/2)^2-(^2}$ is the generalized Rabi frequency appearing the the strong-coupling limit, $\Gamma = \gamma_{pl}-\gamma_{qd}$, $K = \gamma_{pl}+\gamma_{qd}$, $\Delta = \omega_{pl}-\omega_{qd}$, and $\Omega = \omega-\omega_{pl}$.

I have a few issues with this equation used as model for photoluminescence. First, it is not clear that the idealized quantum optical model presented in the paper applies to a plasmonc nanopaticle. The damping rate γ_{pl} comes from a Weisskopf-Vigner integration over the same bath states that are considered for the spectrum in Eq. 3.57, which I would think implies only the radiative decay of the plasmon mode. Second, Eq. 3.57 describes the spectral density of the bath states only coupled to the plasmon and not the emitter. From the classical perspective (and all the work I have done thinking about interference), I would think it necessary to account for direct dot emission as well as the interference, neither of which appears from this equation.

One idea to remedy the second concern is to couple both emitters to the same bath. But I am now remembering conversations about Niket Thakkar's Quantum Beats paper [155] that it might be redundant to couple the two emitters directly as well as through a bath. I am not sure if this was ever resolved, but likely is within work by Kevin C. Smith.

A simple thing to start with in this direction is to take the standard Weisskopf-Vigner decay and get a spectrum to try fitting to a dye emission sepctrum. From Scully [140] Section 6.3, a single two-level system coupled to a bath through the interaction Hamiltonian in the rotating wave and dipole approximations is described by the Hamiltonian,

$$H_i = \hbar\sum_{\mathbf{k}}\left[g_{\mathbf{k}}^*\sigma_+ a_{\mathbf{k}}e^{i(\omega-\nu_{\mathbf{k}})t}+\mathrm{H.c.}\right] \tag{3.58}$$

Considering the two-level system to initially be in the excited state, then only 1 excitation

exists in the system and the general state vector for the system can be written

$$|\Psi(t)\rangle = c_a(t)\,|a,0\rangle + \sum_{\mathbf{k}} c_{b,\mathbf{k}}(t)\,|b,1\rangle\,. \tag{3.59}$$

Under the Markov approximation, the emitter excitation amplitude $c_a(t)$ can not depend on its past history through the bath. We also make the approximation that the observation time t is long compared the relevant timescales of emitter-bath interaction. The emitter excitation amplitude becomes

$$c_a(t) = e^{-\frac{\Gamma}{2}t} \tag{3.60}$$

where

$$\Gamma = \frac{1}{4\pi\epsilon_0}\frac{4p_{ab}^2\omega^3}{3\hbar c^3} \tag{3.61}$$

Although I was never able to derive it, the aforementioned Cui and Raymer paper [46] claims that the spectral density of photon bath is apparently

$$S(\Omega) = 2\frac{\gamma}{\pi}\mathrm{Re}\left[\int_0^\infty \mathrm{d}\tau\, e^{i\Omega\tau}\int_0^\infty \mathrm{d}t\, c_a(t)c_a^*(t+\tau)\right] \tag{3.62}$$

where $\gamma = \Gamma/2$ from above.

$$\begin{aligned}
S(\Omega) &= \frac{\Gamma}{\pi}\mathrm{Re}\left[\int_0^\infty \mathrm{d}\tau\, e^{i\Omega\tau}\int_0^\infty \mathrm{d}t\, e^{-\frac{\Gamma}{2}(2t+\tau)}\right] \\
&= \frac{\Gamma}{\pi}\mathrm{Re}\left[\int_0^\infty \mathrm{d}\tau\, e^{i\Omega\tau}\left(\frac{e^{-\frac{\Gamma}{2}(2t+\tau)}}{-\Gamma}\bigg|_{t=0}^{\infty}\right)\right] \\
&= \frac{\Gamma}{\pi}\mathrm{Re}\left[\int_0^\infty \mathrm{d}\tau\, e^{i\Omega\tau}\left(0 - \frac{e^{-\frac{\Gamma}{2}\tau}}{-\Gamma}\right)\right] \\
&= \frac{1}{\pi}\mathrm{Re}\left[\int_0^\infty \mathrm{d}\tau\, e^{i\Omega\tau}e^{-\frac{\Gamma}{2}\tau}\right] \\
&= \frac{1}{\pi}\mathrm{Re}\left[\frac{e^{i\Omega\tau}e^{-\frac{\Gamma}{2}\tau}}{i\Omega-\Gamma/2}\bigg|_0^\infty\right. \\
&= \frac{1}{\pi}\mathrm{Re}\left[\frac{-1}{i\Omega-\Gamma/2}\right] \\
&= \frac{1}{\pi}\mathrm{Re}\left[\frac{+i\Omega+\Gamma/2}{(i\Omega-\Gamma/2)(-i\Omega-\Gamma/2)}\right] \\
&= \frac{1}{\pi}\frac{\Gamma/2}{\Omega^2+(\Gamma/2)^2}
\end{aligned} \tag{3.63}$$

This, combined with the work in Appendix 8 is a good place to start for a future graduate student interested in extending the plasmon-enhanced imaging models to the quantum-classical boundary.

Part II

PLASMON-ENHANCED SINGLE MOLECULE IMAGING

The diffraction limit causes traditional optical images, like those captured in fluorescence microscopy, to be blurred by the overlap of PSFs from many neighboring fluorescent molecules. Although the relative positions of two proximal fluorescent molecules are masked by diffraction, the light from an isolated emitter reveals more information about the position of its source then one might expect with a naive interpretation of the diffraction limit. The diffraction limit is really a statement about how close two objects may reside and still be identified as distinct. This resolution limit can therefore be subverted by imaging molecules one at a time. By fitting the distinct emission from individual molecules to the microscope's PSF, single molecule positions can be deduced. In practice, fluorescent molecules in a sample of interest can be actively controlled to emit in bursts at very low concentrations. A single image will therefore contain a small statistical sampling of fluorescent molecules, which can each be located. Repeating the procedure with new subsamples of emitters can produce a super resolution map of the sample structure at single molecule resolution.

In the last few decades, researchers exploring different methods of actively restricting the emitting population of fluorophores have founded a variety of Super Resolution Fluorescence Microscopy (SRFM) techniques [138]. The first reported demonstrations of SRFM utilized photoactivatable molecules with very low intensity activation [69, 19]. The method relevant to the experiments I am exploring uses stochastic adsorption of fluorescent molecules to a surface, where they generate a signal detectable over the background fluorescence of molecules diffusing in solution. This procedure, termed points accumulation for imaging nanoscale topography (PAINT) [144], provides a means of SRFM with passive control of the emitting population by solution control of molecule adsorption kinetics.

Contemporary SRFM methodology has advanced to the point where molecule localization precision is limited only by the accuracy of the fit PSF to the raw emission data [49]. Because the functional fit certainty is dictated by signal-to-noise ratio, super resolution precision scales with the number of photons collected before a fluorophore moves or photobleaches. As Purcell taught us in his seminal work on spontaneous emission coupled to resonant optical cavities, the emissive properties of a fluorescent molecule are strongly influenced by the

dielectric environment [126]. Utilizing this knowledge to increase single molecule resolving power, researchers have begun to engineer and optimize systems for enhancement of both fluorescence rates and quantum yields near material interfaces [33]. In particular, it is well understood that coupling to the plasmon resonance of nearby metal nanoparticle provides both increased excitation and emission rates within a certain range of plasmon-fluorophore separations [7, 74]. Important for super resolution precision, plasmon-fluorophore hybridization decreases fluorescence lifetimes, which leads to higher photon counts before photobleaching [78, 133, 169].

Plasmon enhanced fluorescence has inspired incorporation of plasmonic nanoparticles into SRFM experiments in search of better single molecule localization precision, but the results have been convoluted. Multiple groups [159, 160, 150, 128] have demonstrated that super resolution maps of fluorophores near an appropriately tuned plasmonic nanoparticle yield unjustified aggregation of the PSF centroids at the center of the nanoparticle. This mislocalization of the dye molecules persists after background subtracting the isolated plasmon emission, which one might expect would eliminate dependence of plasmonic coupling. Without a reason to expect inhomogeneity in fluorophore distribution, plasmon-enhanced SRFM suffers an apparent loss of direct correlation between the centroid of the PSF fit and the fluorophore position.

The mislocalization phenomenon is even more complicated then a simple shift of the molecule's apparent position onto the nanoantenna. Although this is most often observed, multiple groups have reported mislocalization in the opposite direction. The plasmon-coupled-molecule image shifts away from the nanoantenna with centroid outside the two emitters. This outer mislocalization has been confirmed physical in computation studies, and shown to be consistent with interference effects [136] and Super resolution Raman calculations [67]. Despite this understanding, no model existed in the literature to explain the circumstances supporting inner *versus* outer mislocalization.

In the following chapters, I present a simple coupled dipole model of the plasmon-enhanced single molecule image that explains several previously open questions in the plasmon-

enhanced single-molecule imaging literature. The main dilemma addressed in Chapter 5 is illustrated in Fig. 3.2 and summarizes as such: Why is inner mislocalization observed so much more often the outer mislocalization, and what physical features of the system support one observation or the other? The answer turns out to be found in the relationships between both the plasmon-molecule coupling strength and molecule orientation with the quality of interference, constructive or destructive. At the end of Chapter 5, we demonstrate the potential of the coupled-dipole image model as a new super-resolution fit function capable of determining the molecule location in one dimension at greater accuracy then the Gaussian localization procedure.

In Chapter 6, model is generalized to two dimensions, where fluorescent molecules are resonantly coupled to a nanorod. The model compares favorably to simulation, explaining experimentally observed mispolarization effects in terms of interference, analogous to the mislocalization discussed in the previous chapter. The model image also performs better then the Gaussian localization at reclaiming both molecule location and orientation when fitting simulated data.

In Chapter 7, the coupled-dipole image model is fit to experimental plasmon-enhanced single-molecule images in order to reclaim the single molecule location and orientation. Without knowing the true molecule location or orientation, it is impossible to benchmark the model fits directly. But working with what we have, the statistical uncertainties of the least squares fit are compared to the case of the Gaussian fit to asses potential accuracies and resolution of the mislocalization problem.

Finally, Chapter 8 details a quantum mechanical model of molecular emission capable of describing the fluorescence spectra of the dye molecules used for single-molecule localization microscopy. Although not yet incorporated into a model plasmon-enhanced fluorescence, this would be a good starting point for a future graduate student.

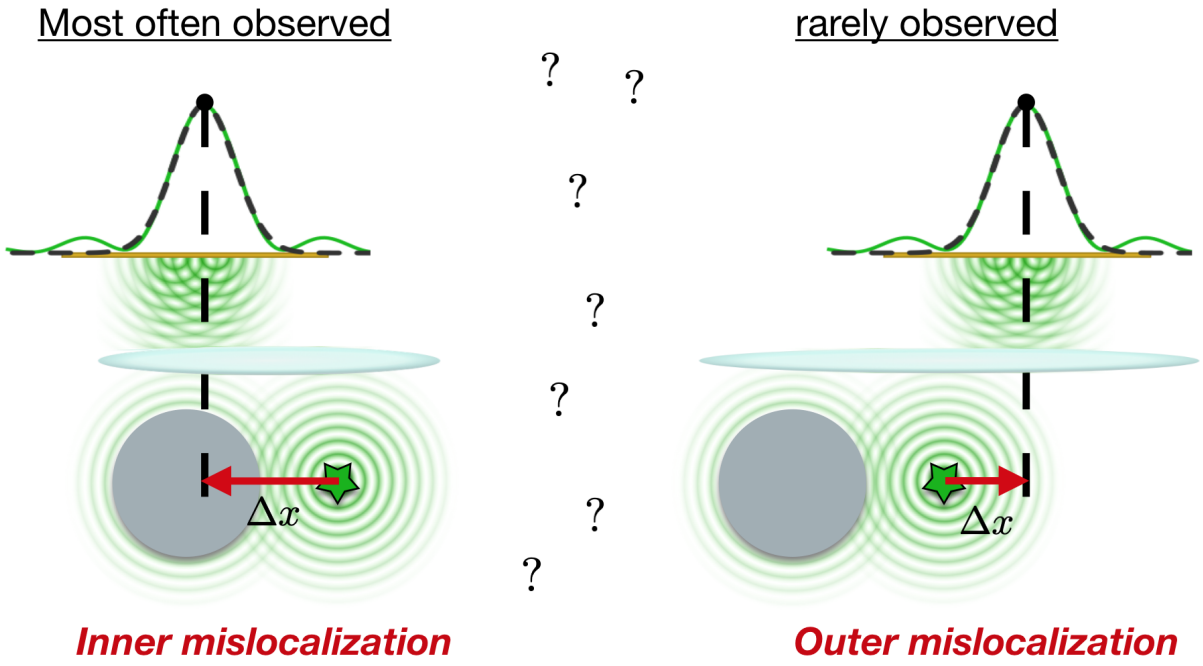

Figure 3.2: There seemed to be an unreconciled rift in the plasmon-enhanced single-molecule imaging literature. Most studies reported seeing the image centroid mislocalize onto the nanoparticle centroid. This is an intuitive consequence of nanoparticle emission dominating the observed image, an antenna working as expected. but a minority of studies reported mislocalization in the opposite direction; the image centroid appears outside the pair of emitters. This phenomenon of *outer* mislocalization can only be explained by interference effects, as proposed in Ref. [136]. At this point, no model had been proposed to predict when outer mislocalization would occur or explain the prevalence of observations of *inner* mislocalization.

Chapter 4

MODEL OF PLASMON-ENHANCED SINGLE-MOLECULE IMAGING

This section details the parameterization procedure of the plasmon-enhanced single molecule image model. With the plasmonic nanoparticle and emissive molecule transition modeled as classical electric dipoles, we will related the polarizabilities discussed in Chapter 3 to the physical plasmonic nanoparticle and emissive molecule. The parameter values and figures in the chapter correspond to the nanorod experiments detailed in Chapter 6, but the same procedure was used to parameterize the sphere system studied in Chapter 5

4.1 Parameterization of the nanoparticle polarizability for predictions

The scattering cross section can be used to parameterize the coupled dipole model by fitting a model expression to experimental or simulated spectra for the nanorod. The scattering cross section σ_s is defined as the power scattered P_s per incident field intensity I_{inc}, and can be derived using the expressions for the fields radiated by a dipole. The scattering cross section of an ideal dipole with polarizability $\alpha(\omega)$ in an isotropic and non-dissipative background is:

$$\sigma_s(\omega) \equiv \frac{P_s}{I_{\text{inc}}} = \frac{8\pi}{3}\frac{k^4}{n_b}|\hat{\epsilon}\cdot\boldsymbol{\alpha}(\omega)|^2, \tag{4.1}$$

where $k = \frac{\omega n_b}{c}$ and $n_b = \sqrt{\epsilon_b}$ is the background refractive index and $\hat{\epsilon}$ is the polarization vector of the incident field.

For the purpose of modeling a nanorod, the frequency-dependent polarizability $\alpha(\omega)$ is set to be the modified long-wavelength tensor in Eq. (3.10) with components given by Eq. (3.14). The dielectric permittivity is assigned the Drude model in Eq. (3.23). This procedure yields $\sigma_s(\omega)$ determined by five free parameters, $\{a, b, \epsilon_\infty, \omega_p, \gamma\}$. First, the polarizability is fundamentally geometric and likewise, the two semi-radii of the prolate spheroid appear; (1)

a along the long axis and (2) the short semi-radius b. Next, the three material properties determining the Drude model; (3) the high frequency limit of the permittivity ϵ_∞, (4) the plasma frequency ω_p containing the characteristic response time of the conduction electrons, and (5) electron scattering rate γ that serves as a damping on electronic motion.

The simulated nanorod is assigned dielectric data for gold from Johnson and Christy [81]. Its geometry is a cylinder with radius of 20 nm and length of 24 nm with hemispherical end-caps of matching radius. The parameters resulting from the best fit of the two spectra in Fig. 4.1 are:

$$a = 51.7770\,\text{nm} \tag{4.2}$$

$$b = 15.9601\,\text{nm} \tag{4.3}$$

$$\epsilon_\infty = 28.9857 \tag{4.4}$$

$$\hbar\omega_p = 13.5885\,\text{eV} \tag{4.5}$$

$$\hbar\gamma = 0.0977\,\text{eV}. \tag{4.6}$$

The deviation of these values from the true rod geometry and optimized Drude model fit is expected because of differences in optical response between a spheroidal and cylindrical rod. Another contribution to error in these best-fit parameters is the relative inaccuracy of the transverse mode fit. This can be attributed to the low-energy tail of the gold interband transitions that overlap this portion of the spectrum and are not well accounted for by the Drude model dielectric function. Despite these challenges, the prolate spheroid parameterized by the listed parameters adequately models the physical and simulated systems for our purposes.

4.2 The molecule's emissive transition as an electric dipole

In the case of plasmon-enhanced fluorescence, the molecule's emissive transition dipole sources the plasmonic excitation. To simplify model construction, the molecule is treated as a classical oscillating dipole moment with polarizability given in Eq. (3.14) with geometric

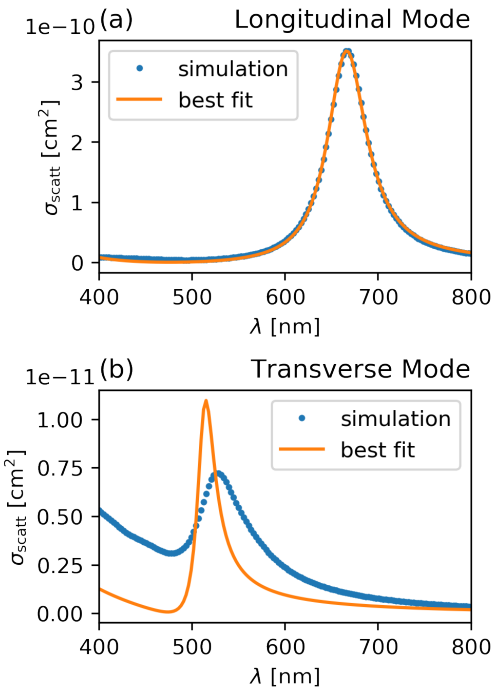

Figure 4.1: Parameterization of the nanorod polarizability along the long (a) and short (b) principal-axes of the nanorod from scattering spectra calculated by the Maxwell equations solver MNPBEM17 Toolbox for MATLAB [73]. Simulated cross sections were calculated by aligning the polarization of the incident light along either rod axis, and fit simultaneously to the corresponding model expression in Eq. (4.1) with appropriate component of the polarizability in terms of the five free parameters, $\{a, b, \epsilon_\infty, \omega_p, \gamma\}$ discussed in the main supplementary text. The relative inaccuracy of transverse mode fit can be attributed to the low-energy tail of gold interband transitions that overlap this portion of the spectrum and are not well accounted for by the Drude model dielectric function. This spectra is slightly blue-shifted compared to the time-domain simulations presented in SI Fig. S15 and experimental scattering spectra shown in Fig 1 due to the absence of a glass substrate in the frequency-domain simulations. This quantitative difference does not impact the qualitative results provided by the analytic model, which is parameterized by the frequency-domain calculation.

radii taken to 0. The dyadic nature considered fixed to the molecule's orientation in space, so that the polarizability is nonzero only in one direction $\boldsymbol{\alpha}_{\text{mol}} = \alpha_{\text{mol}}\hat{\mathbf{e}}\hat{\mathbf{e}}$. The free parameters required from fit are then $\{m, \omega_0, \gamma_{\text{nr}}\}$. Because fitting the mass requires knowledge of the absolute magnitude of the molecule emission cross section, it is easer to first determine the mass from the supplier listed molar extinction coefficient. For the Cyanine5.5 NHS ester used in the nanorod experiments, $\varepsilon = 198000\,\text{L}\,\text{mol}^{-1}\,\text{cm}^{-1}$ [1].

Following Novotny's *Nano Optics*, Section 9.3 [117], the extinction coefficient can be related to the molecular absorption cross section σ_a by the molar concentration,

$$\begin{aligned} e^{-\frac{N}{V}\sigma_a z} &= 10^{-\epsilon[M]z} \\ -\frac{N}{V}\sigma_a &= -\epsilon[M]\ln 10 \\ &= -\epsilon\frac{1}{N_A}\frac{N}{V}\ln 10 \\ \sigma_a &= \frac{\epsilon\ln 10}{N_A} \end{aligned} \tag{4.7}$$

We next relate this expression to that of the oscillator by combining equations $\sigma_a = 4\pi k\,\text{Im}[\hat{\epsilon}\cdot\boldsymbol{\alpha}(\omega)]$ from Ref [25] and (3.30),

$$\sigma_a = \quad = \frac{4\pi e^2}{mcn}\frac{\gamma\omega^2}{(\omega_0^2-\omega^2)^2+\gamma^2\omega^2}. \tag{4.8}$$

At resonance, this expression reduces to depend only on the linewidth,

$$\sigma_a(\omega=\omega_0) = \frac{4\pi e^2}{mcn}\frac{1}{\gamma}. \tag{4.9}$$

and the effective mass becomes

$$m = \frac{4\pi e^2 N_a}{\varepsilon\ln(10)cn_b\gamma_{nr}} \tag{4.10}$$

Although this procedure is approximate, numerical calculations have shown that only the global magnitude of plasmon enhanced fluorescence emission is dependent on the mass on the molecule emissive oscillator.

After determining the mass, the remaining parameters ω_0 and γ_{nr} can be fit directly from the normalized fluorescence emission spectrum.

---

[1] https://www.lumiprobe.com/p/cy55-nhs-ester, accessed December 8, 2020.

Chapter 5

MISLOCALIZATION IN PLASMON-ENHANCED SINGLE-MOLECULE FLUORESCENCE MICROSCOPY AS A DYNAMICAL YOUNG'S INTERFEROMETER

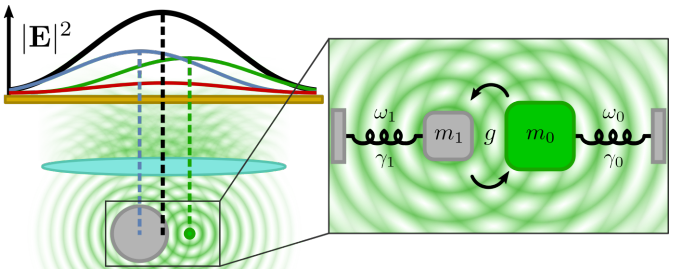

Reproduced in part with permission from:

Harrison J. Goldwyn, Kevin C. Smith, Jacob A. Busche, and David J. Masiello

ACS Photonics 2018 5 (8), 3141-3151

DOI: 10.1021/acsphotonics.8b00372

abstract

Mislocalization is a quantitative measure of the inability to locate the positions of individual molecular emitters in plasmon-enhanced super-resolution fluorescence microscopy. It is due to an unfortunate side-effect that scrambles the spatial profile of a molecule's fluorescence signal when plasmonic nanoantennas are introduced to boost that signal. In this manuscript, we present an understanding of the mislocalization problem in plasmon-enhanced super-resolution fluorescence microscopy based upon a simple and intuitive theoretical model. In particular, we derive an analytic expression for mislocalization and demonstrate explicitly

how it depends upon both the macroscopic interference of the coherent emission from molecular and plasmonic emitters as well as the microscopic dynamics of the coupled system. To derive this expression we draw upon an analogy to the Fano interference problem and show that the spatial asymmetry in the intensity profile can be encapsulated into a single effective parameter that depends rigorously upon basic system properties. We further elucidate the causes of mislocalization within the context of hybridization between molecular and plasmonic emitters and show analytically how the localization error depends upon the relative separation, orientation, detuning, and polarizability of the emitters. Lastly, we derive a new model-based form of the plasmon-enhanced single-molecule fluorescence image for specified molecular dipole orientations and demonstrate that it significantly outperforms standard Gaussian fitting in locating the position of the molecule.

5.1 Introduction

Super-resolution fluorescence microscopy [68, 107, 137, 19, 123, 49, 23] has today reached spatial resolutions on the order of 20 nm [77] while providing molecular specificity in environments inaccessible to near-field probing such as live biological systems [56, 76, 101]. By switching molecules one at a time between emissive and non-emissive states [42, 105], such microscopies infer the location of each emitter from the centroid position of their isolated fluorescence signals. The intrinsically weak intensity of these images, however, limits localization precision and has motivated the incorporation of plasmonic nanoantennas known to boost the signal from individual molecules [87, 57, 95]. Unsurprisingly though, the image centroid no longer encodes the exact molecular position when both molecule and plasmonic nanoantenna are within the same diffraction-limited spot. Instead, the Airy disk pattern associated with a microscope's point spread function (PSF) reports a convolution of the emission from both sources, with its maximum lying along the line connecting the two, potentially even lying external to the sources. Naively, one might subtract the isolated nanoantenna's PSF from the observed image to reclaim the location of the molecule as the centroid of a two-dimensional Gaussian fit. However, the plasmon-enhanced image is not simply the sum of

PSFs of each emitter, but instead depends upon both the 1) underlying microscopic dynamical interaction between molecular emitter and induced polarization in the nanoantenna, and 2) the macroscopic radiative interference between their resulting fields. The difference between the apparent position dictated by the Gaussian maximum and the exact molecular position is commonly called the localization error or mislocalization.

Here we present an idealized yet fully analytical model of mislocalization based upon the radiative emission of two coupled and interfering dipoles, one representing the fluorescent molecule and the other representing the polarization induced in a nearby metallic nanoantenna. A vast body of literature has already been devoted to imaging molecular emitters in the vicinity of plasmonic metal surfaces and nanoparticles; see, e.g., Ref. [162] for a recent review. Among this work, both experimental and computational efforts have been made to elucidate the physical phenomena underlying mislocalization in plasmon-enhanced single-molecule optical imaging. Specifically, the image centroid has been observed to shift towards the geometric center of the nanoantenna, even at molecule-nanoantenna separations where enhancement is not expected, a feature that has been related to the portion of radiated power directed through the nanoantenna instead of emitted directly from the molecule to free space using numerical electrodynamics simulation [159]. By specifying the exact molecule location relative to the nanoantenna with molecular spacers, mislocalization has been quantitatively extracted from experiment [24, 128], even for three-dimensional systems with additional geometric mislocalization caused by projection onto a two-dimensional image [59]. Unintuitively, the image centroid has also been observed outside of the region between the emitters in both experiment and simulation [160, 136, 99, 151]. Ref. [136] suggested this observation to be a result of interference between the molecule and nanoantenna emission and presented an intuitive explanation based on Young's interference. Refs. [159, 160, 24, 128, 59, 136, 99, 151] use electromagnetic simulation to interpret observation as well as to explore dependence upon certain experimentally accessible parameters. Such simulations are useful for these purposes, but can obscure the physics in that they provide no analytic understanding of the underlying physical mechanisms. For spherical nanoantenna geometries, Mie theory provides

a middle ground, combining analytical insight with simulation. Towards understanding the origins of mislocalization in surface-enhanced Raman scattering [67], generalized Mie theory has demonstrated the importance of interference among higher-order plasmon modes on image distortion when the molecule is located within the fluorescence quenching zone ($\lesssim 5$ nm from the nanoantenna surface) necessary for Raman scattering. Despite this body of work, to date, there has been no simple theoretical model that describes the mislocalization problem completely analytically. Such a model is important because it makes explicit the dependence of mislocalization upon each parameter, devoid of the complexity of Mie theory and obfuscation by electrodynamics simulation. It is the purpose of this Paper to provide a model containing the minimal ingredients necessary to reproduce observation while clearly demonstrating the dependence of mislocalization on basic system parameters.

In the following, we begin by reviewing Young's double-slit experiment and make an analogy between the wave mechanics of two-slit diffraction and a pair of radiating dipole oscillators as suggested in Ref. [136]. With the second dipole representing the nanoantenna polarization induced by the first, we then develop a description of their coupled dynamics and resulting electromagnetic radiation. After focusing this radiation with a lens, parallels are drawn between Young's diffraction pattern and the image, where the latter incorporates the mutual, self-consistent coupling between molecular dipole and plasmonic nanoantenna. In analogy to Fano's characterization of spectral antiresonance line shapes in terms of basic parameters [55], we derive an analytical measure of the system's fluorescence mislocalization that depends only upon the distance- and orientation-dependent dipole-dipole coupling strength and nanoantenna polarizability. Lastly, we compare our analytical image intensity to that of full-wave numerical electrodynamics simulation of the coupled system and demonstrate that fitting our model to the numerically exact image of a dipole-driven gold nanoantenna significantly outperforms Gaussian fitting to the same image in the determination of molecular position. Taken together our work provides a critically needed understanding of the origins of mislocalization in plasmon-enhanced super-resolution fluorescence imaging and can be used to extract a more accurate estimate of the molecule's position than is provided

by current methods.

5.2 Analogy between 2-slit interference and 2-dipole emission

An illustration of a coupled molecule-nanoantenna system together with a convoluted signal typical of plasmon-enhanced single-molecule fluorescence is displayed in Fig. 5.1a. The system image behaves according to the following generic intensity

$$\begin{aligned} I(x,y) &= \frac{c}{8\pi}\left|\mathbf{E}_0+\mathbf{E}_1\right|^2 \\ &= \frac{ck^6}{8\pi}\Big[|p_0|^2 f_{\mathrm{PSF}}(x,y;d)+|p_1|^2 f_{\mathrm{PSF}}(x,y)+2|p_0||p_1| f_{\mathrm{IF}}(x,y;d)\cos\Phi\Big], \end{aligned} \tag{5.1}$$

measured on a photo-detector positioned at height $z = h$ above and parallel to the (x, y) plane containing the sources. Independent molecule and nanoantenna PSFs (f_{PSF}) contribute to this signal as does an interference function (f_{IF}). Each component is scaled by a separation- and orientation-dependent dipole amplitude (p_0 for the molecule and p_1 for the nanoantenna) that determines the relative weighting of their individual PSFs as well as that of the interference; the latter is further modulated by a phase Φ dictating the sign of the interference, i.e., constructive or destructive. Figs. 5.1b and c show the effects of dipole orientation relative to separation ($\mathbf{d} = d\hat{\mathbf{e}}_x$) upon the image as well as its underlying components.

Although the intensity in Eq. (5.1) is expressed in the language of diffracted-limited imaging, it is a general description of wave interference from two distinct sources. With the functional form of f_{PSF} and f_{IF} kept general for now, qualitative intuition for the shape and apparent centroid position of a plasmon-enhanced fluorescence image can be gained by analogy to the double-slit experiment. When the slit size is small in comparison to the slit separation d and distance to the detector h, the diffracted waves emanating from the slits appear spherical as if emitted by two oscillating dipoles $\mathbf{p}_i(t) = |p_i|e^{-i(\omega t-\phi_i)}\hat{\mathbf{p}}_i$ $(i = 0, 1)$, each located within a slit. Fig. 5.2 displays the duality between a plane wave passing through two slits and two dipole emitters. Panel a illustrates the case of normal incidence where there is no inherent phase difference between spherical wave sources, while Panel b illustrates the

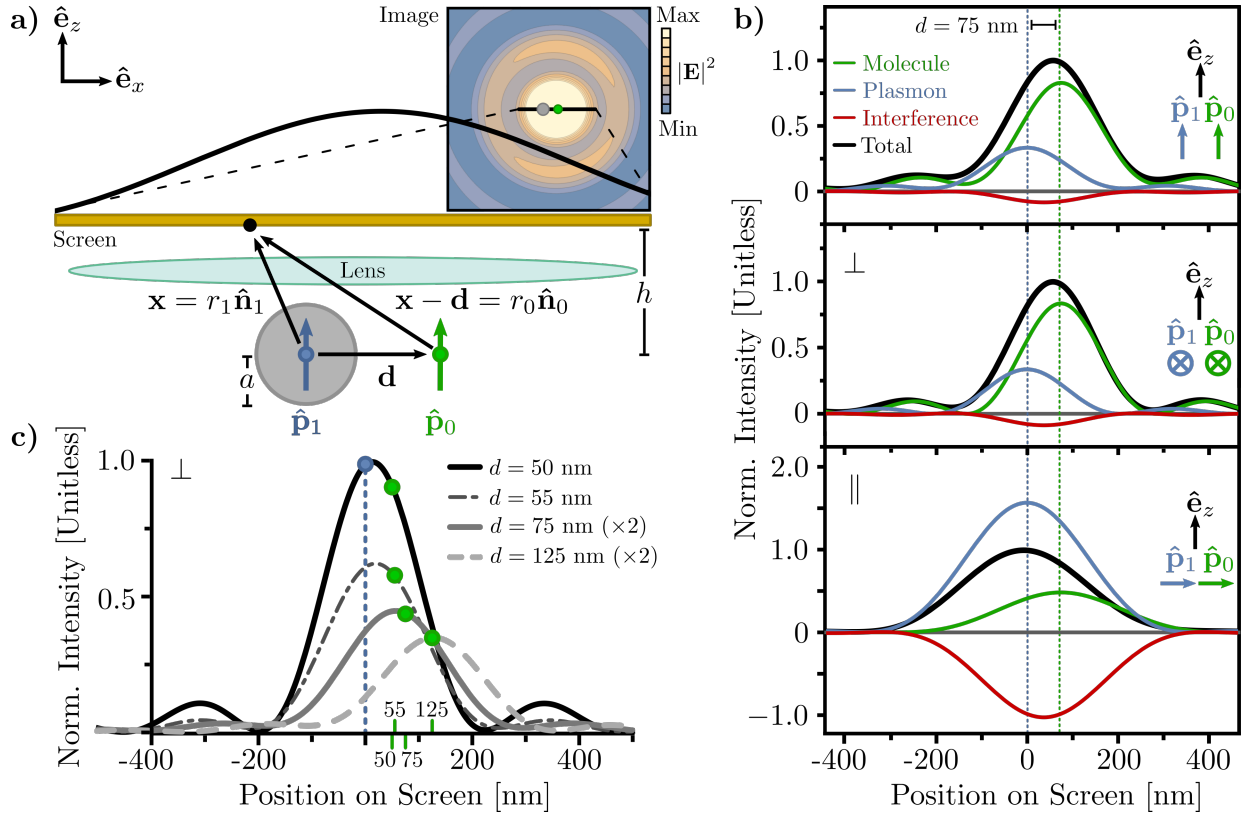

Figure 5.1: Plasmon-enhanced single-molecule fluorescence images. (a) Illustration of a fluorescent molecule (green dipole) and plasmonic nanoantenna (blue dipole) separated by the distance $\mathbf{d} = d\hat{\mathbf{e}}_x$. The dipole radiation fields are diffracted through a lens and imaged on the screen at $(x, y, z = h)$. (b) Calculated intensity images (black) for all three unique dipole emitter orientations are displayed; from top to bottom, the orientations are named as coaxial ($\hat{\mathbf{p}} = \hat{\mathbf{e}}_z$), perpendicular ($\hat{\mathbf{p}} = \hat{\mathbf{e}}_y \perp \mathbf{d}$), and parallel ($\hat{\mathbf{p}} = \hat{\mathbf{e}}_x \parallel \mathbf{d}$). Also plotted are the molecule PSF (green), plasmon nanoantenna PSF (blue), and interference function (red) that sum to form each image. Comparison between the image and its components illustrates the complexity of the observable. (c) A progression of images versus molecule-nanoantenna separation is displayed for dipoles oriented $\perp \mathbf{d}$. The true position of the molecule has been explicitly labeled on the axis (thin tick marks) and curves (green circles) as an aid for the eye.

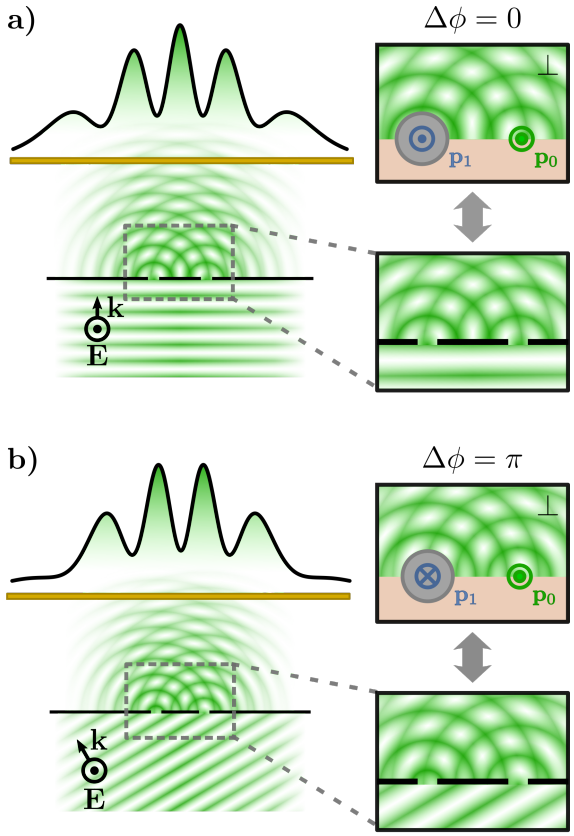

Figure 5.2: Analogy between Young's double slit and a pair of radiating electric dipoles. (a) A normally-incident plane wave emerges from the slits as two spherical waves of equal phase, as if two dipole emitters aligned with the field polarization and oscillating in phase are located within each slit. Constructive interference appears along rays of equal path length, placing the maximum intensity between the slit/emitter positions. (b) An oblique-incident plane wave produces a relative phase that depends upon the incident angle. The case of $\Delta\phi = \pi$ is illustrated to demonstrate that destructive interference displaces the maximum intensity away from the emitters' center. Regardless of incident angle, the relative emitter brightness can shift the interference maximum asymmetrically towards and even past the brighter emitter location. Wavelength, screen height, slit/emitter separation, and interference pattern (from Eq. (5.2)) are drawn to scale for dipoles of equal amplitude, however, the slit widths are not.

case of oblique incidence with phase difference $\Delta\phi = \phi_1 - \phi_0$ depending upon the incident field direction.

If the distance h between the dipole emitters and the observation screen is much larger than the emission wavelength $\lambda = 2\pi/k = 2\pi c/\omega$, then the fields from each dipole take their radiation zone forms $\mathbf{H}_i(r_i\hat{\mathbf{n}}_i) = k^2\hat{\mathbf{n}}_i \times \mathbf{p}_i(t)e^{ikr_i}/r_i$ and $\mathbf{E}_i(r_i\hat{\mathbf{n}}_i) = \mathbf{H}_i(r_i\hat{\mathbf{n}}_i)\times\hat{\mathbf{n}}_i$ in free space, where r_i connects the location of each dipole to the observation point $r_i\hat{\mathbf{n}}_i$ as displayed in Fig 5.1a; i.e., $r_0\hat{\mathbf{n}}_0 = \mathbf{x} - \mathbf{d}$ for the molecule and $r_1\hat{\mathbf{n}}_1 = \mathbf{x}$ for the nanoantenna. Inserting these radiated fields into Eq. (5.1) makes explicit the form of the radiative intensity I from two dipoles in free space. Visualization and discussion of this intensity is facilitated by limiting the observation to points along the x-axis of the photodetector. In the form of Eq. (5.1), the unfocused image of the intensity from two $\perp$-polarized ($\hat{\mathbf{p}} = \hat{\mathbf{e}}_y \perp \mathbf{d}$) dipoles along the line $(x, 0, h)$ is

$$I(x) = \frac{ck^6}{8\pi}\left[|p_0|^2\frac{1}{(kr_0)^2} + |p_1|^2\frac{1}{(kr_1)^2} + 2|p_0||p_1|\frac{1}{(kr_0)(kr_1)}\cos\left(k(r_1 - r_0) + \Delta\phi\right)\right], \quad (5.2)$$

where $(kr_i)^{-2}$ and $[(kr_0)(kr_1)]^{-1}$ are the free space equivalents of f_{PSF} and f_{IF}. Similar forms for I can be derived for the parallel ($\hat{\mathbf{p}} = \hat{\mathbf{e}}_x \parallel \mathbf{d}$) and coaxial ($\hat{\mathbf{p}} = \hat{\mathbf{e}}_z$) dipole orientations. While the free space PSFs are different than in the focused image, they are similarly peaked above the source locations as dictated by the denominator $r_i = ((x - x_i)^2 + h^2)^{1/2}$, where $x_0 = d$ and $x_1 = 0$. The latter spatially-dependent interference function is the product of two functions peaked respectively at the location of each dipole emitter. For $h \gg d$, the widths of the free space PSFs in Eq. (5.2) are large in comparison to d and combine to produce a single-peaked envelope modulated by interference fringes.

Analogy to the double slit experiment is better demonstrated by equating the dipole amplitudes $p_0 = p_1 = p$ and approximating $r_0 \approx r_1 = r$ in the denominators of the free-space PSFs. Care must be taken, however, in evaluating the spatially-dependent phase $k(r_1 - r_0) = kd\sin\theta$, which can be well approximated for small diffraction angles by $kd\theta$. Taken together these approximations lead to the familiar Young's interference pattern

$$I(\theta) \to I_{\mathrm{inc}}\left[2 + 2\cos\left(kd\theta + \Delta\phi\right)\right] \quad (5.3)$$

with $I_{\text{inc}} = ck^4p^2/8\pi r^2$ inheriting the role of incident field intensity and with an additional phase factor $\Delta\phi$ dictated by the incidence angle or equivalently the relative phase between dipoles. For an aberration-free but diffraction-limited microscope, the ray interference due to the spatially dependent phase $kd\theta$ is negligible, leaving the sign of the interference dependent only on $\Delta\phi$. This absence of optical path length dependence in the phase changes the qualitative nature of the interference. Without spatial oscillations, the interference is either constructive or destructive across the entire observation window and biases the centroid towards (if constructive) or away (if destructive) from the center of the two emitters. This intuition is the beginning of understanding how observed trends in mislocalization are manifested in Young's interference.

Inserting a lens between the dipole emitters and detector changes the spatial form of the intensity quantitatively, but the PSFs remain peaked about their respective source position. The interference term is similarly peaked but at the midpoint between the emitters resulting from the cross product of the focused fields from each dipole. This means that the intuition gained from understanding the image as composed of three distinct peaked functions in double-slit interference may be applied directly to the diffraction-limited image of a microscope by replacing the fields in Eq. (5.1) with the focused and diffracted dipole fields. Analytic forms for f_{PSF} and f_{IF} for all three unique dipole orientations can be approximated by assuming the microscope to be an ideal, infinity-corrected and aberration-free optical system with numerical aperture NA = 1. Details of computing the image fields via the Debye-Wolf diffraction integral are presented in the Methods Section.

5.3 Coupled dipole interaction model

Up to this point, the underlying microscopic dynamics of the dipole emitters and associated relative phase have been left unspecified. We now show how to model the interacting molecule-nanoantenna system as a pair of coupled dipole oscillators. In previous work [36, 39], we demonstrated the mapping of multipolar localized surface plasmon resonances onto corresponding mechanical oscillators, each with an associated effective mass m_ℓ and

resonance frequency ω_ℓ in the quasistatic limit. $\ell = 1$ corresponds to the dipole plasmon mode. However, for any ℓ, the mass is inversely proportional to the static (zero-frequency) polarizability α_{sp} and resonance frequency, the latter determined by material- and geometry-specific parameters related to both atomically bound and free conduction electronic response of the plasmon nanoantenna as will be discussed later. Similar correspondence between a molecular transition (i.e., fluorescence emission) dipole moment and a harmonic oscillator follows directly from Schödinger's equation, with the transition's effective mass m_0, transition frequency ω_0, and damping constant γ_0 parametrized by the free molecule's fluorescence spectrum.

The interaction between molecular dipole and plasmonic nanoantenna is well-known to involve higher-order plasmon modes beyond the dipole whenever the two are in close proximity (shown for a spherical gold nanoantenna of radius $a = 40$ nm to be edge-to-molecule separations of $d - a \lesssim 10$ nm [7]). At such close distances, inefficient coupling of the higher-order plasmon modes to the radiation field quench the molecule's fluorescence and allow weaker molecular optical processes to persist, such as Raman scattering [115, 89, 103, 30]. However, since this Paper focuses only on understanding mislocalization in the regime where fluorescence emission is dominant ($d-a \gtrsim 10$ nm) using the most simple analytic model possible, we neglect all higher-order plasmon multipole moments and couple the remaining nanoantenna dipole mode to the molecular transition via the fully-retarded dipole-dipole interaction. The resulting equations of motion describing the plasmon-enhanced single-molecule fluorescence are classical in appearance,

$$\begin{aligned}
\ddot{p}_0 &= -\omega_0^2 p_0 - \gamma_0 \dot{p}_0 + \frac{e^2}{m_0}\hat{\mathbf{p}}_0 \cdot \mathbf{E}_1(\mathbf{d}) + \frac{2e^2}{3m_0c^3}\dddot{p}_0 + \frac{e^2}{m_0}E_F e^{-i\omega t} \\
\ddot{p}_1 &= -\omega_1^2 p_1 - \gamma_1 \dot{p}_1 + \frac{e^2}{m_1}\hat{\mathbf{p}}_1 \cdot \mathbf{E}_0(\mathbf{0}) + \frac{2e^2}{3m_1c^3}\dddot{p}_1,
\end{aligned} \tag{5.4}$$

where the physical oscillation amplitude and phase of each dipole moment is determined by the complex magnitude $|p_i|$ and phase angle $\phi_i = \tan^{-1} \mathrm{Im}\, p_i / \mathrm{Re}\, p_i$. Here, $(e^2/m_0)\hat{\mathbf{p}}_0 \cdot \mathbf{E}_1(\mathbf{d}) \equiv (g/m_0)p_1$ and $(e^2/m_1)\hat{\mathbf{p}}_1 \cdot \mathbf{E}_0(\mathbf{0}) \equiv (g/m_1)p_0$, where $g \equiv g(\mathbf{d}) \equiv e^2\hat{\mathbf{p}}_0 \cdot \mathbf{G}(\mathbf{d}) \cdot \hat{\mathbf{p}}_1$ is the dipole-dipole coupling strength between molecular transition dipole $\mathbf{p}_0$ and the induced

polarization in the nanoantenna, the latter treated as a point dipole $\mathbf{p}_1$ located at the center of a sphere of radius a. $\mathbf{G}(\mathbf{d}) = [(3\hat{\mathbf{d}}\hat{\mathbf{d}} - 1)(1/d^3 - ik/d^2) - (\hat{\mathbf{d}}\hat{\mathbf{d}} - 1)k^2/d]e^{ikd}$ is the dyadic Green's function [117], γ_1 is the nanoantenna's nonradiative linewidth, and the dipole jerk terms account for the effects of radiation reaction. $\mathbf{E}_1(\mathbf{d})$ and $\mathbf{E}_0(\mathbf{0})$ are the electric dipole fields of the nanoantenna at $\mathbf{x} = \mathbf{0}$ and molecule at $\mathbf{x} = \mathbf{d}$, each evaluated at the position of the other. Note that g is identical for the coaxial and perpendicular dipole orientations illustrated in Fig. 5.1, and the orientation of the induced dipole $\mathbf{p}_1$ is completely determined by the molecular transition dipole $\mathbf{p}_0$ and $\mathbf{d}$ since $\mathbf{p}_1 = \alpha_1\mathbf{E}_0(\mathbf{0}) = \alpha_1\mathbf{G}(\mathbf{d})\cdot\mathbf{p}_0$. The form of $\mathbf{G}(\mathbf{d})$ also reveals that the induced plasmon dipole $\mathbf{p}_1$ in the nanoantenna will be parallel to the molecule dipole moment $\mathbf{p}_0$ only when $\mathbf{p}_0 \parallel \mathbf{d}$ or $\mathbf{p}_0 \perp \mathbf{d}$.

A fictitious harmonic electric field E_F of frequency ω is applied to the molecular oscillator to model population of the emissive state by absorption of the real excitation field and subsequent vibrational relaxation characteristic of fluorescence. In this way the molecule oscillator represents the emissive transition dipole and ω can therefore be interpreted as a single Fourier component of molecular fluorescence, taken here to be at the peak of the emission spectrum, i.e., at $\omega = \omega_0$. At this Stokes-shifted frequency the plasmon oscillator is not directly driven by E_F because plasmon photoluminescence is negligible in comparison to the molecule's fluorescence [100].

Although the intense near-field of the plasmonic nanoantenna will enhance molecular absorption, mislocalization is independent of the absorption rate [102] modeled here by E_F. This absorption independence of the coupled system's radiative emission profile takes origin as linear dependence between p_1 and p_0 in the steady-state solution to Eq. (5.4), i.e, $\mathbf{p}_1 = \alpha_1\mathbf{E}_0(\mathbf{0}) = \alpha_1\mathbf{G}(-\mathbf{d})\cdot\mathbf{p}_0$. Using this result, the focused diffraction-limited intensity at height $z = h$ presented in Eq. (5.1) can be normalized by the molecule emission $I_0 \equiv (ck^6/8\pi)|p_0|^2$ without loss of spatial information contributing to mislocalization. The image shape is then defined by

$$\frac{I(x,y)}{I_0} = f_{\mathrm{PSF}}(x,y;d) + \left|\frac{p_1}{p_0}\right|^2 f_{\mathrm{PSF}}(x,y) + 2\mathrm{Re}\left[\frac{p_1}{p_0}\right] f_{\mathrm{IF}}(x,y;d). \tag{5.5}$$

Note that $E_F = |\mathbf{E}_F|$ only appears within I_0 because $\mathbf{p}_0 = \alpha_0[\mathbf{E}_F + \mathbf{E}_1(\mathbf{d})] = [\alpha_0^{-1} - \mathbf{G}(\mathbf{d})\alpha_1\mathbf{G}(\mathbf{0})]^{-1}\mathbf{E}_F$, which clearly demonstrates that the absorption rate only scales the intensity profile and does not contribute to mislocalization. What is critical in controlling the shape of the system image is the relative amplitude of the two emitters, $p_1/p_0 = |p_1/p_0|e^{i\Delta\phi}$.

The ratio of dipole amplitudes p_1/p_0 can be determined by the equations of motion in Eq. (5.4), which approximate the electronic response of the plasmon nanoantenna as a free-electron gas. But better quantitative agreement with simulation is achieved by generalizing the nanoantenna polarizability to account for the response of the metal's bound and free electrons as

$$\begin{aligned}\frac{p_1}{p_0} &= a^3\frac{\varepsilon(\omega_0)-1}{\varepsilon(\omega_0)+2}\frac{g(\mathbf{d})}{e^2} \\ &= \left[a^3\frac{\varepsilon_\infty - 1}{\varepsilon_\infty + 2} + \frac{e^2/m_1}{\omega_1^2 - \omega_0^2 - i\omega_0\gamma_1^R}\right]\frac{g(\mathbf{d})}{e^2},\end{aligned} \tag{5.6}$$

where $\varepsilon(\omega) = \varepsilon_\infty - \omega_p^2/\omega(\omega + i\gamma_D)$ is the bulk Drude dielectric function expressed in terms of the standard Drude parameters. The first term in square brackets, $\alpha_\infty = a^3(\varepsilon_\infty - 1)/(\varepsilon_\infty + 2)$, represents the instantaneous response of the nanoantenna's bound core electrons to the molecular dipole field, while the second term, $\alpha_f(\omega_0) = \alpha_{sp}\omega_1^2/(\omega_1^2 - \omega_0^2 - i\omega_0\gamma_1^R)$, with $\alpha_{sp} = 3a^3/(\varepsilon_\infty + 2) = e^2/m_1\omega_1^2$, represents the causal response of its free conduction electrons. It is the dynamic polarizability in the second term that is important and that is described completely by the coupled equations of motion (Eq. (5.4)). Writing the ratio $p_1/p_0 = \alpha_1(\omega_0)(g/e^2)$, where $\alpha_1(\omega) = \alpha_\infty + \alpha_f(\omega)$ is the polarizability of the plasmon nanoantenna, emphasizes the generality of this model since the nanoantenna may be of arbitrary shape or size as long as its polarizability can be determined.

The relative contributions to the imaged intensity in Eq. (5.5) from molecule, nanoantenna, and interference are compared as functions of separation in the insets in Fig. 5.6a. The three terms composing Eq. (5.5) are each plotted as a function of position in the image plane in the Supplementary Information to gain intuition on the image composition. In these plots and in what follows, the parameters describing the isolated plasmon oscillator are determined by fitting the scattering cross section derived from the equation of motion for

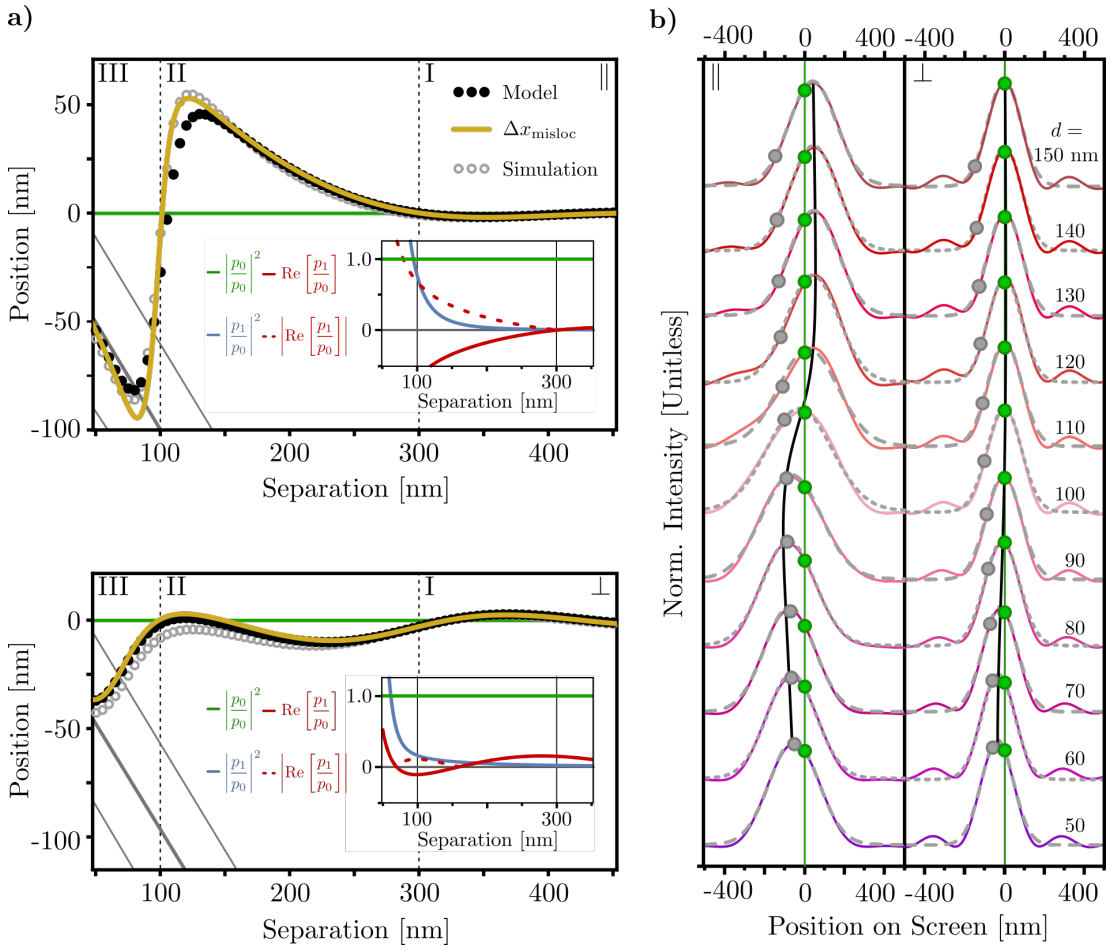

Figure 5.3: Gaussian mislocalization in modeled and simulated plasmon-enhanced single molecule fluorescence images as a function molecule-nanoantenna separation d. (a) Mislocalization for $\hat{\mathbf{p}} \parallel \mathbf{d}$ (top) and $\hat{\mathbf{p}} \perp \mathbf{d}$ (bottom) determined by fitting a two-dimensional Gaussian to electrodynamics simulation (gray circles) or to the image intensity given in Eq. (5.5) (black circles) is compared to prediction using the analytic mislocalization measure $\Delta x_{\text{misloc}}(d)$ in Eq. (5.10) (yellow). An $a = 40$ nm spherical gold nanoantenna in vacuum is used in each case. The location of the molecule (green) and the locations of the center and edges (gray) of the nanoantenna are plotted for reference. Three qualitatively distinct separation regimes are marked by roman numerals : (I) mislocalization is negligible, (II) interference dominates, and (III) plasmon PSF dominates. (b) Normalized plasmon-enhanced single molecule images (red–purple) calculated from Eq. (5.5) are overlaid with two-dimensional Gaussian fits (gray, dashed) at separations $d = 50-150$ nm. Δx_{misloc} is plotted in black along with the true locations of the nanoantenna (gray circles) and molecule (green circles) as a guide for the eye.

the uncoupled plasmon $\ddot{p}_1 + \gamma_1^R \dot{p}_1 + \omega_1^2 p_1 = (e^2/m_1) E e^{-i\omega t}$ to the simulated scattering cross section of an $a = 40$ nm gold sphere in vacuum, but could also be obtained from experiment. Radiation reaction effects increase the linewidth according to $\gamma_i^R = \gamma_i + (2e^2/3m_i c^3)\omega^2$. The resonance energy, linewidth, and effective mass of the nanoantenna plasmon are $\hbar\omega_1 = 2.55$ eV, $\hbar\gamma_1 \equiv \hbar\gamma_D = 0.06$ eV, and $m_1 = 8.31 \times 10^{-7} m_e$. The fluorophore parameters are obtained from the same procedure, but using the equation of motion for the uncoupled molecule emission $\ddot{p}_0 + \gamma_0^R \dot{p}_0 + \omega_0^2 p_0 = (e^2/m_0) E e^{-i\omega t}$ to fit typical fluorescence cross sections for dyes commonly used in super-resolution imaging. The resonance energy, linewidth, and effective mass of the molecule's transition dipole are $\hbar\omega_0 = 2.60$ eV, $\hbar\gamma_0 = 0.075$ eV, and $m_0 = 1.22 \times 10^3 m_e$. All other parameters, such as the coupling strength and radiation reaction force are computed from these parameters (and fundamental constants such as the mass m_e and charge $-e$ of the electron). Note that the effective mass of the plasmon is ten orders of magnitude smaller than that of the molecular transition dipole, a fact that will be of importance in the following. This scale difference is due to the difference in polarizabilities between the two emitters, since effective mass is inversely proportional to polarizability as described above. Also note that the above parameters make the nanoantenna-molecule detuning $\omega_1^2 - \omega_0^2$ negative. However, a positive detuning would only interchange the role of constructive and destructive interference.

To aid in the analysis and interpretation of the PSF image and resulting mislocalization, it is instructive to revisit Eqs. (5.5) and (5.6) from the viewpoint of hybridized modes. The response of the nanoantenna core electrons and friction are temporarily neglected and the dipole-dipole coupling is restricted to the near-field interaction. These approximations, while not quantitatively exact, retain the essential features of the system while providing intuition about mislocalization based upon hybridization. As a function of dipole-dipole separation, orientation, detuning, and relative polarizability, the molecule and nanoantenna dipoles will mix to varying extent as described by the mixing angle $\beta =$

$(1/2)\tan^{-1} 2g(\mathbf{d})/\sqrt{m_0 m_1}(\omega_1^2 - \omega_0^2)$ to produce the hybridized modes

$$\begin{aligned} p_+ &= p_0\left(\frac{m_0}{m_1}\right)^{1/4}\cos\beta + p_1\left(\frac{m_1}{m_0}\right)^{1/4}\sin\beta \\ p_- &= p_1\left(\frac{m_1}{m_0}\right)^{1/4}\cos\beta - p_0\left(\frac{m_0}{m_1}\right)^{1/4}\sin\beta \end{aligned} \tag{5.7}$$

with radiative spatial profiles that reflect the degree of mixing in their asymmetry. β takes values between 0 and $\pm\pi/4$, with $\beta = 0$ corresponding to no mixing and $|\beta| = \pi/4$ corresponding to maximal mixing of the uncoupled molecule and nanoantenna modes. In terms of β, Eq. (5.5) becomes

$$\frac{I(x,y)}{I_0(\beta)} \approx \sqrt{\frac{m_1}{m_0}}\cos^2\beta f_{\mathrm{PSF}}(x,y;d) + \sqrt{\frac{m_0}{m_1}}\sin^2\beta f_{\mathrm{PSF}}(x,y) + 2\sin\beta\cos\beta f_{\mathrm{IF}}(x,y;d), \tag{5.8}$$

where $I_0(\beta) = (ck^6/8\pi\cos^2\beta)|p_0|^2\sqrt{m_0/m_1}$ and where the relative brightness $p_1/p_0 = (1/2)\sqrt{m_0/m_1}\tan 2\beta$ can be interpreted as a measure of mixing p_0 and p_1 into the hybridized molecular excitonic-plasmonic normal modes p_+ and p_-. As discussed previously, the degree of mislocalization is determined entirely by the relative weights of the three prefactors of the individual PSFs and interference function. At the separations distances of interest (i.e., $d - a \approx 10 - 450$ nm), $2g(\mathbf{d})/\sqrt{m_0 m_1}(\omega_1^2 - \omega_0^2) \ll 1$ and $\beta \ll 1$, justifying the small angle approximation, i.e., $p_1/p_0 \approx \sqrt{m_0/m_1}\tan\beta$. For oscillators of equal mass, this would indicate weak hybridization and produce an image dominated by the molecule PSF. However, here, the extreme mismatch in oscillator masses (or, equivalently, polarizabilities) causes the amplitude of the nanoantenna PSF to be appreciable and even dominant over the molecule PSF for relatively small values of the mixing angle, reflecting the non-negligible contribution of the plasmon nanoantenna to the normal modes of the composite system.

Fitting a two-dimensional Gaussian function to the plasmon-enhanced fluorescence image in Eq. (5.5) quantifies the balance of the molecule, nanoantenna, and interference PSFs. The resulting Gaussian centroid location relative to the exact location of the molecule—called the centroid offset or mislocalization—is plotted in Fig. 5.3 for dipoles oriented parallel and perpendicular to $\mathbf{d}$; the third orientation with dipoles aligned along the optical axis, displayed

in Fig. 5.1a, is not shown because it is nearly identical to that of the perpendicular orientation as described above. Three qualitatively different regimes (denoted by I, II, III) are identified in Fig. 5.3: At separations d greater than the diffraction limit, i.e., $d \gtrsim \lambda/2\text{NA} \approx 240$ nm, two uncorrelated emitters would be resolvable by the Rayleigh criterion. But in this system, mislocalization remains beyond 240 nm because of the coupling-induced interference between coherent molecule and nanoantenna emission. I) This means that mislocalization is negligible only at separations $d \gtrsim 300$ nm, where both the Rayleigh criterion holds and the contribution from interference is bounded by $|p_1/p_0| \lesssim 0.1$. At these large separations, the coupling strength $|g/e^2| \lesssim 0.1/|\alpha_1(\omega_0)|$ and the mixing angle $\beta \approx 0$ as the plasmon receives minimal energy from the molecule's emissive transition. In this regime the normal modes are very weakly mixed and the molecule PSF dominates the image as in normal super-resolution microscopy. II) As the molecule approaches the nanoantenna, g and β increase and the relative amplitude $|p_1/p_0| \sim 1$. While $|p_1/p_0| < 1$, the interference begins to impact the image before the nanoantenna PSF because of its linear scaling with $\text{Re}[p_1/p_0] = |p_1/p_0| \cos\Delta\phi$. If the interference is destructive, f_{IF} will subtract from the imaged intensity between the emitters and shift the centroid to the right (see Fig. 5.1a for an illustration). If the interference is constructive, the system image is weighted towards the center of the emitters even before the nanoantenna PSF contributes. III) For $d \lesssim 100$ nm, g and β increase further and $|p_1/p_0| \gtrsim 1$. In this regime, the quadratic scaling of the nanoantenna PSF's amplitude causes the nanoantenna to dominate the image, shifting the total image onto the nanoantenna emission center or even past it slightly if the interference remains destructive.

The preceding analysis of mislocalization versus separation explains the dominant experimental observation: the centroid is much more likely to collapse onto the nanoantenna than to shift away due to destructive interference. It is only in the intermediate separation region (II) where interference can shift the image centroid outside the two emitters. This occurrence is made more rare by the fact that interference will only be destructive for certain dipole orientations, given the nature of g to change sign as a function of $\hat{\mathbf{p}} \cdot \mathbf{d}$.

Because the molecular dipole is randomly oriented in most experiments, destructive interference will often be washed out by molecules located at the same location but of different orientation. In simulation, the dipole orientation can be set explicitly and observation of positive mislocalization is more accessible. Because the plasmon PSF is always positive, the image centroid inevitably collapses onto the nanoantenna at close proximities regardless of dipole orientation. As discussed previously, this collapse of the system image centroid onto the plasmonic nanoantenna is well documented in the plasmon-enhanced single-molecule fluorescence literature. See, e.g., Ref. [162] for a recent review.

5.4 Fano-like asymmetry as a measure of mislocalization

While the centroid offset can be predicted for arbitrary molecule-nanoantenna separation via a Gaussian fit of the intensity in Eq. (5.5), it is also possible to derive an analytic expression for the centroid offset directly from the imaged intensity function. In 1961, Fano described asymmetric antiresonance lineshapes in Helium auto-ionization spectra in terms of the interference between bright and dark scattering channels, and encapsulated the deviation from a symmetric lineshape into an effective parameter that depends upon basic system properties [55]. The problem considered here of two coupled oscillators, one driven (i.e., the molecule, in analogy to the bright mode) and one undriven (i.e., the plasmon nanoantenna, in analogy to the dark mode), is of similar form. Interestingly, not only can such interferences arise in spectra [156] but so too can they manifest in the spatial profiles of absorbed [11] and emitted radiation. We make this analogy by factoring Eq. (5.5) into even and odd contributions about the location of the molecule projected onto the image screen, thus separating the terms that do not contribute to the centroid offset from those that do. Factoring out the spatially symmetric terms renders the image as a product of a symmetric function and a factor that is inherently antisymmetric. Taylor expansion allows us to map this factored form onto the product of a Gaussian (centered at the molecule location projected onto the image screen) with amplitude A and variance σ^2, and a line with slope η, all rigorously defined in terms of the nanoantenna polarizability α_1 and coupling strength g. All together,

the spatial asymmetry of the image is characterized by the approximate image function

$$\frac{I(x)}{Ae^{-x^2/2\sigma^2}} \approx 1 + \eta \cdot kx \tag{5.9}$$

with its maximum defining the apparent molecule location, or mislocalization,

$$\Delta x_{\text{misloc}}(d) = \frac{\sqrt{1 + (2\eta k\sigma)^2} - 1}{2\eta k}. \tag{5.10}$$

This mislocalization function is plotted versus molecule-nanoantenna separation d in Fig. 5.3 alongside the mislocalization resulting from numerical Gaussian fits to images computed from the oscillator model as well as from full-wave numerical electrodynamics simulation of the coupled-dipole system. It is evident that $\Delta x_{\text{misloc}}(d)$ not only recovers both Gaussian-fit-based measures of mislocalization, but more importantly, makes explicit the parameters that mislocalization depends upon. Further, $\Delta x_{\text{misloc}}(d)$ enables prediction of mislocalization without need for simulation once the independent oscillators are parametrized. Although simple to implement, the explicit dependence of η and σ on d is complicated and reserved for the Supplementary Information. Details of the procedure for obtaining Eq. (5.10) are presented in the Methods Section.

Up to this point, the nanoantenna-molecule detuning has been fixed so that the parallel dipole orientation produces primarily destructive interference at close proximity while the perpendicular orientation is constructive. The interference quality of these two orientations has resulted in different mislocalization trends as the molecule approaches the antenna, but the relationship between mislocalization sign and interference quality ($\cos\Delta\phi$) is ubiquitous across detuning. Fig. 5.4 expands upon this concept for a range of molecular emission energies (corresponding to the observation energy) relative to the fixed plasmon resonance energy, $\hbar\omega_1 = 2.55$ eV. For all separations, detunings, and orientations investigated, the image centroid appears between emitters when interference is constructive and outside emitters when destructive. At separations $d > 300$ nm, coupling is weak and mislocalization is minimal in all cases. Regions of large mislocalization appearing as dark red and blue in Fig. 5.4a dominate at close molecule-nanoantenna proximity, but persist to larger separations when

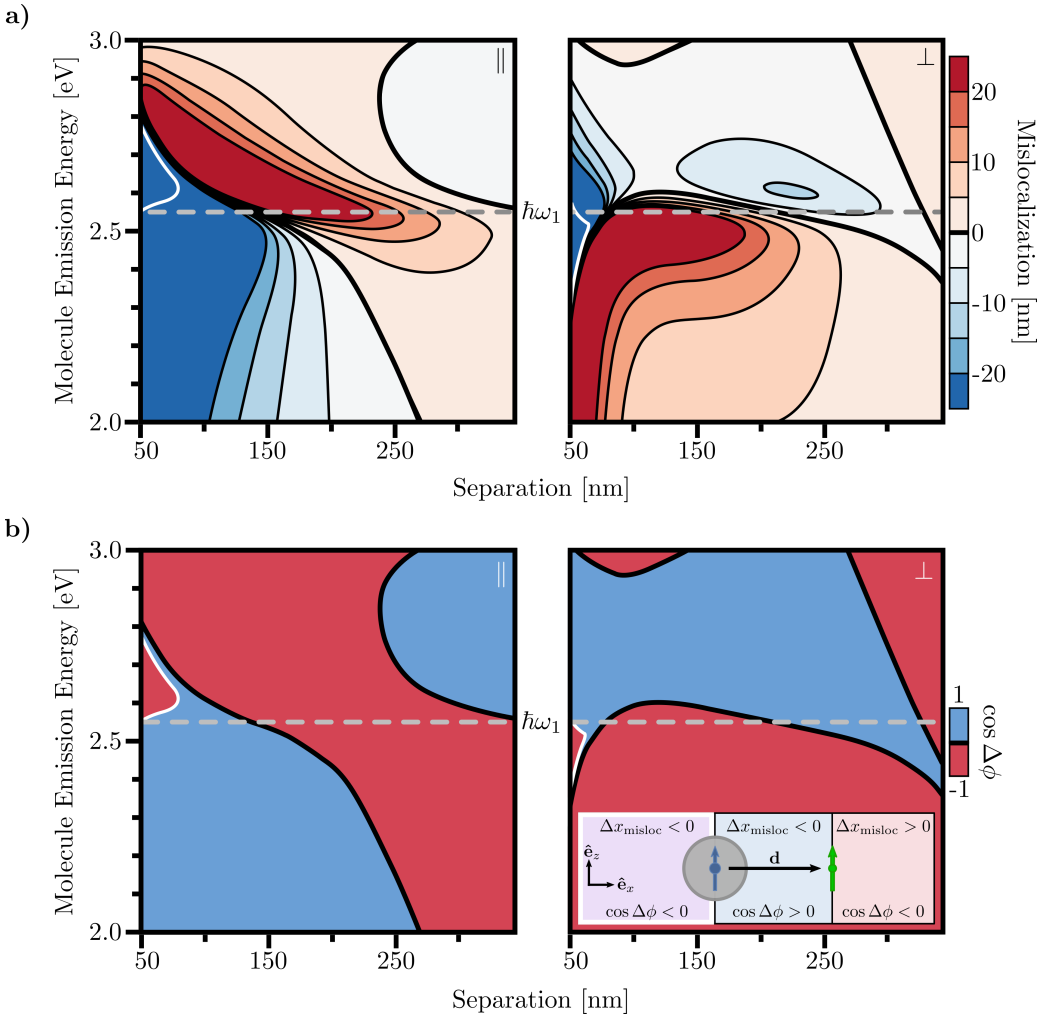

Figure 5.4: Correlation between mislocalization and interference quality. (a) Contour maps of mislocalization as a function of molecule emission energy $\hbar\omega_0$ and emitter separation d for $\parallel$ (left) and $\perp$ (right) dipole orientations. The fixed plasmonic nanoantenna resonance energy $\hbar\omega_1$ is marked by the horizontal line. Positive mislocalization corresponds to centroid displacement to the right of the antenna and negative mislocalization corresponds to the image centroid appearing between the two emitter locations except for when $\Delta x_{\text{misloc}} < -d$ (white outline) where the centroid lies to the left of the nanoantenna. (b) Binary interference quality maps show the sign of $\cos\Delta\phi = \text{Re}[p_1/p_0]/|p_1/p_0|$ as a function of $\hbar\omega_0$ and d. The inset displays the correspondence between mislocalization and interference quality. With constructive interference ($\cos\Delta\phi > 0$), the centroid appears in the region between the molecule and the nanoantenna. With destructive interference ($\cos\Delta\phi < 0$) the centroid may appear in either the region to the right of the molecule location or in the region to the left of the nanoantenna location (white outline), depending on the strength of the emitter-plasmon interaction.

$\hbar\omega_1 \approx \hbar\omega_0$ because $\alpha_1(\omega_0) \propto (\omega_1^2 - \omega_0^2)^{-1}$. Near zero detuning, the largest mislocalization at mid-range $150 < d < 250$ nm lies in the regions of destructive interference for both orientations, indicating a stronger impact on the observable than constructive interference at equal coupling strength. The tendency for interference quality and mislocalization direction to be opposite for dipoles $\parallel$ and $\perp$ $\mathbf{d}$ can be qualitatively understood by considering that the lowest energy dipole alignment from just the near field interaction ($g_{\mathrm{NF}} \propto d^{-3}$). If the dipoles were allowed to equilibrate quasistatically they would align head-to-tail. With fixed orientation, head-to-tail dipoles will be in phase if $\hat{\mathbf{p}} \parallel \mathbf{d}$ but out of phase for $\hat{\mathbf{p}} \perp \mathbf{d}$. Quantitatively, this result appears in the opposite sign of g for these orientations, which determines the relative phase of oscillation through $\mathrm{Re}[p_1/p_0]$. The transition between dark red and dark blue regions indicates a sharp change of the image centroid from one side of the molecule to the other as it approaches the nanoantenna. This type of transition can be seen in Fig. 5.3a for the $\parallel$ orientation at $d = 100$ nm and is due to a flip in interference quality while the coupling is relatively strong, as illustrated in Fig. 5.4b.

5.5 Alternative to gaussian fitting

From Fig. 5.3, it is clear that Gaussian fitting performs poorly when both emitters are located within the same diffraction-limited spot. Instead, we propose to use the derived analytic form for the image shape in Eq. (5.5) as a super-resolution fit function. Assuming that the observed dipole orientation is fixed relative to $\mathbf{d}$ by a polarizing filter [136], Eq. (5.5) can be applied directly to experimental data using only $\mathbf{d}$ as a fit parameter. For an arbitrarily oriented molecular emitter, the fields presented in the Methods Section for the three orthogonal dipole orientations can be weighted and summed to yield a more general analytic expression for the image where both d and the two angles specifying the molecular transition dipole orientation are fit parameters. As a proof of concept in the former case, the image shape on the right hand side of Eq. (5.5) is fit to the diffraction-limited image produced by a full-wave numerical electrodynamics description of a dipole-driven gold nanosphere together with numerical evaluation of the Debye-Wolf diffraction integral. The performance

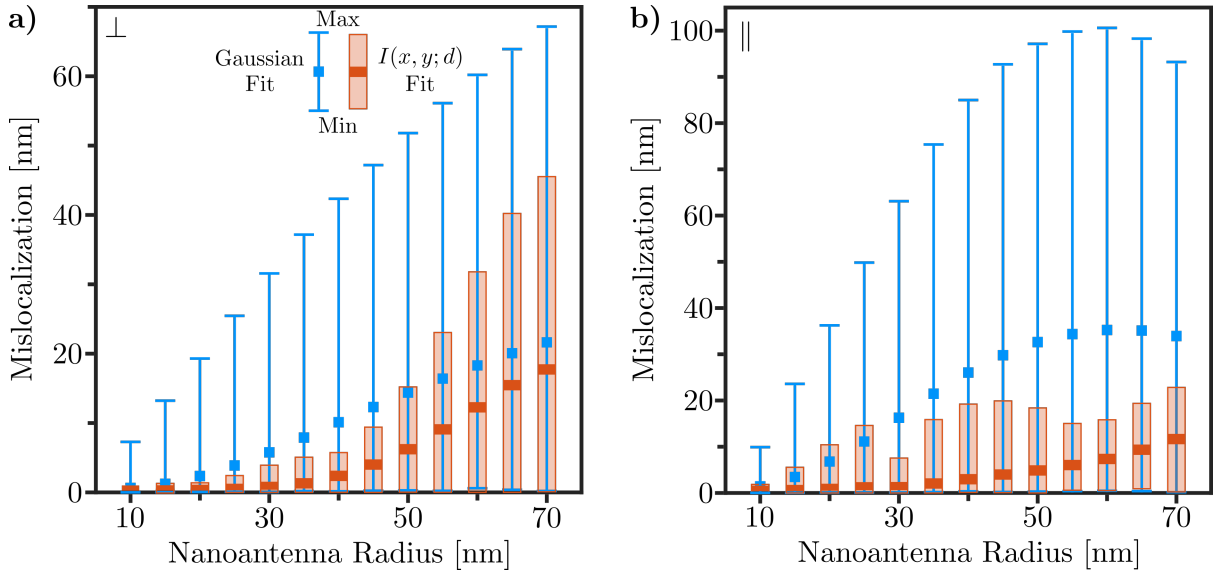

Figure 5.5: Extraction of molecule location from simulated plasmon-enhanced single molecule fluorescence images using the analytic image function $I(x, y; d)$ (orange) derived in Eq. (5.5) and a two-dimensional Gaussian fit (blue). Both fitting methods are tested against molecule-nanoantenna separations $a + 5 \leq d \leq 350$ nm for a range of spherical nanoantenna radii a in both $\parallel$ (a) and $\perp$ (b) dipole orientations. For each radius, the average, minimum, and maximum mislocalization are determined by comparing d to the fit position d_0 in $I(x, y; d_0)$ or to the centroid position (x_0) in a two-dimensional Gaussian function. The corresponding average mislocalization is denoted as a rectangle and the minimum and maximum mislocalization are indicated by vertical bars. $I(x, y; d)$ in Eq. (5.5) and the two-dimensional Gaussian are both fit to the same set of numerical electrodynamics simulations of a dipole-driven gold nanoantenna in vacuum. Across the wide range of nanoantenna radii sampled, fits to Eq. (5.5) provide a better estimate of molecule position than standard Gaussian fitting techniques.

of this new localization procedure is assessed by inference of the molecule position d by fitting both the analytic image function in Eq. (5.5) and a two-dimensional Gaussian function to the same electrodynamics simulation. These two procedures are contrasted in Fig. 5.5 for two of the three unique dipole orientations; again the third orientation is identical to the $\perp$ case and is included in the SI. The average, maximum, and minimum mislocalization across $a + 5 \leq d \leq 350$ nm are presented for various spherical nanoantenna radii from $10 - 70$ nm. Across all radii considered, the model fit is superior to the Gaussian fit, both in the average mislocalization as well as in the minimum and maximum localization errors.

In conclusion, we have presented a simple and intuitive theoretical model of plasmon-enhanced single-molecule fluorescence microscopy. The model draws on an analogy between Young's two-slit interference and a pair of radiating dipoles to organize the diffraction-limited image of the system into the superposition of three distinct contributions: the molecule PSF, nanoantenna PSF, and interference that can shift the intensity distribution towards or away from the center-point between emitters. The relative weight of each and resulting mislocalization are determined by the underlying microscopic coupled-dipole dynamics. Modeling the molecule-nanoantenna system by a pair of coupled oscillators accurately recovers the mislocalization calculated in full-wave electrodynamics simulation of a dipole-driven plasmonic nanoantenna. With this model, we draw on hybridization theory to discuss mislocalization from the perspective of mode mixing between molecule and plasmon degrees of freedom. We find that significant plasmon character is inherited by the hybrid modes at larger than expected separation distances due to the nanoantenna's significantly larger polarizability. Inspired by the Fano interference problem, we further derive an analytic measure of mislocalization that depends explicitly upon fundamental system parameters such as the relative separation, orientation, detuning, and polarizability of the emitters. This measure can be used to predict mislocalization without simulation, requiring only knowledge of the uncoupled emitters' emission/scattering spectra. Lastly, we propose a new model-based form of the plasmon-enhanced single-molecule fluorescence image that is appropriate for specified molecular dipole orientations and demonstrate that it significantly outperforms standard Gaussian

fitting in locating the molecule's position in electrodynamics simulation. This model provides a clear path towards generalizing the fit function to account for unknown molecular orientation, which will form the basis for future work.

5.6 Methods

Calculation and analytic approximation of image fields. The Debye-Wolf integral [163] allows accurate calculation of the PSF produced by diffraction-limited optical systems with large numerical aperture common in single-molecule fluorescence imaging [50]. For an idealized infinity-corrected microscope, the field composing the image is constructed by refraction at the objective lens, and then focusing at a top lens into image space where it is subject to diffraction. As outlined in Ref. [71], both the objective and top lens are considered spherical refracting surfaces with focal lengths f_{obj} and f respectively. The objective is defined by spherical coordinates $(\xi_{\text{obj}}, \zeta_{\text{obj}}, f_{\text{obj}})$ relative to the antenna location. The top lens is defined by (ξ, ζ, f) relative to the focal point in image space.

The image field is related to the scattered field at the objective by

$$\mathbf{E}(\rho,\varphi,z) = -\frac{ikfe^{ikf}}{2\pi}\int_0^{\xi_m} d\xi \sin\xi \int_0^{2\pi} d\zeta \sqrt{\frac{\cos\xi}{\cos\xi_{\text{obj}}}}\mathbf{E}^{\text{scat}}(\xi,\zeta)e^{ik[\rho\sin\xi\cos(\varphi-\zeta)+(z-h)\cos\xi]}. \tag{5.11}$$

The scattered field is evaluated at points on the objective by the relationship $\sin\xi = (f_{\text{obj}}/f)\sin\xi_{\text{obj}}$ and $\zeta = \zeta_{\text{obj}}$. The ratio of cosines appearing in the square root accounts for the two refractions. The term $e^{ik(z-h)\cos\xi}$ describes defocusing and defines the focal plane at $z = h$. The rotational symmetry of the lens/aperture allows analytic solution of the azimuthal ζ integral, leaving cylindrical Bessel functions. The remaining polar integral is evaluated numerically to produce images from all field data computed via full-wave electrodynamics simulation.

To obtain a simple closed form for the image fields, the numerical aperture is fixed at NA = 1 as well as the magnification, $f/f_{\text{obj}} = 1$. The effect of magnification can be restored theoretically by choosing a small, high-resolution image detection plane [67]. Under these

conditions, the image field in the focal plane produced by a single dipole source located along the optical axis ($\hat{\mathbf{e}}_z$) and oriented in (x, y)-plane is[1]

$$\mathbf{E}_i(\rho, \varphi, z = h) = -ik^3 e^{2ikf} p_i \begin{pmatrix} [\cos^2(\varphi + \psi) + \cos(2\varphi + 2\psi)] \frac{j_1(k\rho)}{k\rho} + \sin(\varphi + \psi)^2 j_0(k\rho) \\ \sin(\varphi + \psi)\cos(\varphi + \psi) j_2(k\rho) \\ -\cos(\varphi + \psi) \frac{J_2(k\rho)}{k\rho} \end{pmatrix}, \tag{5.12}$$

where the dipole moment points at an angle ψ relative to $\hat{\mathbf{e}}_x$. For a dipole moment parallel to the optical axis, the field takes the form

$$\mathbf{E}_i(\rho, \varphi, z = h) = -ik^3 e^{2ikf} p_i \begin{pmatrix} -\cos(\varphi) \frac{J_2(k\rho)}{k\rho} \\ -\sin(\varphi) \frac{J_2(k\rho)}{k\rho} \\ \frac{2}{3} j_0(k\rho) - \frac{1}{3} j_2(k\rho) \end{pmatrix}. \tag{5.13}$$

The analytic expressions for plasmon-enhanced single-molecule fluorescence images are obtained by the summing the dipole image fields above with the molecule translated to match its location in the scattering plane, i.e.,

$$I(x, y; d) = \frac{c}{8\pi} |\mathbf{E}_0(x - d, y, z = h) + \mathbf{E}_1(x, y, z = h)|^2. \tag{5.14}$$

We have found that these analytic images are numerically equivalent to direct computation of the Debye-Wolf integral for the combined scattered field from both emitters. The analytic PSFs and interference function are obtained simply from the expansion of Eq. (5.14). The one-dimensional PSFs used throughout this Paper are

$$\begin{aligned} f^{\parallel}_{\mathrm{PSF}}(x_i) &= 4 \left(\frac{j_1(kx_i)}{kx_i} \right)^2 + \left(\frac{J_2(kx_i)}{kx_i} \right)^2 \\ f^{\perp}_{\mathrm{PSF}}(x_i) &= \left(\frac{j_1(kx_i)}{kx_i} - j_0(kx_i) \right)^2 \end{aligned} \tag{5.15}$$

[1] Note that this expression for the focused and diffracted fields required a rotation that is not discussed here if the molecule is oriented at any angle between the perfectly parallel and perpendicular cases discussed in this more. This subtly is discussed in detail within Chapter 2 (specifically Eq. (2.45)). There are also small inconsistencies between Eqs. (5.12) and (5.13) and the equivalent expressions in Chapter 2. I believe Eqs. (2.46) and (2.68) are more accurate, but since their differences from what was originally published is minor, I have left the expressions in this chapter unchanged for historical accuracy.

and for the coaxial orientation,

$$f^{\odot}_{\mathrm{PSF}}(x_i) = \left(\frac{J_2(kx)}{kx}\right)^2 + \left(\frac{2}{3}j_0(kx_i) - \frac{1}{3}j_2(kx_i)\right)^2. \tag{5.16}$$

The one-dimensional interference function follows by replacing $x_i \to x - d$ and $x_i \to x$ in the first and second term respectively of each square as well as multiplication by $1/2$.

Analytic analysis of the Gaussian mislocalization.

To derive the parameters in Eq. (5.10), we start with the intensity evaluated along $(x, 0, h)$,

$$I(x;d) = \frac{ck^6}{8\pi}|p_0|^2\left(f_{\mathrm{PSF}}(x) + \left|\frac{p_1}{p_0}\right|^2 f_{\mathrm{PSF}}(x;d) + 2\mathrm{Re}\left[\frac{p_1}{p_0}\right] f_{\mathrm{IF}}(x;d)\right). \tag{5.17}$$

Note that, contrary to some of the work above, we have placed the molecule at the origin $x = 0$. It is then straightforward to split $I(x;d)$ into even and odd contributions about the molecule's position. Factoring out the even terms and noting that all resulting singularities are far outside the separation distances of interest, we have

$$I(x;d) = I_{\mathrm{even}}(x;d)\left[1 + \frac{I_{\mathrm{odd}}(x;d)}{I_{\mathrm{even}}(x;d)}\right]. \tag{5.18}$$

We then Taylor expand both $I_{\mathrm{even}}(x,d)$ and $I_{\mathrm{odd}}(x,d)/I_{\mathrm{even}}(x;d)$ in powers of kx and approximate their functional forms by a Gaussian and a line, respectively. That is

$$\begin{aligned} I_{\mathrm{even}}(x;d) &= I^{(0)} + \frac{1}{2}I^{(2)}(kx)^2 + \ldots \approx Ae^{-x^2/2\sigma^2} \\ \frac{I_{\mathrm{odd}}(x;d)}{I_{\mathrm{even}}(x;d)} &= \eta kx + \ldots. \end{aligned} \tag{5.19}$$

Computing η is straightforward as it is nothing more than a first order expansion coefficient. To compute A and σ, we match expansion coefficients of $I_{\mathrm{even}}(x;d)$ with those of a Gaussian up to second order. Doing so, we find $A = I^{(0)}$ and $\sigma = (1/k)\sqrt{-I^{(0)}/I^{(2)}}$. All expansion coefficients are reported in the SI.

5.7 Supplementary information

The analytic form of the mislocalization $\Delta x_{\text{misloc}}(d)$ presented in Eq. 5.10 depends on basic system parameters and separation through the expansion coefficients described in Eq. 5.19 and the surrounding Methods. Here we present the expansion coefficients for dipoles $\hat{\mathbf{p}} \parallel \mathbf{d}$ and $\hat{\mathbf{p}} \perp \mathbf{d}$ oriented within the focal plane. These coefficients were used to generate the $\Delta x_{\text{misloc}}(d)$ curves in Fig. 5.4. The expansion coefficients for the third orthogonal orientation $\hat{\mathbf{p}} = \hat{\mathbf{e}}_z$ have been omitted because of the similarity of mislocalization for dipoles perpendicular to $\mathbf{d}$, whether within or normal to the focal plane. For $\hat{\mathbf{p}} \parallel \mathbf{d}$:

$$
\begin{aligned}
\eta_{\perp} =& \frac{6\widetilde{j_2}(kd)[3\left|\frac{p_1}{p_0}\right|^2\widetilde{j_1}(kd) - 2kd\mathrm{Re}\left(\frac{p_1}{p_0}\right)]}{9\widetilde{j_1}(kd)[\left|\frac{p_1}{p_0}\right|^2\widetilde{j_1}(kd) - \frac{4}{3}kd\mathrm{Re}\left(\frac{p_1}{p_0}\right)] + 4(kd)^2} \\
I_{\perp}^{(0)} =& \frac{4}{9} + \left|\frac{p_1}{p_0}\right|^2\left[\frac{\widetilde{j_1}(kd)}{kd}\right]^2 - \frac{4}{3}\mathrm{Re}\left(\frac{p_1}{p_0}\right)\frac{\widetilde{j_1}(kd)}{kd} \\
I_{\perp}^{(2)} =& -\frac{16}{45} + 2\left|\frac{p_1}{p_0}\right|^2\left[\left(\frac{\widetilde{j_2}(kd)}{kd}\right)^2 - \frac{\widetilde{j_1}(kd)}{(kd)^2}\left(\frac{\widetilde{j_2}(kd)}{kd} - \widetilde{j_3}(kd)\right)\right] \\
&+ 2\frac{\mathrm{Re}\left(\frac{p_1}{p_0}\right)}{kd}\left[\frac{4}{15}\widetilde{j_1}(kd) + \frac{2}{3}\left(\frac{\widetilde{j_2}(kd)}{kd} - \widetilde{j_3}(kd)\right)\right]
\end{aligned}
\tag{5.20}
$$

and for $\hat{\mathbf{p}} \perp \mathbf{d}$:

$$
\begin{aligned}
\eta_{\parallel} =& \frac{18\left|\frac{p_1}{p_0}\right|^2\left[\frac{3J_2(kd)^2}{kd} - J_2(kd)J_1(kd) + 4j_1(kd)j_2(kd)\right] - 6kd\mathrm{Re}\left(\frac{p_1}{p_0}\right)\left[\frac{3}{8}J_2(kd) - 4j_2(kd)\right]}{9\left|\frac{p_1}{p_0}\right|^2\left[J_2(kd)^2 + 4j_1(kd)^2\right] + 24kd\mathrm{Re}\left(\frac{p_1}{p_0}\right)j_1(kd) + 4(kd)^2} \\
I_{\parallel}^{(0)} =& \frac{4}{9} + \left|\frac{p_1}{p_0}\right|^2\left[4\left(\frac{j_1(kd)}{kd}\right)^2 + \left(\frac{J_2(kd)}{kd}\right)^2\right] + \frac{8}{3}\mathrm{Re}\left(\frac{p_1}{p_0}\right)\frac{j_1(kd)}{kd} \\
I_{\parallel}^{(2)} =& -\frac{211}{1440} + 8\left|\frac{p_1}{p_0}\right|^2\left[\left(\frac{j_2(kd)}{kd}\right)^2 - \left(\frac{j_1(kd)}{kd}\right)^2 + 4\left(\frac{j_1(kd)j_2(kd)}{(kd)^3}\right)\right. \\
&\left. + \frac{3}{4}\frac{J_2(kd)}{(kd)^3}\left(7\frac{J_2(kd)}{kd} - 3J_1(kd)\right) + \frac{1}{4}\left(\frac{J_1(kd)}{kd}\right)^2 - \frac{1}{4}\left(\frac{J_2(kd)}{kd}\right)^2\right] \\
&+ 2\frac{\mathrm{Re}\left(\frac{p_1}{p_0}\right)}{kd}\left[\frac{1}{4}\left(J_1(kd) - 3\frac{J_2(kd)}{kd}\right) - 8\left(\frac{1}{5}j_1(kd) - \frac{2}{3}\frac{j_2(kd)}{kd}\right)\right],
\end{aligned}
\tag{5.21}
$$

where

$$
\widetilde{j_\nu}(kd) = j_\nu(kd) - kdj_{\nu-1}(kd). \tag{5.22}
$$

Supplement to Figs. 5.3 and 5.5

In Fig. 5.6, the relative contributions to the analytic image from the (green) molecule PSF, (blue) plasmon PSF, and (red) interference function are examined in 3 qualitatively different regimes. All physical parameters are consistent with the values used thus far for the $a = 40$ nm gold sphere in vacuum and molecular emitter with fluorescence emission peak at $\hbar\omega_0 = 2.6$ eV and are contained in the complex amplitude ratio $p_1/p_0 = \alpha_1(\omega_0)g/e^2$. (a) Prefactors weighting plasmon PSF and interference function for (top) $\hat{\mathbf{p}} \parallel \mathbf{d}$ and (bottom) $\hat{\mathbf{p}} \perp \mathbf{d}$ are plotted as functions of separation d normalized by the molecule brightness $|p_0|^2$ as in Eq. 5.6. The magnitude of $\mathrm{Re}[p_1/p_0]$ has been plotted dashed to compare magnitude of destructive interference to the plasmon PSF. The separation dependence of these prefactors provides context for understanding the image slices in the next panel, taken at separations marked by vertical lines. (b) Image slices and constituent pieces normalized by the molecule brightness $|p_0|^2$ are depicted at four separations. At $d = 300$ nm, emitters with $\hat{\mathbf{p}} \parallel \mathbf{d}$ form an image unperturbed by the plasmon, due to the absence of far-field coupling between collinear dipoles. Dipoles oriented $\perp \mathbf{d}$ couple at longer range, which is visible in the larger contribution of the interference at ~ 300 nm from $\mathrm{Re}[p_1/p_0]$. At 150 nm, the plasmon PSF is still negligible, but the $\hat{\mathbf{p}} \parallel \mathbf{d}$ interference prefactor is greater in magnitude than the plasmon PSF and negative, causing noticeable destructive interference and visually shifting the image to the right as well as reducing its magnitude. For the dipoles $\perp \mathbf{d}$, the $\mathrm{Re}[p_1/p_0]$ crosses zero due to the standing wave character of the dipole-dipole coupling. The image then appears unperturbed from the molecule PSF. Near 100 nm, the prefactors for the interference and plasmon PSF are equal and opposite sign in both $\parallel$ and $\perp$ cases. Destructive interference here effectively attenuates the signal of the molecule without noticeably distorting PSF shape. At 60 nm separation, the molecule is 20 nm from the surface of the nanoparticle. At these near proximities, the plasmon PSF grows rapidly due to the quadratic dependence on the coupling strength, leading to the image collapsing onto the nanoparticle's emission center. For dipoles $\parallel \mathbf{d}$, interference is destructive at close proximities given the set resonance detuning, yielding

a dimmer overall signal. But in the other case of $\hat{\mathbf{p}} \perp \mathbf{d}$ the interference is constructive and the observed image is brighter.

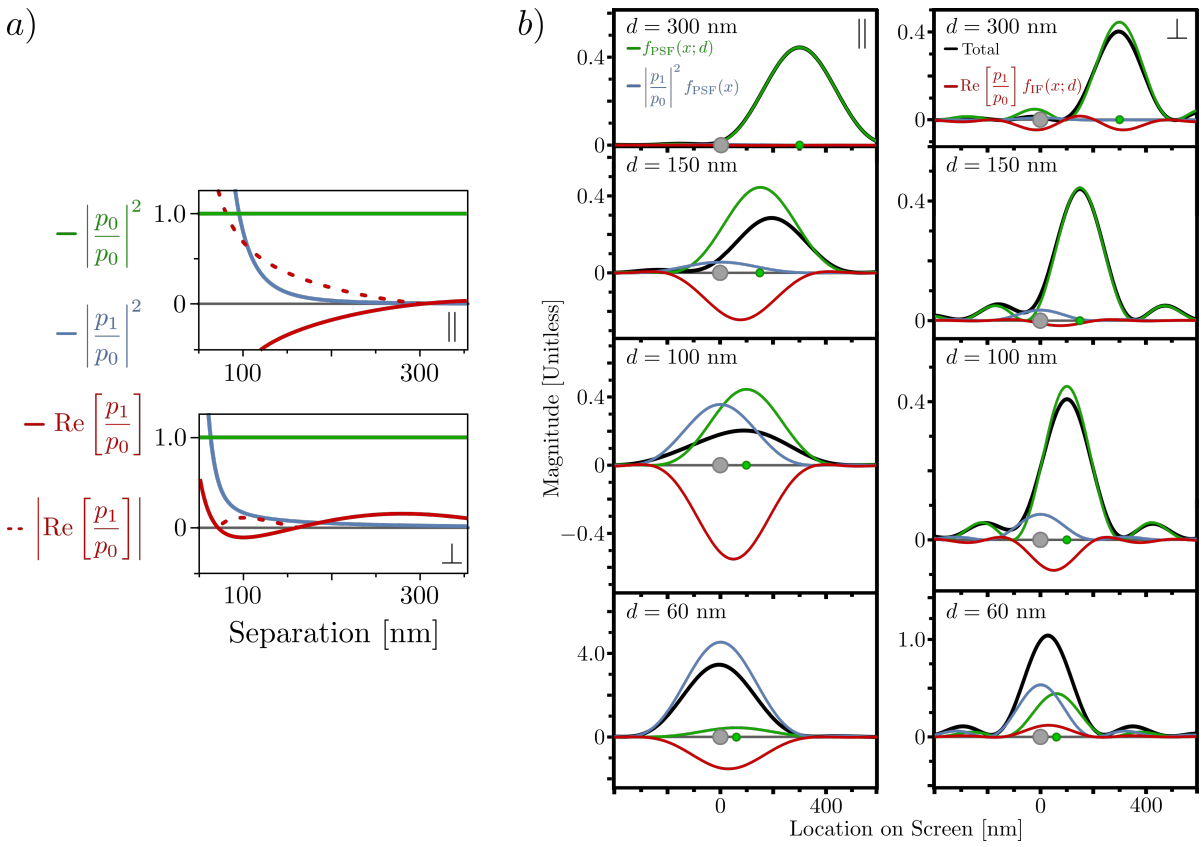

Figure 5.6: Evolution with coupling of the relative contributions to the analytic image from the (green) molecule PSF, (blue) plasmon PSF, and (red) interference function. All physical parameters are consistent with the values used thus far for the $a = 40$ nm gold sphere in vacuum and molecular emitter with fluorescence emission peak at $\hbar\omega_0 = 2.6$ eV and are contained in the complex amplitude ratio $p_1/p_0 = \alpha_1(\omega_0)g/e^2$. (a) Prefactors weighting plasmon PSF and interference function for (top) $\hat{\mathbf{p}} \parallel \mathbf{d}$ and (bottom) $\hat{\mathbf{p}} \perp \mathbf{d}$ are plotted as functions of separation d normalized by the molecule brightness $|p_0|^2$ as in Eq. 5.6. The magnitude of $\mathrm{Re}[p_1/p_0]$ has been plotted dashed to compare magnitude of destructive interference to the plasmon PSF. (b) Image slices and constituent pieces normalized by the molecule brightness $|p_0|^2$ are depicted at four separations.

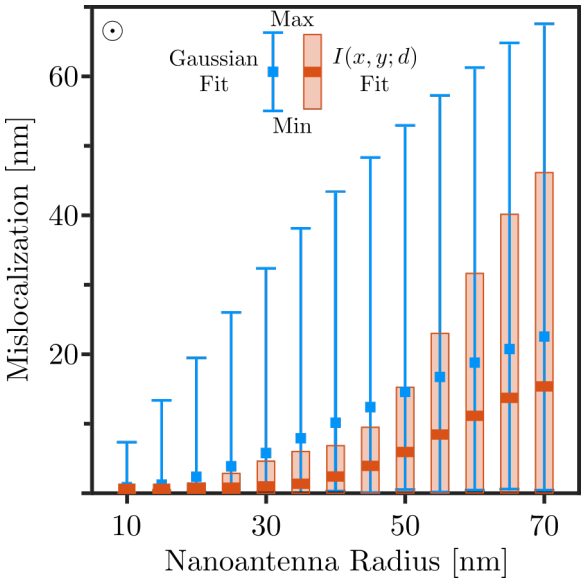

Figure 5.7: Extraction of molecule location from simulated plasmon-enhanced single molecule fluorescence images using the analytic image function $I(x, y; d)$ (red) derived in Eq. 5.6 and a two-dimensional Gaussian fit (blue). Both fitting methods are tested against molecule-nanoantenna separations $a + 5 \leq d \leq 350$ nm for a range of spherical nanoantenna radii a for the coaxial dipole orientation. For each radius, the average, minimum, and maximum mislocalization are determined by comparing d to the fit position d_0 in $I(x, y; d_0)$ or to the centroid position (x_0) in a two-dimensional Gaussian function. The corresponding average mislocalization is denoted as a square and the minimum and maximum mislocalization are indicated by vertical bars. $I(x, y; d)$ in Eq. 5.6 and the two-dimensional Gaussian are both fit to the same set of numerical electrodynamics simulations of a dipole-driven gold nanoantenna in vacuum. Across the wide range of nanoantenna radii sampled, fits to Eq. 5.6 provide a better estimate of molecule position than standard Gaussian fitting techniques.

Chapter 6

ROTATION OF SINGLE-MOLECULE EMISSION POLARIZATION BY PLASMONIC NANORODS

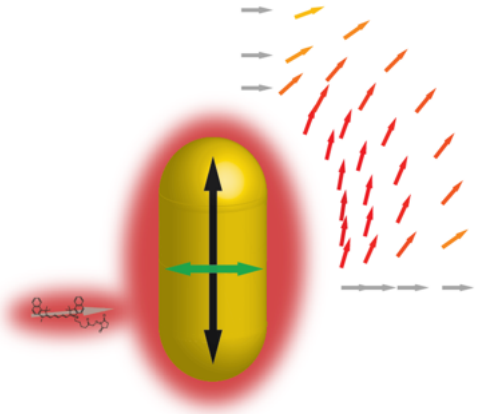

Reproduced in part with permission from:

Tiancheng Zuo, Harrison J. Goldwyn, Benjamin P. Isaacoff, David J. Masiello, and Julie S. Biteen

The Journal of Physical Chemistry Letters 2019 10 (17), 5047-5054

DOI: 10.1021/acs.jpclett.9b02270

T.Z. and H.J.G. contributed equally to this work.

Abstract

The strong light-matter interactions between dyes and plasmonic nanoantennas enable the study of fundamental molecular-optical processes. Here, we overcome conventional limitations with high-throughput single-molecule polarization-resolved microscopy to measure dye

emission polarization modifications upon near-field coupling to a gold nanorod. We determine that the emission polarization distribution is not only rotated toward the nanorods dominant localized surface plasmon mode as expected, but is also unintuitively broadened. With a reduced-order analytical model, we elucidate how this distribution broadening depends upon both far-field interference and off-resonant coupling between the molecular dipole and the nanorod transverse plasmon mode. Experiments and modeling reveal that a nearby plasmonic nanoantenna affects dye emission polarization through a multicolor process, even when the orthogonal plasmon modes are separated by approximately three times the dye emission linewidth. Beyond advancing our understanding of plasmon-coupled emission modifications, this work promises to improve high-sensitivity single-molecule fluorescence imaging, biosensing, and spectral engineering.

6.1 Introduction

Nanoantennas couple the far field to the near field by converting propagating waves to localized fields [118]. Understanding and measuring how optical nanoantennas couple to their local environment is a critical step toward controlling and enhancing near-field properties for applications as diverse as biosensors [8, 52], light-emitting devices [122, 28], surface-enhanced Raman spectroscopy [116, 44], and super-resolution microscopy [168, 3, 162, 23]. Noble metal nanoparticles respond strongly to light and are efficient nanoantennas. Upon optical excitation, localized surface plasmons (LSPs)collective oscillations of the metal conduction-band electronsare created at the nanoparticle surface and concentrate radiation into intense near fields through which optical processes in the surrounding local environment can be enhanced. One intriguing near-field effect of plasmonic nanoparticles is their ability to interact with nearby fluorescent dye molecules. Reported experimental and theoretical studies of the coupling of single dye molecules with metal nanoparticles have described how these nanoantennas modify the rate [44, 87, 20, 135, 9, 124, 7] spatial distribution [162, 26, 136], spectrum [135], and polarization [168, 106, 154, 153, 145, 47, 132], of fluorescence emission. Single-molecule experiments, which avoid ensemble averaging [162], have further shown that

single-molecule fluorescence emission is re-directed by a plasmonic nanoantenna [160], and recent theory has proposed that this so-called mislocalization can be attributed to the superposition and interference of the molecule and nanoantenna far-field emission as well as to the near-field coupling between the two emitters [136, 64]. In general, the excitation and decay of coupled fluorescent molecules and nanoantennas can be treated as separate processes as there is no coherence between plasmon-coupled molecular absorption and emission [135, 86], and experiments have shown that emission mislocalization is independent from enhanced absorption [160, 102]. Despite this research activity, the interaction between nanoantennas and nearby molecules is still not fully understood. Previous studies have demonstrated that emission polarization of a single emitter can be modified by the orientation of a nearby asymmetric nanoantenna such as a nanorod or Yagi-Uda antenna [154, 145, 132]. Here, we extend these previous studies by using Points Accumulation for Imaging in Nanoscale Topography (PAINT) experiments [168, 144, 60, 58] to sample thousands of molecules that transiently adsorb on the coverslip near each antenna. We also explicitly subtract the contribution of plasmonic particle photoluminescence [79], and develop novel understanding of how this dye-nanoantenna coupling influences the polarization of emitted light by combining single-molecule experiments with a reduced-order analytical model. The model results not only agree with simulation and provide a faster route to polarization prediction, but elucidate the mechanisms underlying emission polarization modification from a coupled dye-antenna system by isolating effects from the nanoantennas two orthogonal dipole plasmon modes. The model also reveals the contributions to emission polarization from near-field coupling and far-field interference, both of which vary differently with dye-nanoantenna position and orientation. More specifically, we investigate the polarization changes that result from plasmon-coupled emission by measuring the emission polarization of single dye molecules coupled to individual plasmonic nanorods. By correlating the single-molecule emission polarization angle with the nanorod orientation and fluorescence wavelength, we observe that the molecular emission polarization is significantly rotated toward the angle of the nanoantenna dominant plasmon mode as previously reported [106, 154, 153, 145, 47, 132], and can

be as large as 90. We use single-molecule polarization-resolved microscopy to measure the angle distribution of this mispolarization for two different dyesone red, Cy5.5 (max = 710 nm) and one bluer, Cy3 (max = 570 nm), and we find that measurable mispolarization occurs even when off resonance from the plasmon. This emission effect is therefore different from the fluorescence intensity and fluorescence emission spectrum, which are affected by both plasmon-coupled absorption and plasmon-coupled fluorescence emission [160].

6.2 Single-molecule polarization-resolved microscopy

To measure the emission polarization of single dye molecules coupled to gold nanorods, we achieve a sparse distribution of fluorescent molecule detections by placing a drop of nanomolar dye solution over a nanorod-coated coverslip (Fig. 6.1a). In this PAINT experiment [168, 144, 60, 58], most molecules diffuse rapidly in solution and are not detected by the camera (at 10 frames/s); only those molecules that transiently adsorb on the coverslip are captured by the camera. The high magnification of the microscope (160 nm/imaging pixel) and low concentration of dye molecules enable us to characterize one molecule at a time. A polarizing beam displacer (PBD) in the emission pathway of our single-molecule microscope (Fig. 6.1a) separates the emission into two orthogonally polarized output beams, which are then offset from one another and projected onto the camera (white Center channel and Off-center channel boxes in Fig. 6.1a). In this two-channel, one-camera setup, the emission from each single dye molecule appears in two channels (e.g., cyan circles in Fig. 6.1a), but the intensity is different in each channel. The apparent emission polarization angle, ϕ_{apparent}, of each fluorescent molecule and photoluminescent nanorod is thus related to the intensity ratio recorded in these two channels according to:

$$\phi_{\text{apparent}} = \tan^{-1}\sqrt{\frac{\langle I_{\text{offcenter}}\rangle}{\langle I_{\text{center}}\rangle}} \tag{6.1}$$

where $\langle I_{\text{center}}\rangle$ and $\langle I_{\text{off-center}}\rangle$ are the detected intensities in the center and off-center images, respectively, integrated over a diffraction-limited area. This expression maps all angles into the first quadrant (between 0 and 90) because phase information is lost from both field

components. Single-molecule polarization-resolved microscopy measures the average emission polarization in the image plane, which corresponds to the physical dipole orientation for isolated single emitters (dye molecules or nanorods) lying flat on the microscope coverslip. The dark-field scattering of the nanorod (blue curve) is strongly polarized along the nanorod longitudinal axis and is consistent with the nanorod having a larger polarizability along its long axis [135, 148, 147]. This angle is measured with respect to the PBD axis. In these microscopy experiments, the large numerical aperture (NA) objective produces some intensity cross-talk between the channels. This cross-talk is demonstrated in full-field electromagnetic simulations in SI Fig. S1 of the published manuscript, Ref. [170]. We use the two-channel experiment to investigate how detuning the dye emission spectrum from the nanorod LSP spectrum affects the emission polarization from the coupled dye-nanorod system. For gold nanorods, the single-nanorod PL polarization has been found to closely resemble the dominant, longitudinal LSP mode, observed in dark-field scattering [54, 29]. The fluorescence emission spectrum of the red dye Cy5.5 (Fig. 6.1b; solid red line) overlaps with the nanorod longitudinal LSP scattering resonance (Fig. 6.1b; blue line). The intensity of the longitudinal LSP mode, which peaks at 700 nm, is much stronger than transverse mode, which peaks at 560 nm (Fig. 6.1b; blue line). Therefore, by exciting the dye with a 635-nm laser, whose wavelength is far detuned from the nanorod LSP resonance (Fig. 6.1b; red arrow), we avoid fluorescence absorption enhancement to isolate the effects of coupling in the fluorescence emission. As a control experiment, similar measurements were performed with the red dye Cy3 whose emission and excitation peaks are both far detuned from the longitudinal LSP resonance (Fig. 6.1b; yellow lines).

6.3 Detection of plasmon-induced emission polarization rotation from resonantly coupled dye molecules

We selected a group of seven nanorods with different orientations determined by Eq. (6.1) and measured the fluorescence polarization of single Cy5.5 molecules near each NR. The dark-field scattering spectra and relative angles of those nanorods are displayed in SI Fig.

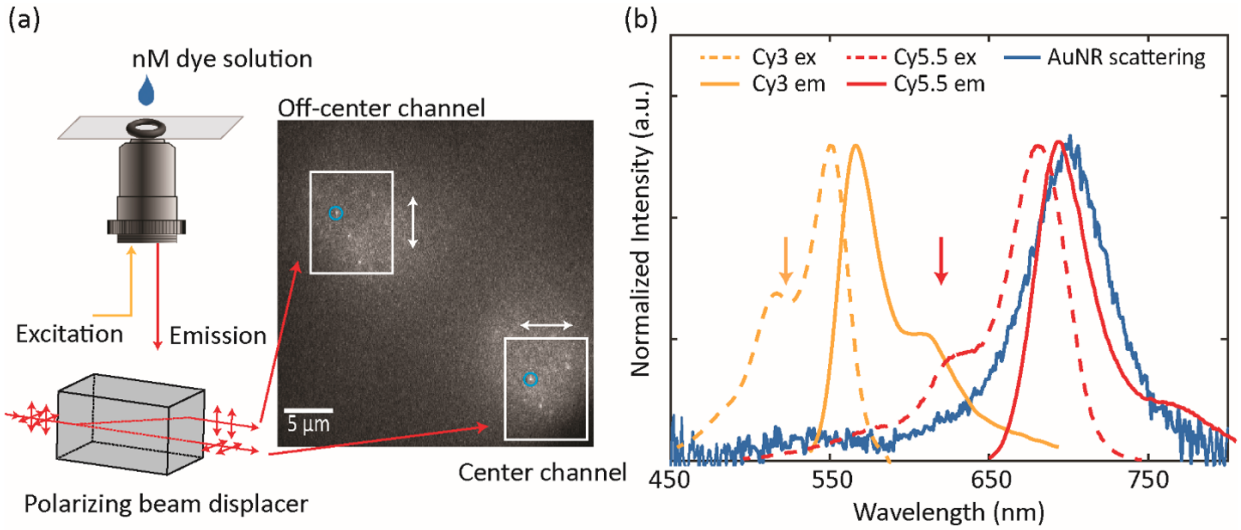

Figure 6.1: Experimental setup and spectral design. (a) Single-molecule polarization-resolved microscopy experiment setup. A low-concentration dye solution is excited by circularly polarized laser illumination (yellow). A polarizing beam displacer (PBD) separates the emission (red) into two orthogonally polarized output channels (white boxes; the white arrows indicate the polarization direction). The cyan circles indicate the same molecule detected in both channels. (b) Dark-field scattering spectrum of an isolated nanorod immobilized on a coverslip (blue); Cy3.5 fluorescence excitation and emission spectra (yellow dashed and solid lines, respectively); Cy5.5 fluorescence excitation and emission spectra (red dashed and solid lines, respectively). Yellow and red arrows indicate the excitation wavelengths for Cy3 and Cy5.5 respectively.

S2 of Ref. [170]. Each system was rotated three times to sample 21 different nanorod orientations relative to the PBD axis. Simulation and model results show that molecules located more than 150 nm from the center of the nearest nanorod experience negligible mispolarization or mislocalization, and therefore these molecules experience no significant plasmonic interaction [58]. We refer to molecules located more than 400 nm from the nanorod centers as Off-nanorod and molecules located within 120 nm of the nanorod centers On-nanorod molecules. Intermediate molecules were not considered to allow differentiation between the two populations. For the Off-nanorod molecules, the distribution of emission polarizations measured for the Off-nanorod Cy5.5 dyes (Fig. 6.2a) peaks at 45. Since the molecules adsorb non-specifically to the surface with no known favored orientation, purely z-oriented emitters would contribute equally in the x and y channels, leading to an artificially enhanced 45 population. Moreover, this symmetrically peaked distribution is also attributed to artifacts introduced in background-subtraction that systematically invalidate data points at low or high angles due to signal-to-noise constraints. Additionally, even in the absence of noise, the polarization cross-talk generated by the high NA objective bounds the angle domain to 17 - 73. A quantitative analysis of these artifacts is presented with simulated single-molecule data in SI Fig. S3 of Ref. [170]. We also investigated whether this peak is due to a physical rotation of the molecules on the coverslip surface, but we found no significant time-dependent broadening of the distribution within the imaging frame integration time of the experiment, 100 ms/frame (SI Fig. S4 of Ref. [170]), which supports the assumption of each molecule having a well-defined dipole moment orientation. For the On-nanorod molecules, Fig. 6.2b-c shows the distributions of measured polarizations for On-nanorod Cy5.5 molecules, in which the nanorod longitudinal axis is oriented at 67 and 28, respectively (black arrows). Though the physical orientation of the Cy5.5 molecules here is random as in the Off-nanorod case (Fig. 6.1a), the polarization distributions in Fig. 6.1b and c are shifted away from the 45 peak in Fig. 6.2a, and toward the nanorod orientation. The distributions of the On-nanorod Cy5.5 molecules of all 21 nanorod orientations are given in SI Fig. S5 of Ref. [170].

The On-nanorod distributions (Fig. 6.1b-c, SI Fig. S5 of Ref. [170]) still include some

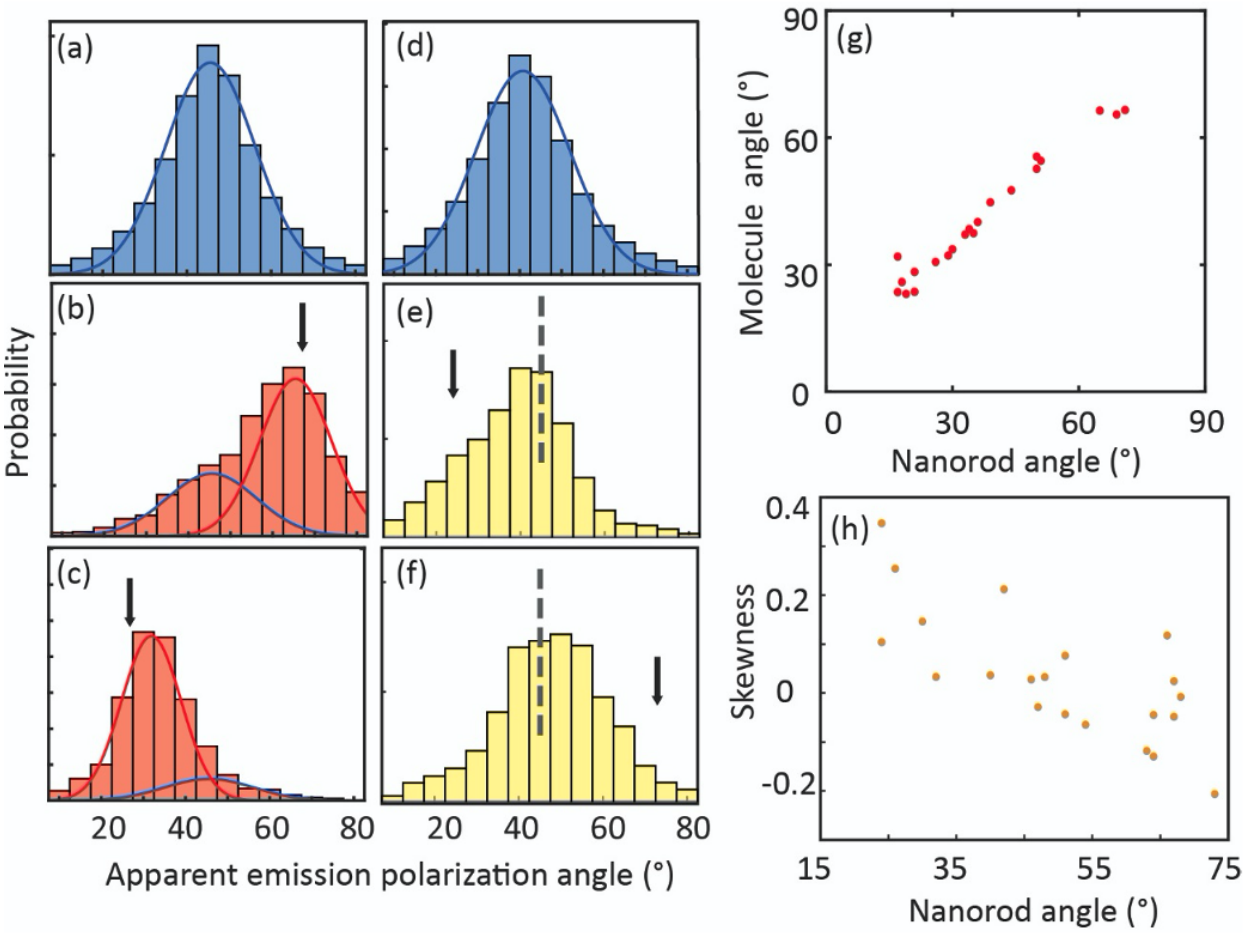

Figure 6.2: Characterization of Cy5.5 and Cy3 molecule apparent polarization angles, ϕ_{apparent}. (a, d) Emission polarization angle distributions of Off-nanorod Cy5.5 and Off-nanorod Cy3 single molecules, respectively, and Gaussian curve fits. (b, c) Emission polarization angle of On-nanorod Cy5.5 single molecules. (e, f) emission polarization angle of On-nanorod Cy3 single molecules. Each histogram in (a - f) collects the apparent emission polarization angles of 2,000 - 6,000 single molecules. The black arrows in b, c, e, and f indicate the measured orientation angle of the nanorod. The vertical dashed lines in e and f indicate 45. The histograms in b, c, e, and f are fit to the sum of two Gaussian curves: the blue one has center and width corresponding to the blue curve in a or d, and the red one is not constrained. (g) Measured Cy5.5 average polarization angles vs. nanorod orientation angle. Each point comes from the peak of a red curve as in b and c. (h) Skewness of the measured Cy3 molecule emission polarization angle distribution vs. nanorod orientation angle.

molecules very weakly coupled to the nanorod due to the dependence of coupling both on separation and orientation [64]. To quantify the On-nanorod distribution shifts, we fit the emission polarization distribution to the sum of two Gaussian distributions: the blue curves in Fig. 6.1b-c, and SI Fig. S5 of Ref. [170] have center and width corresponding to the blue fit in Fig. 6.1a, and the red curves represent the ϕ_{apparent} distribution of the truly coupled On-nanorod Cy5.5 molecules. The peak angles of these 21 red curves are compared to the nanorod longitudinal axis orientation in Fig. 6.2g. In Fig. 6.2g, it is evident that the molecular ϕ_{apparent} has a bias toward the nanorod longitudinal axis, in agreement with the simulation (SI Fig. S6 of Ref. [170]). Furthermore, resonant coupling to the nanorod leads to an average 2-fold enhancement in PL intensity; this enhancement is greatest when ϕ_{apparent} is aligned with the nanorod angle (SI Fig. S7 of Ref. [170]). Polarization-sensitive detection of off-resonance molecular emission. As a control experiment, we investigated the single-molecule polarization of Cy3 molecules. Off-nanorod Cy3 molecules also appear to adsorb on the coverslip surface without preferred orientation, based on their ϕ_{apparent} distribution that peaks at 45 (Fig. 6.1d). Even in this off-resonance case, the On-nanorod polarization angle distributions are shifted away from the 45 peak (dashed lines in Fig. 6.1e-f) and toward the nanorod orientation (black arrows in Fig. 6.1e-f). For instance, the nanorod aligned at 25 in Fig. 6.1e shifts the distribution to the left relative to 45 and the nanorod aligned at 74 in Fig. 6.1f shifts the distribution to the right of 45. The dark-field scattering spectra and relative angles of the nanorods are given in SI Fig. S8 of Ref. [170] and the full set of polarization distributions is given in SI Fig. S9 of Ref. [170]. Interestingly, though the Cy3 spectrum is significantly detuned from the longitudinal LSP mode of the nanorod (Fig. 6.1b), the emission polarization rotates in the direction of the much stronger longitudinal mode. Still, this coupling is much weaker than that observed for the resonantly coupled Cy5.5 molecules. Thus, we characterize the shift by calculating the skewness of the polarization distributions: Fig. 6.2e shows a positively skewed distribution and the Fig. 6.2f distribution has a negative skewness. In Fig. 6.2h, the skewness from Cy3 emission polarization distributions for all 21 nanorod orientations is compared to the nanorod longitudinal axis orientation. There

is a strong negative linear correlation between skewness and nanorod orientation (Pearsons correlation coefficient = 0.74, p-value = 0.0001). Even in this off-resonant coupling, the longitudinal nanorod LSP mode modifies the Cy3 emission polarization. This observation is consistent with simulation (SI Fig. S10 of Ref. [170]). Accordingly, no obvious fluorescence enhancement is found for On-nanorod Cy3 (SI Fig. S7 of Ref. [170]).

6.4 Coupled dipole interaction model

Because the true location and orientation of individual molecules are obscured by plasmon coupling and the interference of emitted or scattered fields, current experiments are unable to relate these effects to the configuration-dependent interaction between molecule and plasmonic nanorod. We therefore turn to a simple analytical model of both the near-field interaction and far-field radiative emission to elucidate the essential details [9, 64]. With the model, the effects of the nanorod longitudinal and transverse dipolar LSP modes are independently studied for molecules at specified locations and orientations. The individual influence of each mode on the observed mispolarization can then be explicitly isolated, along with its dependence on interference effects. The fluorescence emission from the nanorod-coupled molecule is modeled as two coupled electric dipoles radiating into the far field. The governing dynamical equations for the molecule emissive transition dipole $\mathbf{p}_0$ and the induced plasmon dipole $\mathbf{p}_1$ are

$$\mathbf{p}_0 = \boldsymbol{\alpha}_0 \cdot \left(\mathbf{E}_F + \mathbf{E}_1\left(\mathbf{x}_0\right)\right) \ , \tag{6.2}$$

$$\mathbf{p}_1 = \boldsymbol{\alpha}_1 \cdot \mathbf{E}_0\left(\mathbf{x}_1\right) \ . \tag{6.3}$$

The orientation-dependent optical responses of the molecule and nanorod are encoded by their respective linear dyadic polarizabilities, $\boldsymbol{\alpha}_i$. The fictitious harmonic field $\mathbf{E}_F = E_0\hat{\mathbf{e}}_x e^{-i\omega t}$ drives only the molecular transition dipole, which forces both dipoles to oscillate harmonically and represents the continuous population of the molecule emissive state by absorption of the excitation laser and subsequent fluorescence relaxation. The molecule and plasmon are coupled by the fully retarded dipole fields, $\mathbf{E}_i\left(\mathbf{x}_j\right) = \mathbf{G}\left(\mathbf{x}_j, \mathbf{x}_i\right) \cdot \mathbf{p}_i$, generated by the ith

dipole evaluated at the location of the jth dipole; here $\mathbf{G}$ is the standard electric dipole relay tensor (Section 3.2) [117]. Upon substituting $\mathbf{E}_i(\mathbf{x}_j)$ for the dipole fields in Eqs. (6.2) and (6.3), the coupled equations can be solved to yield the complex dipole moments containing both oscillation magnitude and phase as functions of the polarizabilities and dipole-dipole orientation (Section 3.2). With an analytical relationship between the two dipole moments, the dyadic polarizabilities can be parameterized from spectra of the uncoupled molecules and nanorod. For this purpose, the molecule emissive dipole transition is modeled by a Lorentz oscillator polarizable only in one direction fixed by the molecular orientation; i.e., $\boldsymbol{\alpha}_0 = \hat{\mathbf{e}}_x \alpha_{mol} \hat{\mathbf{e}}_x$ in the reference frame of the molecule. The nanorod is approximated as a prolate spheroid in the modified long-wavelength approximation,40 with polarizability $\boldsymbol{\alpha}_1 = \hat{\mathbf{e}}_{x'} \alpha_{\text{short}} \hat{\mathbf{e}}_{x'} + \hat{\mathbf{e}}_{y'} \alpha_{\text{long}} \hat{\mathbf{e}}_{y'} + \hat{\mathbf{e}}_{z'} \alpha_{\text{short}} \hat{\mathbf{e}}_{z'}$ in the basis aligned with the nanorod principal axes. The prolate spheroid geometry idealizes the true nanorod geometry to allow for a closed form solution to Maxwells equations including radiation damping for the dipolar LSPs. Both components of $\boldsymbol{\alpha}_1$ are parameterized by the two unique semi-radii of the cylindrical nanorod (here 44 nm and 20 nm) and three material parameters built into the Drude model dielectric function describing the electronic responses of bulk gold (Section 3.1). To compute the two-channel diffraction-limited images generated by the PBD, the fields emitted by the coupled dipoles in Eq. (6.2) and (6.3) are propagated through an idealized microscope. The resulting image contains the superposition of the focused and diffraction-limited fields, $\mathbf{E}_0^{\text{im}}$ and $\mathbf{E}_1^{\text{im}}$, which are proportional to each dipole moment respectively (Section 2). In accordance with our experiment, orthogonal polarization components of the total field are split to form separate images, each with the form:

$$I_q = \frac{cn}{8\pi}\left(\left|\mathbf{E}_0^{\text{im}} \cdot \hat{\mathbf{e}}_q\right|^2 + \left|\mathbf{E}_1^{\text{im}} \cdot \hat{\mathbf{e}}_q\right|^2 + 2\, Re[\mathbf{E}_0^{\text{im}} \cdot \hat{\mathbf{e}}_q\ \mathbf{E}_1^{\text{im}} \cdot \hat{\mathbf{e}}_q]\right), \tag{6.4}$$

where $q \in \{x, y\}$ are analogous to the center and off-center experimental image channels, c is the speed of light in vacuum, and n is the refractive index of the background medium (here water). Combining this polarized image intensity with Eq. (6.1) makes explicit how the average emission polarization measured in experiment is determined by the

orientation-dependent relay tensor **G** that influences the dipole moment magnitudes and phases according to Eqs. (6.2) and (6.3). The polarizabilities in the latter equations are parametrized from the independent dye emission and nanorod scattering spectra. By assuming the nanorod location and orientation are determined, Eq. (6.4) provides an analytical measure of the imaged intensities and observed polarization as a function of molecule position and orientation.

6.5 Analysis of the isolated contributions from the transverse and longitudinal LSP modes and interference

By manually setting the short- or long-axis components of the nanorod polarizability to zero in the model, the independent contributions of the transverse and longitudinal LSP modes on ϕ_{apparent} can be studied. As in the experiments, ϕ_{apparent} (Eq. (6.1)) maps onto an angle range slightly smaller than 0 - 90 due to the inherent cross-talk. In both the analytical model and the simulations, the calculated polarization is mapped back onto a 0 - 90 range by inverting the one-to-one mapping between the true dipole orientation in plane and ϕ_{apparent} (SI Fig. S1 of Ref. [170]). To determine how interference affects the PBD-resolved emission polarization16, we also compare the full emission polarization with that produced by the isolated plasmon modes in the absence of the interference term in Eq. (6.4). Four geometries are studied: 0-oriented molecular dipoles analogous to Cy5.5 (i.e., parallel to and resonant with the longitudinal LSP mode), 0-oriented molecular dipoles analogous to Cy3 (i.e., parallel to and off resonance with the longitudinal LSP mode), 90-oriented dipoles analogous to Cy5.5 (i.e., perpendicular to and resonant with the longitudinal LSP mode), and 90-oriented dipoles analogous to Cy3 (i.e., perpendicular to and off resonance with the longitudinal LSP mode); SI Figs. S11 - S14. The most significant mispolarization is shown in the configuration of the 0-oriented molecular dipoles resonant with the longitudinal LSP (Fig. 6.3a). Fig. 6.4b-c shows the decomposition of the ϕ_{apparent} of these molecules by projecting onto either the transverse or longitudinal LSP modes in isolation. Comparing among the panels in Fig. 6.3, it is clear that the experimentally measured skew of molecule emission polarization toward

the nanorod long axis displayed in Fig. 6.2 is mostly due to superposition of the longitudinal plasmon mode scattering with the molecular emission. Molecules not aligned with the main nanorod axis still couple to and drive the long-axis dipole plasmon, which emits mostly light polarized along its axis and biases the average polarization across an image in its favor. However, similar polarization maps for 90-oriented dipoles resonant with the longitudinal LSP (Fig. 6.3d-i) show that the influence of the longitudinal LSP upon ϕ_{apparent} is more complicated: as in the case for 0 orientation, the longitudinal LSP strongly mispolarizes the molecular emission toward the longitudinal LSP mode (aligned along the y-axis) by superposition with fluorescence emission redirected through the plasmon (Fig. 6.3d-f); additionally, for the 90 case, the longitudinal LSP mode mispolarizes dipoles that are parallel to y-axis toward the transverse mode axis (aligned along the x-axis) orientation because of destructive interference effects in the y-oriented fields (Fig. 6.3g-i). This

interference effect results from the far-fields of the molecule and nanorod that are parallel to their dipole moments being out of phase, thereby turning the last term in Eq. (6.4) negative for both components, which reduces the argument of the arctangent in Eq. (6.1) and therefore reduces the observed polarization angle below 90°. The transverse plasmon mode produces mispolarization of 90° molecules close in proximity to its dipole moment by superposition similar to how the longitudinal mode mispolarizes x-oriented molecules. However, as the electric field of the transverse LSP mode is much weaker than that of the longitudinal mode, the transverse mode does not change the polarization as much as the longitudinal mode even for resonant molecules (SI Fig. S13 of Ref. [170]).

6.6 Model fit for extraction of molecule polarization and location.

Previous work demonstrated that plasmon-induced deformation of single-molecule fluorescence produces a difference between the true and apparent single-molecule position27 and polarization [154, 145, 132]. Here, we measure single-molecule polarization with high-throughput experiments and demonstrate how to model the observable ϕ_{apparent} analytically. The model-generated image (Eq. (6.4)) can also be used as a simultaneous localization and

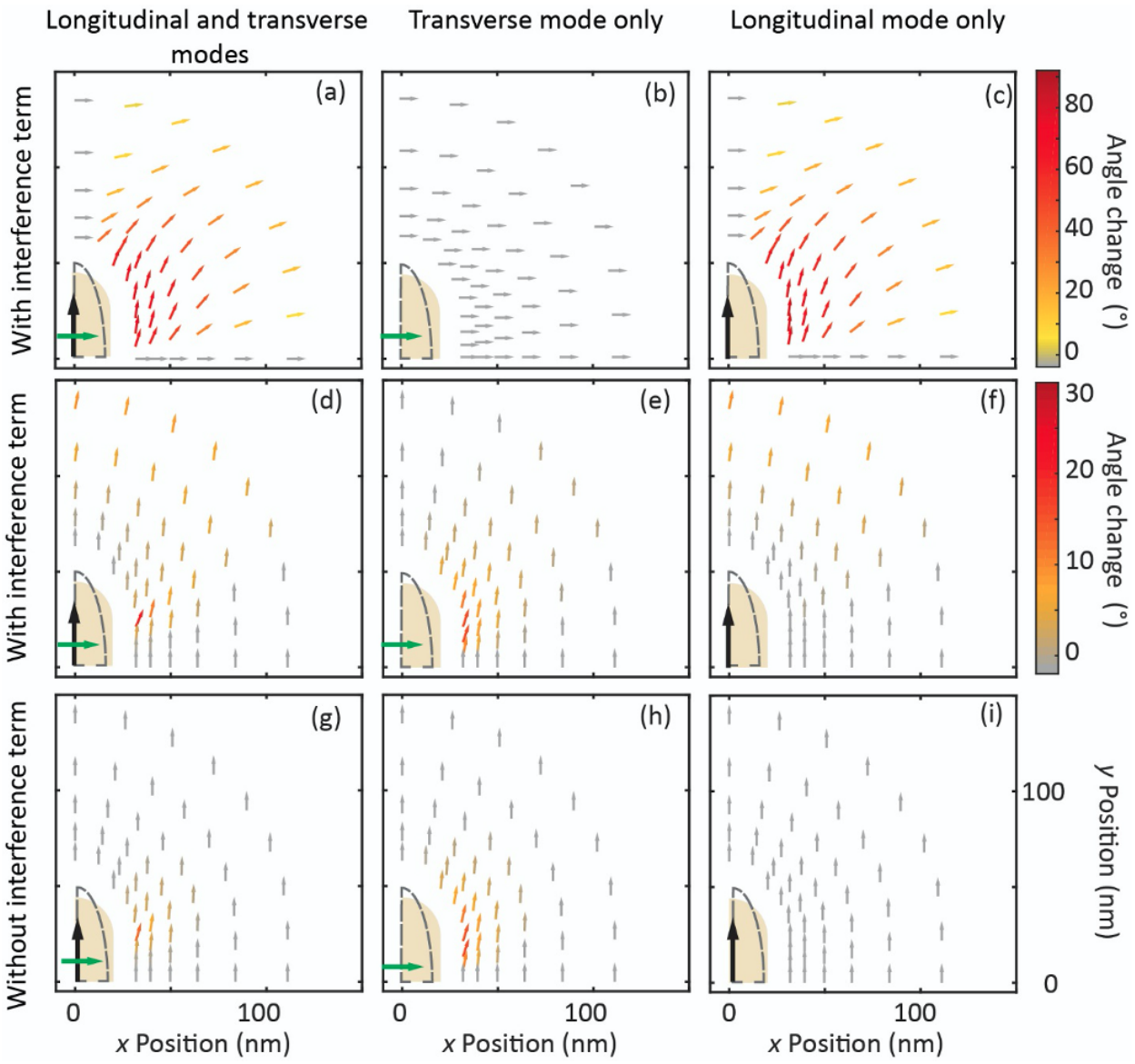

Figure 6.3: Mispolarization map calculated from the coupled-dipole model. (a) - (c) ϕ_{apparent} maps corresponding to 0-oriented molecular dipoles resonant with the longitudinal LSP. (d) - (i) ϕ_{apparent} maps corresponding to 90-oriented molecular dipoles that are also resonant with the longitudinal LSP. The black and green arrows indicate the longitudinal and transverse LSP modes, respectively, of the nanorod. The tan shapes in (a) - (i) represent a quarter of the simulated nanorod. The black dashed outline represents the prolate spheroid model of the nanorod (best fit geometric and material parameters are given in Section 3.1).

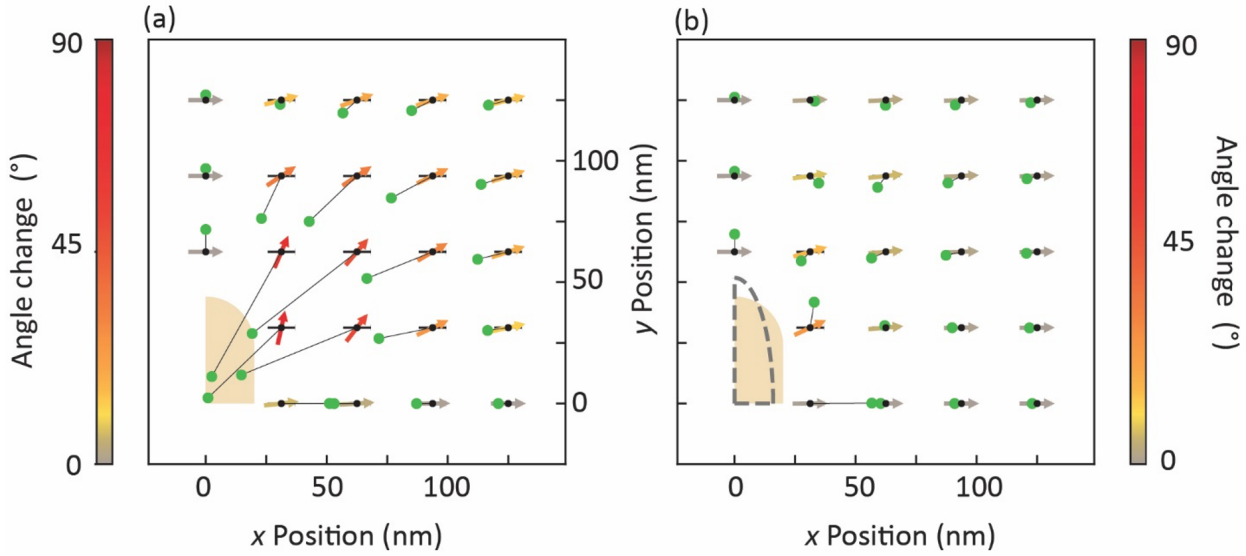

Figure 6.4: Comparison of the best fit results for dipole position (green) and polarization (colored arrows) determined in simulated diffraction-limited images (at a single frequency matching the longitudinal LSP peak in SI Fig. S18 of Ref. [170]) of 23 simulated single-molecule dipoles (black dots) oriented parallel to the x-axis and placed near a nanorod (shaded tan) up to 150 nm away from the center of the nanorod. (a) Gaussian localization of the total intensity paired with molecule orientation as would be determined by polarization-resolved microscopy reveals the familiar mislocalization of x-oriented molecules mostly toward the nanorod (apparent locations marked by green dots connected to the true molecule location in black) is accompanied by mispolarization of the molecules due to superposition of fluorescence emission redirected through the nanorod. (b) Least-squares fit of the model-generated images to simulated images.

polarization fit function to recover the true position and orientation of nanorod-coupled dye molecules. Fig. 6.4 compares the accuracy of molecular polarization and location determined by a least-squares model fit to simulated images (Fig. 6.4b) with that determined by the PBD and typical Gaussian fitting (Fig. 6.4a). The molecules in Fig. 6.4 are aligned along the x-axis (0); other geometries are considered in Section 2 and SI Figs. S19 - S21. For the model fits in Fig. 6.4b, the molecule and nanorod dipoles are parametrized, leaving only three fit parameters for residual minimization: the x and y coordinates of the molecular transition dipole relative to the center of the nanorod, and the dipole angle. The model-based localization and polarization significantly outperforms Gaussian localization and effectively eliminates the mispolarization observed in ϕ_{apparent} for all molecules studied here except those closest to the nanorod corner. The mislocalization error is greatly reduced because, unlike Gaussian fitting, the molecule location is estimated with full knowledge of the interaction and configuration-dependent far-field radiation pattern produced by coupled dipoles. Any error left in the determined molecule location is not due to convolution of molecule and nanorod emission, but is likely a due to the slight deficiency of the Drude model dielectric function for describing the optical response of gold in the frequency range spanning the longitudinal and transverse mode resonances (SI Fig. S18 of Ref. [170]). Although a model dielectric function with greater predictive power and more fit parameters can easily be employed, the degree of success achieved here demonstrates that the relevant physics underlying the diffraction-limited image of coupled molecule and nanorod can be qualitatively captured with only the three Drude material parameters. The in-plane molecule orientation is determined by the model fit in a qualitatively different manner from the way ϕ_{apparent} is calculated. While the latter is a measure of the average polarization of a dye molecule in the focused image field, the model fit angle is a direct estimation of the orientation of the molecule emissive transition dipole moment during the time span of photon collection. At close molecule-nanorod separations, the localization provided by the model fit seems to be no more reliable than Gaussian fitting. This fitting error is due to the simplicity of the model rather than the fitting process. For instance, greater accuracy could be achieved by including the nanorod

quadrupolar LSP response which becomes increasingly important at close proximity. In conclusion, using high-throughput single-molecule polarization-resolved microscopy, we have discovered that emission polarization is a measure of the coupling strength between molecular emitters and plasmonic nanoantennas. The stronger the coupling of the molecule to a plasmonic nanoantenna, the more the molecule emission polarization will rotate toward the polarization of the nanoantenna LSP mode. While this effect is apparent for an ensemble of single molecule measurements, simulations and analytical modeling demonstrate that the mispolarization of single molecules with known location and orientation is much more complicated. ϕ_{apparent} is rotated both toward and away from the nanorod long-axis by two distinct physical phenomena, even for molecules that are resonant with the nanorod longitudinal LSP mode. Either constructive or destructive interference can dominate depending on the molecule orientation and location relative to the nanorod. Significantly, the emission polarization is a more sensitive measure of coupling than fluorescent intensity enhancement because, even for weakly coupled Cy3 where no apparent fluorescent enhancement is observed, the emission polarization change is appreciable. The complex relationship between ϕ_{apparent} and the configuration-dependent electromagnetic interaction between molecule and nanorod facilitates simultaneous extraction of molecule orientation and location by fitting an analytical model of the coupled-dipole image to experimental data. The model developed exceeds the accuracy of the best fits achieved through standard Gaussian localization as well as PBD-based determination of the in-plane polarization angle for simulated molecule-nanorod images. Future work will use this model fit to extract the true molecule location and orientation from experimental images.

Associated Content The Supporting Information is available free of charge on the ACS Publications website at DOI: Details of the experimental and computational methods, description of experimental corrections, dark field scattering spectra of the nanorods, measured emission polarization angle distributions of all Cy5.5 and Cy3 molecules, simulated apparent emission polarization distributions, single-molecule fluorescence enhancement measurements, apparent emission polarizations from electrodynamics simulations at the Cy3 and

Cy5.5 wavelengths and in two orthogonal directions, detailed description of the analytical model: the two coupled dipole model, the polarizability, and the diffraction-limited dipole image fields, supplementary references.

Model-based localization and polarization determination

Model localization and polarization determination is accomplished by least-squares fit of the model generated images to the simulated images with no noise. Simulated images are calculated by first generating far-fields in the MNPBEM MATLAB toolbox [73] with the same nanorod used in parameterization. These fields are then propagated through the idealized microscope by numerically computing the Debye-Wolf integral in Eq. (2.1).

The model fits take only 3 free parameters, since molecules are assumed to lie in the focal plane (physical for the PAINT procedure used in this work) with dipole moment located in the focal plane (unknown physicality but assumed for simplicity and proof of concept). The initial guesses for molecule location are determined by the result of Gaussian localization and fits are insensitive to the guess of the molecule orientation. When the molecule is close to the nanorod and the images become dominated by plasmon emission, each image does not change much with molecule location and fits become numerically unstable. With this naive initial guess procedure, these fits often converge to molecule locations on top of the nanorod, which is unphysical because such molecules should be quenched. To resolve this issue, a smarter initial guess algorithm was implemented. If the initially guessed molecule location provided by the Gaussian localization procedure is located on top of the nanoparticle, the guess location is pushed outside the quenching zone of the nanorod (defined as 10 nm added to the prolate spheroid radius). This algorithm was found to yield numerically stable fit results, showcasing the best-fit possible with the current model and parameterization presented in this work.

Gaussian localization fits a two-dimensional Gaussian function to the normalized simulated images with the 5 free parameters; the two centroid coordinates (x, y), two standard deviations, and a rotation angle. Initial guesses for least-squares minimization of the residual

for the centroid coordinates are determined by the (numerical) detector pixel of maximum intensity. Initial guesses for the widths are fixed near the diffraction limit, and the initial rotation angle was not found to have consequence on the fit convergence.

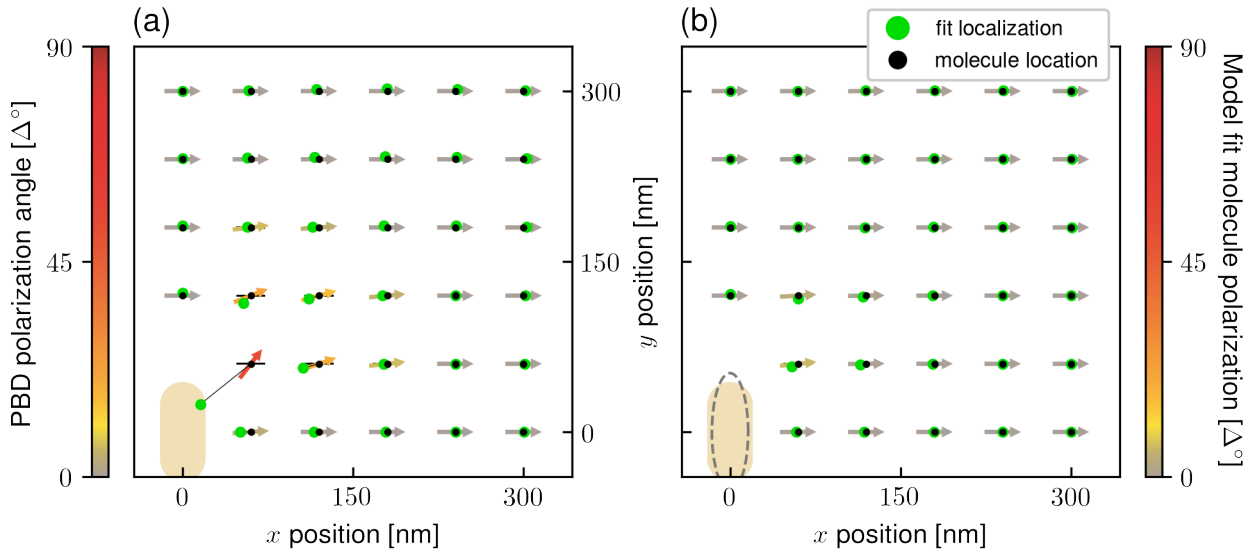

Figure 6.5: Comparison of the best fit results for molecule position (green) and polarization (colored arrows) determined in simulated diffraction-limited images (at a single frequency matching the longitudinal LSP peak in SI Fig. 4.1, with wavelength $\lambda = 667$ nm) of 23 simulated x-axis oriented single-molecule dipoles (black dots) near a nanorod (shaded tan) up to 300 nm away from the center of the nanorod. (a) Gaussian localization of the total intensity paired with molecule orientation as would be determined by polarization-resolved microscopy reveals the familiar mislocalization of x-oriented molecules mostly toward the nanorod (apparent locations marked by green dots connected to the true molecule location in black) is accompanied by mispolarization of the molecules due to superposition of fluorescence emission redirected through the nanorod. (b) Least-squares fit of the model-generated images to simulated images.

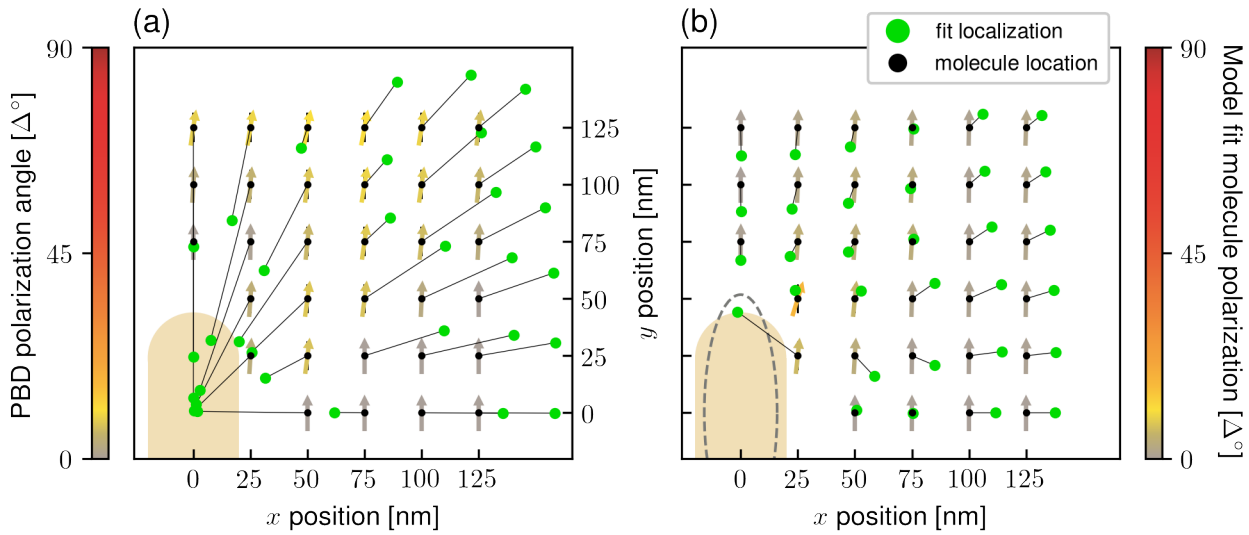

Figure 6.6: Comparison of the best fit results for molecule position (green) and polarization (colored arrows) determined in simulated diffraction-limited images (at a single frequency matching the longitudinal LSP peak in SI Fig. 4.1, with wavelength $\lambda = 667$ nm) of 23 simulated y-axis oriented single-molecule dipoles (black dots) near a nanorod (shaded tan) up to 150 nm away from the center of the nanorod. (a) Gaussian localization of the total intensity paired with molecule orientation as would be determined by polarization-resolved microscopy reveals the familiar mislocalization of y-oriented molecules both toward the nanorod (apparent locations marked by green dots connected to the true molecule location in black) and away from the nanorod depending on the molecule's true location. This mislocalization is not simply correlated with mispolarization since the far-field interference generating mislocalization away from the nanorod plays a more complicated role in PBD measured mispolarization. (b) Least-squares fit of the model-generated images to simulated images.

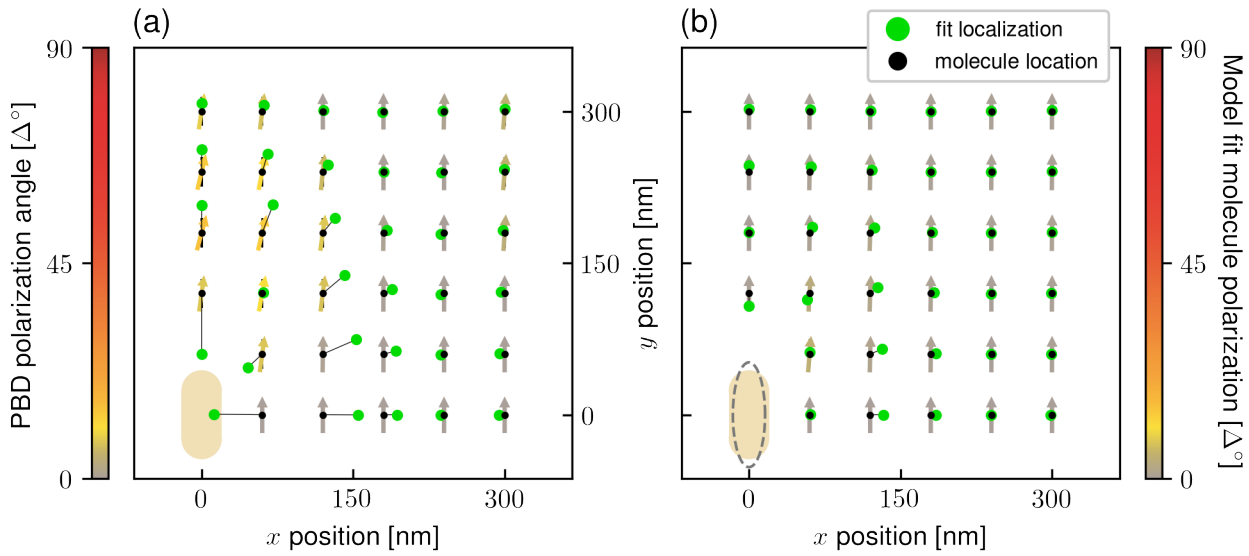

Figure 6.7: Comparison of the best fit results for molecule position (green) and polarization (colored arrows) determined in simulated diffraction-limited images (at a single frequency matching the longitudinal LSP peak in SI Fig. 4.1, with wavelength $\lambda = 667$ nm) of 23 simulated y-axis oriented single-molecule dipoles (black dots) near a nanorod (shaded tan) up to 300 nm away from the center of the nanorod. (a) Gaussian localization of the total intensity paired with molecule orientation as would be determined by polarization-resolved microscopy reveals the familiar mislocalization of y-oriented molecules both toward the nanorod (apparent locations marked by green dots connected to the true molecule location in black) and away from the nanorod depending on the molecule's true location. This mislocalization is not simply correlated with mispolarization since the far-field interference generating mislocalization away from the nanorod plays a more complicated role in PBD measured mispolarization. (b) Least-squares fit of the model-generated images to simulated images.

Chapter 7

TOWARDS INFERENCE FROM EXPERIMENTAL IMAGES

In order to test the ultimate utility of the plasmon-enhanced single-molecule image model as a super-resolution fit function, we need an experimental benchmark to determine how well we predict molecule locations *in situ*. While it is difficult to design and execute an experiment where the fluorescent molecule location and orientation relative to the nanoparticle can be known, Tiancheng Zuo *et al.* from the lab of Julie S. Biteen performed high SNR PAINT experiments on 80 nm gold spheres in order to best reduce fit inaccuracies. Although we do not know the true location of the molecules in this case, we can get some sense of the potential success for the model fits by comparing model fits to Gaussian fits relative to the fit uncertainties.

Figure 7.1 diagrams the fit routine to experimental data. The model polarizabilities are parameterized as described in Section 3.1, but the experimental darkfield scattering spectrum of the nanosphere was fit instead of simulation. To minimize noise from the background fluorescence inherent to PAINT experiments, the images are background subtracted by separating signal with time correlation persistent beyond that of fluorescence blinking. The SMALL-LABS algorithm was developed for this purpose and was employed here [79]. If a plasmonic nanoparticle resides within the image frame, its photoluminescence dominates the background image. This background photoluminescence can then be fit with a 2D Gaussian to ascertain the nanoparticle location.

With this location the model is fully parameterized and can be fit to the experimental images with 3 fit parameters: the (x, y) location of the molecule in the focal plane relative to the nanoparticle and its orientation, which is assumed to be such that the emissive transition dipole lies in the focal plane.

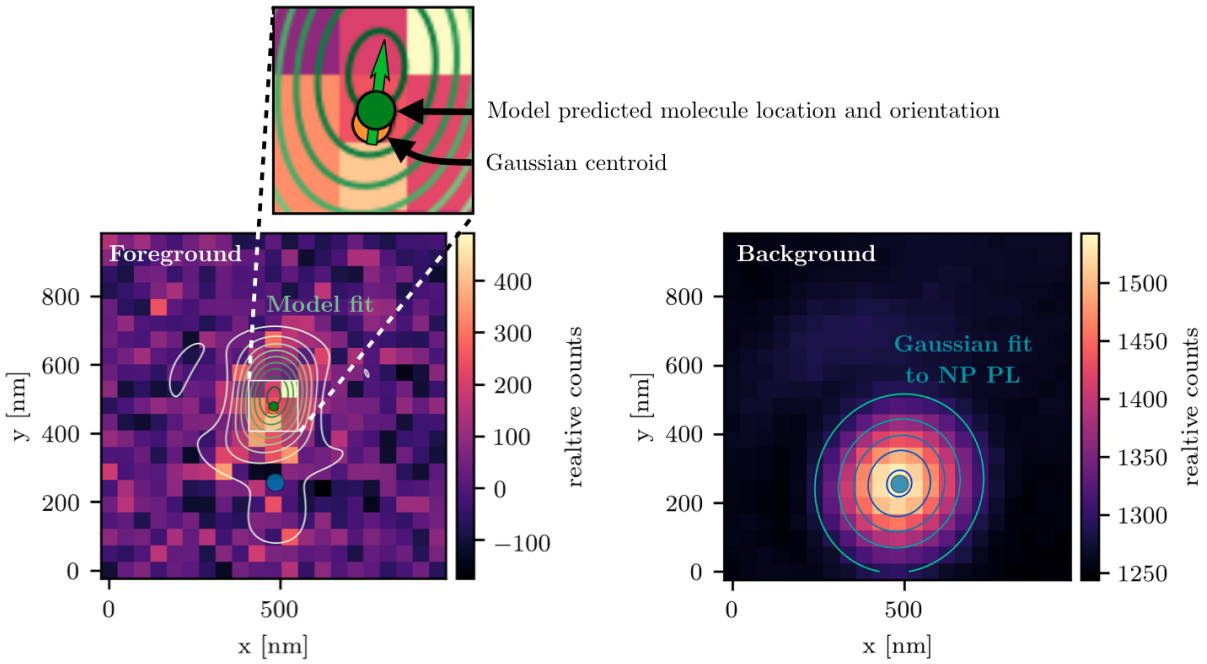

Figure 7.1: This is an example of the experimental fit routine after model parameterization as discussed in Section 3.1. (left) Model image (green contours) fit to background-subtracted image. The inset shows the estimated molecule location and orientation (green) and the Gaussian mislocalization in orange. Predicted mislocalization (difference between Gaussian centroid and model predicted molecule location) and uncertainties are given in Table 7.1. (right) Background image showing nanoparticle photoluminescence (NP PL) with the Gaussian fit overlaid in blue contours with the estimated nanoparticle location marked by the blue dot. With magnification, pixel size is 48 nm.

[nm]	$\Delta x_0^{\text{Gauss}}$	$\Delta y_0^{\text{Gauss}}$	$\Delta x_0^{\text{model}}$	$\Delta y_0^{\text{model}}$	$\lvert\Delta \mathbf{x}_0^{\text{Gauss}} - \Delta \mathbf{x}_0^{\text{model}}\rvert$
Fig. 7.1	116.20	175.62	29.23	150.26	8.80
Fig. 7.2a	95.89	79.17	88.05	23.56	27.44
Fig. 7.2b	128.92	455.626	6438.49	5843.87	33.87
Fig. 7.2c	127.61	456.93	49.51	456.97	19.83

Table 7.1: Fit uncertainties for image fits shown in Figs. 7.1 and 7.2 in (data columns 1 & 2) Gaussian centroid position corresponding to the typical measure of single-molecule localization precision and (data columns 3 & 4) the image model predicted molecule location. The last column presents the model estimates mislocalization. All uncertainties are reported in nm.

Figures 7.1 and 7.2a-c offer 4 examples of model fits to experimental images characteristic of different qualitative results. We can examine the fit uncertainty in molecule location returned by the model fit in comparison to the Gaussian centroid uncertainty which dictates the resolution limit in typical localization based super-resolution microscopy (details in Table 7. This measure helps us determine the performance of the model fit function relative to the typical measure of single-molecule localization. For Fig. 7.1, the model fit uncertainty is less then the Gaussian equivalents, but comparable in the y direction closely aligned with the predicted molecule-antenna separation vector. So it's hard to say whether or not the model fit was an improvement, especially with the predicted mislocalization only ~ 8 nm. The image fit in Fig. 7.2a similarly has comparable drop in fit uncertainty from Gaussian to image-model fits, but this time the drop does occur in the y direction. In other words, the model-image fit results in $\sim$ half-pixel certainty in the molecule distance away from the antenna. This is a promising result, indicating likely correction of 27 nm mislocalization. Since we can not know the absolute accuracy of the model without knowing the molecule's true location, we are unable with these experiments to reveal potential bias in the model, but results are promising none-the-less.

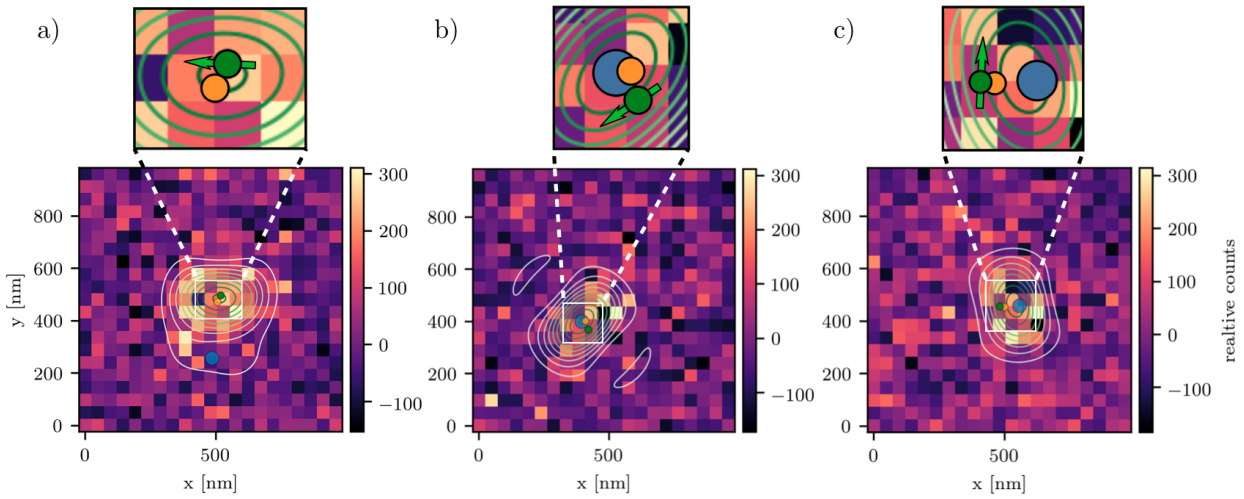

Figure 7.2: Three characteristic examples of model fits to experimental images. The following discussion relies on the fit uncertainties listed in Table 7.1. (a) An example where the model image fits better than the Gaussian. Notably, the model fit also restricts the molecule location uncertainty down to 1/2 a pixel in the y direction. Given that is approximately the direction of mislocalization, it is likely in this case the the model fit is correctly accounting for mislocalization. (b) An example where neither the Gaussian or model is a good fit to the noisy data, but still the time correlation analysis indicates a likely candidate for molecule emission neat a NP. The Gaussian and model both predict the molecule to lie very close to the NP, which explains the massive uncertainty of the model fit. It is expected that the model performs relatively poorly when the molecule is very close to the NP. (c) An example where the molecule is predicted to be within a couple pixels of the nanoparticle, but model fit certainty is improved over the Gaussian fit. This cause demonstrated a potential success of the model in its most disadvantaged situation.

The image fit in Fig. 7.2b reveal a fundamental challenge for the image-model fit. When the molecule is strongly coupled to the antenna, the image centroid collapses onto the antenna. When this occurs, there is little information in the image as to where the molecule is located within the ring around the antenna. The larger uncertainties in model fit for Fig. 7.2b (again, see the Table) indicate this ill-conditioning of the fit. Likely, future work will have to account for the statistical properties of the image noise in a more sophisticated way in order to extract as much information as possible from images like this. It is also possible that incorporation of polarization information or hyper-spectral imaging would reveal the molecule location to higher certainty. It may also be the case that some images are doomed to this uncertainty problem, but others of similar molecule location will fit ok. Fig. 7.2c is an example where the molecule was predicted very close to the antenna, but model-fit uncertainty was at worst equivalent to the Gaussian fit, and significantly better in the predicted molecule-antenna separation direction.

The experimental details are as follows. The excitation laser wavelength is 515 nm. The dye is R6G NHS ester with peak absorption peak at $\sim$ 530 nm and emission peak at $\sim$ 550 nm, which is very close to the scattering peak of the 80 nm sphere.

Chapter 8

A MODEL OF MOLECULAR EMISSION

As mentioned in Section 3.2, I attempted many times to come up with a classical-quantum hybrid model of plasmon-molecule interaction that would preserve the simplicity of the classical coupled dipole approach while incorporating the spectral shape of molecular emission. The classical model works fine for single frequencies near the emission peak, but the spectrum of the dye is modeled as Lorentzian, which clearly leaves out some qualitative features of the dye emission spectrum. Fig. 6.2 contains a representative example, with most dye molecules containing two Gaussian looking peaks, one major and one secondary shoulder. I also dreamed of using the plasmon-fluorophore system as a case study for bridging the classical-quantum transition, but this did not pan out in time.

Despite not having success at a building a classical-quantum hybrid model of the plasmon-molecule interaction, my interest in a quantum mechanical explanation of the dye molecule fluorescence spectra led me to dive deeply into the model derived in this chapter. Coincidentally, this work did find its way to usefulness in my time, leading to a productive collaboration with Emily J. Rabe *et al.* [129]. The following was contained in the supplementary information of that work.

8.1 Introduction to the model

Here I present a model of the adiabatic coupling between an emissive electronic transition and vibrational states and the resulting emission spectrum. This model was mostly sourced from Mukamel's text [113], where it is refereed to as the Brownian (or more intuitively, displaced) oscillator model. In practice it is simply a quantum-optical description of the classic Franck-Condon Diagram that every Chemist knows and loves. Where I have diverged from Mukamel,

I have taken heavy inspiration from the work of Anda *et al.*'s generalization of the displaced oscillator to any polynomial potential surfaces [6], which simplified the treatment of the intrinsic linewidth of individual vibrionic peaks. This paper was especially insightful (despite some unit issues) because they compare Mukamel's Cumulant based approach with the more transparent method of computing overlap integrals of vibrational wavefunctions. Here I took the Cumulant approach because of it's potential to scale well for fitting spectra with significant anharmonic effects, as discussed by Anda *et al.*

To be clear, we do not claim this work is new, but only an explicit derivation of the model outlined in Mukamel's text with a simpled treatment of the damping following Anda *et al.*'s proscription. In fact, it has been recommended by some that this section be shortened to just Eq. 8.43, since it is a known result. However, we believe that this derivation published in full detail is a contribution to the field, and may assist future graduate students.

We start by identifying the observable of interest and relating it to a physical quantity we can model. Mukamel claims that we can arrive at the linear absorption and emission lineshapes from Fermi's Golden Rule, and we will take it for granted that they are given in integral normalized form by the following expressions in the Condon approximation[1]

$$\sigma_a(\omega) = \frac{1}{2}\mathrm{Re}\int_0^\infty \mathrm{d}t \exp[i(\omega - \omega_{eg})t - g(t)] \tag{8.1}$$

$$\sigma_f(\omega) = \frac{1}{2}\mathrm{Re}\int_0^\infty \mathrm{d}t \exp[i(\omega - \omega_{eg} + 2\lambda)t - g^*(t)] \tag{8.2}$$

where ω_{eg} is the average transition frequency defined by $\hbar\omega_{eg} = \langle H_e - H_g \rangle$, where from here forward angle brackets indicate a thermal average. λ is the difference between this average and the zero point energy of the ground electronic state $\lambda \equiv \omega_{eg} - \omega_{eg}^0$. The linebroadening function $g(t)$ will be discussed in detail in the following sections. It is defined in terms of

[1] These lineshapes are equivalent to those given by Mukamel times a factor of $\pi/2$, which I found I needed for integral normalization.

the electronic dipole-dipole correlation function

$$\begin{aligned} J(t) &= \langle \mu_{ge}(t)\mu_{eg}(0)\rho(-\infty)\rangle \\ &= |\mu_{ge}^{(g)}|^2 e^{-i\omega_{eg}t - g(t)}, \end{aligned} \tag{8.3}$$

which arises in the definition of the linear response function. Combining Eqs. 8.1 and 8.3 makes clear the often cited fact that the lineshapes are proportional to the Fourier transform of the dipole-dipole correlation function $J(t)$. It is therefore this correlation function that we seek to model.

8.2 Model of the dipole-dipole correlation function

We begin with a Hamiltonian for a two level electronic system coupled adiabatically to one (or later multiple) harmonic vibrational modes.

$$H_0 = |g\rangle H_g \langle g| + |e\rangle H_e \langle e| \tag{8.4}$$

where we the eigenvalues of the electronic system are operators in nuclear space. Written in terms of the nuclear position and momentum operators, q and p, the nuclear Hamiltonians

$$H_g = \frac{p^2}{2m} + \frac{1}{2} m\omega_0^2 q^2 \tag{8.5}$$

$$H_e = \frac{p^2}{2m} + \frac{1}{2} m\omega_0^2 (q-d)^2 + \hbar\omega_{eg}^0, \tag{8.6}$$

describe a harmonic oscillator in the electronic ground state centered about the origin, and oscillator of equal frequncy in the electronic excited state with equilibrium position shifted by the displacement d.

As stated above, we are in interested in computing the correlation function $J(t) \equiv \langle \mu(t')\mu(0)\rho(-\infty)\rangle$. In order to consider the thermal average, we define the equilibrium density matrix $\rho(-\infty) = |g\rangle\langle g|\rho_g$ where

$$\rho_g = \frac{e^{-\beta H_g}}{\mathrm{Tr}[e^{-\beta H_g}]} \tag{8.7}$$

describes the Boltzmann distribution of vibrational states in the electronic ground state. The dipole operator appearing in $J(t)$ is represented in the interaction picture, and therefore has time dependence

$$\mu(t) = e^{\frac{i}{\hbar}H_0 t}\mu e^{-\frac{i}{\hbar}H_0 t}, \tag{8.8}$$

therefore, the second dipole operator in the correlation function acts on the equilibrium density matrix to yield

$$\begin{aligned}\mu(t)\rho(-\infty) &= e^{\frac{i}{\hbar}H_0 t}\mu e^{-\frac{i}{\hbar}H_0 t}|g\rangle\rho_g\langle g| \\ &= e^{\frac{i}{\hbar}H_0 t}\mu|g\rangle e^{-\frac{i}{\hbar}H_g t}\rho_g\langle g| \\ &= e^{\frac{i}{\hbar}H_0 t}|e\rangle\langle e|\mu|g\rangle e^{-\frac{i}{\hbar}H_g t}\rho_g\langle g| \\ &= |e\rangle e^{\frac{i}{\hbar}H_e t}\mu_{eg}e^{-\frac{i}{\hbar}H_g t}\rho_g\langle g| \end{aligned} \tag{8.9}$$

where the second step involves inserting the identity in electronic states and noting that the two-level dipole operator is antidiagonal. Projecting the leading ket onto the other dipole operator in the correlation function yields

$$J(t) = \langle \mu_{ge}(t)\mu_{eg}(0)\rho(-\infty)\rangle, \tag{8.10}$$

where $\mu_{ge}(t) \equiv |g\rangle e^{\frac{i}{\hbar}H_g t}\mu_{ge}e^{-\frac{i}{\hbar}H_e t}\langle e|$. The correlation function written in this form clearly describes the initial excitation of the equilibrium mixed state followed by excitation some time t later.

This correlation function still contains operators in both nuclear subspaces and is therefore going to be unwieldy to work with directly. To resolve this issue and compute the expectation value, it is useful and rather intuitive to introduce the the electronic energy gap fluctuation operator

$$\begin{aligned} U &= H_e - H_g - \langle (H_e - H_g)\rho(-\infty)\rangle \\ &= H_e - H_g - \hbar\omega_{eg} \end{aligned} \tag{8.11}$$

where $\hbar\omega_{eg} \equiv \frac{1}{2}m\omega_0^2 d^2 + \hbar\omega_{eg}^0$, as can be computed directly. This operator described the difference between any instantaneous gap and the thermal average. Substituting U in for H_e

inside $\langle g|\mu_{ge}(t)|e\rangle$,

$$\begin{aligned} e^{\frac{i}{\hbar}H_g t}\mu_{ge}e^{-\frac{i}{\hbar}H_e t} &= e^{\frac{i}{\hbar}H_g t}\mu_{ge}e^{-\frac{i}{\hbar}(H_g+U+\hbar\omega_{eg})t} \\ &= e^{-\frac{i}{\hbar}\hbar\omega_{eg}t}\underbrace{e^{\frac{i}{\hbar}H_g t}\mu_{ge}e^{-\frac{i}{\hbar}H_g t}}_{\mu_{eq}^{(g)}(t)}\exp_+[-\tfrac{i}{\hbar}\int_0^t \mathrm{d}\tau U(\tau)] \end{aligned} \tag{8.12}$$

where $\exp_+$ is the time ordered exponential operator[2]. The time dependence of the dipole operator is now expressed in terms of the interaction picture with respect to the electronic ground state. We can now take advantage of this by noting that the operator $\mu_{eq}^{(g)}(t)$ will be approximately stationary in the Frank-Condon Approximation. This approximation consists of assuming that the dipole transition is only parametrically dependent on the vibrational coordinate q and therefore independent of time with respect to the electronic ground state alone.

With the time dependence of $\mu_{eq}^{(g)}$ neglected, we return to the correlation function. Both dipole operators can be combined and the correlation function written

$$J(t) = e^{-i\omega_{eg}t}|\mu_{ge}^{(g)}|^2\langle\exp_+[-\tfrac{i}{\hbar}\int_0^t \mathrm{d}\tau U(\tau)]\rangle. \tag{8.15}$$

In order to evaluate the expectation value of the time ordered exponential, we will evolve the Cumulant expansion, which effective replaces the expectation value of an exponential with exponentials of expectation values. Conveniently, the Cumulant expansion happens to

---

[2] The time ordered exponential operator is defined by

$$\begin{aligned} \exp_+\left[-\frac{i}{\hbar}\int_0^t \mathrm{d}\tau U(t)\right] &= 1 + -\frac{i}{\hbar}\int_0^t \mathrm{d}\tau_1 U(\tau_1) + \left(-\frac{i}{\hbar}\right)^2\int_0^t \mathrm{d}\tau_1\int_0^{\tau_1}\mathrm{d}\tau_2 U(\tau_1)U(\tau_2) + \cdots \\ &= 1 + \sum_{n=1}^{\infty}\left(-\frac{i}{\hbar}\right)^n\int_0^t \mathrm{d}\tau_n\int_0^{\tau_n}\mathrm{d}\tau_{n-1}\cdots\int_0^{\tau_2}\mathrm{d}\tau_1 U(\tau_n)U(\tau_{n-1})\cdots U(\tau_2)U(\tau_1). \end{aligned} \tag{8.13}$$

It can be derived in the given context by assuming

$$e^{-\frac{i}{\hbar}(H_g+U)t} = e^{-\frac{i}{\hbar}H_g t}A(t) \tag{8.14}$$

and showing that the operator $A(t)$ satisfies the Heisenberg equation $\dot{A} = -\frac{i}{\hbar}U(t)A$ in the interaction picture with respect to H_g. By integrating the Heisenberg equation, $A(t)$ becomes the evolution operator of U which takes the form of Eq. 8.13.

truncate exactly for the harmonic potential surfaces we are concerned with here[113]. The first step is to assume an expansion of the form

$$\langle \exp_+[-\tfrac{i}{\hbar}\int_0^t \mathrm{d}\tau U(\tau)]\rangle = e^{-g(t)} = 1 - g(t) + \frac{1}{2}g^2(t) + \cdots . \tag{8.16}$$

Next, we expand $g(t)$ in powers of U and match terms with the time ordered exponential.

$$e^{-g(t)} = 1 - (g_0 + g_1 + g_2 + \cdots) + \tfrac{1}{2}(g_0 + g_1 + g_2 + \cdots)^2 + \cdots \tag{8.17}$$

$$= \underbrace{(1 - g_0 + \tfrac{1}{2}g_0^2 + \cdots)}_{\propto U^0} + \underbrace{(-g_1 + g_0 g_1 + \cdots)}_{\propto U^1} + \underbrace{(-g_2 + \tfrac{1}{2}g_1^2 + g_0 g_2 + \cdots)}_{\propto U^2} + \cdots , \tag{8.18}$$

and comparing terms,

$$1 = (1 - g_0 + \tfrac{1}{2}g_0^2 + \cdots) \rightarrow g_0 = 0 \text{ to all order in g} \tag{8.19}$$

$$-\frac{i}{\hbar}\int_0^t \mathrm{d}\tau_1 \cancelto{0}{\langle U(\tau_1)\rangle} = (-g_1 + 2\tfrac{1}{2}\cancelto{0}{g_0 g_1} + \cdots) \rightarrow g_1 = 0 \text{ by definition} \tag{8.20}$$

$$\left(\frac{i}{\hbar}\right)^2 \int_0^t \int_0^{\tau_1} \mathrm{d}\tau_2 \mathrm{d}\tau_1 \langle U(\tau_1)U(\tau_2)\rangle = (-g_2 + \tfrac{1}{2}\cancelto{0}{g_1^2} + \cancelto{0}{g_0 g_2} + \cdots) \rightarrow -g_2 = \frac{-1}{\hbar^2}\int_0^t \int_0^{\tau_1} \mathrm{d}\tau_2 \mathrm{d}\tau_1 \langle U(\tau_1)U(\tau_2)\rangle , \tag{8.21}$$

and we will trust Mukamel that the higher order terms disappear. The function $g(t)$ can be accurately referred to as the line shape broadening function based on its influence on the linear observables. Because the two time expectation value is invariant to time translation, the U correlation function under the integral can be replaced by $\langle U(\tau_1)U(\tau_2)\rangle \rightarrow \langle U(\tau_2)U(0)\rangle$, yielding[3]

$$g(t) = \frac{1}{\hbar^2}\int_0^t \mathrm{d}\tau_1 \int_0^{\tau_1} \mathrm{d}\tau_2 \langle U(\tau_2)U(0)\rangle \tag{8.25}$$

---

[3] I found this non-trivial, so here is a note. First, by time translation invariance of the two-time expectation value (aka assumption of equilibrium),

$$\int_0^t \mathrm{d}\tau_1 \int_0^{\tau_1} \mathrm{d}\tau_2 \langle U(\tau_1)U(\tau_2)\rangle = \int_0^t \mathrm{d}\tau_1 \int_0^{\tau_1} \mathrm{d}\tau_2 \langle U(\tau_2 - \tau_1)U(0)\rangle \tag{8.22}$$

Next, we make the substitution $\tau_1 - \tau_2 = t'$, which yields the differential relation $\mathrm{d}\tau_2 = -\mathrm{d}t'$. The

with this definition of the line broadening function,

$$J(t) = |\mu_{ge}^{(g)}|^2 e^{-i\omega_{eg}t - g(t)} \tag{8.26}$$

and we have accomplished our goat of moving the expectation value to the inside of the exponential, along with truncating the time ordered exponential series.

If we wish to evaluate the model and fit to some data, we need to get rid of the operators and replace them with good old c-numbers. For convenience, we redefine the line broadening function to be the double time integral $g(t) = \int_0^t \int_0^{\tau_1} C(\tau_2) \mathrm{d}\tau_2 \mathrm{d}\tau_1$ over the energy gap correlation function $C(t) = \langle U(\tau_2)U(0)\rangle$. Noting that $U(t) = m\omega_0^2 qd$, the energy gap correlation is proportional to the nuclear coordinate correlation function

$$C(t) = \left(\frac{m\omega_0^2 d}{\hbar}\right)^2 \langle q(\tau_2)q(0)\rangle \tag{8.27}$$

Our goal now will be to project the $C(t)$ onto the eigenstates of H_g.

Expanding the equilibrium desnsity matrix projects the expectation value into the ground nuclear subspace

$$\begin{aligned} \mathrm{Tr}[q(\tau)q(0)\rho(\infty)] &= \sum_{\alpha=e,g}\sum_{j=0}^{\infty} \langle \alpha, j|q(\tau)q(0)\rho_g|g\rangle\langle g|\alpha, j\rangle \\ &= \sum_{j=0}^{\infty} \langle j|q(\tau)q(0)\rho_g|j\rangle \end{aligned} \tag{8.28}$$

where the states $|j\rangle$ are defined such that $H_g|j\rangle = \hbar\omega_j|j\rangle$. In the harmonic potential, $\omega_j = j\omega_0$. With the density matrix defined in Eq. 8.7, off diagonal components are zero. Inserting the identity in the form of the completeness relation for eigenstates of H_g to the

---

integration bounds reverse because

$$\text{when} \quad \tau_2 = 0, \quad t' = \tau_1 \tag{8.23}$$
$$\text{when} \quad \tau_2 = \tau_1, \quad t' = 0, \tag{8.24}$$

but the negative sign from the differential substitution flips the bounds back.

left of the density matrix and again between the nuclear coordinate operators yields

$$\begin{aligned}
\sum_{j=0}^{\infty}\langle j|q(\tau)q(0)\rho_g|j\rangle &= \sum_{j=0}^{\infty}\sum_{k=0}^{\infty}\langle j|q(\tau)q(0)|k\rangle\langle k|j\rangle\rho_{jj}^{g} \\
&= \sum_{j=0}^{\infty}\langle j|q(\tau)q(0)|j\rangle\rho_{jj}^{g} \\
&= \sum_{j=0}^{\infty}\sum_{l=0}^{\infty}\langle j|q(\tau)|l\rangle\langle l|q(0)|j\rangle\rho_{jj}^{g} \\
&= \sum_{j=0}^{\infty}\sum_{l=0}^{\infty}\langle j|e^{\frac{i}{\hbar}H_g t}qe^{-\frac{i}{\hbar}H_g t}|l\rangle\langle l|q|j\rangle\rho_{jj}^{g} \\
&= \sum_{j=0}^{\infty}\sum_{l=0}^{\infty}q_{jl}q_{lj}\rho_{jj}^{g}e^{-i(\omega_l-\omega_j)t} \qquad (8.29)
\end{aligned}$$

Now that the operators are back in the Schrödinger picture, we can utilize their representation in terms of the raising and lowering operates $q=\sqrt{\frac{\hbar}{2m\omega}}(a^{\dagger}+a)$ to establish their action on the eigenstates of H_g,

$$q|j\rangle = \sqrt{\frac{\hbar}{2m\omega}}\left(\sqrt{j+1}|j+1\rangle+\sqrt{j}|j-1\rangle\right) \qquad (8.30)$$

$$\langle l|q|j\rangle = \sqrt{\frac{\hbar}{2m\omega}}\left(\sqrt{j+1}\delta_{l,j+1}+\sqrt{j}\delta_{l,j-1}\right). \qquad (8.31)$$

Evaluating the matrix elements in this fashion,

$$\begin{aligned}
\frac{\langle j|q|l\rangle\langle l|q|j\rangle}{\hbar/2m\omega} &= \left(\sqrt{l+1}\delta_{j,l+1}+\sqrt{l}\delta_{j,l-1}\right)\left(\sqrt{j+1}\delta_{l,j+1}+\sqrt{j}\delta_{l,j-1}\right) \\
&= \left(\sqrt{l+1}\delta_{l,j-1}+\sqrt{l}\delta_{j+1,l}\right)\left(\sqrt{j+1}\delta_{l,j+1}+\sqrt{j}\delta_{l,j-1}\right) \\
&= ((j+1)\delta_{l,j+1}+j\delta_{l,j-1}) \qquad (8.32)
\end{aligned}$$

Incorporating this back under the summation, the correlation function of the nuclear coordinates becomes

$$\begin{aligned}
C(t) &= \left(\frac{m\omega_0^2 d}{\hbar}\right)^2\frac{\hbar}{2m\omega}\sum_{j=0}^{\infty}\sum_{l=0}^{\infty}\left((j+1)\delta_{l,j+1}+j\delta_{l,j-1}\right)\rho_{jj}^{g}e^{-i(\omega_l-\omega_j)t} \\
&= \frac{\omega_0^2}{2}\underbrace{\frac{m\omega_0}{\hbar}d^2}_{\equiv d_0^2}\sum_{j=0}^{\infty}\left((j+1)e^{-i(\omega_{j+1}-\omega_j)t}+je^{-i(\omega_{j-1}-\omega_j)t}\right)\rho_{jj}^{g}, \qquad (8.33)
\end{aligned}$$

and since the energy spacing in the harmonic potentials is constant, $\omega_{j+1} - \omega_j = -(\omega_{j-1} - \omega_j) = \omega_0$, so

$$\begin{aligned} C(t) &= \omega_0^2 \frac{d_0^2}{2} \sum_{j=0}^{\infty} \left((j+1)e^{-i\omega_0 t} + j e^{i\omega_0 t} \right) \rho_{jj}^g \\ &= \omega_0^2 \frac{d_0^2}{2} \sum_{j=0}^{\infty} \left((j+1)e^{-i\omega_0 t} + j e^{i\omega_0 t} \right) \frac{e^{-j\beta\hbar\omega_0}}{\sum_{k=0}^{\infty} e^{-k\beta\hbar\omega_0}}. \end{aligned} \tag{8.34}$$

We can then evaluate the 3 summations with the following equalities

$$\sum_{n=0}^{\infty} e^{-\alpha n} = \frac{e^{\alpha}}{e^{\alpha} - 1} \tag{8.35}$$

$$\sum_{n=0}^{\infty} n e^{-\alpha n} = \frac{e^{\alpha}}{(e^{\alpha} - 1)^2} \tag{8.36}$$

$$\sum_{n=0}^{\infty} (n+1) e^{-\alpha n} = \frac{e^{2\alpha}}{(e^{\alpha} - 1)^2} \tag{8.37}$$

and finally the correlation function can be written in terms of classical numbers

$$\begin{aligned} C(t) &= \omega_0^2 \frac{d_0^2}{2} \left(\frac{e^{2\beta\hbar\omega_0}}{(e^{\beta\hbar\omega_0} - 1)^2} e^{-i\omega_0 t} + \frac{e^{\beta\hbar\omega_0}}{(e^{\beta\hbar\omega_0} - 1)^2} e^{i\omega_0 t} \right) \frac{e^{\beta\hbar\omega_0} - 1}{e^{\beta\hbar\omega_0}} \\ &= \omega_0^2 \frac{d_0^2}{2} \frac{e^{\beta\hbar\omega_0} e^{-i\omega_0 t} + e^{i\omega_0 t}}{e^{\beta\hbar\omega_0} - 1} \\ &= \omega_0^2 \frac{d_0^2}{2} \left((\overline{n} + 1) e^{-i\omega_0 t} + \overline{n} e^{i\omega_0 t} \right) \end{aligned} \tag{8.38}$$

where in the last line we have expressed the correlation function in terms of the thermally averaged occupation number $\overline{n} \equiv (e^{\beta\hbar\omega_0} - 1)^{-1}$. In terms of the real and imaginary parts,

$$\begin{aligned} C(t) &= \omega_0^2 \frac{d_0^2}{2} \left((\overline{n} + 1) \left[\cos(\omega_0 t) - i \sin(\omega_0 t) \right] + \overline{n} \left[\cos(\omega_0 t) + i \sin(\omega_0 t) \right] \right) \\ &= \omega_0^2 \frac{d_0^2}{2} \left[(2\overline{n} + 1) \cos(\omega_0 t) - i \sin(\omega_0 t) \right]. \end{aligned} \tag{8.39}$$

With a numerical form for the nuclear coordinate correlation function, we can turn back to the linebroadening function and take the double time integral analytically. Noting that $C(t)$ contains only time dependence of the form

$$C(t) = \sum_i A_i e^{-\alpha_i t} \tag{8.40}$$

we can use the integral

$$\int_0^t \int_0^{\tau_1} e^{-\alpha\tau_2} \mathrm{d}\tau_2 \mathrm{d}\tau_1 = \frac{e^{-\alpha t} + \alpha t - 1}{\alpha^2} \tag{8.41}$$

to write the line broadening function

$$\begin{aligned} g(t) = & -\frac{d_0^2}{2}\left[(\overline{n}+1)(e^{-i\omega_0 t} + i\omega_0 t - 1) + \overline{n}(e^{i\omega_0 t} - i\omega_0 t - 1)\right] \\ = & \frac{d_0^2}{2}\left[(2\overline{n}+1)(1-\cos(\omega_0 t)) + i(\sin(\omega_0 t) - \omega_0 t)\right] \end{aligned} \tag{8.42}$$

Bringing it all together, the emission (fluorescence) lineshape is computed and used in fit routine described in the main text as

$$\begin{aligned} \sigma_f(\omega) &= \frac{1}{2}\mathrm{Re}\int_0^\infty \mathrm{d}t \exp[i(\omega + \omega_{eg} - 2\omega_{eg}^0)t - g^*(t)]e^{-}\gamma \\ &= \frac{1}{2}\mathrm{Re}\int_0^\infty \mathrm{d}t \exp\left[i(\omega + \omega_{eg} - (2+\tfrac{d_0^2}{2})\omega_{eg}^0)t + i\tfrac{d_0^2}{2}\sin(\omega_0 t) - \tfrac{d_0^2}{2}(2\overline{n}+1)(1-\cos(\omega_0 t)) - \gamma\right] \end{aligned} \tag{8.43}$$

where we have accounted for the intrinsic linewidth of each vibronic peak by multiplying the correlation function by the exponential decay $e^{-\gamma t}$. This could also be interpreted as adding the real constant γ to the linebroadening function.

For more then one vibrational mode, as was used in the main text, the correlation functions (and therefore the linebroadening functions) simply sum.

Part III

PHOTOTHERMAL HETERODYNE IMAGING OF PLASMONIC NANOPARTICLES

Chapter 9

RESOLVING RESONANCE EFFECTS IN THE THEORY OF PHOTOTHERMAL IMAGING

9.1 Introduction

From Hooke and Leeuwenhoek's first glimpse of microorganisms in the 1600s [63, 75] until today, optical microscopy has provided a fundamental characterization tool of the microscale. Optical microscopy has endured hundreds of years of technological advancement, owing to the remarkable signal to noise, biocompatibility, and molecular specificity of fluorescence [134]. More recently, with the development of robust single molecule detection [121, 85, 109] and super-resolution imaging [138, 69, 19, 144, 49], optical microscopy has even been extended to operate below the diffraction limit, resolving the details of individual molecules and their interactions with their environment [109]. However, despite the success of such fluorescence-based imaging techniques, most absorbing molecules do not efficiently fluoresce, but instead convert optical excitation into heat through nonradiative downconversion. This reason alone has compelled researchers to develop alternative methods to characterize the microscopic world based solely upon absorption.

Detecting not only the appearance of photons but also their disappearance would provide a complete understanding of how a nanoscale object processes light. But isolating absorption from emission and scattering is difficult. The first absorption based single molecule detection was demonstrated in 1989 at liquid helium temperatures, where molecular absorption cross sections are 10^6 times larger than at ambient conditions due to quick thermal dephasing [108]. Performing such measurements at room temperature would require large laser intensities, introducing the problem of detecting the depletion of a few photons from many. Even with ultrasensitive photodetectors, this kind of measurement would be difficult to achieve since

background scattering by interfaces and an inhomogeneous environment can conflate true absorption within an extinction measurement [91, 32]. To isolate absorption from a nanoscale object like a single molecule, a direct measurement may not be ideal.

Photothermal heterodyne imaging (PHI) overcomes the difficulties of detecting individual nanoscale absorbers by measuring absorption second hand [158, 27, 45, 14]. The technique relies on lock-in detection to changes in scattering of a probe laser by an object with fluctuating absorption of a second pump laser. This is accomplished by amplitude modulating the pump laser, which induces an oscillating "thermal lens" around the absorber as heat diffuses into the environment. Based on this approach together with a some variations, detection [61, 2] and even spectroscopy [167, 16, 17, 15, 83, 82, 166, 2, 88, 70, 13, 12, 93, 94, 165, 41] of single particle absorption at room temperature is now possible. Fig. 9.1 illustrates the principles underlying PHI in comparison with traditional fluorescence imaging.

Due to their large absorption efficiencies, plasmonic nanoparticles make excellent nanoheaters [90, 114] and have been commonly employed test cases for photothermal detection. Soon after the development of PHI the demonstration of high signal-to-noise detection of nanometer-sized gold and silver nanoparticles was reported with corresponding theory that explained potential optimization of photothermal signal [27, 14, 18]. The theoretical trends in signal amplitude and spatial resolution with beam-aperture, heating beam intensity, and modulation frequency [18] demonstrated good agreement with experiment while maintaining relative simplicity, setting the standard for theoretical interpretations of the measurement. But over time, alternative models and associated interpretations have been presented [143] that explain the measured data equally well. Simultaneously, interest has also developed in the PHI of larger plasmonic particles with non-negligible scattering [21], a feature missing from the original models aimed at detecting single molecule absorption. Even for the metal nanoparticles employed as test targets during development of the PHI measurement, accounting for scattering is unnecessary for absorbers that are small in comparison to the wavelength of light. Taken together, the apparent differences in photothermal models as well as their omission of resonant scattering effects highlight the need for an improved understanding of PHI

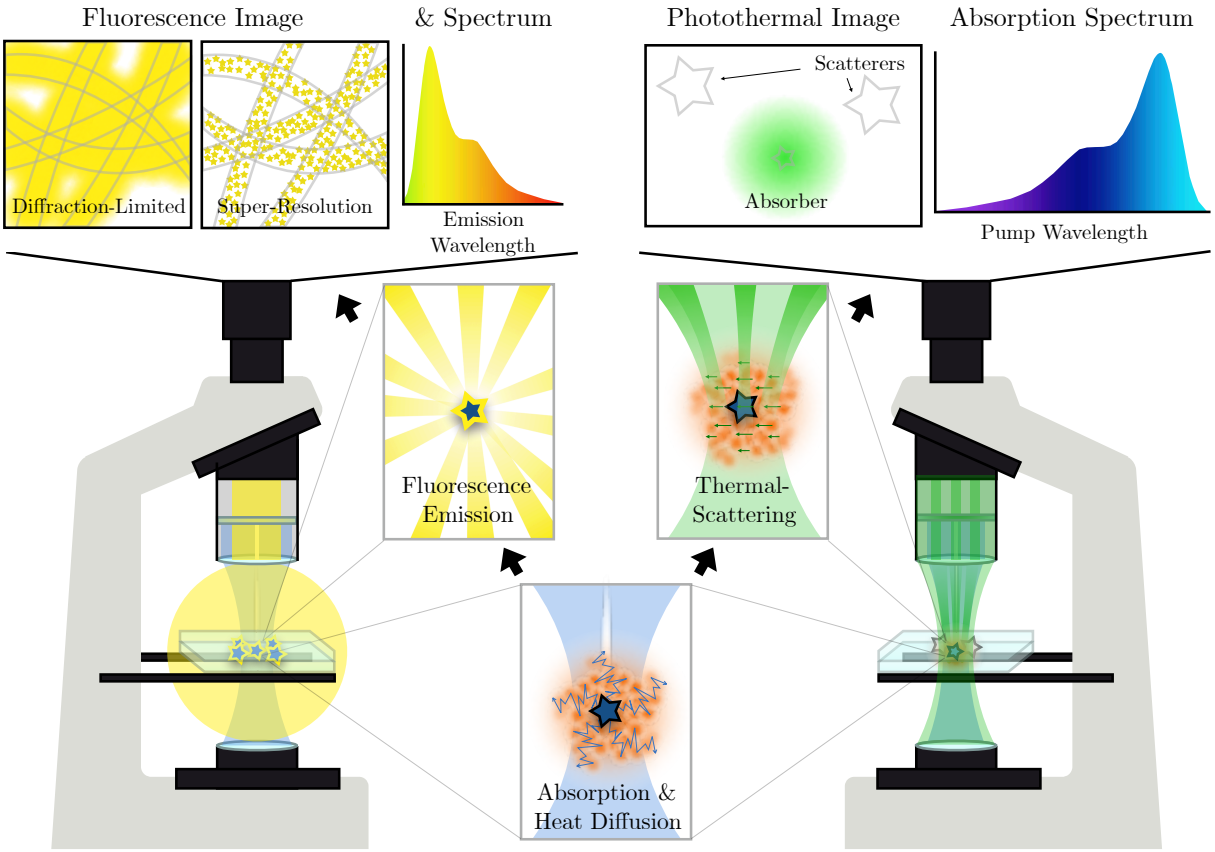

Figure 9.1: Illustrated comparison of fluorescence imaging and spectroscopy (left) with photothermal imaging and photothermal absorption spectroscopy (right), the latter being capable of optically detecting non-fluorescent absorbers. In fluorescence microscopy or spectroscopy, sample is illuminated with light tuned to fluorescence absorption (blue). The fluorescent molecules absorb and later emit at a Stokes shifted wavelength (yellow). This emission is filtered from excitation background and either directed to a camera to form an image or to a spectrometer to form a fluorescence emission spectrum. At the single molecule limit, the molecular point spread function can be fit to form a sub-diffraction-limited map of single molecule locations, known as a super-resolution image [138, 69, 19, 144, 49]. With isolated emission from single molecules, single molecule spectra are obtainable [5, 107, 96]. In the photothermal measurement, the same absorption process occurs. But in this case the heat dissipated by the absorbing molecule or particle is used as a "thermal lens". A second probe beam (green) scatters off of the heated region surrounding the absorber due to slight variations in the refractive index with temperature. Locking in to modulation of the absorbed pump beam (undepicted) allows for detection of single molecules [61] with minimal background from non-absorbing scatterers [27]. Single particle absorption spectra can also be measured by tuning the pump wavelength [167].

theory.

It is the purpose of this Chapter to unify existing photothermal imaging data and related models within a common theoretical formalism and use it to demonstrate the full complexity of the photothermal signal, including the effects of resonant scattering. This viewpoint validates the use of previously published interpretations in certain physical limits while exposing important differences that can arise in other regions of parameter space. Beyond this understanding, the influence of the target's scattering resonances upon the photothermal signal represents an important new direction of inquiry that may be exploited to enhance signal or locate windows of spectral transparency to perform photothermal experiments in the absence of scattering resonance effects. We begin by first reviewing the theoretical background of PHI, highlighting both approaches in common use in the literature. Next we formulate a comprehensive theoretical approach to PHI that explicitly includes the lock-in detection process and mechanisms of probe scattering such as the effects of thermal retardation and target scattering resonances. Finally, a set of detailed examples are presented to illustrate the effects of the background medium thermal and optical properties as well as single-particle resonances upon the measured photothermal image.

9.2 Theoretical Background

Significant advances in the analysis of the heterodyne photothermal signal (PTS) were made in 2010 by Orrit and coworkers [62] with the aim of pushing detection to the limit of a single molecule. Their analysis expanded upon earlier work with Lounis and coworkers [27], and examined the trend in PTS-to-noise with the thermo-optical properties of the thermally conductive environment. Theory and experiment both showed a linear trend in PTS with the so-called *photothermal strength* of the background medium (proportional to the product of the inverse thermal conductivity κ and thermo-optic coefficient dn/dT). Link and coworkers later demonstrated that this analysis could be used to push the sensitivity of PHI even further by immersing the absorbers in thermotropic liquid crystals [34]. This study extended the theoretical-experimental agreement on the trend in signal-to-noise with

background photothermal strength significantly, as the liquid crystal used had approximately three times the photothermal strength of the the strongest medium studied by Orrit, a path they have continued to innovate on [51].

Despite these theoretical advances in modeling the PTS, explicit treatment of the lock-in detection is missing. Instead, the signal is often taken to be proportional to the interference of the fluctuating component of the scattered probe field $\mathbf{E}_\Omega$ with the transmitted/reflected (depending on experimental geometry) probe field $\mathbf{E}_{\mathrm{pr}}^{\mathrm{tr/re}}$ observed in absence of the target sample. Written in terms of these complex fields with assumed harmonic time dependence, the photothermal image power takes the form [18]

$$P_{\mathrm{PT}}^{(1)} \propto \mathrm{Re}[\mathbf{E}_{\mathrm{pr}}^{\mathrm{tr/re}} \cdot \mathbf{E}_\Omega^*] \tag{9.1}$$

with the proportionality constant depending only upon basic material and incident light field parameters.

Independently, three distinct yet complementary theoretical constructions of the PTS were published by Cichos and coworkers in 2012: a generalized Lorenz-Mie theory to solve the scattering problem rigorously including effects of aberration on focused laser beams [143], a simplified Frauenhofer diffraction approach yielding analytical expressions [142], and a ray-optics treatment taking advantage Gaussian matrix optics [141]. These theoretical models all start with the assumption that lock-in measurement underlying the PTS reduces to the difference in probe scattering with the pump beam on and off. Said differently, the photothermal image is the difference between images of the heated and room temp systems,

$$P_{\mathrm{PT}}^{(2)} \propto P_{\mathrm{hot}} - P_{\mathrm{room}}. \tag{9.2}$$

The assumption that the modulated experiment can be modeled by a static theory was tested phenomenologically by comparing demodulated images to their steady state equivalents [143], with good agreement found between the theory and experiment. Nevertheless, Eq. (9.2) is not obviously compatible with that defined previously in Eq. (9.1).

With the ever increasing capabilities of lithographically engineered nanostructures, interest has arisen in controlling the nanoscale temperature distribution within absorbing nan-

oclusters composed of plasmonic particles. In 2019, Willets, Link, Masiello and coworkers adapted PHI toward quantifying the temperature distribution within and around interacting plasmonic nanoclusters as a form of optical thermometry [21]. Because detection was not the primary goal, these systems are larger than the common subjects of PHI, with dimensions on the order of the pump wavelength. Consequently their scattering cross sections exceed absorption, yet the effect of metal scattering on the photothermal image was at that point unestablished. Regardless, reasonable agreement was found between experiment and simulated photothermal images (following Eq. (9.2)) accounting only for the effect of the metal nanostructure on the photothermal image, despite the literature precedent of neglecting the any role of the metal beyond its role as an absorber. This agreement between simulation and experiment served as evidence that the plasmonic target had reached a new size regime where the metal scattering was the dominant contribution to the PTS and not scattering through heated background matrix. More recent theoretical work has acknowledged that as nanoparticle size increases, the room temperature scattering contributes to the photothermal signal even after lock-in detection [146].

In this Chapter, we seek to unify past assumptions behind models of the photothermal signal and reconcile their relationship in regimes where the target hosts it own unique scattering resonances as well as when it does not. The former is the regime of plasmonic nanoparticles, which will be the target sample of choice henceforth. However, the theory presented here can equally be applied to individual molecular absorbers/scatterers with appropriate modification of the target polarizability. To accomplish these objectives we present a simple analytic theory that extends to larger particle sizes where scattering from the target's dipole resonance contributes to the photothermal signal. Following an explicit derivation of the lock-in measurement, we show that the photothermal signal is actually the sum of Eqs. (9.1) and (9.2). We then investigate the physical differences between these two terms and discuss the experimental and physical factors controlling their relative contribution to the total signal. This discussion is most clear in the thermally-static limit, which is developed in greatest detail and followed with a comprehensive discussion of the more accurate

thermally-retarded model that is used for calculation of all presented Figures. The model predictions are compared to previously published data on the trend in PTS with background medium and then extended to larger particles. We observe probe wavelength dependence that is clearly connected to the particle scattering cross sections and background medium. Finally we assess the qualitative difference in photothermal images produced by Eqs. (9.1) and (9.2) in the context of past work.

9.3 Outline of the model: Lock-in detected photothermal signal

The lock-in detected photothermal signal can be understood by first working through a simplified version of the model. A diagram of the experiment is shown in Fig. 9.2. As in the rest of this Chapter, we will assume two monochromatic lasers are focused onto a sample containing an isolated absorbing nanoparticle. We distinguish the lasers as the pump and probe beams with intensities in the focal spot I_{pump} and I_{probe} with corresponding optical frequencies ω_{pu} and ω_{pr}. The pump beam is amplitude modulated and the probe beam is continuous. The probe beam is scattered by the sample, which is collected in either a reflection or transmission (diagrammed) geometry. Although the experimental geometry does affect some subtle aspects of the analysis, the basic physics is invariant. The probe-frequency light collected at the detector is demodulated electronically in order to select the PTS produced by temperature induced changes in scattering, which should have the time dependence as the pump beam modulation.

In what follows, we will break the model into distinct physical steps: (9.3.1) the absorption of the modulated pump beam by the nanoparticle, (9.3.2) the heating of the nanoparticle and surrounding background medium, (9.3.3) scattering of the continuous wave probe beam by the heated nanoparticle, and (9.3.4) detection and demodulation of the photothermal signal to extract the temperature induced scattering. Gaussian units are used throughout.

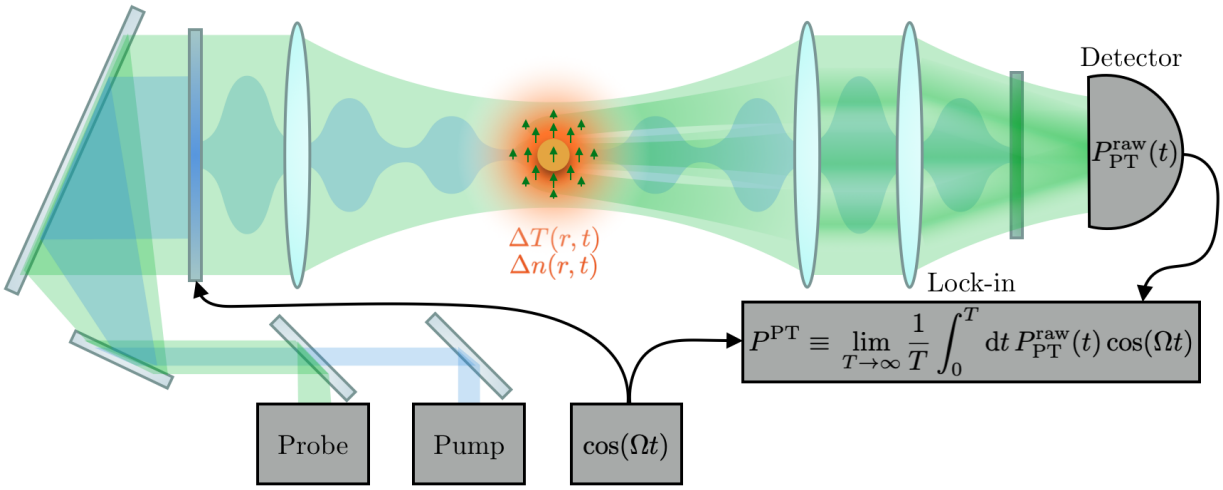

Figure 9.2: Illustration of the photothermal imaging setup as modeled. The pump beam (blue) passes through a modulating filter and is focused onto the gold nanoparticle. The nanoparticle absorbs the pump beam and acts as an oscillatory source of heat. The heat diffuses and generates the temperature distribution $\Delta T(r,t)$. The continuous wave probe beam (green) is also focused onto the nanoparticle, and scatters not only off of the nanoparticle, but also the space and time varying refractive index perturbation $\Delta n(r,t)$ resulting local temperature increase. The scattered and transmitted probe light is focused onto a photodetector and this raw photothermal $P_{\mathrm{PT}}^{\mathrm{raw}}$ fed to a lock-in amplifier. The lock-in integrates the raw photothermal signal against the modulation reference signal $\cos\Omega t$ to filter out static background from the photothermal signal.

9.3.1 Absorption

The pump beam is amplitude modulated at frequency Ω ($\sim$ kHz) much slower then optical frequencies, such that the detectable intensity varies in time as

$$I_{\text{pump}}(t;\omega_{\text{pu}}) = I_{\text{pu}} \cdot \frac{1}{2}\left(1+\cos\Omega t\right) \tag{9.3}$$

$$= \frac{cn}{8\pi}\left|\mathbf{E}_{\text{pu}}e^{-i\omega_{\text{pu}}t}\right|^2 \cdot \frac{1}{2}\left(1+\cos\Omega t\right), \tag{9.4}$$

where $I_{\text{pu}} \equiv (cn/8\pi)\left|\mathbf{E}_{\text{pu}}e^{-i\omega_{\text{pu}}t}\right|^2$ is the plane wave intensity pre-modulation. The spatial dependence of the beam is implicit within the field amplitude $\mathbf{E}_{\text{pu}}$. The intensity I_{pump} varies at two different time scales. Assuming that the modulation is slow compared to optical frequencies, the nanoparticle can be considered as continuously absorbing the wave I_{pu} with overall scaling $(1/2)\left(1+\cos\Omega t\right)$. The power absorbed by the nanoparticle located at point $\mathbf{x}_0$ is therefore

$$P_{\text{abs}}(t) = \sigma_{\text{abs}}(\omega_{\text{pu}})I_{\text{pu}} \cdot \frac{1}{2}(1+\cos\Omega t), \tag{9.5}$$

where variation in the field across the absorbing nanoparticle at location $\mathbf{x}_0$ has been neglected. We see that the effect of the modulated pump beam is simply to modulate the power absorbed due to their linear relationship under the given assumptions. In the following, the absorption cross section of the nanoparticle target will be modeled in the long wavelength limit, so that it can be described by its dipole polarizability.

9.3.2 Heating

For simplicity, we will first assume that the nanoparticle heats up and reaches thermal equilibrium with the surrounding medium much faster than the modulation time $2\pi/\Omega$. The system can then be considered to quasistatically oscillate between hot and room temperature states, with the temperature following the steady state heat-diffusion equation. For a spherical particle absorbing power P_{abs}, we assume all of this energy is converted to heat sufficiently quickly to equate the modulated absorbed power with the heat flux leaving the sphere's

surface. With the radius a and isotropic background thermal conductivity $\kappa_b \ll \kappa_{\text{metal}}$, the sphere is heated to the uniform temperature

$$\Delta T_{\text{NP}}(t) \equiv T_{\text{NP}}(t) - T_0 = \frac{P_{\text{abs}}(t)}{4\pi\kappa_b a} \tag{9.6}$$

$$= \langle T_{\text{NP}} \rangle (1 + \cos \Omega t), \tag{9.7}$$

where the average nanoparticle temperature across a modulation cycle is defined by

$$\langle T_{\text{NP}} \rangle = \frac{1}{2} \frac{\sigma_{\text{abs}}(\omega_{\text{pu}}) I_{\text{pu}}}{4\pi\kappa_b a} \tag{9.8}$$

and T_0 is the ambient (room) temperature in the absence of the pump. For other shapes the denominator varies, but the linear scaling with power absorbed is maintained [10], and this analysis proceeds as general.

The thermally static limit evoked above enforces the particle temperature to oscillate with the same time dependence as the heating beam, but the surrounding medium does as well. Specifically, the temperature outside the sphere will follow

$$\Delta T_b(\mathbf{x}, t) \equiv T_b(\mathbf{x}, t) - T_0 = \frac{a}{|\mathbf{x}|} \Delta T_{\text{NP}}(t). \tag{9.9}$$

At the elevated temperatures attainable in experiment, the refractive indices for both medium and metal (both real and imaginary parts) increase linearly with temperature as

$$n(T) = n(T_0) + \left. \frac{dn}{dT} \right|_{T_0} \cdot (T(\mathbf{x}, t) - T_0). \tag{9.10}$$

Therefore, the thermally modulated refractive index profile will inherit the same time dependence as the temperature.

9.3.3 Scattering

To detect this refractive index fluctuation, a probe beam illuminates the sample throughout the heating modulation. The probe is a continuous wave optical laser with field in the focal region described by $\mathbf{E}_{\text{probe}}(t) = \mathbf{E}_{\text{pr}} e^{-i\omega_{\text{pr}} t}$. As with the pump beam, the spatial dependence

of the probe beam profile is implicit in $\mathbf{E}_{\mathrm{pr}}$. This field is scattered by the nanoparticle and surrounding thermal lens at beat frequencies $\omega_{\mathrm{pr}} \pm \Omega$ as the hot and cold system scatter differently. As for the absorption process, we make the long wavelength approximation, allowing us to treat the probe beam scattering off of metal nanoparticle and its surrounding heated region of fluctuating refractive index as sourced by an induced electric dipole $\mathbf{p}(t) = \boldsymbol{\alpha}(T_{\mathrm{NP}}) \cdot \mathbf{E}_{\mathrm{probe}}(t)$, with polarizability defined by the nanoparticle temperature but accounting for polarization of the heated background surrounding the nanoparticle as well. Cichos and coworkers have discussed the limitations of this point dipole model [142, 143, 141], however, it is our aim here only to present the simplest model of the photothermal signal. If the change in all refractive indices is small compared to the room temperature indices, i.e., $(dn/dT|_{T_0})/n \ll 1$, then the polarizability (accounting for the dipole response of both metal and heated background) can be Taylor expanded and truncated at first order as

$$\alpha(T_{\mathrm{NP}}) \approx \alpha_{T_0} + \left.\frac{d\alpha}{dn}\frac{dn}{dT}\right|_{T_0} (T_{\mathrm{NP}}(t) - T_0). \tag{9.11}$$

Note that while the polarizability model is still left unspecified, its linear response inherits time dependence directly from $T_{\mathrm{NP}}(t) - T_0 \propto (1 + \cos \Omega t)/2$.

The scattered field sourced by the induced dipole $\mathbf{p}(t)$ separates into the time-independent and time-dependent contributions

$$\mathbf{E}_{\mathrm{scat}}(\mathbf{x}, t) = [\mathbf{E}_0(\mathbf{x}) + \mathbf{E}_\Omega(\mathbf{x}) \cos \Omega t]\, e^{-i\omega t}. \tag{9.12}$$

The time-independent scattered field can be written in terms of the polarizability components as

$$\begin{aligned} \mathbf{E}_0(\mathbf{x}) &\equiv \mathbf{G}(\mathbf{x}, \mathbf{x}_0) \cdot \boldsymbol{\alpha}_0 \cdot \mathbf{E}_{\mathrm{pr}}(\mathbf{x}_0) \\ &= \mathbf{G}(\mathbf{x}, \mathbf{x}_0) \cdot \left(\boldsymbol{\alpha}_{T_0} + \left.\frac{d\boldsymbol{\alpha}}{dn}\frac{dn}{dT}\right|_{T_0} \langle T_{\mathrm{NP}} \rangle \right) \cdot \mathbf{E}_{\mathrm{pr}}(\mathbf{x}_0), \end{aligned} \tag{9.13}$$

which contains the sum of the room temperature scattering and a static offset resulting from the amplitude modulation of the particle temperature oscillating about some value greater

than room temperature. The time-dependent or fluctuational component of the scatted field reads

$$\begin{aligned}\mathbf{E}_{\Omega}(\mathbf{x},t) &\equiv \mathbf{G}(\mathbf{x},\mathbf{x}_0)\cdot\boldsymbol{\alpha}_{\Omega}(t)\cdot\mathbf{E}_{\mathrm{pr}}(\mathbf{x}_0)\\ &= \mathbf{G}(\mathbf{x},\mathbf{x}_0)\cdot\left(\frac{d\boldsymbol{\alpha}}{dn}\frac{dn}{dT}\bigg|_{T_0}\langle T_{\mathrm{NP}}\rangle\cos\Omega t\right)\cdot\mathbf{E}_{\mathrm{pr}}(\mathbf{x}_0),\end{aligned} \tag{9.14}$$

arising from the temperature-induced variation in the local refractive index. Here $\mathbf{G}(\mathbf{x},\mathbf{x}_0)$ is the standard dipole relay tensor in the far-field limit [80].

Both scattered fields will increase in complexity upon addition of thermal retardation and the resonant scattering, but the separation of the field into static and fluctuating components will remain useful nevertheless. In this case, the contribution of the nanoparticle temperature to the static scattered field will also have interesting consequences on the photothermal signal.

9.3.4 Detection

After frequency filtering the the pump beam out of the detection path, the light focused onto the photodetector can be interpreted as the superposition of the transmitted/reflected probe field and the scattered probe field. This raw (pre-lock-in) photothermal intensity arriving at the detector can be represented by

$$I_{\mathrm{PT}}^{\mathrm{raw}}(\mathbf{x},t) = \frac{cn}{8\pi}\left|\mathbf{E}_{\mathrm{pr}}^{\mathrm{tr/re}}(\mathbf{x}) + \mathbf{E}_{\mathrm{scat}}(\mathbf{x},t)\right|^2 , \tag{9.15}$$

but this is not exactly representative of the experimentally measured photothermal signal. The common experimental setup involves measuring a single voltage reported by a photodiode, which is then fed to the lock-in amplifier to filter out unwanted background. In this case, it is more accurate to consider the integrated intensity profile at the detector to be the raw photothermal signal $P_{\mathrm{PT}}^{\mathrm{raw}}(t) = \int_D I_{\mathrm{PT}}^{\mathrm{raw}}(\mathbf{r}_D,t)dA$ that will be converted to a voltage by the photodiode. We can calculate this integration at the detector by making another simplifying assumption. Given that the scattered fields have already been approximated as electric dipole radiation, we assume that the transmitted/reflected probe field differs negligibly in spatial distribution. With both fields assumed to be dipolar, we employ conservation

of energy to perform the integration on the scattered intensity (before focusing) across a spherical surface spanning a solid angle defined by the collection objective. As discussed in Appendix A.1 in the context of modeling the magnitude of the transmitted/reflected probe field, the spatial form of the intensity is now $I_{\mathrm{PT}}^{\mathrm{raw}}(\mathbf{r}_D) = I_{\mathrm{PT}}^{\mathrm{raw}}(\hat{\mathbf{p}}^2 - (\hat{\mathbf{r}}_D \cdot \hat{\mathbf{p}})^2)/(k_{\mathrm{pr}} r_D)^2$, where $\mathbf{r}_D = r_D \hat{\mathbf{r}}_D \equiv \mathbf{x}_D - \mathbf{x}_0$ is the vector connecting the nanoparticle position to the observation point in the integration domain and the wave vector magnitude for all collected fields is $k_{\mathrm{pr}} = \omega_{\mathrm{pr}} n/c$. Integration over the spatial dependence of the collected intensity simply scales the entire signal as a function of the collection angle θ_{col}. It will therefore be useful to employ the result of the detection integral $P_{\mathrm{PT}}^{\mathrm{raw}}(t) = I_{\mathrm{PT}}^{\mathrm{raw}} f(\theta_{\mathrm{col}})/k_{\mathrm{pr}}^2$, to introduce a scalar notation for the collected fields E_i without their spatial dependence, defined by $\mathbf{E}_i(\mathbf{r}_D) = E_i(\hat{\mathbf{p}} - \hat{\mathbf{r}}_D \hat{\mathbf{r}}_D \cdot \hat{\mathbf{p}}) e^{ik_{\mathrm{pr}} r_D}/(k_{\mathrm{pr}} r_D)$. The functional form of $f(\theta_{\mathrm{col}})$ is derived in Appendix A.1.

A photothermal image produced by this technique is analogous to confocal microscopy, generated by rastering the sample (nanoparticle at point $\mathbf{x}_0$) through the beam path (focused onto point $\mathbf{x}_f$) and recording the photothermal signal as a function of sample position. This procedure is elaborated on in Section 9.6, but the spatial dependence of the rastered image arises implicitly through the spatial profile of the probe beam $\mathbf{E}_{\mathrm{pr}}(\mathbf{x}_0; \mathbf{x}_f)$ in Eqs. (9.13) and (9.14) as well as the pump beam spatial profile hidden for now within the temperature dependent polarizability. In principle the intensity profile of the focused image at the detector $I_{\mathrm{PT}}^{\mathrm{raw}}(\mathbf{r}_D)$ could be recorded directly by replacing the photodiode with a lock-in camera, analogous to a wide-field microscope image. We will leave a detailed treatment of the latter case behind for now and focus on the confocal geometry, but most results presented below are straightforward to translate to widefield measurement.

To model the demodulation of the signal experimentally accomplished with a lock-in amplifier, we integrate the raw photothermal signal arriving at the photodetector against the reference signal $\cos \Omega t$. In the idealized thermally-static limit we have already enforced, any phase difference between the reference and the photothermal signal can be neglected

since all time dependence of the scattered field is proportional to $E_\Omega(t) = E_\Omega \cos \Omega t$. Thus,

$$\begin{aligned} P^{\mathrm{PT}} &\equiv \lim_{\tau\to\infty} \frac{1}{\tau} \int_0^\tau dt\, P_{\mathrm{PT}}^{\mathrm{raw}} \cos(\Omega t) \\ &= \frac{cn}{4\pi} \mathrm{Re}\left[E_{\mathrm{pr}}^{\mathrm{tr}} \cdot E_\Omega^* + E_0 \cdot E_\Omega^*\right] \frac{f(\theta_{\mathrm{col}})}{k^2} \\ &\equiv P_{\mathrm{PI}}^{\mathrm{PT}} + P_{\mathrm{SI}}^{\mathrm{PT}}. \end{aligned} \tag{9.16}$$

The photothermal signal consists of two terms of different physical origin. The first, recognizable from Eq. (9.1), describes the interference between the transmitted/reflected probe field and the modulated component of the scattered field. We will refer to it as the *probe-interference* term, $P_{\mathrm{PI}}^{\mathrm{PT}} \equiv (cn/4\pi)\mathrm{Re}\left[E_{\mathrm{pr}}^{\mathrm{tr}} \cdot E_\Omega^*\right] f(\theta_{\mathrm{col}})/k_{\mathrm{pr}}^2$. The second describes the interference of the static and modulated components of the scattered field, or the *self-interference* of the scattered probe field, $P_{\mathrm{SI}}^{\mathrm{PT}} \equiv (cn/4\pi)\mathrm{Re}\left[E_0 \cdot E_\Omega^*\right] f(\theta_{\mathrm{col}})/k_{\mathrm{pr}}^2$. This self-interference term can be manipulated into a recognizable form by noting the relationship between the scattered fields and the nanoparticle temperature in Eq. (9.7). The total field scattered by the thermal lens at its hottest and coldest temperatures is defined by

$$\begin{aligned} E_{\mathrm{scat}}^H &= E_0 + E_\Omega \\ E_{\mathrm{scat}}^C &= E_0 - E_\Omega. \end{aligned} \tag{9.17}$$

Substitution reveals the self-interference term to be the difference in scattered intensity from the hot and cold systems

$$P_{\mathrm{SI}}^{\mathrm{PT}} = \frac{cn}{8\pi} \left[|E_{\mathrm{scat}}^H|^2 - |E_{\mathrm{scat}}^C|^2\right] \frac{f(\theta_{\mathrm{col}})}{k_{\mathrm{pr}}^2}. \tag{9.18}$$

as posited in Eq. (9.2). Interestingly, the photothermal image derived in the thermally static limit is exactly the sum of Eqs. (9.1) and (9.2). In light of this result together with the past literature, it is natural to ask: are there two separate regimes where each of these two terms are representative of the photothermal signal? We will attempt to answer this and related questions moving forward through rigorous modeling of the various scattering processes that contribute to the observed signal.

9.4 Models and mechanisms of probe scattering

Here we develop a model of photothermal scattering from the heated background medium surrounding the target nanoparticle only. Both thermal retardation and effects of the metal on scattering are neglected for simplicity (but later accounted for in Appendices A.2 and A.3). This approach, along with its deviations from the more accurate theory that follows, will reveal the physical origin of the photothermal signal in various parameter regimes. Following literature precedent, we will examine the dependence of the PTS on the thermo-optical properties of the background medium and compare results to data from Refs. [62, 34]. We will then eliminate these two approximations and assess the impact. In all models, the spatial profile of the temperature-induced refractive index perturbation in the background medium is averaged over. Therefore, some aspects of the thermal lensing discussed in Refs. [143, 142, 141] are not captured. Nevertheless, what the point-dipole model loses in quantitative accuracy of the spatial distribution of scattered light is made up for in the transparency of the role of its parameters.

9.4.1 Background ball model

Before moving forward with a model of the scattering process that accounts for both the target nanoparticle and surrounding thermal lens, we will first follow the literature precedent and proceed under the assumption that the nanoparticle can be neglected from the scattering process and serves only as a heater to generate the thermal lens. The photothermal signal is therefore created by scattering only from the heated region of background material surrounding the nanoparticle, typically glycerol. We will first model the scattering polarizability as an isotropic sphere of heated background medium immersed in an infinite room temperature thermal background, and refer to this scenario as the *background ball* model. Since the polarizability is the same in all three space directions, it reduces to the scalar polarizability α.

The sphere of heated background material has no room temperature polarizability, but

does respond linearly to temperature increases. Accounting for optical retardation effects as discussed in Appendix A.3, the polarizability varies with temperature according to

$$\left.\frac{d\alpha}{dn}\right|_{T_0} = \frac{2}{3}b^3\frac{1}{n_b(2q_s-1)^2}, \tag{9.19}$$

defined by the wavelength-dependent retardation factor $q_s = (1/3)[1-(kb)^2 - i(2/3)(kb)^3]$, the wave vector magnitude $k = \omega_{\rm pr}n_b/c$, the ball radius b, and the background index at room temperature n_b. To define the temperature of this heated background ball, we assign it the volume averaged temperature of the thermal lens. Carrying out the volume integral of Eq. 9.9, the average temperature of this ball is related to the nanoparticle temperature by

$$\Delta T_{\rm gly} = \frac{3}{2}\frac{f^2-1}{f^3-1}\Delta T_{\rm NP}, \tag{9.20}$$

where $f = (a/b)^3$ is the volume ratio of the metal absorber to the background-ball. The background-ball radius is set equal to the cross-sectional radius of the probe focal spot to represent the optically active region of heated background.

The scattered field can now be constructed from this heated background ball. Remembering that the spatial dependence of the dipole field has already been integrated out, dipole relay tensor post integration is defined by $G(\mathbf{x}_D,\mathbf{x}_0) = G(\mathbf{1}-\hat{\mathbf{r}}_D\hat{\mathbf{r}}_D)e^{ik_{\rm pr}r_D}/(k_{\rm pr}r_D)$ and therefore $G = k_{\rm pr}^3$. The fluctuating scattered field takes the form

$$\begin{aligned} E_\Omega &= G\cdot\left(\frac{d\alpha}{dn}\frac{dn}{dT_{\rm NP}}\bigg|_{T_0}\langle T_{\rm NP}\rangle\right)\cdot E_{\rm pr}(\mathbf{x}_0) \\ &= \left(\frac{\omega_{\rm pr}n_b}{c}\right)^3\cdot\left(\frac{2}{3}b^3\frac{1}{n_b(2q_s-1)^2}\frac{3}{2}\frac{f^2-1}{f^3-1}\left.\frac{dn_b}{dT}\right|_{T_0}\langle T_{\rm NP}\rangle\right)\cdot\frac{4}{w_{\rm pr}}\sqrt{\frac{P_{\rm pr}}{cn_b}}\,. \end{aligned} \tag{9.21}$$

The probe field magnitude in the focal spot is defined assuming the nanoparticle lies at the focus of a Gaussian beam with waist $w_{\rm pr}$ determined by the numerical aperture of the illumination objective $\mathrm{NA}_{\rm ill}$ (see Section A.4).

Before sorting terms in Eq. (9.21), it is instructional to note the source of different physical factors. Specifically, we will analyze the dependence of the PTS on the background refractive index. In past work the refractive index dependence of this expression has been

assumed to follow $n(\frac{dn}{dT}|_{T_0})$, which would arise by taking the factor of n^2 out of G and combining with the polarizability. Here we find that if the incident probe field is defined by the laser power, it should also have background dependence. In addition, the time-averaged nanoparticle temperature

$$\langle T_{\mathrm{NP}} \rangle = \frac{1}{2} \frac{I_{\mathrm{pu}}}{4\pi\kappa_b a} 4\pi \frac{\omega_{\mathrm{pu}} n_b}{c} \mathrm{Im}\left[\alpha^{\mathrm{metal}}_{\mathrm{sphere}}(\omega_{\mathrm{pu}})\right] \tag{9.22}$$

contains background dependence both explicitly from the a factor of the wave vector magnitude $k = \omega n_b/c$ that comes with the definition of the absorption cross section and implicitly in the polarizability. Assuming the pump intensity is also defined by the beam power, it should not have n dependence as the prefactor will cancel with $n_b^{-1/2}$ dependence of the pump field (see Appendix A.4).

Separating the geometry- and frequency-dependence from the thermo-optical properties of the background (outside the absorbing polarizability),

$$E_\Omega(d) = K_\Omega(\omega_i, a, b) L_\Omega(P_i, w_i) M(n, \frac{dn}{dT}, \kappa) \mathrm{Im}\left[\alpha^{\mathrm{metal}}_{\mathrm{sphere}}(\omega_{\mathrm{pu}})\right], \tag{9.23}$$

where the spectral and geometric parameters are contained within the retardation index $K_\Omega(\omega_i, a, b)$, the pump/probe power and focal waist are contained within the laser index $L_\Omega(P_i, w_i)$, and the thermo-optical properties of the background medium are contained within the material index $M_{\mathrm{PI}}(n, \frac{dn}{dT}, \kappa)$ that we will find is inherited by the probe-interference. Explicitly,

$$K_\Omega(\omega_i, a, b) = \left(\frac{b^3}{a} \frac{1}{(2q_s - 1)^2} \frac{f^2 - 1}{f^3 - 1} \frac{\omega_{\mathrm{pr}}^3 \omega_{\mathrm{pu}}}{c^4}\right) \tag{9.24}$$

$$L_\Omega(P_i, w_i) = 4\sqrt{\frac{\pi}{c}} \sqrt{\frac{P_{\mathrm{pr}}}{\pi w_{\mathrm{pr}}^2}} \frac{P_{\mathrm{pu}}}{\pi w_{\mathrm{pu}}^2} \tag{9.25}$$

$$M_{\mathrm{PI}}(n, \frac{dn}{dT}, \kappa) = \left(\frac{n_b^{5/2}}{\kappa_b} \left.\frac{dn_b}{dT}\right|_{T_0}\right). \tag{9.26}$$

Combing this expression for the modulated scattered field with a model for the transmitted probe field discussed in Eq. (A.7), we can write the probe-interference component of

the locked-in photothermal signal defined by $P_{\mathrm{PI}}^{\mathrm{PT}} \equiv (cn_b/4\pi)\mathrm{Re}\left[E_{\mathrm{pr}}^{\mathrm{tr}} \cdot E_{\Omega}^{*}\right] f(\theta_{\mathrm{col}})/k_{\mathrm{pr}}^2$ as,

$$P_{\mathrm{PI}}^{\mathrm{PT}} = \mathrm{Re}[K_{\mathrm{PI}}(\omega_i, a, b)]L_{\mathrm{PI}}(P_i, w_i)M_{\mathrm{PI}}(n, \frac{dn}{dT}, \kappa)\mathrm{Im}\left[\alpha_{\mathrm{sphere}}^{\mathrm{metal}}(\omega_{\mathrm{pu}})\right] \ , \tag{9.27}$$

with modified retardation and laser indices

$$K_{\mathrm{PI}}(\omega_i, a, b) = K_{\Omega}(\omega_i, a, b)\frac{c}{\omega_{\mathrm{pr}}} \tag{9.28}$$

$$L_{\mathrm{PI}}(P_i, w_i) = \sqrt{\frac{3P_{\mathrm{pr}}}{cf(\theta_{\mathrm{col}})}}L_{\Omega}(P_i, w_i)f(\theta_{\mathrm{col}}) = \sqrt{3f(\theta_{\mathrm{col}})}\frac{P_{\mathrm{pr}}}{\pi w_{\mathrm{pr}}}\frac{P_{\mathrm{pu}}}{\pi w_{\mathrm{pu}}^2} \tag{9.29}$$

where $\theta_{\mathrm{col}} = \sin^{-1}(\mathrm{NA}_{\mathrm{col}}/n_b)$. It is now clear how the photothermal signal varies with background medium, assuming that the probe-interference term dominates and the change in absorption cross section with background is negligible. The accuracy of this assumption is tested in Fig. 9.3 by plotting the linear trend in $P_{\mathrm{PI}}^{\mathrm{PT}}$ with M_{PI} against experimental data from Refs. [62, 34] as well as the more accurate model developed below. For the $a = 10$ nm particles investigated in those studies and the appropriate experimental parameters, the self-interference term is completely negligible. Despite good agreement between this simple linear model and the data, the data presents some variation away from the linear trend. Some of this can be accounted for by acknowledging change in the absorption cross section with background medium not captured in M_{PI}, and more so by adding the effects of thermal retardation and metal scattering to the model as we will discuss in the following section.

For all calculations presented here, the absorbing metal polarizability has been taken to be the exact dipolar Mie polarizability (See SI Section I). The main effect of changing the refractive index on the absorbing polarizability is to red-shift the resonance with increasing n_b. This would affect the PTS if the resonance shifts onto or off of resonance with background medium change. We consider pump wavelengths near the interband transitions to avoid this effect.

In the context of this background-ball model it is especially convenient to compare the probe- and self-interference terms, pointing to why the self-interference is negligible in the Fig. 9.3 example. In this case the static and fluctuational scattered fields are equivalent

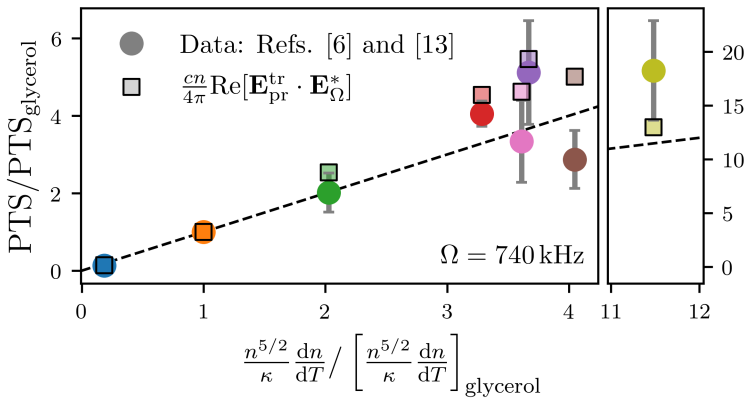

Figure 9.3: Analytical model accounting for thermal-retardation and metal scattering qualitatively predicts experimentally observed trend in PTS with background medium. The model and data are plotted against the background material thermo-optical properties as they appear in the thermally-static model neglecting metal scattering (M_{PI}, see Eq. (9.26)). The model contains no free parameters, but both model and data are normalized to their values in glycerol. The data is from Refs. [62] and [34] (experiment performed in reflection geometry). The photothermal signal from $a = 10$ gold nanoparticles generally increases with the background material index (x-axis). Deviations of the model from the line of slope 1 (dashed black) are primarily caused by changes in the absorption cross section with n_b, and the effect of the glass substrate on the absorption and scattering steps. Better agreement between model and data would require a quantitative model of (1) the reflection coefficient determining the reflected probe field magnitude and (2) the effect of the glass as a heat sink in the heat diffusion step of the model. Preliminary evidence for these pieces of the physics leading to the nonlinear shape of the data is described in SI Section **III**. Parameters used for calculation are as reported is Ref. [62], with pump wavelength $\lambda_{\mathrm{pu}} = 514$ nm, pump power $P_{\mathrm{pu}} = 270$ μW, probe wavelength $\lambda_{\mathrm{pr}} = 800$ nm, probe power $P_{\mathrm{pr}} = 23$ mW, $\mathrm{NA}_{\mathrm{ill}} = \mathrm{NA}_{\mathrm{col}} = 1.4$, $\Omega = 740$ kHz.

except for an overall $\cos\Omega t$, therefore $E_\Omega = E_0$. The self-interference is proportional to the complex magnitude squared of the field in Eq. (9.21),

$$P_{\mathrm{SI}}^{\mathrm{PT}} = |K_{\mathrm{PI}}(\omega_i, a, b)|^2 L_{\mathrm{SI}}(P_i, w_i) M_{\mathrm{SI}}(n, \frac{dn}{dT}, \kappa) \mathrm{Im}\left[\alpha_{\mathrm{sphere}}^{\mathrm{metal}}(\omega_{\mathrm{pu}})\right]^2 \ , \tag{9.30}$$

which again separates into retardation, laser, and material indices. The probe-interference retardation index shows up again here but squared, while the self-interference laser and material indices are

$$L_{\mathrm{SI}}(P_i, w_i) = 4 f(\theta_{\mathrm{col}}) \frac{P_{\mathrm{pr}}}{\pi w_{\mathrm{pr}}^2} \left(\frac{P_{\mathrm{pu}}}{\pi w_{\mathrm{pu}}^2}\right)^2 \ , \tag{9.31}$$

$$M_{\mathrm{SI}}(n, \frac{dn}{dT}, \kappa) = \left(\frac{n_b^2}{\kappa_b} \left.\frac{dn_b}{dT}\right|_{T_0}\right)^2 . \tag{9.32}$$

Both probe- and self-interference terms scale linearly with the probe power, but the self-interference scales quadratically with the pump power. This means that in absence of experimental constrains (like detection limits at low power and nanoparticle melting at high power), the relative contribution of $P_{\mathrm{PI}}^{\mathrm{PT}}$ and $P_{\mathrm{SI}}^{\mathrm{PT}}$ could be tuned by the pump power. Alternatively, we can interpret the different pump power dependence of the probe- and self-interference as linear vs. quadratic scaling with the average nanoparticle temperature $\langle T_{\mathrm{NP}} \rangle$. The self interference also scales differently with the background thermo-optical properties, therefore the self-interference will increase in relative contribution for background media with larger refractive optical constants and smaller thermal constants.

Another apparent difference between probe- and self-interference terms is their dependence on the numerical aperture of the illumination and collection objectives. In the reflection setup, there is only one objective, but in the transmission setup $\mathrm{NA}_{\mathrm{ill}}$ and $\mathrm{NA}_{\mathrm{col}}$ can be different. In the model presented, the illumination objective determines the beam waist of the probe and pump beams. For sake of example, we assume here the near diffraction limited resolution $\mathrm{FWHM}_i = 0.61(\lambda_i/\mathrm{NA}_{\mathrm{illu}})$. The Gaussian beam width is related to the FWHM by $w_i = \mathrm{FWHM}_i/\sqrt{2\ln 2}$, which in terms of the wavelength and numerical aperture is

$$w_i = 0.52 \frac{\lambda_i}{\mathrm{NA}_{\mathrm{illu}}}, \tag{9.33}$$

for i being the pump or probe. The effect of the collection objective is visible in the influence of θ_{col} within Eqs. (9.29) and (9.31). The difference between the two results because the magnitude of the transmitted/reflected probe beam picks up its own dependence on θ_{col} when defined by the total transmitted/reflected power.

One last difference of note between the probe- and self-interference is that the probe field is linear in the reflection (r)/transmission (t) coefficient of the experimental geometry. If reflection is dominated by the glass/background interface inside the sample, then the reflection coefficient r is 0.02 to 0.2 times t. Therefore when switching from the transmission to the reflection geometry of the experiment, the probe-interference will decrease by 1-2 orders of magnitude relative to the self-interference term.

9.4.2 Thermal retardation

Although the derivation is somewhat more involved, it adds little complexity to the final result to include the full time dependence of the heat diffusion equation describing the time-dynamics of the the induced thermal field. We will leave the details to Section A.2 and discuss the implications here. The solution to the steady-state heat diffusion equation in Eq. (9.9) is replaced with the solution to the time-dependent heat diffusion equation around a sphere of oscillating heat source density. This generalization accounts for the finite speed of heat diffusion through the background medium, or in our context the finite modulation frequency that characterizes the system's time dependence. The resulting temperature distribution around the spherical particle in Eq. (A.11) can be averaged across the probe beam focal spot just as before to define an effective temperature of the optically active region of heated background.

The main difference from the thermally static theory presented above is that the temperature, and therefore the time-dependent scattered field, is no longer proportional to $\cos \Omega t$. Instead the temperature describes the superposition of four different thermal waves propagating away from the nanoparticle. All of them have the same frequency Ω and propagate through to the pre-lock-in photothermal signal, but only one is in phase with the heat source

$\propto \cos\Omega t$. The lock-in now plays the additional role of selecting a single phase component from the modulated signal. We therefore generalize the post-lock-in photothermal signal to $P^{\mathrm{PT}}(\phi) \equiv \lim_{\tau\to\infty} \frac{1}{\tau}\int_0^\tau dt\, I_{\mathrm{PT}}^{\mathrm{raw}}(t)\cos(\Omega t - \phi)$ which contains a tunable phase. In reality, the experimental setup may introduce unwanted phase delays along various beam paths and by electronic components. The phase is therefore selected to maximize the signal-to-noise, which we also do for all calculations herein.

One complexity worth noting from the introduction of thermal retardation is that the connection between the self-interference term and the difference in static hot and room-temperature images described in Eq. (9.18) is lost. But in all calculations performed here, despite using the thermally-retarded solutions, we did not find results qualitatively different from the thermally static limit. This can justified by the large modulation frequency (or all time variation slow) but an simple quantifier of this regime change is the thermal radius $r_{\mathrm{th}} = \sqrt{\frac{2\kappa}{C_p\Omega}}$, which characterizes the length scale of thermal diffusion away from out nanoheater in terms of previously defined parameters and the background thermal conductivity per volume C_p. If the thermal radius approaches the optically active volume of heated background (or probe beam radius w_{pr}), than the effects of thermal retardation will be nonnegligible [10]. But for the modulation frequency used in Figs. 9.4-9.7, $\Omega = 100$ kHz, and $r_{\mathrm{th}} \approx 1499$ nm in glycerol and 1237 nm in pentane, so $r_{\mathrm{th}} \gg b$.

9.4.3 Metal scattering

As the target nanoparticle size increases beyond $a \sim 20$ nm, the metal becomes a larger fraction of the optically active volume. Even with the metal's $\frac{dn_c}{dT}$ off resonance it can be comparable to the background medium and it is clear that the metal could affect the probe scattering and resulting photothermal signal. Again leaving a detailed discussion to Appendix A.3, scattering of the heated metal nanoparticle and surrounding background can be described analytically by the polarizability of a spherical core-shell system. Expanding this polarizability to first order in the temperature of the nanoparticle and temperature of the local background (treated again as a volume average over the spatial temperature

distribution) results in

$$\alpha_{\rm cs}(T) = \alpha(T_0) + \frac{d\alpha}{dn_c}\frac{dn_c}{dT}\Delta T_{\rm core} + \frac{d\alpha}{dn_s}\frac{dn_s}{dT}\langle \Delta T(r,t)\rangle_{V_{\rm shell}}. \tag{9.34}$$

The room temperature polarizability $\alpha(T_0)$ is that of the metal absorber. The linear terms describe the change in polarizability with the complex refractive index of the metal core n_c as well as the refractive index of the heated background shell n_s. The expansion coefficients $d\alpha/dn_c$ and $d\alpha/dn_s$ are written explicitly in Section A.3 for both the electrostatic (Eqs. (A.25), (A.26), and (A.27)) and retardation corrected (Eqs. (A.29), (A.30), and (A.31)) regimes. The nanoparticle temperature can be defined as before in either the thermally static or retarded limits, by evaluating the temperature distribution outside the particle at the sphere surface. With these expansion coefficients defined, the full photothermal signal can be developed following the same procedure as for the background-ball model in the previous section. This with the thermal retardation correction is the model used for calculations in all figures.

The main effect of the metal scattering is that the plasmon resonance affects the probe scattering in a way that is non-trivially related to the particle's room temperature cross section. Fig. 9.4 demonstrates the evolution of the trend in PTS with background medium as the particle size is increased. Different from Fig. 9.3, the thermally retarded equivalent of the material index is used, replacing κ with C_p. This is analogous to the photothermal strength coined in past publications with additional factors of n_b we believe to be correct. In the top left panel, a slightly larger sphere of radius $a = 20$ nm shows no variation in PTS trend with background between two example probe wavelengths. This may be expected from looking at the scattering cross sections (top right) in glycerol and pentane, which sees the strongest PTS enhancement of the given backgrounds. In either case, the two chosen probe wavelengths (dashed-gray) are off-resonance. But for a much larger sphere of radius $a = 75$ (lower row, Fig. 9.4) where the scattering peak overlaps both $\lambda_{\rm pr}$, the photothermal signal trend with background increases by approximately a factor of two. This effect is difficult to understand looking at just the room temperature cross sections as an indicator of

increased metal scattering with sphere size. Especially looking at the $a = 75$ in pentane, the scattering cross sections provide only confusion. At $\lambda_{\text{pr}} = 633$ nm, the metal scatters more in pentane than glycerol, but at $\lambda_{\text{pr}} = 785$ nm the particle scatters more in glycerol than pentane, despite the particle in pentane generating near 18 times the photothermal signal. The photothermal signal clearly depends on the metal's resonance in a non-trivial way.

9.5 The photothermal resonance

The simple structure of the model presents a clear path to understand resonance effects, even without analyzing the complicated mathematical form of the polarizability expansion factors and the effective temperatures. The core-shell polarizability alters the static and modulated polarizabilities α_0 and α_Ω defined in Eqs. (9.13) and (9.14). First, the metal scattering at room temperature contributes directly to the time independent polarizability α_0 through $\alpha(T_0)$ and will increase with particle size. The static scattered field E_0 and fluctuational scattered field E_Ω are therefore no longer equal, and the self interference term will clearly grow in significance with α_0. But even in the $a = 20$ nm case discussed above where the self-interference was completely negligible, resonance effects can be seen. Fig. 9.5 demonstrates this by plotting the PTS as a function of probe wavelength in both glycerol (left) and pentane (right). Clearly the probe-interference (red) term dominates the total signal (black). A small sigmoid shape is observed in the PTS near $\lambda_{\text{pr}} \approx 550$ nm, where the scattering resonance appears in Fig. 9.4, top right panel. The resonance lineshape in the PTS is small in the sense that its range is comparable to the variation in the PTS at longer wavelengths, where Rayleigh scattering of the background dominates and $I_{\text{PT}} \propto \lambda_{\text{pr}}^{-2}$. Looking at the two probe wavelengths investigated above (dashed-gray), the PTS has returned to Rayleigh behavior in both glycerol (Fig. 9.5, left) and pentane (Fig. 9.5, right) and shows no effect of the metal. This is consistent with the lack of λ_{pr} dependence in the PTS trend with background plotted in Fig. 9.4.

The probe-interference depends only on E_Ω, which excludes the metal's room temperature scattering, as one may hope to do when employing the photothermal measurement

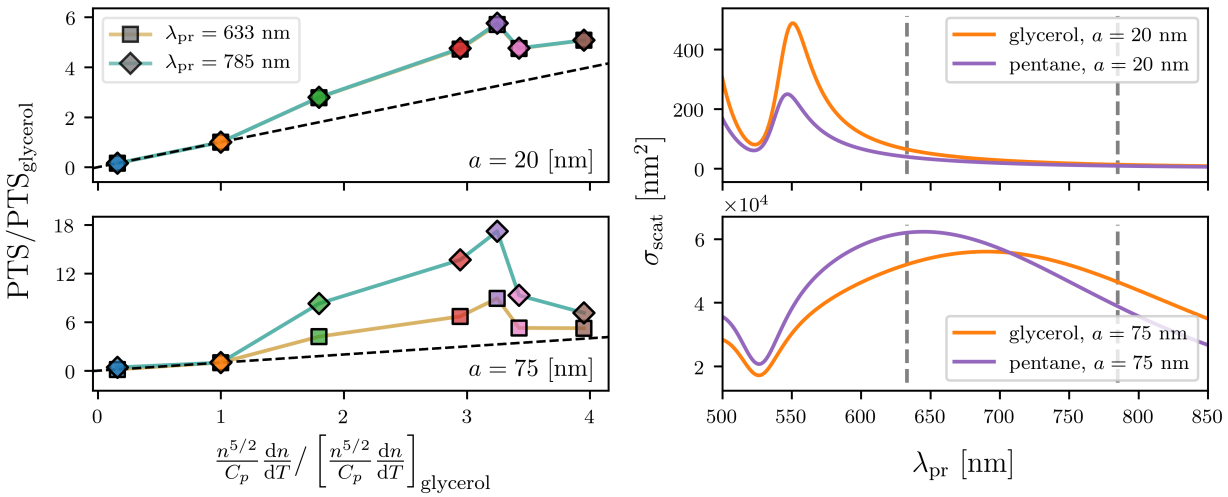

Figure 9.4: Photothermal signal trend with background medium (left) changes with probe wavelength for bigger particles (bottom), but not for smaller particles (top). This effect is not explainable by simply looking at the room temperature nanoparticle scattering on the glass substrate (right). The two probe wavelengths chosen (633 and 785 nm) are overlaid on the scattering cross sections (vertical dashed-gray lines). Despite the photothermal signal increasing ~ 18 times moving from glycerol to pentane at $\lambda_{pr} = 785$ nm, the metal scattering decreases. Meanwhile the metal scattering does increase at $\lambda_{pr} = 633$ nm, but the PTS increase is similar to that of the smaller $a = 20$ nm spheres. Parameters used for calculation were chosen for experiments to be performed by Stephan Link and coworkers, with pump wavelength $\lambda_{pu} = 532$ nm, pump power $P_{pu} = 25$ μW, probe power $P_{pr} = 250$ μW, $NA_{ill} = 1.4$, $NA_{col} = 0.7$, and $\Omega = 100$ kHz.

in practice. The effect of the metal on the signal is therefore through the linear expansion coefficients $d\alpha/dn_c$ and $d\alpha/dn_s$, which will have static and time-dependent pieces, as in the background-ball case. It is intuitive that the change in polarizability with core index, $d\alpha/dn_c$, would be resonance dependent. Surprisingly, we find that the metal resonance also invades the shell term $d\alpha/dn_s$, and even dominates the signal. This is consistent with the literature precedent that the primary source of the photothermal signal is the region of heated background medium surrounding the nanoparticle, but that does not mean the metal resonance can always be neglected. Looking at the forms of $d\alpha/dn_s$ it is clear that the resonance denominator shows up in both the electrostatic (Eq. (A.26)) and electrodynamic (Eq. (A.26)) limits.

We can examine the role of the resonance in more detail by looking the real and the imaginary components of α_0 and α_Ω plotted in the lower half of Fig. 9.5. In this probe-interference dominated system, really only $\mathrm{Re}[\alpha_\Omega]$ (dark purple) impacts the signal (because $E_{\mathrm{pr}}^{\mathrm{tr}}$ is considered real). The shape of the resonance in the probe-interference and total PTS in this case is therefore set by the shape of $\mathrm{Re}[\alpha_\Omega(\lambda_{\mathrm{pr}})]$. This polarizability does not look like, and is even an order of magnitude smaller in glycerol than the static polarizability, which looks qualitatively like the bare particle polarizability but red-shifted due to the static component of the glycerol modulation. This qualitative difference between the room temperature metal resonance and that which appears in the photothermal signal becomes much more significant as the sphere size increases.

Larger particles scatter more. As one might expect, the contribution of the metal resonance to the probe-interference becomes increasingly significant as the nanoparticle size increases. Fig. 9.6 extends the analysis in Fig. 9.5 to the larger particles of radius $a = 75$ nm. The sigmoidal resonance in the smaller particle PTS has red-shifted and dropped below zero before returning to a broad positive peak and then falling as $\lambda_{\mathrm{pr}}^{-2}$. The negative peak again aligns with the typical looking peak in $\mathrm{Im}[\alpha_0]$, but clearly matches the shape of the $\mathrm{Re}[\alpha_\Omega]$, which governs the non-Rayleigh shape of the probe-interference.

It is this relatively narrow negative feature that is responsible for the λ_{pr} dependence of

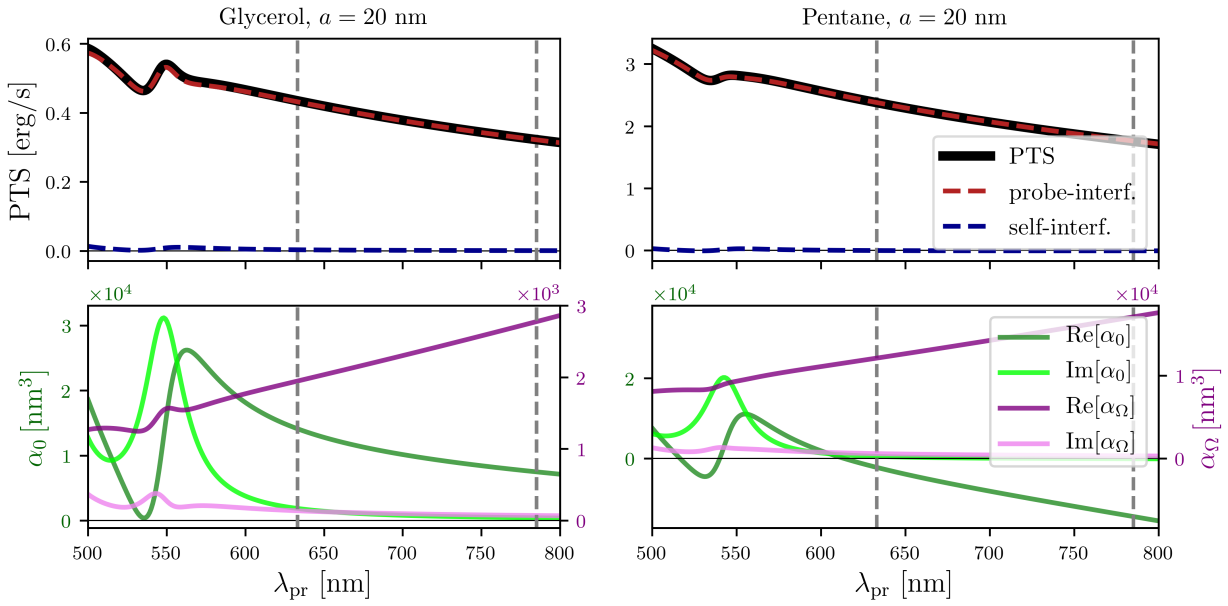

Figure 9.5: Photothermal signal (top) for smaller $a = 20$ nm particles shows minimal resonance effect in glycerol (left) and pentane (right), with only trivial dependence on the probe wavelength, $\propto 1/\lambda_{pr}^2$ (see Eq. (9.24)) at the two off-resonant λ_{pr}'s considered in Fig. 9.4 (dashed-gray). A small resonance effect in the PTS can seen near peak in Im[α_0] (light green), the static polarizability, but the shape of the PTS resonance is very similar to Re[α_Ω], the fluctuating polarizability. This is expected, considering the PTS is dominated by the probe-interference term (red), which is proportional to Re[α_Ω]. Parameters used for calculation are the same as those for Fig. 9.5.

the PTS trend with background visualized in Fig. 9.4. Moving from glycerol to pentane, the negative peak in PTS shifts onto the $\lambda_{\mathrm{pr}} = 785$ nm line (dashed-gray), drastically boosting the signal upon background change. Comparing this to the $\lambda_{\mathrm{pr}} = 785$ nm line, the signal is negligible and surprisingly flat. Resonance shifting with background will therefore have little effect in this photothermally transparent region where the blue half of the room temperature resonance occurs.

The larger particle also generates non-negligible self-interference (dashed-blue) due to the increased room temperature scattering contribution to α_0. In considering the y-axis range on the lower panels of Figs. 9.5 and 9.6, the ratio of $|\alpha_0|/|\alpha_\Omega|$ has increased by an order of magnitude from small to larger spheres. The self-interference appears as a typical peak, falling to zero off resonance. The peak is also redshifted from even the $\mathrm{Im}[\alpha_0]$ peak, instead coinciding with the peak in $\mathrm{Im}[\alpha_0]$, or more accurately, the product $\mathrm{Im}[\alpha_0] \cdot \mathrm{Im}[\alpha_\Omega]$. By definition of the self-interference, $P_{\mathrm{PI}}^{\mathrm{PT}} \propto k^4(\mathrm{Re}[\alpha_0] \cdot \mathrm{Re}[\alpha_\Omega] + \mathrm{Im}[\alpha_0] \cdot \mathrm{Im}[\alpha_\Omega])$, but due to the shape of the factor of $k^4 \propto \lambda_{\mathrm{pr}}$ damps the product of real components by nature of their shape.

The metal resonance also disrupts the simple trend with pump power dependence predicted by the thermally static theory above. There it seemed that P_{pu} would modulate between significance of the probe- and self-interference contributions to the PTS. The pump power dependence of the photothermal signal is explored in Fig. 9.7. Increasing pump power to $P_{\mathrm{pu}} = 100$ μW (top row) and then $P_{\mathrm{pu}} = 600$ μW (bottom row), we note that the self-interference does not simply increase with P_{pu}. Instead, the self-interference (dashed-blue) decreases and swings negative before finally increasing in magnitude as expected from the simple background-ball model. This effect follows $\mathrm{Im}[\alpha_0]$, which is overlaid in light green with range given by the right axis. The imaginary part of the static polarizability becomes negative with increasing P_{pu}, starting with its red side, and therefore flips the sign of $P_{\mathrm{SI}}^{\mathrm{PT}}$.

This can be explained by noting the balance between the room temperature metal scattering and the static offset contributed by the background perturbation in Eq. (A.16). The metal perturbation term is negligible, so we need only consider the balance of the room

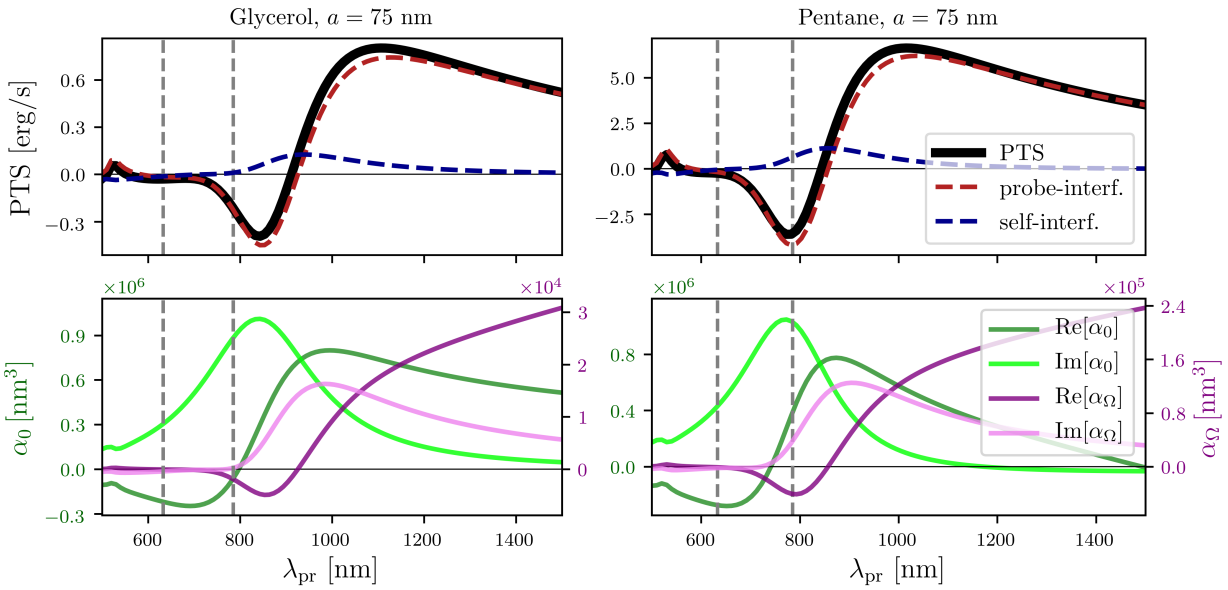

Figure 9.6: Photothermal signal (top) for larger $a = 75$ nm particles shows significant resonance effect with surprisingly narrow features that shift from glycerol (left) and pentane (right). The negative peak shifts onto the $\lambda_{pr} = 785$ nm probe in pentane, explaining the large increase in signal seen in Fig. 9.4. The self-interference term arises as a simple peak at longer wavelength then the scattering resonance. This is due to the increased magnitude of $\alpha_0 \sim 10^6$ compared to the smaller particles in Fig. 9.5, consistent with the room temperature polarizability increasing with particle size. The shape of the self-interference appears to follow the product of Im[α_Ω] (light purple) and Im[α_Ω], which follows from the definition of P_{SI}^{PT}.

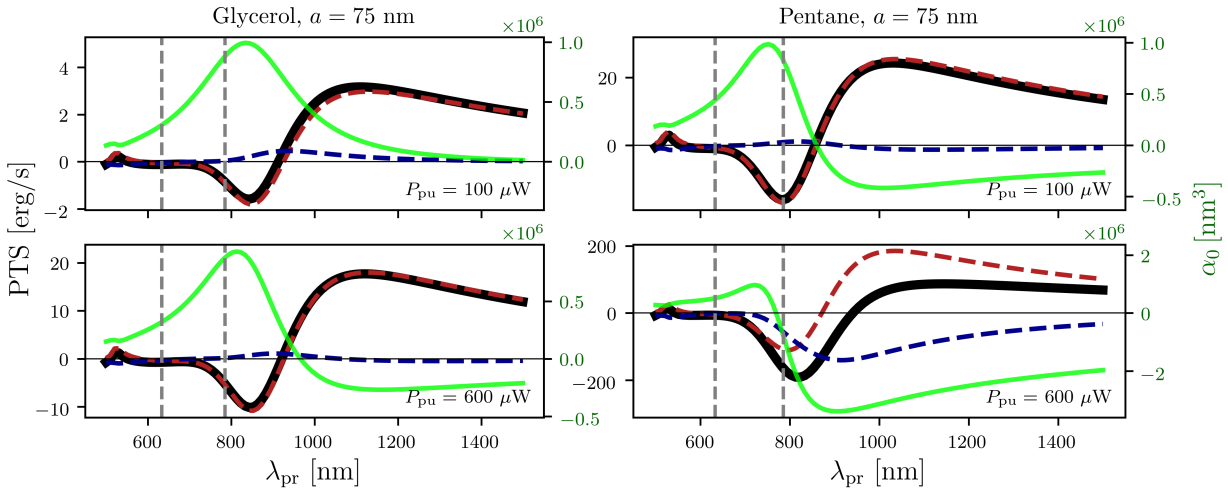

Figure 9.7: With thermal retardation, increasing pump power does not simply increase self-interference. The self-interference first decreases, and then starts increasing in magnitude only after becoming negative. This is effect is entirely governed by the the imaginary component of the static polarizability $\mathrm{Im}[\alpha_0]$ (light green, right axis). The room temperature scattering dominates the self-interference at low pump powers and happens to contribute positively. As the pump power increases, the heated background dominates the self-interference, which happens to flip sign because the change in background index with temperature is negative.

temperature polarizability of the metal $\alpha(T_0)$ and the static offset of the background fluctuations $\propto (d\alpha/dn_s)(dn_s/dT)P_{\text{abs}}$. At low pump power, the first term will dominate, and we know that $\text{Im}[\alpha(T_0)] > 0$. The background term is negligible at low pump power, where P_{abs} is small but negative because of $dn_s/dT < 0$ for all the liquid background media considered here. As the pump power, temperature, and then P_{abs} increase, the negative $d\alpha/dn_s$ term dominates the self-interference. After going negative, the self-interference grows in magnitude with P_{pu} as predicted in absence of the metal scattering.

The self-interference crosses zero at different pump powers for different background media. For the radius $a = 75$ nm sphere in glycerol (Fig. 9.7, left column), $P_{\text{SI}}^{\text{PT}}$ just crosses zero at $P_{\text{pu}} = 600$ μW, but this occurs near $P_{\text{pu}} = 100$ μW in pentane (Fig. 9.7, right column). This can be attributed to the photothermal strength of pentane being significantly larger than glycerol. The background contribution to α_0 therefore overtakes the metal contribution at lower pump power.

With all of these considerations, it is clear some of the intuition established with the simple background-ball model carries into the thermally and optically retarded regimes, as well as to larger particles with some modifications. In most parameters regimes explored here, the probe-interference dominated the total PTS. The influence of the metal on the photothermal signal, within both the probe- and self-interference terms, does not affect the signal until the particle is about 20 nm in radius. At this point, the resonance appears in the PTS as a function of probe wavelength as a sigmoid shape in the probe-interference. With increasing particle size and scattering cross section, the sigmoid drops the total signal to zero, eventually creating a photothermally-transparent window between approximately $\lambda_{\text{pr}} = 550 - 750$ nm (in glycerol). The peak emerging (here negative for chosen phase) blue of the transparent window is much narrower than the particle's scattering peak, and the signal is therefore sensitive to spectral shifts in the resonance (with consequences observed in Fig. 9.4 when changing background medium). It is also clear that for certain choices of the probe wavelength, the self-interference dominates the signal. This is true for a wider set of λ_{pr} values when the pump power has passed a certain threshold, as demonstrated in Fig.

9.7. It is likely that in other systems, such as particles suspended in a solid [143], that the self-interference term will be more significant at smaller particle sizes.

9.6 The photothermal image

Past literature has paid significant attention to the spatial form of the photothermal image. Although the simple dipole scattering model explored here will fail to capture certain aspects of the thermal lensing, we can compare the spatial form of the probe- and self-interference images to get a qualitative sense for their behavior.

In the typical experimental setup, a photothermal image is formed by rastering the nanoparticle target through the beam path. The image is therefore the PTS at various positions, which we can define as the difference between the nanoparticle location $\mathbf{x}_0$ and the beam focal point $\mathbf{x}_f$ (assuming for simplicity that both beams share the same focal spot). The spatial dependence of the photothermal signal appears explicitly in the pump and probe intensities driving the absorption and scattering, respectively. Although both probe- and self-interference terms are linear in the probe power, the transmitted/reflected probe field accounted for a factor of $\sqrt{P_{\mathrm{pr}}}$ in Eq. (9.29). The probe-interference term

$$P_{\mathrm{PI}}^{\mathrm{PT}}(\mathbf{x}_f - \mathbf{x}_0) \propto \sqrt{I_{\mathrm{pr}}(\mathbf{x}_f - \mathbf{x}_0)} I_{\mathrm{pu}}(\mathbf{x}_f - \mathbf{x}_0) \tag{9.35}$$

therefore has spatial dependence defined by the incident beam intensities in the scattering region. Following Eq. (9.31), the self-interference term is related to the square of the $P_{\mathrm{PI}}^{\mathrm{PT}}$ spatial dependence as

$$P_{\mathrm{SI}}^{\mathrm{PT}}(\mathbf{x}_f - \mathbf{x}_0) \propto I_{\mathrm{pr}}(\mathbf{x}_f - \mathbf{x}_0) I_{\mathrm{pu}}^2(\mathbf{x}_f - \mathbf{x}_0). \tag{9.36}$$

These intensities describe the focal spots of the probe and pump beams.

To qualitatively asses the differences in the contribution of $P_{\mathrm{PI}}^{\mathrm{PT}}$ and $P_{\mathrm{SI}}^{\mathrm{PT}}$ to the image, we will approximate both focal spots as that of a Gaussian beam. Taking the focal plane of both beams to contain the nanoparticle, $z = z_0 = 0$, the spatial form of each beam

($i =$ pump or probe) then reduces from Eq. (A.32) to

$$I_i(r) = 2\frac{P_i}{\pi\omega_i^2}e^{-\frac{2r^2}{{w_i}^2}} \tag{9.37}$$

where $r = \sqrt{x^2+y^2}$ is the radial coordinate in the focal plane and the peak intensity has been related to the experimentally measured beam power with Eq. (A.33). Combining this with the above expressions for the probe- and self-interference terms

$$P_{\mathrm{PI}}^{\mathrm{PT}}(\mathbf{x}_f - \mathbf{x}_0) \propto \sqrt{\frac{2P_{\mathrm{pr}}}{\pi w_{\mathrm{pr}}^2}}\frac{2P_{\mathrm{pu}}}{\pi w_{\mathrm{pu}}^2}e^{-r^2\left(\frac{w_{\mathrm{pu}}^2 w_{\mathrm{pr}}^2}{w_{\mathrm{pu}}^2+2w_{\mathrm{pr}}^2}\right)^{-1}} \tag{9.38}$$

$$P_{\mathrm{SI}}^{\mathrm{PT}}(\mathbf{x}_f - \mathbf{x}_0) \propto \frac{2P_{\mathrm{pr}}}{\pi w_{\mathrm{pr}}^2}\left(\frac{2P_{\mathrm{pu}}}{\pi w_{\mathrm{pu}}^2}\right)^2 e^{-r^2\left(\frac{1}{2}\frac{w_{\mathrm{pu}}^2 w_{\mathrm{pr}}^2}{w_{\mathrm{pu}}^2+2w_{\mathrm{pr}}^2}\right)^{-1}}, \tag{9.39}$$

each term remains Gaussian, but has modified width. Approximating the resolution by the the full width at half max $\mathrm{FWHM} = 2\sqrt{2\ln 2}\sigma$, defined by the standard deviation σ:

$$\mathrm{FWHM}_{\mathrm{PI}} = 2\sqrt{\ln 2}\frac{w_{\mathrm{pu}}w_{\mathrm{pr}}}{\sqrt{w_{\mathrm{pu}}^2+2w_{\mathrm{pr}}^2}} \tag{9.40}$$

$$\mathrm{FWHM}_{\mathrm{SI}} = \frac{1}{\sqrt{2}}\mathrm{FWHM}_{\mathrm{PI}} \tag{9.41}$$

The self-interference term has $\sim 71\%$ the width of the probe-interference term.

This difference in width between probe- and self-interference components of the single particle photothermal image may not be distinguishable in experiment. Especially considering that the two terms will be superimposed, this similarity between the spatial form of $P_{\mathrm{PI}}^{\mathrm{PT}}(\mathbf{x}_f - \mathbf{x}_0)$ and $P_{\mathrm{SI}}^{\mathrm{PT}}(\mathbf{x}_f - \mathbf{x}_0)$ may be the cause of the discrepancies in the published theoretical assumptions underlying the PTS.

9.7 Conclusions

In this chapter, we have shown that previous assumptions behind the source of the photothermal heterodyne image unify into a single theoretical model. The model contains the full complexity of the post-lock-in photothermal image, including signal contributions from interference between thermally induced scattering and the transmitted/reflected probe field

(probe-interference), as well as interference between the thermal scattering and its own stationary offset (self-interference). With the photothermal signal being the sum of these two components, we demonstrated how to increase the model's complexity to increase accuracy while tracing intuition from the simplest form of the model. This approach revealed that probe- and self-interference play different roles in the photothermal spectrum, particularly in probe wavelength. With so many parameters at play, isolating the role of these two terms in a given experiment may be difficult. Differentiating probe- and self-interference is not much simpler in terms of the spatial dependence of the photothermal image, with the self-interference point spread function only $\sim 70\%$ wider than the probe-interference. This may explain the past success of using either term in modeling experiment. With the complexity of the photothermal image elucidated by the presented model, we expect the resonance effects and photothermally-transparent spectral windows attributed to scattering particles to be exploitable for further optimization. Taken together, the understanding presented herein provides a stepping stone to quantitative correlation of the measured PTS and the local temperature, leading towards an all-optical nano-thermometer. Future work will extend this model to aggregates of interacting plasmonic nanoparticles, with the hope of spatially resolving their temperature profiles in experiment.

A.1 Model of probe interference contribution

If we neglect differences in the spatial modulation of the probe and scattered fields, we can approximate the transmitted/reflected probe field in the collection region to have the spatial form of a radiating dipole with effective polarizability or scattering volume V. Using the scalar notation presented in Section 9.3.4 to omit the spatial dependence of the fields that is integrated out at the detector,

$$E_{\mathrm{pr}}^{\mathrm{tr}} \approx G \cdot V \cdot E_{\mathrm{pr}}(\mathbf{x}_0). \tag{A.1}$$

The product of effective scattering volume and the probe field in the focal spot can be parameterized by the experimentally measured probe power. Defining the collection aperture

in the background medium by the polar angle $\theta_{\rm col} = \sin^{-1}({\rm NA}_{\rm col}/n_b)$, the power radiated by an electric dipole oriented perpendicular to the optical axis through the solid angle $(\theta_{\rm col}, 2\pi)$ is

$$P_{\rm scatt}(\theta_{\rm col}) = \int_0^{\theta_{\rm col}} \int_0^{2\pi} r^2 \sin\theta \, d\theta d\phi \, I_{\rm scatt}(r,\theta,\phi) \tag{A.2}$$

$$= \int_0^{\theta_{\rm col}} d\theta r^2 \sin\theta \int_0^{2\pi} d\phi \, \frac{ck_{\rm pr}^4}{3} |\mathbf{p}|^2 \frac{1-\sin^2\theta\cos^2\phi}{r^2} \tag{A.3}$$

$$= \frac{ck_{\rm pr}^4}{3} |\mathbf{p}|^2 f(\theta_{\rm col}). \tag{A.4}$$

The $\theta_{\rm col}$ dependent factor that determines the fraction of total scattered dipole radiation that makes it through the aperture is

$$f(\theta) = \left[\frac{3}{4}(1-\cos\theta) - \frac{1}{2}(2+\cos\theta)\sin^4\frac{\theta}{2} \right] , \tag{A.5}$$

which increases monotonically from 0 to 1/2 for $\theta \in \{0, \pi/2\}$. For a background medium of glycerol and a numerical aperture of ${\rm NA}_{\rm col} = 0.7$, $f(\theta_{\rm col}) = 0.085$.

Equating the scattered power from our effective dipole $|p| = V \cdot |E_{\rm probe}(\mathbf{x}_0)|$ to the experimentally measured probe power yields,

$$V \cdot |E_{\rm probe}(\mathbf{x}_0)| \approx \sqrt{\frac{1}{f(\theta_{\rm col})} \frac{3P_{\rm pr}^{\rm exp}}{ck_{\rm pr}^4}} \, . \tag{A.6}$$

The transmitted probe field in the model then takes the form

$$E_{\rm pr}^{\rm tr} \approx G \cdot \sqrt{\frac{1}{f(\theta_{\rm col})} \frac{3P_{\rm pr}^{\rm exp}}{ck_{\rm pr}^4}} = k_{\rm pr} \sqrt{\frac{1}{f(\theta_{\rm col})} \frac{3P_{\rm pr}^{\rm exp}}{c}} \, , \tag{A.7}$$

where in the last line we have used the fact that in the scalar notation $G = k_{\rm pr}^3$. The $k_{\rm pr}$ (and therefore n_b) dependence of $E_{\rm pr}^{\rm tr}$ does not propagate to the observable, as it will cancel with denominator in the integrated expression $P_{\rm PT}^{\rm raw}(t) = I_{\rm PT}^{\rm raw} f(\theta_{\rm col})/k_{\rm pr}^2$.

A.2 Accounting for thermal retardation in the core and shell temperature

For a sphere of radius a in isotropic background absorbing at a rate,

$$P_{\rm abs}(t) = P_{\rm abs} \frac{1+\cos\Omega t}{2} \tag{A.8}$$

the temperature increase from room is given by solving the time dependent heat diffusion equation outside the sphere with the boundary condition at the surface of the sphere,

$$P_{\text{abs}}\frac{1+\cos\Omega t}{2} = -4\pi\kappa a^2 \left.\frac{\partial T}{\partial r}\right|_{r=a}, \tag{A.9}$$

which equates the heat flow out of the sphere following absorption to the integral of the temperature gradient across the sphere surface. This boundary condition assumes a uniform temperature on the particle, which is accurate for noble metal particles with thermal constants much greater then that of the background and smaller in size then the thermal radius. The solution satisfying this boundary condition as well as the radial heat diffusion equation,

$$r^2\frac{\partial}{\partial t}T - \frac{\kappa}{C_p}\frac{\partial}{\partial r}\left(r^2\frac{\partial}{\partial r}T\right) = 0 \tag{A.10}$$

can be written as

$$\Delta T(r,t) = \frac{P_{\text{abs}}}{4\pi\kappa r}\cdot\frac{1}{2}\left(1+\frac{e^{-\frac{r-a}{r_{\text{th}}}}}{(\frac{r_{\text{th}}+a}{r_{\text{th}}})^2+(\frac{a}{r_{\text{th}}})^2}\left[\frac{r_{\text{th}}+a}{r_{\text{th}}}\cos(\Omega t-\tfrac{r-a}{r_{\text{th}}})+\frac{a}{r_{\text{th}}}\sin(\Omega t-\tfrac{r-a}{r_{\text{th}}})\right]\right) \tag{A.11}$$

where the temperature inside the sphere is defined by $r \to a$ if $r < a$. This spatially varying expression is coarsely approximated by a shell of uniform temperature. To assign an effective temperature, we volume average the temperature over the shell of radius b,

$$\langle\Delta T(r,t)\rangle_{V_{\text{shell}}} = \frac{4\pi}{V_{\text{shell}}}\int_r r^2\Delta T(r,t) \tag{A.12}$$

$$\begin{aligned}= \frac{P_{\text{abs}}}{4\kappa V_{\text{shell}}}\Big[&b^2-a^2+r_{\text{th}}^2\sin(\Omega t)\\ &-\frac{e^{-\frac{b-a}{r_{\text{th}}}}}{(\frac{r_{\text{th}}+a}{r_{\text{th}}})^2+(\frac{a}{r_{\text{th}}})^2}\Big(r_{\text{th}}(b-a)\cos(\Omega t-\tfrac{b-a}{r_{\text{th}}})\\ &+(r_{\text{th}}(b+r_{\text{th}})+a(2b+r_{\text{th}}))\sin(\Omega t-\tfrac{b-a}{r_{\text{th}}})\Big)\Big]\end{aligned} \tag{A.13}$$

Defining this value as the shell temperature $\Delta T_{\text{shell}} = \langle\Delta T(r,t)\rangle_{V_{\text{shell}}}$ and the core temp to be

$$\Delta T_{\text{core}} = \Delta T(r=a,t) = \frac{P_{\text{abs}}}{4\pi\kappa a}\cdot\frac{1}{2}\left(1+\frac{\frac{r_{\text{th}}+a}{r_{\text{th}}}\cos(\Omega t)+\frac{a}{r_{\text{th}}}\sin(\Omega t)}{(\frac{r_{\text{th}}+a}{r_{\text{th}}})^2+(\frac{a}{r_{\text{th}}})^2}\right) \tag{A.14}$$

the core-shell polarizability (to first order in T) can be written generally to first order in temperature fluctuations as

$$\alpha_{\rm cs}(T) = \alpha(T_0) + \frac{d\alpha}{dn_c}\frac{dn_c}{dT}\Delta T_{\rm core} + \frac{d\alpha}{dn_s}\frac{dn_s}{dT}\langle \Delta T(r,t)\rangle_{V_{\rm shell}} \ , \tag{A.15}$$

which we have found agrees with experimental data. Separating the polarizability into static and time varying components, $\alpha_{\rm cs}(t) = \alpha_0 + \alpha_\Omega(t)$, and noting that $V_{\rm shell} = \frac{4\pi}{3}(b^3 - a^3)$, the time independent piece can be written

$$\alpha_0 = \alpha(T_0) + \frac{d\alpha}{dn_c}\frac{dn_c}{dT}\frac{P_{\rm abs}}{8\pi\kappa a} + \frac{d\alpha}{dn_s}\frac{dn_s}{dT}\frac{3P_{\rm abs}}{16\pi\kappa}\frac{b^2-a^2}{b^3-a^3} \tag{A.16}$$

and the time-dependent (fluctuational) polarizability is

$$\begin{aligned}
\alpha_\Omega(t) = {} & \frac{d\alpha}{dn_c}\frac{dn_c}{dT}\frac{P_{\rm abs}}{8\pi\kappa a}\frac{\frac{r_{\rm th}+a}{r_{\rm th}}\cos(\Omega t) + \frac{a}{r_{\rm th}}\sin(\Omega t)}{(\frac{r_{\rm th}+a}{r_{\rm th}})^2 + (\frac{a}{r_{\rm th}})^2} \\
& + \frac{d\alpha}{dn_s}\frac{dn_s}{dT}\frac{3P_{\rm abs}}{16\pi\kappa(b^3-a^3)} \\
& \times \Bigg[r_{\rm th}^2\sin(\Omega t) - \frac{e^{-\frac{b-a}{r_{\rm th}}}}{(\frac{r_{\rm th}+a}{r_{\rm th}})^2 + (\frac{a}{r_{\rm th}})^2}\Big(r_{\rm th}(b-a)\cos(\Omega t - \tfrac{b-a}{r_{\rm th}}) \\
& \qquad + (r_{\rm th}(b+r_{\rm th}) + a(2b+r_{\rm th}))\sin(\Omega t - \tfrac{b-a}{r_{\rm th}})\Big)\Bigg]
\end{aligned} \tag{A.17}$$

$$\begin{aligned}
\equiv {} & \alpha_\Omega^{(0)}\cos(\Omega t) + \alpha_\Omega^{(\pi/2)}\sin(\Omega t) \\
& + \alpha_\Omega^{(\phi_{r_{\rm th}})}\cos(\Omega t - \tfrac{b-a}{r_{\rm th}}) + \alpha_\Omega^{(\pi/2+\phi_{r_{\rm th}})}\sin(\Omega t - \tfrac{b-a}{r_{\rm th}})
\end{aligned} \tag{A.18}$$

where we have defined four components to the polarizability based on their phase delay from the absorption process.

We can now express the scattered field in terms of its static and fluctuating components just as in the thermally-static case,

$$\begin{aligned}
\mathbf{E}_{\rm scattered}(t) &= \mathbf{G}\cdot(\boldsymbol{\alpha}_0 + \boldsymbol{\alpha}_\Omega(t))\cdot\mathbf{E}_{\rm pr}(\mathbf{x}_0)e^{-i\omega t} \\
&\equiv \left[\mathbf{E}_0 + \mathbf{E}_\Omega(t)\right]e^{-i\omega t} \ ,
\end{aligned} \tag{A.19}$$

which we can then use to calculate the lock-in-integrated photothermal signal as above, this time with a generalized phase delay ϕ,

$$P^{\mathrm{PT}} \equiv \lim_{\tau\to\infty}\frac{1}{\tau}\int_0^\tau dt\, I_{\mathrm{PT}}^{\mathrm{raw}}(t)\cos(\Omega t-\phi) \tag{A.20}$$

$$= \frac{cn}{8\pi}\lim_{\tau\to\infty}\frac{1}{\tau}\int_0^\tau dt\,\left|\left[\mathbf{E}_{\mathrm{pr}}^{\mathrm{tr}}+\mathbf{E}_0+\mathbf{E}_\Omega(t)\right]\right|^2\cos(\Omega t-\phi) \tag{A.21}$$

$$= \frac{cn}{8\pi}\mathrm{Re}\Big[(\mathbf{E}_{\mathrm{pr}}^{\mathrm{tr}}+\mathbf{E}_0)^*\cdot\Big(\mathbf{E}_\Omega^{(0)}\cos(\phi)+\mathbf{E}_\Omega^{(\pi/2)}\sin(\phi) + \mathbf{E}_\Omega^{(\phi_{r_{\mathrm{th}}})}\cos(\phi-\tfrac{b-a}{r_{\mathrm{th}}})+\mathbf{E}_\Omega^{(\pi/2+\phi_{r_{\mathrm{th}}})}\sin(\phi-\tfrac{b-a}{r_{\mathrm{th}}})\Big)\Big] \tag{A.22}$$

$$= \frac{cn}{8\pi}\mathrm{Re}\Big[(\mathbf{E}_{\mathrm{pr}}^{\mathrm{tr}}+\mathbf{E}_0)^*\cdot\mathbf{E}_\Omega(t=\phi/\Omega)\Big] \tag{A.23}$$

where the four field components are defined by $\mathbf{E}_\Omega^i = \mathbf{G}\cdot\boldsymbol{\alpha}_\Omega^i\cdot\mathbf{E}_{\mathrm{pr}}(\mathbf{x}_0)$.

A.3 Temperature dependence of the polarizability

Here we detail the core-shell polarizability used to model the scattering by the nanoparticle and its surrounding region of heated background. We start with a quasi-static model appropriate for particles much smaller than the relevant wavelength of light and then introduce a retardation-corrected model, in what is often called the Modified Long Wavelength Approximation (MLWA) [104, 111]. In either case, the heated background surrounding each particle is approximated by a spherical shell around the spherical metal core. The metal is assigned a temperature dependent dielectric function by fitting a Drude-Lorentz model to ellipsometry data [22] (discussed further in SI Section **II**). All background media are assumed to have optical properties that vary linearly with temperature, with values specified in SI Table 1.

In the QS limit, the polarizability of these core-shell model particles can be written in closed form, as derived electro-statically in reference [25],

$$\alpha_{cs} = b^3\frac{(\epsilon_s-\epsilon_b)(\epsilon_c+2\epsilon_s)+f(\epsilon_c-\epsilon_s)(\epsilon_b+2\epsilon_s)}{(\epsilon_s+2\epsilon_b)(\epsilon_c+2\epsilon_s)+f(2\epsilon_s-2\epsilon_b)(\epsilon_c-\epsilon_s)} \tag{A.24}$$

where ϵ_s is the electric permeability of the heated background shell, ϵ_c is the permeability of the metal core. $f=a^3/b^3$ is the ratio of core volume to total core-shell volume.

To model the temperature dependence of the scattering process, the polarizability will be expanded to linear changes in temperature. We have found that to reasonable accuracy the refractive indices for both the metal core (with complex index $n_c = n_c' + in_c'' = \sqrt{\epsilon_c}$) and the background shell (real index $n_s = \sqrt{\epsilon_s}$) cab be treated as change linear in temperature across the range of temperatures reachable in relevant experiments. The rate of change with temperature is approximately $\sim \frac{dn}{dT} \approx 10^{-4}$ for all background mediums considered here [62], as well as the metal. This small rate of refractive index change facilitates the expansion of the polarizability α_{cs} to first order in change of all refractive indices with temperature. With $\Delta n \equiv \frac{dn}{dT}\big|_{T=T_0}$ small for all $n \in \{n_b, n_c', n_c''\}$, the expanded polarizability written generally in Eq. (A.15) is justified.

In the electrostatic limit, the core-shell polarizability in Eq. A.24 expanded to linear order yield the coefficients

$$\alpha_{\text{cs}}^{\text{QS}}(T_0) = a^3 \frac{\epsilon_c - \epsilon_b}{\epsilon_c + 2\epsilon_b} \tag{A.25}$$

$$\frac{d\alpha^{\text{QS}}}{dn_c} = 6a^3 \frac{\epsilon_b}{(\epsilon_c + 2\epsilon_b)^2} n_c \tag{A.26}$$

$$\frac{d\alpha^{\text{QS}}}{dn_s} = \frac{2(b^3 - a^3)}{3} \left[1 + 2a^3/b^3 \left(\frac{\epsilon_c - \epsilon_b}{\epsilon_c + 2\epsilon_b}\right)^2\right] \frac{1}{n_s}. \tag{A.27}$$

It's clear in that the room temperature contribution is simply the Clausius-Mossati relation well known to give the static polarization response of a sphere. The core contribution notably scales with the volume of the core similar to the room temperature polarizability and has a denominator with similar poles. The shell contribution scales overall with the volume of the shell, and contains a linear combination of a core-independent piece with a term that depends on the core resonance and scales with the core volume.

In the electrodynamic limit, the core-shell polarizability can be corrected for retardation effects to the resonance structure is the modified long-wavelength approximation (MLWA). The procedure for solid spherical and spheroidal nanoparticles is well documented [104, 111], and provides an expression for the retardation corrected polarizability as a function of the static polarizability and the wavevector magnitude $k = \omega n/c$. This procedure was extended

in 2009 to shelled particles [43] by finding an effective permittivity to fill a solid particle such that this hypothetical particle has equivalent static polarizability to the shelled particle. With this new effective polarizability, the solid-particle formula for the MLWA polarizability can be used. In our case, the MLWA polarizability for the sphere with core radius a and shell radius b, the polarizability can be shown to be

$$\alpha_{\mathrm{cs}}^{\mathrm{ML}} = \frac{b^3}{3}\frac{(\epsilon_s-\epsilon_b)(\epsilon_c q_c-\epsilon_s[q_c-1])b^3-(\epsilon_c-\epsilon_s)(\epsilon_s[q_s-1]-\epsilon_b q_s)a^3}{(\epsilon_c q_c-\epsilon_s[q_c-1])(\epsilon_s q_s-\epsilon_b[q_s-1])b^3-(\epsilon_c-\epsilon_s)(\epsilon_s-\epsilon_b)q_s(q_s-1)a^3}\,, \tag{A.28}$$

where the retardation factors $q_i = \frac{1}{3}[1-(ka_i)^2 - i\frac{2}{3}(ka_i)^3]$ are defined by the core and shell radii, $a_c = a$ and $a_s = b$. The coefficients resulting from a linear expansion of Eq. A.28 are

$$\alpha^{\mathrm{ML}}(T_0) = \frac{a^3}{3}\frac{\epsilon_c-\epsilon_b}{\epsilon_c q_c+\epsilon_b[q_c-1]} \tag{A.29}$$

$$\frac{d\alpha^{\mathrm{ML}}}{dn_c} = \frac{2}{3}a^3\frac{\epsilon_b}{(\epsilon_c q_c+\epsilon_b(q_c-1))^2}n_c \tag{A.30}$$

$$\begin{aligned}\frac{d\alpha^{\mathrm{ML}}}{dn_s} = \frac{1}{3b^3 n_s(\epsilon_b(q_c-1)-\epsilon_c q_c)}\Big[&b^6(\epsilon_b(q_c-1)-\epsilon_c q_c)^2 + a^6((\epsilon_c-\epsilon_b)^2(q_s-1)q_s) \\ &+ a^3b^3(\epsilon_c^2 q_c(1-2q_s)+\epsilon_b^2(q_c-1+2q_s-2q_c q_s))+2\epsilon_c\epsilon_b(-q_s+q_c(2q_s-1))\Big].\end{aligned} \tag{A.31}$$

Here, the room temperature contribution and core temperature contribution both follow the qualitatively from above. The room temperature contribution is the standard MLWA polarizability for a sphere, and the core fluctuation coefficient takes the same relationship to the room temperature polarizability as it does in the quasi-static limit. The form of the shell fluctuation term has so far thwarted efforts at simplification, but may reveal similar structure to it's QS analog.

Even for small particles ($a \sim 10$ nm), we found the MLWA polarizability to yield qualitatively different photothermal signal (as a function of probe wavelength) than the QS polarizability. This is likely due to the fact that, in calculations, we have set the radius of the background shell b equal to the probe beam waist w_{pr} to represent the optically active region of heated background medium in the the scattering part of the problem. This radius is on the order of 100s of nm on resonance with the metal, which is likely big enough to break

QS assumptions. All of the calculations presented in this work therefore use the MLWA model and the QS polarizability is presented only for completeness and analogy.

A.4 Gaussian beam

For simplicity, we assume the focused probe field in the sample region takes the form of a Gaussian beam [152]. This approximation is known to fail for large numerical aperture objectives, but we proceed with the Gaussian as a qualitative predictor of effects related to focal spot size. The electric field in the focal spot is therefore defined by,

$$\mathbf{E}(r,z) = E_0 \hat{e}_x \frac{w_0}{w(z)} e^{-\frac{r^2}{w(z)^2}} e^{-i\left(kz + k\frac{r^2}{2R(z)^2} - \psi(z)\right)} , \tag{A.32}$$

where $w(z) = w_0\sqrt{1+(\frac{z}{z_R})^2}$ is the beam waist along the optical axis (z). $z_R = \frac{\pi w_0^2 n}{\lambda}$ defines the Rayleigh length in terms of the focus beam waist w_0, the background refractive index n and the vacuum wavelength λ, which marks the distance from the focal plane where the beam waist falls to $\sqrt{2}w_0$ and the intensity is half its peak values. The wavefront radius of curvature is defined by $R(z) = z[1+(\frac{z}{z_R})^2]$ and the Gouy phase is $\psi = \arctan(\frac{z}{z_r})$.

The field magnitude is defined by the peak intensity at the center of the focal spot $I_0 = \frac{cn}{8\pi}|E_0|^2$. This peak intensity is simply related to the total power transmitted by

$$\frac{I_0}{2} = \frac{P_{\text{exp}}}{\pi w_0^2} , \tag{A.33}$$

which we can use to define the field amplitude in terms of an experimentally determined laser power,

$$E_0 = \frac{4}{w_0}\sqrt{\frac{P_{\text{exp}}}{cn}} . \tag{A.34}$$

For all calculations presented, the pump and probe beam waists are assigned by the numerical aperture of the illumination objective by equating the FWHM to the an experimentally realizable resolution $\text{FWHM} = 0.61\frac{\lambda_i}{\text{NA}_{\text{illu}}} = \sqrt{2\ln 2}w_i$,

$$w_i = \frac{0.61}{\sqrt{2\ln 2}}\frac{\lambda_i}{\text{NA}_{\text{illu}}} = 0.52\frac{\lambda_i}{\text{NA}_{\text{illu}}} \tag{A.35}$$

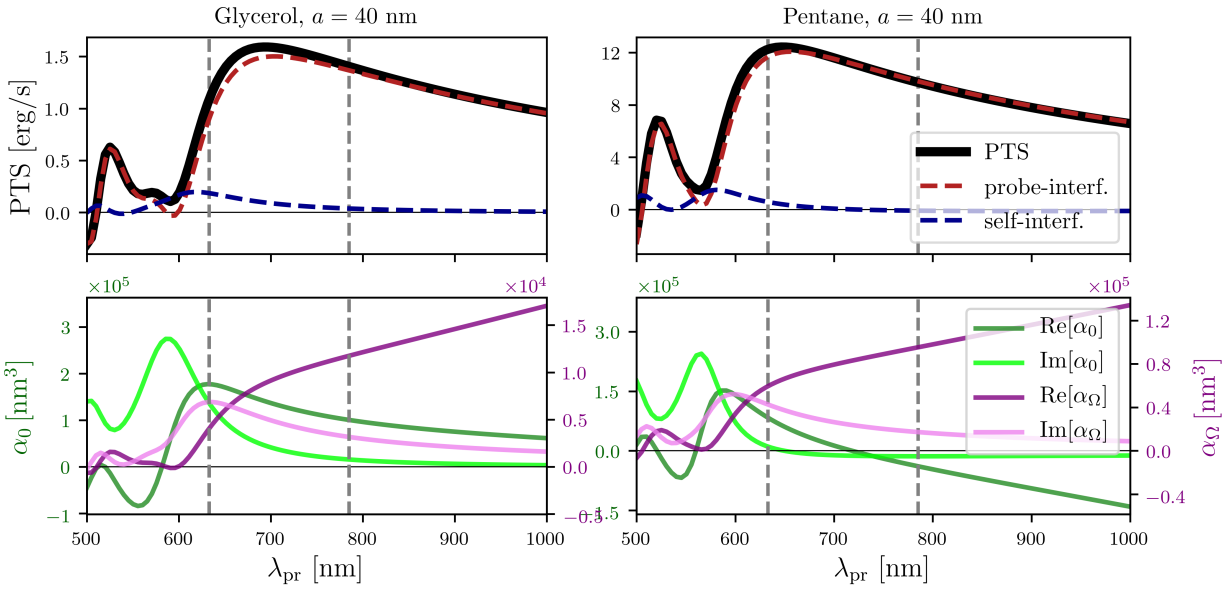

Figure A.1: Photothermal signal (top) for $a = 40$ nm particles in glycerol (left) and pentane (right) shows the evolution of the photothermal resonance with increasing particle size when compared to Figs. 4 and 5 in the main text (for $a = 20$ and $a = 75$ nm particles respectively). Similar analysis to that in the caption of Fig. 5 can be applied here to connect the components of polarizability with the probe- and self-interference terms.

A.5 Absorbing polarizability

For all calculations, the absorbing polarizability was assigned the exact dipolar Mie polarizability,

$$\alpha_{\text{Mie}} = \frac{i3}{2k^3} a_{\text{Mie}} \tag{A.36}$$

where the dipole Mie coefficient is

$$a_{\text{Mie}} = \frac{\epsilon_r^2 j_1(\epsilon_r ka)(j_1(ka) + kaj_1'(ka)) - j_1(ka)j_1(\epsilon_r ka) + \epsilon_r kaj_1'(\epsilon_r ka)}{\epsilon_r^2 j_1(\epsilon_r x)(h_1(ka) + kah_1'(ka)) - h_1 ka(j_1(\epsilon_r ka) + \epsilon_r kaj_1'(\epsilon_r ka))} \tag{A.37}$$

in terms of the relative permittivity $\epsilon_r = \epsilon_c/\epsilon_b$, the wavevector magnitude $k = \omega_{\text{pu}} n_b/c$ and the spherical Bessel and Hankel functions j and h. To better see the dependence of the background optical properties, we can use the MLWA polarizability with little loss in accuracy [104],

$$\alpha_{\text{sphere}}^{\text{ML}} = \frac{a^3}{3} \frac{\epsilon_c(\omega_{\text{pu}}) - \epsilon_b}{\epsilon_c(\omega_{\text{pu}}) q_c(\omega_{\text{pu}}) + \epsilon_b[q_c(\omega_{\text{pu}}) - 1]} \tag{A.38}$$

where $q_c = \frac{1}{3}[1 - (ka)^2 - i\frac{2}{3}(ka)^3]$.

A.6 Change in metal refractive index with temperature

The metal dielectric function was modeled by fitting a Drude-Lorentz model to temperature dependent dielectric data of gold from Bilchak and Fakhraai [22]. The data consisted of ellipsometry determined vales for the real and imaginary parts of the refractive index at 1 K increments from room temp to +100 K at wavelengths between 550 and 1047 nm. A separate model was fit at each temperature, emphasizing accuracy at small wavelengths near the small particle resonance.

For the linear polarizability model, the real and imaginary parts of $\frac{dn}{dT}$ were determined by finite difference from the modeled refractive index. These values have surprising temperature and frequency dependence, which is plotted in Fig. A.2.

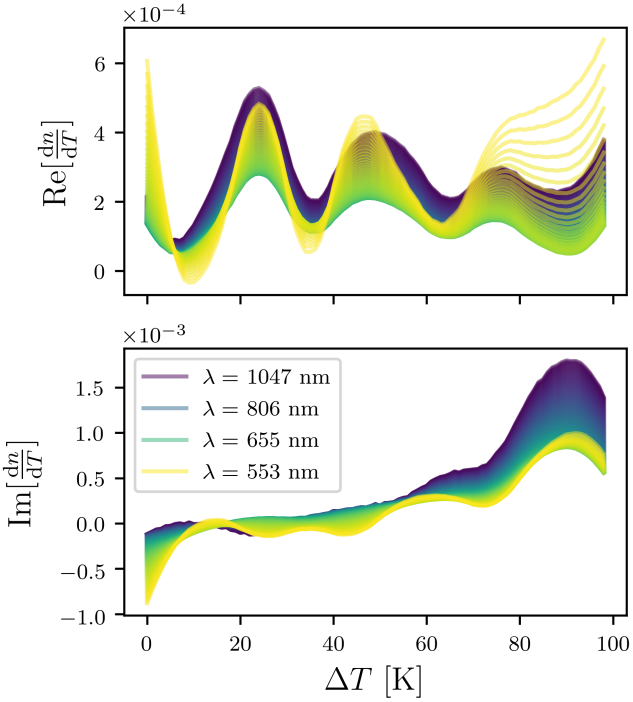

Figure A.2: Modeled change in gold refractive index with temperature from Drude-Lorentz fit to data [22] at each temperature independently. The frequency dependence is nontrivial, the imaginary part especially varies from $\ll 10^{-4}\frac{1}{\mathrm{K}}$ (typical of solvents) to $> 10^{-3}$.

Medium	n	$\frac{dn}{dT}$	C_p [J/m^{3}K]	κ [W/mK]	SNR, Ref. [62]
water	1.33	-9×10^{-5}	4.2×10^6	0.6	0.133
glycerol	1.473	-2.70×10^{-4}	2.60×10^5	0.292	0.989
ethanol	1.36	-4.40×10^{-4}	1.93×10^6	0.167	1.994
hexane [48]	1.37	-5.50×10^{-4}	1.50×10^6	0.124	4.008
pentane	1.358	-5.99×10^{-4}	1.45×10^6	0.111	5.056
chloroform	1.45	-6.12×10^{-3}	1.434×10^6	0.13	2.839
dichloromethane	1.422	-6.12×10^{-4}	1.576×10^6	0.1392	3.3
5CB$_e$ [120]	1.72	-3.01×10^{-3}	2.00×10^6	0.16	n/a
5CB$_o$ [120]	1.54	6.37×10^{-4}	2.00×10^6	0.16	n/a

Table A.1: Thermal and optical properties for background media. Most values for the change in refractive index with temperature are from Refs. [62, 34].

A.7 Effect of the substrate

Figs. A.3, A.4, and A.5 illustrate a qualitative model of the effects of the substrate on the trend in photothermal signal with background medium presented in main text Fig. 2. The substrate should impact the measurement in two primary ways not accounted for by the model. First, the data from in Ref. [62] was acquired in the reflection geometry, so the refractive index change at the substrate/background interface should affect the photothermal signal. To explore this, the reflection coefficient at the various interfaces involved was calculated neglecting the field phase. The second effect is on heat diffusion due to the increased thermal conductivity of glass cover slip compared to the solvents assumed to be isotropic background in the model. This was explored here by naively averaging the thermal conductivity of glass and background. Combining there two effects (Fig. A.3) qualitatively reproduces the trend in the data arguably better then when neglecting these effects in the main text. But the qualitative nature of these additions clearly has problems, with a no-

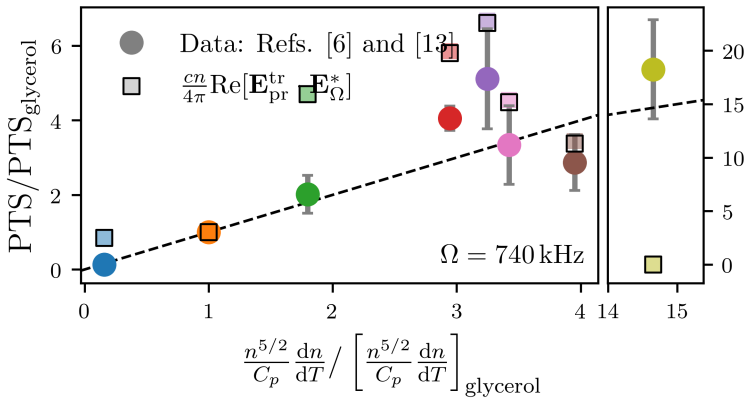

Figure A.3: Including the qualitative effects of reflection at the glass/background/glass interfaces as well as the glass substrate on thermal diffusion. The reflection was done neglecting interference effects between reflected rays at each interface. The glass correction to the temperature was done by naively averaging the glass thermal conductivity with the background and treating the sphere as still in isotropic medium.

ticeable offset for ethanol, hexane, and pentane, as well as the prediction for 5CB trending to zero. The work presented here is taken as evidence that a more quantitative model of substrate effects may recover the experimental trend in the data precisely.

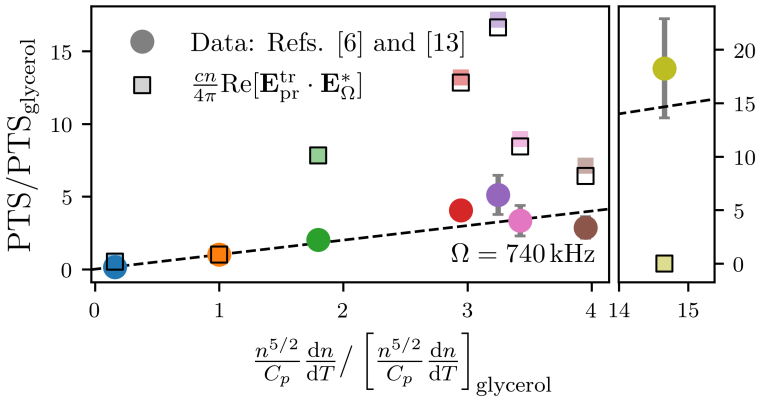

Figure A.4: Including the qualitative effect of the glass/background/glass interfaces on the reflection coefficient (but not the thermal effect of the substrate). In this case the self-interference term contributes non-negligibly. The probe-interference term is therefore shown by the shaded+colored squares and the total photothermal signal is shown in the square outlines.

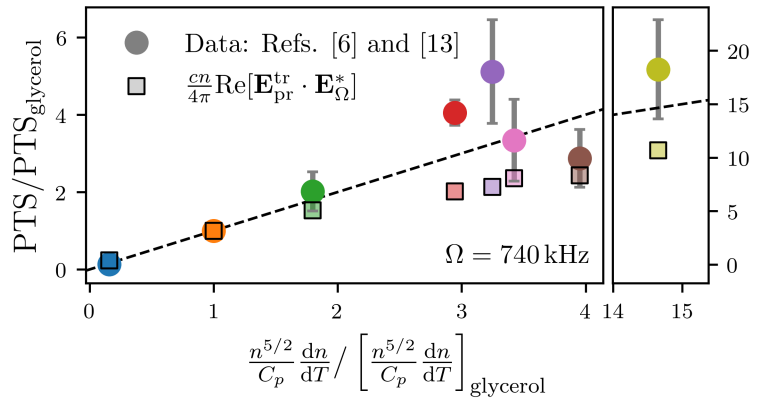

Figure A.5: Including the qualitative effect of the glass substrate as a heat sink (but not the reflective effect of the substrate). This was done naively by averaging the thermal conductivity for glass and background and treating the sphere as still in isotropic medium.

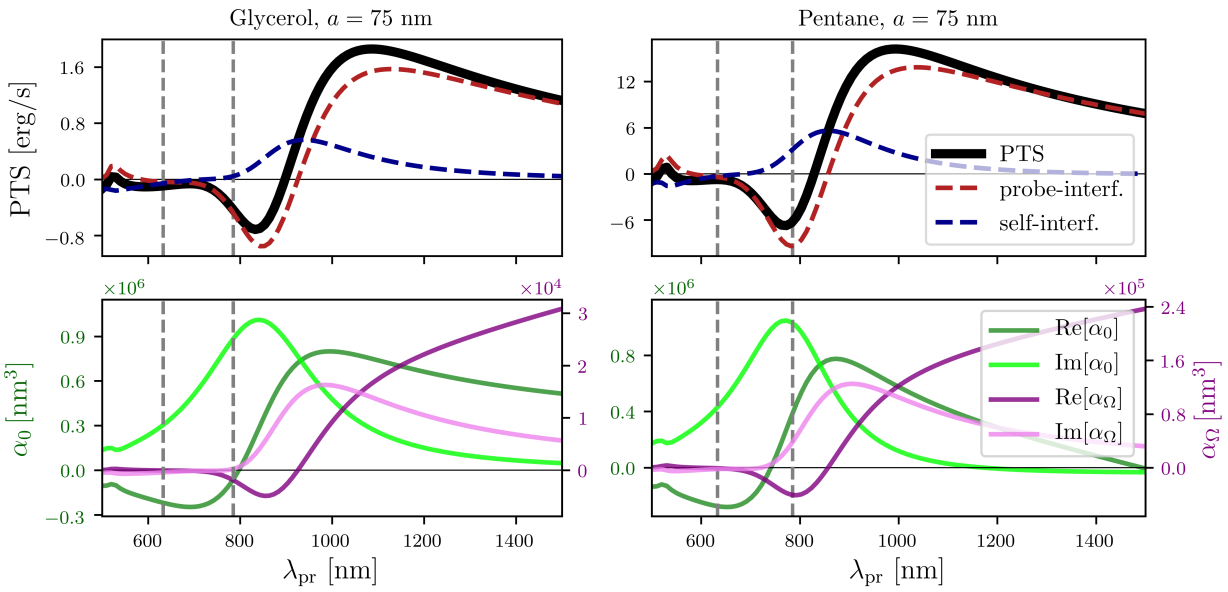

Figure A.6: Photothermal signal (top) and polarizability components for larger $a = 75$ nm particles at $\mathrm{NA_{col}} = 1.4$ compared to $\mathrm{NA_{col}} = 0.7$ in main text Fig. 5. The increased self-interference contribution (blue) demonstrates an example of tuning the probe- and self-interference by numerical aperture of the collection objective. Increasing the $\mathrm{NA_{col}}$ generates more photothermal signal, but here the pump and probe powers have been kept fixed. The transmitted/reflected probe field therefore increases less relative to the other fields, and the self-interference gains on the probe-interference.

Chapter 10

STEADY STATE TEMPERATURE AROUND AN ABSORBING SPHERE DIMER

In this section, I solve the stead state heat diffusion equation on a sphere dimer with Neumann boundary conditions. I could not find this in the literature (specifically for the heterodimer, Section 10.2) and believe it to be effectivly novel and hopefully useful to future graduate students. This problem, corresponds to finding the temperature around two spheres under steady state illumination+absorption and assuming uniform temperature across each sphere (valid as long as the background thermal conductivity remains much less then that of the spheres, which is true for plasmonic metals in normal laboratory solutions/solvents). Combining these results with the theory of the single particle photothermal image presented in the previous chapter would make for an interesting contribution to the field, and further pave the way towards photothermal imaging as a nano-localized optical thermometer.

The solution to this problem is analytic but complicated. If you are interested in implementing it, I'd recommend starting with my implementation on Github: at https://github.com/theomnipanda/photothermal_image_model/blob/master/python/modules/twosphere_temperature.py.

10.1 Heat diffusion

Following the work of Kang *et al.* [84], I will here derive the temperature at the surface and around two unequally sized spheres with different but constant heat fluxes across their surfaces. But first, since Kang's results will serve as a useful sanity check at multiple points in the derivation of the heterodimer solution I will outline Kang's solution with emphasis on the steps that were omitted from that work. Note that Ref. [4] was also instructive for this

work.

Sticking to Kang's notation, the equations to solve can be stated as

$$\nabla^2 T = 0 \text{ with} \tag{10.1}$$

$$-k\hat{n}\cdot\nabla T = q_s \,\text{for}\, \mathbf{r} \in S_0 \,\text{and}\, T \to T_{\text{inf}} \,\text{as}\, r \to \infty \tag{10.2}$$

or in the nondimentionalized form

$$\nabla^2 \theta = 0 \text{ with} \tag{10.3}$$

$$\hat{n}\cdot\nabla\theta = -1 \,\text{for}\, \tilde{\mathbf{r}} \in S_0 \,\text{and}\, \theta \to 0 \,\text{as}\, \tilde{r} \to \infty\,. \tag{10.4}$$

The general solution of the heat diffusion equation (with azimuthal symmetry) in the bispherical coordinates (ζ, β, ϕ) is

$$\theta = \sqrt{\cosh\zeta - \cos\beta}\sum_{m=0}^{\infty}\left[B_m^{(1)}\sinh(m+1/2)\zeta + B_m^{(2)}\cosh(m+1/2)\zeta\right] \times\left[B_m^{(3)}P_m(\cos\beta) + B_m^{(4)}Q_m(\cos\beta)\right] \tag{10.5}$$

for the cast of two identical spheres with surfaces defined by $\zeta = \zeta_0$ with identical heat flux the solution reduces to

$$\theta = \sqrt{\cosh\zeta - \cos\beta}\sum_{m=0}^{\infty} B_m^{(2)}\cosh(m+1/2)\zeta P_m(\cos\beta) \tag{10.6}$$

with the coefficients B_m to be determined from the constant heat flux boundary conditions

$$\left.\frac{1}{h_\zeta}\frac{\mathrm{d}\theta}{\mathrm{d}\zeta}\right|_{\zeta_0} = -\left.\frac{1}{h_\zeta}\frac{\mathrm{d}\theta}{\mathrm{d}\zeta}\right|_{-\zeta_0} = \frac{\sqrt{\coth\zeta - \cos\beta}}{c} \times\sum_{m=0}^{\infty} B_m^{(2)}[D_m P_m(\cos\beta) - E_m\cos\beta P_m(\cos\beta)] = 1 \tag{10.7}$$

where

$$D_m = \frac{1}{2}\sinh\zeta_0\cosh(m+1/2)\zeta_0 + (m+1/2)\cosh\zeta_0\sinh(m+1/2)\zeta_0 \tag{10.8}$$

$$E_m = (m+1/2)\sinh(m+1/2)\zeta_0 \tag{10.9}$$

Noting that $\cos\beta = P_1(\cos\beta)$, the flux condition in Eq. 10.7 can be integrated directly to yield the relationship between the first two coefficients

$$B_1 = F_0 + B_0 \tag{10.10}$$

using the orthogonality of the Legendre polynomials

$$\int_{-1}^{1} P_m(x)P_n(x)\mathrm{d}x = \begin{cases} 2/(2m+1) & \text{if } m = n \\ 0 & \text{if } m \neq n \end{cases} \tag{10.11}$$

Also, the flux condition can be projected onto the nth order Legendre polynomial using the relations

$$\int_{-1}^{1} P_m(x)P_n(x)x\mathrm{d}x = \begin{cases} \frac{2(m+1)}{(2m+1)(2m+3)} & \text{if } m = n-1 \\ \frac{2m}{(2m-1)(2m+1)} & \text{if } m = n+1 \\ 0 & \text{if } m \neq n \pm 1 \end{cases} \tag{10.12}$$

$$\int_{-1}^{1} \frac{P_m(x)}{\sqrt{\cosh\zeta_0 - x}}\mathrm{d}x = \frac{2\sqrt{2}}{2m+1}e^{-(m+1/2)\zeta_0} \tag{10.13}$$

to yield the second order recurrence relation

$$B_{m+1} = F_m + G_m B_m + (1 - G_m)B_{m-1} \tag{10.14}$$

where

$$F_m = -\frac{2\sqrt{2}\sinh\zeta_0 e^{-(m+1/2)\zeta_0}}{(m+1)\sinh(m+3/2)\zeta_0} \tag{10.15}$$

$$G_m = \frac{1}{m+1}\left[\frac{2m\cosh\zeta_0\sinh(m+1/2)\zeta_0}{\sinh(m+3/2)\zeta_0}\right] \tag{10.16}$$

The last step to determining the solution is to define the first coefficient B_0 from the need for the series to terminate, aka $\lim_{m\to\mathrm{inf}} B_m = 0$. But to connect B_m to B_0 I believe I need to solve the recursion relation, which I will show now in detail. We can rewrite the second order recursion relation as a first order non homogeneous recursion relation with non

constant coefficients.

$$B_{m+1} = F_m + G_m B_m + (1 - G_m) B_{m-1} \tag{10.17}$$

$$B_{m+1} - B_{m-1} = F_m + G_m (B_m - B_{m-1}) \tag{10.18}$$

$$(B_{m+1} - B_m) + (B_m - B_{m-1}) = F_m + G_m (B_m - B_{m-1}) \tag{10.19}$$

$$A_m + A_{m-1} = F_m + G_m A_{m-1} \tag{10.20}$$

$$A_m = F_m + (G_m - 1) A_{m-1} \tag{10.21}$$

where $A_m \equiv (B_{m+1} - B_m)$. This form has the a known solution, which proceeds by first dividing by $\prod_{n=0}^{m}(G_m - 1)$ and serves to eliminate the non constant coefficients.

$$\frac{A_m}{\prod_{n=0}^{m}(G_n - 1)} = \frac{F_m}{\prod_{n=0}^{m}(G_n - 1)} + \frac{(G_m - 1) A_{m-1}}{\prod_{n=0}^{m}(G_n - 1)} \tag{10.22}$$

$$\frac{A_m}{\prod_{n=0}^{m}(G_n - 1)} = \frac{F_m}{\prod_{n=0}^{m}(G_n - 1)} + \frac{A_{m-1}}{\prod_{n=0}^{m-1}(G_n - 1)} \tag{10.23}$$

$$C_m = \frac{F_m}{\prod_{n=0}^{m}(G_n - 1)} + C_{m-1} \tag{10.24}$$

which can be summed directly

$$\sum_{m=1}^{l}(C_m - C_{m-1}) = \sum_{m=1}^{l} \frac{F_m}{\prod_{n=0}^{m}(G_n - 1)} \tag{10.25}$$

$$C_l - C_0 = \tag{10.26}$$

$$\frac{A_l}{\prod_{n=0}^{l}(G_n - 1)} - \frac{A_0}{(G_0 - 1)} = \tag{10.27}$$

$$\frac{B_{l+1} - B_l}{\prod_{n=0}^{l}(G_n - 1)} = \frac{B_1 - B_0}{(G_0 - 1)} + \sum_{m=1}^{l} \frac{F_m}{\prod_{n=0}^{m}(G_n - 1)} \tag{10.28}$$

$$B_{l+1} - B_l = \prod_{n=0}^{l}(G_n - 1) \left[\frac{F_0}{(G_0 - 1)} + \sum_{m=1}^{l} \frac{F_m}{\prod_{n=0}^{m}(G_n - 1)} \right] \tag{10.29}$$

which yields another first order relation with constant coefficients. Another sum provides the solution.

$$B_{k+1} - B_0 = \sum_{l=0}^{k} \left(\prod_{n=0}^{l}(G_n - 1) \left[\frac{F_0}{(G_0 - 1)} + \sum_{m=1}^{l} \frac{F_m}{\prod_{n=0}^{m}(G_n - 1)} \right] \right) \tag{10.30}$$

Now, we can enforce the coefficients converge to zero at high order and determine B_0,

$$B_0 = -\sum_{l=0}^{\infty}\left(\left[\prod_{n=0}^{l}(G_n-1)\right]\left[\frac{F_0}{(G_0-1)}+\sum_{m=1}^{l}\frac{F_m}{\prod_{n=0}^{m}(G_n-1)}\right]\right) \tag{10.31}$$

Strangely Kang writes this solution in the form of another recurrence relation. I am not sure why, but we can derive that from the solution in order to verify agreement. Rewriting Eq. 10.31 as $B_0 = -\lim_{k\to\infty} H_k$ and writing out the first few terms,

$$H_0 = \sum_{l=0}^{0}\left(\left[\prod_{n=0}^{l}(G_n-1)\right]\left[\frac{F_0}{(G_0-1)}+\sum_{m=1}^{l}\frac{F_m}{\prod_{n=0}^{m}(G_n-1)}\right]\right) \tag{10.32}$$

$$= F_0 \tag{10.33}$$

$$H_1 = \sum_{l=0}^{1}\left(\left[\prod_{n=0}^{l}(G_n-1)\right]\left[\frac{F_0}{(G_0-1)}+\sum_{m=1}^{l}\frac{F_m}{\prod_{n=0}^{m}(G_n-1)}\right]\right) \tag{10.34}$$

$$= H_0 + \left[\prod_{n=0}^{1}(G_n-1)\right]\left[\frac{F_0}{(G_0-1)}+\sum_{m=1}^{1}\frac{F_m}{\prod_{n=0}^{m}(G_n-1)}\right] \tag{10.35}$$

$$= H_0 + (G_0-1)(G_1-1)\left[\frac{F_0}{(G_0-1)}+\frac{F_1}{\prod_{n=0}^{1}(G_n-1)}\right] \tag{10.36}$$

$$= H_0 + [(G_1-1)F_0 + F_1] \tag{10.37}$$

$$= G_1F_0 + F_1 \tag{10.38}$$

$$H_2 = \underbrace{H_1}_{\text{first 2 terms}} + \left(\left[\prod_{n=0}^{l}(G_n-1)\right]\left[\frac{F_0}{(G_0-1)}+\sum_{m=1}^{l}\frac{F_m}{\prod_{n=0}^{m}(G_n-1)}\right]\right)_{l=2} \tag{10.39}$$

$$= H_1 + \left[\prod_{n=1}^{2}(G_n-1)F_0 + \prod_{n=2}^{2}(G_n-1)F_1 + F_2\right] \tag{10.40}$$

$$= H_1 + (H_1-H_0)(G_2-1) + F_2 \tag{10.41}$$

$$H_3 = H_2 + \left[\prod_{n=1}^{3}(G_n-1)F_0 + \prod_{n=2}^{3}(G_n-1)F_1 + \prod_{n=3}^{3}(G_n-1)F_2 + F_3\right] \tag{10.42}$$

$$= H_2 + [(H_2-H_1)(G_3-1) + F_3] \tag{10.43}$$

at which point the pattern becomes apparent, and we can write

$$H_k = H_{k-1} + (H_{k-1} - H_{k-2})(G_k - 1) + F_k \tag{10.44}$$

$$= F_k + G_k H_{k-1} + (1 - G_k) H_{k-2} \tag{10.45}$$

which is the recursion relation provided by Kang. But after all of this, I just realized that you can derive the recursion relation for H_k simply by defining $H_k = B_k - B_0$ and plugging in to the recursion relation for B_k!

$$H_{m+1} + B_0 = F_m + G_m(H_m + B_0) + (1 - G_m)(H_{m-1} + B_0) \tag{10.46}$$

$$H_{m+1} = F_m + G_m H_m + (1 - G_m) H_{m-1} + G_m B_0 + (1 - G_m) B_0 - B_0 \tag{10.47}$$

$$H_{m+1} = F_m + G_m H_m + (1 - G_m) H_{m-1} \tag{10.48}$$

This procedure could maybe be motivated by the fact that taking the $k \to \infty$ limit of $H_k = B_k - B_0$ yields a definition of B_0.

10.2 Heterodimer

For two spheres of different radii $\zeta_1 > 0$ and $\zeta_2 < 0$ with constant but different heat fluxes across their surfaces q_1 and q_2, we can redefine the nondimentionalized coordinate

$$\theta \equiv \frac{T - T_\infty}{q_1 l / k}. \tag{10.49}$$

The boundary conditions of constant flux $-k\hat{n}\nabla T = q_s$ are now defined by

$$-\frac{1}{h_\zeta}\frac{\mathrm{d}\theta}{\mathrm{d}\zeta}\bigg|_{\zeta_1} = -1 \tag{10.50}$$

$$+\frac{1}{h_\zeta}\frac{\mathrm{d}\theta}{\mathrm{d}\zeta}\bigg|_{\zeta_2} = -q_2/q_1 \equiv -\tilde{q} \tag{10.51}$$

because $\hat{n}$ points in $-\hat{\zeta}$ on S_1 and $+\hat{\zeta}$ on S_2. In the general solution to the heat equation, we now must keep the terms antisymetric across the $z = 0$ plane

$$\theta = \sqrt{\cosh\zeta - \cos\beta} \sum_{m=0}^{\infty} \left[B_m^{(1)} \sinh(m + 1/2)\zeta + B_m^{(2)} \cosh(m + 1/2)\zeta \right] P_m(\cos\beta) \tag{10.52}$$

and we are left with two coefficients to determine. In order to apply to boundary conditions, we need the ζ component of the gradient. First, taking the derivative of θ results in two terms from the product rule,

$$\begin{aligned}\frac{\mathrm{d}\theta}{\mathrm{d}\zeta} &= \frac{\sinh\zeta}{2\sqrt{\cosh\zeta-\cos\beta}}\frac{\theta}{\sqrt{\cosh\zeta-\cos\beta}} \\ &\quad+\sqrt{\cosh\zeta-\cos\beta}\sum_{m=0}^{\infty}P_m(\cos\beta)\left[B_m^{(2)}((m+1/2)\sinh(m+1/2)\zeta)\right. \\ &\qquad\left.+B_m^{(1)}((m+1/2)\cosh(m+1/2)\zeta)\right]\end{aligned} \tag{10.53}$$

$$\begin{aligned}&= \sum_{m=0}^{\infty}P_m(\cos\beta)\left[B_m^{(2)}\left(\frac{\sinh\zeta}{2\sqrt{\cosh\zeta-\cos\beta}}(m+1/2)\cosh(m+1/2)\zeta\right.\right. \\ &\qquad\left.+\sqrt{\cosh\zeta-\cos\beta}(m+1/2)\sinh(m+1/2)\zeta\right) \\ &\quad+B_m^{(1)}\left(\frac{\sinh\zeta}{2\sqrt{\cosh\zeta-\cos\beta}}(m+1/2)\sinh(m+1/2)\zeta\right. \\ &\qquad\left.\left.+\sqrt{\cosh\zeta-\cos\beta}(m+1/2)\cosh(m+1/2)\zeta\right)\right]\end{aligned} \tag{10.54}$$

which simplifies when multiplied by the inverse scale factor of coordinate system to yield

$$\begin{aligned}\frac{1}{h_\zeta}\frac{\mathrm{d}\theta}{\mathrm{d}\zeta} &= \frac{\sqrt{\coth\zeta-\cos\beta}}{c}\sum_{m=0}^{\infty}P_m(\cos\beta)\left[B_m^{(2)}(D_m-E_m\cos\beta)+B_m^{(1)}(F_m-G_m\cos\beta)\right] \\ &= \begin{cases}1 & \text{at } S_1\\ -\tilde{q} & \text{at } S_2\end{cases}\end{aligned} \tag{10.55}$$

where F_m and G_m take the same form as D_m and E_m (see Eq. 10.8) but with $\coth(m+1/2)\zeta_0$ and $\sinh(m+1/2)\zeta_0$ interchanged. Explicitly,

$$F_m = \frac{1}{2}\sinh\zeta_0\sinh(m+1/2)\zeta_0+(m+1/2)\cosh\zeta_0\cosh(m+1/2)\zeta_0 \tag{10.56}$$

$$G_m = (m+1/2)\cosh(m+1/2)\zeta_0 \tag{10.57}$$

Like the simpler case of the sphere homodimer, this equation can be evaluated at the

boundary and integrated to yield the relationship between the first and second coefficients

$$-cq\sqrt{2}e^{-\frac{1}{2}|\zeta_{1,2}|} = B_0^{(2)}D_0 + B_0^{(1)}F_0 - \frac{B_1^{(2)}D_1 + B_1^{(1)}G_1}{3} \tag{10.58}$$

with the expansion

$$\frac{1}{\sqrt{\cosh\zeta_{1,2} - \cos\beta}} = \sum_{m=0}^{\infty} \sqrt{2}e^{-(m+1/2)|\zeta_{1,2}|}P_m\cos\beta \tag{10.59}$$

(Note that Kang does no include the absolute value because of their definition of the radii as $\pm\zeta_0$, thus Eq (28) in their article or Eq 10.13 in this work). Also, to avoid writing Eq. 10.58 for each b.c., I have introduced the notation

$$q = \begin{cases} -1 & \text{at } S_1 \\ \tilde{q} & \text{at } S_2 \end{cases} \tag{10.60}$$

This expression can then be evaluated at the boundaries and integrated to yield a recursion relation for the coefficients.

$$\begin{aligned} -cq\sqrt{2}e^{-(n+1/2)|\zeta_{1,2}|} = {} & \left(B_n^{(2)}D_n + B_n^{(1)}F_n\right) \\ & - \left(B_{n-1}^{(2)}E_{n-1} + B_{n-1}^{(1)}G_{n-1}\right)\frac{n}{(2n-1)} \\ & - \left(B_{n+1}^{(2)}E_{n+1} + B_{n+1}^{(1)}G_{n+1}\right)\frac{n+1}{(2n+3)} \end{aligned} \tag{10.61}$$

with the same q shorthand.

To build the connection between the coefficients of arbutrary order and the first coefficients, we can use the b.c.'s on both surfaces to eliminate some of the coefficient deoendence. First, taking the integral equation and solving for $B_1^{(2)}$, using

$$D_0 = \frac{1}{2}\sinh(\tfrac{3}{2}\zeta_{1,2}) \tag{10.62}$$

$$F_0 = \frac{1}{2}\coth(\tfrac{3}{2}\zeta_{1,2}) \tag{10.63}$$

$$E_1 = \frac{3}{2}\sinh(\tfrac{3}{2}\zeta_{1,2}) \tag{10.64}$$

$$G_1 = \frac{3}{2}\coth(\tfrac{3}{2}\zeta_{1,2}) \tag{10.65}$$

$$-B_1^{(1)} = \frac{3B_0^{(2)}D_0 + 3B_0^{(1)}F_0 - B_1^{(2)}E_1 + 3\sqrt{2}cqe^{-\frac{1}{2}|\zeta_{1,2}|}}{G_1} \tag{10.66}$$

$$-B_1^{(1)} = \frac{B_0^{(2)}\sinh(\frac{3}{2}\zeta_{1,2}) + B_0^{(1)}\coth(\frac{3}{2}\zeta_{1,2}) - B_1^{(2)}\sinh(\frac{3}{2}\zeta_{1,2}) + 2\sqrt{2}cqe^{-\frac{1}{2}|\zeta_{1,2}|}}{\coth(\frac{3}{2}\zeta_{1,2})} \tag{10.67}$$

and equating $B_1^{(1)}$ at both surfaces yields

$$\frac{B_0^{(2)}\sinh(\frac{3}{2}\zeta_1) + B_0^{(1)}\coth(\frac{3}{2}\zeta_1) - B_1^{(2)}\sinh(\frac{3}{2}\zeta_1) + 2\sqrt{2}c(-1)e^{-\frac{1}{2}|\zeta_1|}}{\coth(\frac{3}{2}\zeta_1)}$$
$$= \frac{B_0^{(2)}\sinh(\frac{3}{2}\zeta_2) + B_0^{(1)}\coth(\frac{3}{2}\zeta_2) - B_1^{(2)}\sinh(\frac{3}{2}\zeta_2) + 2\sqrt{2}c\tilde{q}e^{-\frac{1}{2}|\zeta_2|}}{\coth(\frac{3}{2}\zeta_2)} \tag{10.68}$$

which we can solve for $B_1^{(2)}$ in terms of the 0th order coefficients. With the shorthand $s_{1,2} \equiv \sinh(\frac{3}{2}\zeta_{1,2})$ and etc. for $c_{1,2}$,

$$-B_1^{(2)} = \frac{B_0^{(2)}(s_2c_1 - s_1c_2) + B_0^{(1)}\cancel{(c_2c_1 - c_1c_2)} + 2\sqrt{2}c\left(\tilde{q}e^{-\frac{1}{2}|\zeta_2|}c_1\right) - (-1)e^{-\frac{1}{2}|\zeta_1|}c_2}{s_1c_2 - s_2c_1}. \tag{10.69}$$

Next, we can simplify the hyperbolic trig functions with the relations $s_1c_2 - s_2c_1 = \sinh(\frac{3}{2}(\zeta_1 - \zeta_2))$ as well as the fact that sinh is odd and coth is even.

$$B_1^{(2)} = -\frac{-B_0^{(2)}\sinh(\frac{3}{2}(\zeta_1 - \zeta_2)) + 2\sqrt{2}c\left(\tilde{q}e^{-\frac{1}{2}|\zeta_2|}\coth(\frac{3}{2}\zeta_2) + e^{-\frac{1}{2}|\zeta_1|}\coth(\frac{3}{2}\zeta_1)\right)}{\sinh(\frac{3}{2}(\zeta_1 - \zeta_2))} \tag{10.70}$$

$$= B_0^{(2)} - \frac{2\sqrt{2}c\left(\tilde{q}e^{-\frac{1}{2}|\zeta_2|}\coth(\frac{3}{2}\zeta_2) + e^{-\frac{1}{2}|\zeta_1|}\coth(\frac{3}{2}\zeta_1)\right)}{\sinh(\frac{3}{2}(\zeta_1 - \zeta_2))}. \tag{10.71}$$

To aid in our progress, we can compare this result with Kang's in the limit that $\tilde{q} \to 1$ and $\zeta_2 \to -\zeta_1$.

$$\lim_{\text{Kang}} B_1^{(2)} = B_0^{(2)} - \frac{2\sqrt{2}c\left(2e^{-\frac{1}{2}|\zeta_1|}\coth(\frac{3}{2}\zeta_1)\right)}{\sinh(\frac{3}{2}(\zeta_1 - \zeta_2))} \tag{10.72}$$

Using the angle addition formula for hyperbolic trig functions $\sinh(\frac{3}{2}2\zeta_1) = 2\cosh(\frac{3}{2}\zeta_1)\sin(\frac{3}{2}\zeta_1)$,

$$\lim_{\text{Kang}} B_1^{(2)} = B_0^{(2)} - \frac{2\sqrt{2}ce^{-\frac{1}{2}|\zeta_1|}}{\sin(\frac{3}{2}\zeta_1)} \tag{10.73}$$

which is the same result as Kang! Good.

To get the associated relation for $B_1^{(1)}$, we simply need to interchange the hyperbolic trig functions from the order 1 coefficients, which amounts to the second factor in the products and all four functions in the denominator of Eq. 10.69.

$$\begin{aligned}
-B_1^{(1)} &= \frac{B_0^{(2)}\cancel{(s_2 s_1 - s_1 s_2)} + B_0^{(1)}(c_2 s_1 - c_1 s_2) + 2\sqrt{2}c\left(\tilde{q}e^{-\frac{1}{2}|\zeta_2|}s_1 + e^{-\frac{1}{2}|\zeta_1|}s_2\right)}{c_1 s_2 - c_2 s_1} \\
B_1^{(1)} &= -\frac{B_0^{(1)}\sinh(\frac{3}{2}(\zeta_1 - \zeta_2)) + 2\sqrt{2}c\left(\tilde{q}e^{-\frac{1}{2}|\zeta_2|}s_1 + e^{-\frac{1}{2}|\zeta_1|}s_2\right)}{-\sinh(\frac{3}{2}(\zeta_1 - \zeta_2))} \\
&= B_0^{(1)} + \frac{2\sqrt{2}c\left(\tilde{q}e^{-\frac{1}{2}|\zeta_2|}s_1 + e^{-\frac{1}{2}|\zeta_1|}s_2\right)}{\sinh(\frac{3}{2}(\zeta_1 - \zeta_2))}.
\end{aligned} \tag{10.74}$$

note that the second term goes to zero in the Kang limit due to sinh being odd.

We can now proceed to the projected equation and try a similar strategy to separate terms. Solving for $B_{n+1}^{(1)}$ in Eq. 10.61,

$$\begin{aligned}
B_{n+1}^{(1)} = \frac{1}{G_{n+1}}\Bigg(&- B_{n+1}^{(2)}E_{n+1} + \frac{(2n+3)}{n+1}\Big[\left(B_n^{(2)}D_n + B_n^{(1)}F_n\right) \\
&- \left(B_{n-1}^{(2)}E_{n-1} + B_{n-1}^{(1)}G_{n-1}\right)\frac{n}{(2n-1)} \\
&+ \sqrt{2}cqe^{-(n+1/2)\zeta_{1,2}|}\Big]\Bigg)
\end{aligned} \tag{10.75}$$

Again, we can equate $B_{n+1}^{(1)}$ at both boundaries

$$\begin{aligned}
&\frac{1}{G_{n+1}(\zeta_1)}\Bigg(- B_{n+1}^{(2)}E_{n+1}(\zeta_1) + \frac{(2n+3)}{n+1}\Big[\left(B_n^{(2)}D_n(\zeta_1) + B_n^{(1)}F_n(\zeta_1)\right) \\
&\quad - \left(B_{n-1}^{(2)}E_{n-1}(\zeta_1) + B_{n-1}^{(1)}G_{n-1}(\zeta_1)\right)\frac{n}{(2n-1)} + \sqrt{2}c(-1)e^{-(n+1/2)|\zeta_1|}\Big]\Bigg) \\
&= \frac{1}{G_{n+1}(\zeta_2)}\Bigg(- B_{n+1}^{(2)}E_{n+1}(\zeta_2) + \frac{(2n+3)}{n+1}\Big[\left(B_n^{(2)}D_n(\zeta_2) + B_n^{(1)}F_n(\zeta_2)\right) \\
&\quad - \left(B_{n-1}^{(2)}E_{n-1}(\zeta_2) + B_{n-1}^{(1)}G_{n-1}(\zeta_2)\right)\frac{n}{(2n-1)} + \sqrt{2}c\tilde{q}e^{-(n+1/2)|\zeta_2|}\Big]\Bigg)
\end{aligned}$$

and solve for $B^{(2)}_{n+1}$

$$
\begin{aligned}
&- B^{(2)}_{n+1}[E_{n+1}(\zeta_1)G_{n+1}(\zeta_2) - E_{n+1}(\zeta_2)G_{n+1}(\zeta_1)] \\
&\qquad = G_{n+1}(\zeta_1)\frac{(2n+3)}{n+1}\Bigg[\left(B^{(2)}_n D_n(\zeta_2) + B^{(1)}_n F_n(\zeta_2)\right) \\
&\qquad - \left(B^{(2)}_{n-1}E_{n-1}(\zeta_2) + B^{(1)}_{n-1}G_{n-1}(\zeta_2)\right)\frac{n}{(2n-1)} + \sqrt{2}c\tilde{q}e^{-(n+1/2)|\zeta_2|}\Bigg] \\
&\qquad - G_{n+1}(\zeta_2)\frac{(2n+3)}{n+1}\Bigg[\left(B^{(2)}_n D_n(\zeta_1) + B^{(1)}_n F_n(\zeta_1)\right) \\
&\qquad - \left(B^{(2)}_{n-1}E_{n-1}(\zeta_1) + B^{(1)}_{n-1}G_{n-1}(\zeta_1)\right)\frac{n}{(2n-1)} + \sqrt{2}c(-1)e^{-(n+1/2)|\zeta_1|}\Bigg]
\end{aligned}
$$

This is a mess. We can group the coefficients on the right hand side

$$
\begin{aligned}
&- B^{(2)}_{n+1}[E_{n+1}(\zeta_1)G_{n+1}(\zeta_2) - E_{n+1}(\zeta_2)G_{n+1}(\zeta_1)] \\
&\qquad = \frac{(2n+3)}{n+1}\Bigg[B^{(2)}_n[D_n(\zeta_2)G_{n+1}(\zeta_1) - D_n(\zeta_1)G_{n+1}(\zeta_2)] \\
&\qquad\qquad + B^{(1)}_n[F_n(\zeta_2)G_{n+1}(\zeta_1) - F_n(\zeta_1)G_{n+1}(\zeta_2)] \\
&\qquad - \frac{n}{(2n-1)}\Big(B^{(2)}_{n-1}[E_{n-1}(\zeta_2)G_{n+1}(\zeta_1) - E_{n-1}(\zeta_1)G_{n+1}(\zeta_2)] \\
&\qquad\qquad + B^{(1)}_{n-1}[G_{n-1}(\zeta_2)G_{n+1}(\zeta_1) - G_{n-1}(\zeta_1)G_{n+1}(\zeta_2)]\Big) \\
&\qquad\qquad + \sqrt{2}c\left(\tilde{q}e^{-(n+1/2)|\zeta_2|}G_{n+1}(\zeta_1) + e^{-(n+1/2)|\zeta_1|}G_{n+1}(\zeta_2)\right)\Bigg]
\end{aligned}
\tag{10.76}
$$

Attempting to simplify these products of trig expresions D, E, F, G,

$$
\begin{aligned}
&E_{n+1}(\zeta_1)G_{n+1}(\zeta_2) - E_{n+1}(\zeta_2)G_{n+1}(\zeta_1) \\
&\qquad = (n+3/2)\sinh(n+3/2)\zeta_1 \times (n+3/2)\cosh(n+3/2)\zeta_2 \\
&\qquad\quad - (n+3/2)\sinh(n+3/2)\zeta_2 \times (n+3/2)\cosh(n+3/2)\zeta_1 \\
&\qquad = (n+3/2)^2\sinh(n+3/2)(\zeta_1 - \zeta_2)
\end{aligned}
\tag{10.77}
$$

$$
\begin{aligned}
&G_{n-1}(\zeta_2)G_{n+1}(\zeta_1) - G_{n-1}(\zeta_1)G_{n+1}(\zeta_2) \\
&\qquad = (n-1/2)\cosh(n-1/2)\zeta_2 \times (n+3/2)\cosh(n+3/2)\zeta_1 \\
&\qquad\quad - (n-1/2)\cosh(n-1/2)\zeta_1 \times (n+3/2)\cosh(n+3/2)\zeta_2
\end{aligned}
\tag{10.78}
$$

$$
\begin{aligned}
&E_{n-1}(\zeta_2)G_{n+1}(\zeta_1) - E_{n-1}(\zeta_1)G_{n+1}(\zeta_2) \\
&\qquad = (n-1/2)\sinh(n-1/2)\zeta_2 \times (n+3/2)\cosh(n+3/2)\zeta_1 \\
&\qquad\quad - (n-1/2)\sinh(n-1/2)\zeta_1 \times (n+3/2)\cosh(n+3/2)\zeta_2
\end{aligned}
\tag{10.79}
$$

$$
\begin{aligned}
&D_n(\zeta_2)G_{n+1}(\zeta_1) - D_n(\zeta_1)G_{n+1}(\zeta_2) \\
&\quad = \left(\frac{1}{2}\sinh\zeta_2\cosh(n+1/2)\zeta_2 + (n+1/2)\cosh\zeta_2\sinh(n+1/2)\zeta_2\right) && (10.80)\\
&\qquad \times (n+3/2)\cosh(n+3/2)\zeta_1 \\
&\qquad - \left(\frac{1}{2}\sinh\zeta_1\cosh(n+1/2)\zeta_1 + (n+1/2)\cosh\zeta_1\sinh(n+1/2)\zeta_1\right) \\
&\qquad\quad \times (n+3/2)\cosh(n+3/2)\zeta_2 \\
&\quad = (n+3/2)\Big(n\big[\cosh\zeta_2\sinh(n+1/2)\zeta_2\cosh(n+3/2)\zeta_1 && (10.81)\\
&\qquad\qquad - \cosh\zeta_1\sinh(n+1/2)\zeta_1\cosh(n+3/2)\zeta_2\big] \\
&\qquad\qquad + \frac{1}{2}\left[\sinh\zeta_2\cosh(n+1/2)\zeta_2 + \cosh\zeta_2\sinh(n+1/2)\zeta_2\right]\cosh(n+3/2)\zeta_1 \\
&\qquad\qquad - \frac{1}{2}\left[\sinh\zeta_1\cosh(n+1/2)\zeta_1 + \cosh\zeta_1\sinh(n+1/2)\zeta_1\right]\cosh(n+3/2)\zeta_2\Big) \\
&\quad = (n+3/2)\Big(n\big[\cosh\zeta_2\sinh(n+1/2)\zeta_2\cosh(n+3/2)\zeta_1 && (10.82)\\
&\qquad\qquad - \cosh\zeta_1\sinh(n+1/2)\zeta_1\cosh(n+3/2)\zeta_2\big] \\
&\qquad\qquad + \frac{1}{2}\sinh(n+3/2)\zeta_2\cosh(n+3/2)\zeta_1 \\
&\qquad\qquad - \frac{1}{2}\sinh(n+3/2)\zeta_1\cosh(n+3/2)\zeta_2\Big) \\
&\quad = (n+3/2)\Big(n\big[\cosh\zeta_2\sinh(n+1/2)\zeta_2\cosh(n+3/2)\zeta_1 && (10.83)\\
&\qquad\qquad - \cosh\zeta_1\sinh(n+1/2)\zeta_1\cosh(n+3/2)\zeta_2\big] \\
&\qquad\qquad - \frac{1}{2}\sinh(n+3/2)(\zeta_1-\zeta_2)\Big)
\end{aligned}
$$

$$
\begin{aligned}
&F_n(\zeta_2)G_{n+1}(\zeta_1) - F_n(\zeta_1)G_{n+1}(\zeta_2) \\
&\quad = \left(\frac{1}{2}\sinh\zeta_2 \sinh(n+1/2)\zeta_2 + (n+1/2)\cosh\zeta_2\cosh(n+1/2)\zeta_2\right) && (10.84)\\
&\qquad \times (n+3/2)\cosh(n+3/2)\zeta_1 \\
&\qquad - \left(\frac{1}{2}\sinh\zeta_1 \sinh(n+1/2)\zeta_1 + (n+1/2)\cosh\zeta_1\cosh(n+1/2)\zeta_1\right) \\
&\qquad\quad \times (n+3/2)\cosh(n+3/2)\zeta_2 \\
&\quad = (n+3/2)\Big(n\big[\cosh\zeta_2\cosh(n+1/2)\zeta_2\cosh(n+3/2)\zeta_1 && (10.85)\\
&\qquad\qquad - \cosh\zeta_1\cosh(n+1/2)\zeta_1\cosh(n+3/2)\zeta_2\big] \\
&\qquad\qquad + \frac{1}{2}\left[\sinh\zeta_2\sinh(n+1/2)\zeta_2 + \cosh\zeta_2\cosh(n+1/2)\zeta_2\right]\cosh(n+3/2)\zeta_1 \\
&\qquad\qquad - \frac{1}{2}\left[\sinh\zeta_1\sinh(n+1/2)\zeta_1 + \cosh\zeta_1\cosh(n+1/2)\zeta_1\right]\cosh(n+3/2)\zeta_2\Big) \\
&\quad = (n+3/2)\Big(n\big[\cosh\zeta_2\cosh(n+1/2)\zeta_2\cosh(n+3/2)\zeta_1 && (10.86)\\
&\qquad\qquad - \cosh\zeta_1\cosh(n+1/2)\zeta_1\cosh(n+3/2)\zeta_2\big] \\
&\qquad\qquad + \cancel{\frac{1}{2}\cosh(n+3/2)\zeta_2\cosh(n+3/2)\zeta_1} \\
&\qquad\qquad - \cancel{\frac{1}{2}\cosh(n+3/2)\zeta_1\cosh(n+3/2)\zeta_2}\Big) \\
&\quad = (n+3/2)\Big(n\big[\cosh\zeta_2\cosh(n+1/2)\zeta_2\cosh(n+3/2)\zeta_1 && (10.87)\\
&\qquad\qquad - \cosh\zeta_1\cosh(n+1/2)\zeta_1\cosh(n+3/2)\zeta_2\big]\Big)
\end{aligned}
$$

This does provide some simplification

$$
\begin{aligned}
B^{(2)}_{n+1} = & -\frac{2}{n+1}\Bigg[B^{(2)}_n[D_n(\zeta_2)G_{n+1}(\zeta_1) - D_n(\zeta_1)G_{n+1}(\zeta_2)] \\
& + B^{(1)}_n[F_n(\zeta_2)G_{n+1}(\zeta_1) - F_n(\zeta_1)G_{n+1}(\zeta_2)] \\
& - \frac{n}{(2n-1)}\Big(B^{(2)}_{n-1}[E_{n-1}(\zeta_2)G_{n+1}(\zeta_1) - E_{n-1}(\zeta_1)G_{n+1}(\zeta_2)] \\
& \qquad + B^{(1)}_{n-1}[G_{n-1}(\zeta_2)G_{n+1}(\zeta_1) - G_{n-1}(\zeta_1)G_{n+1}(\zeta_2)]\Big) \\
& + \sqrt{2}c\left(\tilde{q}e^{-(n+1/2)|\zeta_2|}G_{n+1}(\zeta_1) + e^{-(n+1/2)|\zeta_1|}G_{n+1}(\zeta_2)\right)\Bigg] \\
& \times \Big((n+3/2)\sinh(n+3/2)(\zeta_1-\zeta_2)\Big)^{-1}
\end{aligned}
\tag{10.88}
$$

But it too unwieldy to try and simplify anymore as a whole. Let's proceed by breaking it into pieces.

$$
B^{(2)}_{n+1} = [a^{(2)}(n)B^{(2)}_n + a^{(1)}(n)B^{(1)}_n + b^{(2)}(n)B^{(2)}_{n-1} + b^{(1)}(n)B^{(1)}_{n-1} + c(n)] \tag{10.89}
$$

Simplifying the prefactors on the coefficients of order $(n-1)$ using the trigonometric

simplifications in Eqs. 10.79 and 10.78,

$$
\begin{aligned}
&b^{(2)}(n)B^{(2)}_{n-1} + b^{(1)}(n)B^{(1)}_{n-1} \\
&\qquad = \left(\frac{-2}{n+1}\right)\left(\frac{-n}{(2n-1)}\right)\Big(B^{(2)}_{n-1}[E_{n-1}(\zeta_2)G_{n+1}(\zeta_1) - E_{n-1}(\zeta_1)G_{n+1}(\zeta_2)] \\
&\qquad\qquad + B^{(1)}_{n-1}[G_{n-1}(\zeta_2)G_{n+1}(\zeta_1) - G_{n-1}(\zeta_1)G_{n+1}(\zeta_2)]\Big) \\
&= \frac{n\cancel{(n+3/2)}}{n+1}\Big(B^{(2)}_{n-1}[\sinh(n-1/2)\zeta_2\cosh(n+3/2)\zeta_1 - \sinh(n-1/2)\zeta_1\cosh(n+3/2)\zeta_2] \\
&\qquad + B^{(1)}_{n-1}[\cosh(n-1/2)\zeta_2\cosh(n+3/2)\zeta_1 - \cosh(n-1/2)\zeta_1\cosh(n+3/2)\zeta_2]\Big) \\
&\qquad\qquad \times \left(\cancel{(n+3/2)}\sinh(n+3/2)(\zeta_1-\zeta_2)\right)^{-1} \\
&\qquad = \frac{n}{n+1}\Big(\cosh(n+3/2)\zeta_1\big[B^{(2)}_{n-1}\sinh(n-1/2)\zeta_2 + B^{(1)}_{n-1}\cosh(n-1/2)\zeta_2\big] \\
&\qquad\quad - \cosh(n+3/2)\zeta_2\big[B^{(2)}_{n-1}\sinh(n-1/2)\zeta_1 + B^{(1)}_{n-1}\cosh(n-1/2)\zeta_1\big]\Big) \\
&\qquad\qquad \times \big(\sinh(n+3/2)(\zeta_1-\zeta_2)\big)^{-1} \\
&\qquad = \frac{n}{n+1}\Big(\cosh(n+3/2)\zeta_1 A_{n-1}(\zeta_2) - \cosh(n+3/2)\zeta_2 A_{n-1}(\zeta_1)\Big) \\
&\qquad\qquad \times \big(\sinh(n+3/2)(\zeta_1-\zeta_2)\big)^{-1} \qquad (10.90)
\end{aligned}
$$

where in the last line we have defined the new nth order coefficient $A_n(\zeta_{1,2}) \equiv B^{(2)}_n \sinh(n+1/2)\zeta_{1,2} + B^{(1)}_n \cosh(n+1/2)\zeta_{1,2}$

Next try simplifying the coefficients of the order n terms with the denominator.

$$
\begin{aligned}
&a^{(2)}(n)B_n^{(2)} + a^{(1)}(n)B_n^{(1)} \\
&\qquad = -\frac{2}{n+1}\big(B_n^{(2)}[D_n(\zeta_2)G_{n+1}(\zeta_1) - D_n(\zeta_1)G_{n+1}(\zeta_2)] \\
&\qquad\qquad + B_n^{(1)}[F_n(\zeta_2)G_{n+1}(\zeta_1) - F_n(\zeta_1)G_{n+1}(\zeta_2)]\big) \\
&\qquad\qquad \times \big((n+3/2)\sinh(n+3/2)(\zeta_1-\zeta_2)\big)^{-1} \\
&\qquad = -\frac{2}{n+1}B_n^{(2)}\bigg(-\frac{1}{2} + n\big[\cosh\zeta_2\sinh(n+1/2)\zeta_2\cosh(n+3/2)\zeta_1 \\
&\qquad\qquad - \cosh\zeta_1\sinh(n+1/2)\zeta_1\cosh(n+3/2)\zeta_2\big] \\
&\qquad\qquad \times \big(\sinh(n+3/2)(\zeta_1-\zeta_2)\big)^{-1}\bigg) \\
&\qquad\qquad - \frac{2}{n+1}nB_n^{(1)}\bigg(\cosh\zeta_2\cosh(n+1/2)\zeta_2\cosh(n+3/2)\zeta_1 \\
&\qquad\qquad\qquad - \cosh\zeta_1\cosh(n+1/2)\zeta_1\cosh(n+3/2)\zeta_2\bigg) \\
&\qquad\qquad\qquad \times \big(\sinh(n+3/2)(\zeta_1-\zeta_2)\big)^{-1} \\
&= \frac{B_n^{(2)}}{n+1} - \frac{2n}{n+1}\big[\cosh\zeta_2\cosh(n+3/2)\zeta_1\big(B_n^{(2)}\sinh(n+1/2)\zeta_2 + B_n^{(1)}\cosh(n+1/2)\zeta_2\big) \\
&\qquad - \cosh\zeta_1\cosh(n+3/2)\zeta_2\big(B_n^{(2)}\sinh(n+1/2)\zeta_1 + B_n^{(1)}\cosh(n+1/2)\zeta_1\big)\big] \\
&\qquad\qquad \times \big(\sinh(n+3/2)(\zeta_1-\zeta_2)\big)^{-1} \\
&= \frac{B_n^{(2)}}{n+1} - \frac{2n}{n+1}\big[\cosh\zeta_2\cosh(n+3/2)\zeta_1 A_n(\zeta_2) - \cosh\zeta_1\cosh(n+3/2)\zeta_2 A_n(\zeta_1)\big] \\
&\qquad\qquad\qquad\qquad \times \big(\sinh(n+3/2)(\zeta_1-\zeta_2)\big)^{-1} \qquad (10.91)
\end{aligned}
$$

and the constant term

$$
\begin{aligned}
c(n) &= -\frac{2}{n+1}\sqrt{2}c\frac{\tilde{q}e^{-(n+1/2)|\zeta_2|}G_{n+1}(\zeta_1) + e^{-(n+1/2)|\zeta_1|}G_{n+1}(\zeta_2)}{(n+3/2)\sinh(n+3/2)(\zeta_1-\zeta_2)} \\
&= -\frac{2\sqrt{2}c}{n+1}\frac{\tilde{q}e^{-(n+1/2)|\zeta_2|}\cosh(n+3/2)\zeta_1 + e^{-(n+1/2)|\zeta_1|}\cosh(n+3/2)\zeta_2}{\sinh(n+3/2)(\zeta_1-\zeta_2)}
\end{aligned}
\qquad (10.92)
$$

Let's take the Kang limit of these things and see what happens. Note that the Kang limit of the A coefficients is

$$\lim_{\text{Kang}} A_n(\zeta_2) = -B_n^{(2)} \sinh(n+1/2)\zeta_0 + B_n^{(1)} \cosh(n+1/2)\zeta_0 \tag{10.93}$$

$$\lim_{\text{Kang}} A_n(\zeta_1) = B_n^{(2)} \sinh(n+1/2)\zeta_0 + B_n^{(1)} \cosh(n+1/2)\zeta_0 \tag{10.94}$$

$$\begin{aligned}
&\lim_{\text{Kang}} [a^{(2)}(n)B_n^{(2)} + a^{(1)}(n)B_n^{(1)}] \\
&\qquad = \frac{B_n^{(2)}}{n+1} + \frac{4n}{n+1} B_n^{(2)} \sinh(n+1/2)\zeta_0 \cosh\zeta_0 \cosh(n+3/2)\zeta_0 \\
&\qquad\qquad \times \big(\sinh(n+3/2)(2\zeta_0)\big)^{-1} \\
&\qquad = \frac{B_n^{(2)}}{n+1} + \frac{\cancel{2}2n}{n+1} B_n^{(2)} \sinh(n+1/2)\zeta_0 \cosh\zeta_0 \cancel{\cosh(n+3/2)\zeta_0} \\
&\qquad\qquad \times \cancel{(2\cosh(n+\tfrac{3}{2})\zeta_0} \sin(n+\tfrac{3}{2})\zeta_0)^{-1} \\
&\qquad = B_n^{(2)} \frac{1}{n+1} \left[1 + 2n \frac{\sinh(n+1/2)\zeta_0 \cosh\zeta_0}{\sin(n+\frac{3}{2})\zeta_0}\right] = B_n^{(2)} G^{\text{Kang}} \quad \blacksquare
\end{aligned} \tag{10.95}$$

which is good! Next lets try the same limit of the order n terms

$$\begin{aligned}
&\lim_{\text{Kang}} [b^{(2)}(n)B_{n-1}^{(2)} + b^{(1)}(n)B_{n-1}^{(1)}] \\
&\qquad = \frac{n}{n+1} \Big(\cosh(n+3/2)\zeta_1 A_{n-1}(\zeta_2) - \cosh(n+3/2)\zeta_2 A_{n-1}(\zeta_1) \Big) \\
&\qquad\qquad \times \big(\sinh(n+3/2)(\zeta_1 - \zeta_2)\big)^{-1} \\
&\qquad = \frac{n}{n+1} B_{n-1}^{(2)} \frac{\cancel{\cosh(n+3/2)\zeta_0}(-\cancel{2}\sinh(n-1/2)\zeta_0)}{\cancel{2}\cancel{\cosh(n+3/2)\zeta_0} \sinh(n+3/2)\zeta_0} \\
&\qquad = -\frac{1}{n+1} B_{n-1}^{(2)} \frac{n \sinh(n-1/2)\zeta_0}{\sinh(n+3/2)\zeta_0}
\end{aligned} \tag{10.96}$$

This is not obviously equal to $(1 - G^{\text{Kang}})$. Let's see.

$$\begin{aligned} 1 - G^{\text{Kang}} &= 1 - \frac{1}{n+1}\left[1 + 2n\frac{\sinh(n+1/2)\zeta_0 \cosh\zeta_0}{\sin(n+\frac{3}{2})\zeta_0}\right] \\ &= \frac{1}{n+1}\left[\cancel{n+1-1} - 2n\frac{\sinh(n+1/2)\zeta_0 \cosh\zeta_0}{\sin(n+\frac{3}{2})\zeta_0}\right] \\ &= \frac{n}{n+1}\frac{\sin(n+3/2)\zeta_0 - 2\sinh(n+1/2)\zeta_0 \cosh\zeta_0}{\sin(n+3/2)\zeta_0} \end{aligned} \tag{10.97}$$

and apparently,

$$-2\sinh(n+1/2)\zeta_0 \cosh\zeta_0 = -\sinh(n-1/2)\zeta_0 - \sinh(n+3/2)\zeta_0 \tag{10.98}$$

and so

$$1 - G^{\text{Kang}} = \frac{n}{n+1}\frac{\cancel{\sin(n+3/2)\zeta_0} - \sinh(n-1/2)\zeta_0 - \cancel{\sinh(n+3/2)\zeta_0}}{\sin(n+3/2)\zeta_0} \quad \blacksquare \tag{10.99}$$

which is equivalent to Eq. 10.96! Yay.

$$\begin{aligned} \lim_{\text{Kang}} c(n) &= -\frac{2\sqrt{2}c}{n+1}\frac{\tilde{q}e^{-(n+1/2)|\zeta_2|}\cosh(n+3/2)\zeta_1 + e^{-(n+1/2)|\zeta_1|}\cosh(n+3/2)\zeta_2}{\sinh(n+3/2)(\zeta_1 - \zeta_2)} \\ &= -\frac{2\sqrt{2}c}{n+1}\frac{\cancel{\cosh(n+3/2)\zeta_0}\left(\cancel{\tilde{q}}^{1}e^{-(n+1/2)|\zeta_0|} + e^{-(n+1/2)|\zeta_0|}\right)}{2\cancel{\cosh(n+3/2)\zeta_0}\sin(n+3/2)\zeta_0} \\ &= -\frac{2\sqrt{2}c}{n+1}\frac{e^{-(n+1/2)|\zeta_0|}}{\sin(n+3/2)\zeta_0} \quad \blacksquare \end{aligned} \tag{10.100}$$

OK, I am as comfortable as I can be with these expressions now, let's try and put them

back together and see if they can be simplified.

$$
\begin{aligned}
B^{(2)}_{n+1} - c(n) &= \frac{B^{(2)}_n}{n+1} - \frac{2n}{n+1}\frac{\cosh\zeta_2\cosh(n+3/2)\zeta_1 A_n(\zeta_2) - \cosh\zeta_1\cosh(n+3/2)\zeta_2 A_n(\zeta_1)\big]}{\sinh(n+3/2)(\zeta_1-\zeta_2)} \\
&\quad + \frac{n}{n+1}\frac{\cosh(n+3/2)\zeta_1 A_{n-1}(\zeta_2) - \cosh(n+3/2)\zeta_2 A_{n-1}(\zeta_1)}{\sinh(n+3/2)(\zeta_1-\zeta_2)} \qquad (10.101) \\
&= \frac{B^{(2)}_n}{n+1} + \frac{n}{n+1}\Bigg(-2\frac{\cosh\zeta_2\cosh(n+3/2)\zeta_1 A_n(\zeta_2) - \cosh\zeta_1\cosh(n+3/2)\zeta_2 A_n(\zeta_1)\big]}{\sinh(n+3/2)(\zeta_1-\zeta_2)} \\
&\quad + \frac{\cosh(n+3/2)\zeta_1 A_{n-1}(\zeta_2) - \cosh(n+3/2)\zeta_2 A_{n-1}(\zeta_1)}{\sinh(n+3/2)(\zeta_1-\zeta_2)}\Bigg) \qquad (10.102) \\
&= \frac{B^{(2)}_n}{n+1} + \frac{n}{n+1}\Bigg(-\cosh(n+3/2)\zeta_1\big[2\cosh\zeta_2 A_n(\zeta_2) - A_{n-1}(\zeta_2)\big] \\
&\qquad\qquad + \cosh(n+3/2)\zeta_2\big[2\cosh\zeta_1 A_n(\zeta_1) - A_{n-1}(\zeta_1)\big]\Bigg) \qquad (10.103) \\
&\qquad \times \frac{1}{\sinh(n+3/2)(\zeta_1-\zeta_2)} \qquad (10.104)
\end{aligned}
$$

Simplifying the A coefficients

$$
\begin{aligned}
&2\cosh\zeta_2 A_n(\zeta_2) - A_{n-1}(\zeta_2) \\
&\qquad = 2\cosh\zeta_2\left(B^{(2)}_n\sinh(n+1/2)\zeta_2 + B^{(1)}_n\cosh(n+1/2)\zeta_2\right) \\
&\qquad\quad - B^{(2)}_{n-1}\sinh(n-1/2)\zeta_2 - B^{(1)}_{n-1}\cosh(n-1/2)\zeta_2 \\
&\qquad\quad = \Big(B^{(2)}_n[\sinh(n-1/2)\zeta_2 + \sinh(n+3/2)\zeta_2] \\
&\qquad\quad + B^{(1)}_n[\cosh(n-1/2)\zeta_2 + \cosh(n+3/2)\zeta_2\Big) \\
&\qquad\qquad - B^{(2)}_{n-1}\sinh(n-1/2)\zeta_2 - B^{(1)}_{n-1}\cosh(n-1/2)\zeta_2 \qquad (10.105)
\end{aligned}
$$

and combining with the rest of the recursion relation yield

$$
\begin{aligned}
B^{(2)}_{n+1} - c(n) = \frac{B^{(2)}_n}{n+1} + \frac{n}{n+1}\Bigg[& \\
& B^{(2)}_n\Big(-\cosh(n+3/2)\zeta_1\big[\sinh(n-1/2)\zeta_2 + \sinh(n+3/2)\zeta_2\big] \\
& \quad + \cosh(n+3/2)\zeta_2\big[\sinh(n-1/2)\zeta_1 + \sinh(n+3/2)\zeta_1\big]\Big) \\
& + B^{(1)}_n\Big(-\cosh(n+3/2)\zeta_1\big[\cosh(n-1/2)\zeta_2 + \cosh(n+3/2)\zeta_2\big] \\
& \quad + \cosh(n+3/2)\zeta_2\big[\cosh(n-1/2)\zeta_1 + \cosh(n+3/2)\zeta_1\big]\Big) \\
& - B^{(2)}_{n-1}\Big(-\cosh(n+3/2)\zeta_1\sinh(n-1/2)\zeta_2 + \cosh(n+3/2)\zeta_2\sinh(n-1/2)\zeta_1\Big) \\
& - B^{(1)}_{n-1}\Big(-\cosh(n+3/2)\zeta_1\cosh(n-1/2)\zeta_2 + \cosh(n+3/2)\zeta_2\cosh(n-1/2)\zeta_1\Big)\Bigg] \\
& \qquad \times \frac{1}{\sinh(n+3/2)(\zeta_1-\zeta_2)}
\end{aligned}
$$

Noticing that some of the order $B^{(2)}_n$ terms cancel with the denominator because

$$
\begin{aligned}
& -\cosh(n+3/2)\zeta_1\sinh(n-1/2)\zeta_2 + \cosh(n+3/2)\zeta_2\sinh(n+3/2)\zeta_1 \\
& \qquad = \sinh(n+3/2)(\zeta_1-\zeta_2) \quad (10.106)
\end{aligned}
$$

and the associated $B^{(1)}_n$ terms simply cancel,

$$
\begin{aligned}
B^{(2)}_{n+1} - c(n) = \frac{\cancel{(n+1)}B^{(2)}_n}{\cancel{n+1}} + \frac{n}{n+1}\Bigg[& \\
& (-B^{(2)}_n + B^{(2)}_{n-1})\Big(\cosh(n+3/2)\zeta_1\sinh(n-1/2)\zeta_2 - \cosh(n+3/2)\zeta_2\sinh(n-1/2)\zeta_1\Big) \\
& + (-B^{(1)}_n + B^{(1)}_{n-1})\Big(\cosh(n+3/2)\zeta_1\cosh(n-1/2)\zeta_2 - \cosh(n+3/2)\zeta_2\cosh(n-1/2)\zeta_1\Big)\Bigg] \\
& \qquad \times \frac{1}{\sinh(n+3/2)(\zeta_1-\zeta_2)}
\end{aligned}
$$

Now we can define a few n dependent prefactors in analogy to Kang's notation. Note that

with the definitions

$$1-G_n^{(2)}=\frac{n}{n+1}\frac{\cosh(n+3/2)\zeta_1\sinh(n-1/2)\zeta_2-\cosh(n+3/2)\zeta_2\sinh(n-1/2)\zeta_1}{\sinh(n+3/2)(\zeta_1-\zeta_2)} \tag{10.107}$$

$$1-G_n^{(1)}=\frac{n}{n+1}\frac{\cosh(n+3/2)\zeta_1\cosh(n-1/2)\zeta_2-\cosh(n+3/2)\zeta_2\cosh(n-1/2)\zeta_1}{\sinh(n+3/2)(\zeta_1-\zeta_2)} \tag{10.108}$$

and realizing that $1-(1-G^{(2)})=G^{(2)}$, we can write this expression as

$$B_{n+1}^{(2)}-c(n)=G_n^{(2)}B_n^{(2)}+(1-G_n^{(2)})B_{n-1}^{(2)}+(1-G_n^{(1)})(-B_n^{(1)}+B_{n-1}^{(1)}) \tag{10.109}$$

and we have the recursion relation for for $B^{(2)}$ in compact for analogous to Kang. Before moving on to the other relation, I'll take the Kang limit of this expression. The prefactor on the $B_n^{(1)}-B_{n-1}^{(1)}$ cancels exactly and we are left with

$$\begin{aligned}
\lim_{\text{Kang}} B_{n+1}^{(2)}-c(n) &= B_n^{(2)}+\frac{1}{n+1}\frac{2n(B_n^{(2)}-B_{n-1}^{(2)})\cosh(n+3/2)\zeta_0\sinh(n-1/2)\zeta_0}{\sinh(n+3/2)(2\zeta_0)}\\
&= B_n^{(2)}+\frac{1}{n+1}\frac{\cancel{2}n(B_n^{(2)}-B_{n-1}^{(2)})\cancel{\cosh(n+3/2)\zeta_0}\sinh(n-1/2)\zeta_0}{\cancel{2}\cancel{\cosh(n+3/2)\zeta_0}\sin(n+3/2)\zeta_0}\\
&= \frac{1}{n+1}\frac{(n+1)B_n^{(2)}\sin(n+3/2)\zeta_0+n(B_n^{(2)}-B_{n-1}^{(2)})\sinh(n-1/2)\zeta_0}{\sin(n+3/2)\zeta_0}\\
&= \frac{1}{n+1}\frac{B_n^{(2)}[(n+1)\sin(n+3/2)\zeta_0+n\sinh(n-1/2)\zeta_0]-nB_{n-1}^{(2)}\sinh(n-1/2)\zeta_0}{\sin(n+3/2)\zeta_0}\\
&= B_n^{(2)}\left(\frac{1}{n+1}\frac{(n+1)\sin(n+3/2)\zeta_0+n\sinh(n-1/2)\zeta_0}{\sin(n+3/2)\zeta_0}\right)\\
&\qquad -B_{n-1}^{(2)}\left(\frac{1}{n+1}\frac{n\sinh(n-1/2)\zeta_0}{\sin(n+3/2)\zeta_0}\right)
\end{aligned}$$

Introducing the definition of $1-G_n^{\text{Kang}}$,

$$\begin{aligned}
\lim_{\text{Kang}} B_{n+1}^{(2)}-c(n) &= B_n^{(2)}\left(\frac{\cancel{n+1}}{\cancel{n+1}}\frac{\cancel{\sin(n+3/2)\zeta_0}}{\cancel{\sin(n+3/2)\zeta_0}}+\frac{1}{n+1}\frac{n\sinh(n-1/2)\zeta_0}{\sin(n+3/2)\zeta_0}\right)\\
&\qquad +B_{n-1}^{(2)}\left(1-G_n^{\text{Kang}}\right)\\
&= B_n^{(2)}\left(\cancel{1}-(\cancel{1}-G_n^{\text{Kang}})\right)+B_{n-1}^{(2)}\left(1-G_n^{\text{Kang}}\right)\\
&= B_n^{(2)}G_n^{\text{Kang}}+B_{n-1}^{(2)}\left(1-G_n^{\text{Kang}}\right) \quad \blacksquare
\end{aligned}$$

Looking at the associate recursion relation for $B^{(1)}$, we can simply take Eq. 10.76 and interchange the prefactor components G_{n+1} and E_{n+1}. This yields a sign flip on the left hand side

$$\begin{aligned}
&B^{(1)}_{n+1}[E_{n+1}(\zeta_1)G_{n+1}(\zeta_2) - E_{n+1}(\zeta_2)G_{n+1}(\zeta_1)] \\
&\qquad = \frac{(2n+3)}{n+1}\Bigg[B^{(2)}_n[D_n(\zeta_2)E_{n+1}(\zeta_1) - D_n(\zeta_1)E_{n+1}(\zeta_2)] \\
&\qquad\qquad + B^{(1)}_n[F_n(\zeta_2)E_{n+1}(\zeta_1) - F_n(\zeta_1)E_{n+1}(\zeta_2)] \\
&\qquad - \frac{n}{(2n-1)}\Big(B^{(2)}_{n-1}[E_{n-1}(\zeta_2)E_{n+1}(\zeta_1) - E_{n-1}(\zeta_1)E_{n+1}(\zeta_2)] \\
&\qquad\qquad + B^{(1)}_{n-1}[G_{n-1}(\zeta_2)E_{n+1}(\zeta_1) - G_{n-1}(\zeta_1)E_{n+1}(\zeta_2)]\Big) \\
&\qquad\qquad + \sqrt{2}c\left(\tilde{q}e^{-(n+1/2)|\zeta_2|}E_{n+1}(\zeta_1) + e^{-(n+1/2)|\zeta_1|}E_{n+1}(\zeta_2)\right)\Bigg]
\end{aligned} \tag{10.110}$$

which amounts to interchanging $\cosh(n+3/2)\zeta_{1,2}$ with $\cosh(n+3/2)\zeta_{1,2}$ in each of those products.

$$\begin{aligned}
&G_{n-1}(\zeta_2)E_{n+1}(\zeta_1) - G_{n-1}(\zeta_1)E_{n+1}(\zeta_2) \\
&\qquad = (n-1/2)\cosh(n-1/2)\zeta_2 \times (n+3/2)\sinh(n+3/2)\zeta_1 \\
&\qquad\quad - (n-1/2)\cosh(n-1/2)\zeta_1 \times (n+3/2)\sinh(n+3/2)\zeta_2
\end{aligned} \tag{10.111}$$

$$\begin{aligned}
&E_{n-1}(\zeta_2)E_{n+1}(\zeta_1) - E_{n-1}(\zeta_1)E_{n+1}(\zeta_2) \\
&\qquad = (n-1/2)\sinh(n-1/2)\zeta_2 \times (n+3/2)\sinh(n+3/2)\zeta_1 \\
&\qquad\quad - (n-1/2)\sinh(n-1/2)\zeta_1 \times (n+3/2)\sinh(n+3/2)\zeta_2
\end{aligned} \tag{10.112}$$

from Eq. 10.80,

$$
\begin{aligned}
&D_n(\zeta_2)E_{n+1}(\zeta_1) - D_n(\zeta_1)E_{n+1}(\zeta_2) \\
&\quad = (n+3/2)\Big(n\big[\cosh\zeta_2 \sinh(n+1/2)\zeta_2 \sinh(n+3/2)\zeta_1 \qquad (10.113)\\
&\qquad\qquad - \cosh\zeta_1 \sinh(n+1/2)\zeta_1 \sinh(n+3/2)\zeta_2\big] \\
&\qquad\qquad + \frac{1}{2}\cancel{\sinh(n+3/2)\zeta_2 \sinh(n+3/2)\zeta_1} \\
&\qquad\qquad - \frac{1}{2}\cancel{\sinh(n+3/2)\zeta_1 \sinh(n+3/2)\zeta_2}\Big) \\
&\quad = n(n+3/2)\big[\cosh\zeta_2 \sinh(n+1/2)\zeta_2 \sinh(n+3/2)\zeta_1 \qquad (10.114)\\
&\qquad\qquad - \cosh\zeta_1 \sinh(n+1/2)\zeta_1 \sinh(n+3/2)\zeta_2\big]
\end{aligned}
$$

and from 10.84

$$
\begin{aligned}
&F_n(\zeta_2)E_{n+1}(\zeta_1) - F_n(\zeta_1)E_{n+1}(\zeta_2) \\
&\quad = (n+3/2)\Big(n\big[\cosh\zeta_2 \cosh(n+1/2)\zeta_2 \sinh(n+3/2)\zeta_1 \qquad (10.115)\\
&\qquad\qquad - \cosh\zeta_1 \cosh(n+1/2)\zeta_1 \sinh(n+3/2)\zeta_2\big] \\
&\qquad\qquad + \frac{1}{2}\cosh(n+3/2)\zeta_2 \sinh(n+3/2)\zeta_1 \\
&\qquad\qquad - \frac{1}{2}\cosh(n+3/2)\zeta_1 \sinh(n+3/2)\zeta_2\Big) \\
&\quad = (n+3/2)\Big(n\big[\cosh\zeta_2 \cosh(n+1/2)\zeta_2 \sinh(n+3/2)\zeta_1 \qquad (10.116)\\
&\qquad\qquad - \cosh\zeta_1 \cosh(n+1/2)\zeta_1 \sinh(n+3/2)\zeta_2\big] \\
&\qquad\qquad + \frac{1}{2}\sinh(n+3/2)(\zeta_1-\zeta_2)\Big)
\end{aligned}
$$

Applying these differences to Eq. 10.90

$$\begin{aligned}\tilde{b}^{(2)}(n)B^{(2)}_{n-1} + \tilde{b}^{(1)}(n)B^{(1)}_{n-1} \\ = -\frac{n}{n+1}\Big(\sinh(n+3/2)\zeta_1 A_{n-1}(\zeta_2) - \sinh(n+3/2)\zeta_2 A_{n-1}(\zeta_1)\Big) \\ \times \big(\sinh(n+3/2)(\zeta_1-\zeta_2)\big)^{-1}\end{aligned} \tag{10.117}$$

and to Eq. 10.91

$$\begin{aligned}\tilde{a}^{(2)}(n)B^{(2)}_{n} + \tilde{a}^{(1)}(n)B^{(1)}_{n} \\ = \frac{2}{n+1}\big(B^{(2)}_n[D_n(\zeta_2)E_{n+1}(\zeta_1) - D_n(\zeta_1)E_{n+1}(\zeta_2)] \\ + B^{(1)}_n[F_n(\zeta_2)E_{n+1}(\zeta_1) - F_n(\zeta_1)E_{n+1}(\zeta_2)]\big) \\ \times \big((n+3/2)\sinh(n+3/2)(\zeta_1-\zeta_2)\big)^{-1} \\ = \frac{2}{n+1}B^{(2)}_n\Big(n\big[\cosh\zeta_2\sinh(n+1/2)\zeta_2\sinh(n+3/2)\zeta_1 \\ - \cosh\zeta_1\sinh(n+1/2)\zeta_1\sinh(n+3/2)\zeta_2\big] \\ \times \big(\sinh(n+3/2)(\zeta_1-\zeta_2)\big)^{-1}\Big) \\ + \frac{2}{n+1}B^{(1)}_n\Big(\frac{1}{2} + n\big[\cosh\zeta_2\cosh(n+1/2)\zeta_2\sinh(n+3/2)\zeta_1 \\ - \cosh\zeta_1\cosh(n+1/2)\zeta_1\sinh(n+3/2)\zeta_2\big]\Big) \\ \times \big(\sinh(n+3/2)(\zeta_1-\zeta_2)\big)^{-1} \\ = +\frac{B^{(1)}_n}{n+1} + \frac{2n}{n+1}\big[\cosh\zeta_2\sinh(n+3/2)\zeta_1 A_n(\zeta_2) - \cosh\zeta_1\sinh(n+3/2)\zeta_2 A_n(\zeta_1)\big] \\ \times \big(\sinh(n+3/2)(\zeta_1-\zeta_2)\big)^{-1}\end{aligned} \tag{10.118}$$

and the constant term

$$\begin{aligned}\tilde{c}(n) = \frac{(2n+3)}{n+1}\frac{\sqrt{2}c\left(\tilde{q}e^{-(n+1/2)|\zeta_2|}E_{n+1}(\zeta_1) + e^{-(n+1/2)|\zeta_1|}E_{n+1}(\zeta_2)\right)}{(n+3/2)\sinh(n+3/2)(\zeta_1-\zeta_2)} \\ = \frac{2\sqrt{2}c}{n+1}\frac{\tilde{q}e^{-(n+1/2)|\zeta_2|}\sinh(n+3/2)\zeta_1 + e^{-(n+1/2)|\zeta_1|}\sinh(n+3/2)\zeta_2}{\sinh(n+3/2)(\zeta_1-\zeta_2)}\end{aligned} \tag{10.119}$$

$$B_{n+1}^{(1)} - \tilde{c}(n) = \frac{B_n^{(1)}}{n+1} + \Bigg(\frac{2n}{n+1} \big[\cosh\zeta_2 \sinh(n+3/2)\zeta_1 A_n(\zeta_2) - \cosh\zeta_1 \sinh(n+3/2)\zeta_2 A_n(\zeta_1) \big]$$
$$- \frac{n}{n+1} \Big[\sinh(n+3/2)\zeta_1 A_{n-1}(\zeta_2) - \sinh(n+3/2)\zeta_2 A_{n-1}(\zeta_1) \Big] \Bigg)$$
$$\times \big(\sinh(n+3/2)(\zeta_1 - \zeta_2) \big)^{-1}$$
$$= \frac{B_n^{(1)}}{n+1} + \frac{n}{n+1} \Bigg(\sinh(n+3/2)\zeta_1 \left[2\cosh\zeta_2 A_n(\zeta_2) - A_{n-1}(\zeta_2) \right]$$
$$- \sinh(n+3/2)\zeta_2 \left[2\cosh\zeta_1 A_n(\zeta_1) - A_{n-1}(\zeta_1) \right] \Bigg)$$
$$\times \big(\sinh(n+3/2)(\zeta_1 - \zeta_2) \big)^{-1}$$

Putting it all back together yields,

$$B_{n+1}^{(1)} - \tilde{c}(n) = \frac{B_n^{(1)}}{n+1} + \frac{n}{n+1} \Bigg[$$
$$B_n^{(2)} \Bigg(\sinh(n+3/2)\zeta_1 \big[\sinh(n-1/2)\zeta_2 + \cancel{\sinh(n+3/2)\zeta_2} \big]$$
$$- \sinh(n+3/2)\zeta_2 \big[\sinh(n-1/2)\zeta_1 + \cancel{\sinh(n+3/2)\zeta_1} \big] \Bigg)$$
$$+ B_n^{(1)} \Bigg(\sinh(n+3/2)\zeta_1 \big[\cosh(n-1/2)\zeta_2 + \cosh(n+3/2)\zeta_2 \big]$$
$$- \sinh(n+3/2)\zeta_2 \big[\cosh(n-1/2)\zeta_1 + \cosh(n+3/2)\zeta_1 \big] \Bigg)$$
$$- B_{n-1}^{(2)} \Bigg(\sinh(n+3/2)\zeta_1 \sinh(n-1/2)\zeta_2 - \sinh(n+3/2)\zeta_2 \sinh(n-1/2)\zeta_1 \Bigg)$$
$$- B_{n-1}^{(1)} \Bigg(\sinh(n+3/2)\zeta_1 \cosh(n-1/2)\zeta_2 - \sinh(n+3/2)\zeta_2 \cosh(n-1/2)\zeta_1 \Bigg) \Bigg]$$
$$\times \frac{1}{\sinh(n+3/2)(\zeta_1 - \zeta_2)}$$

and from Eq. 10.106, the second trig functions in the prefactors of $B_n^{(1)}$ cancel with the

denominator, yielding a factor of n to added to the first term on the right hand side.

$$
\begin{aligned}
B^{(1)}_{n+1} - \tilde{c}(n) = B^{(1)}_n + \frac{n}{n+1}\Bigg[& \\
& B^{(2)}_n\Big(\sinh(n+3/2)\zeta_1\sinh(n-1/2)\zeta_2 - \sinh(n+3/2)\zeta_2\sinh(n-1/2)\zeta_1\Big) \\
& + B^{(1)}_n\Big(\sinh(n+3/2)\zeta_1\cosh(n-1/2)\zeta_2 - \sinh(n+3/2)\zeta_2\cosh(n-1/2)\zeta_1\Big) \\
& - B^{(2)}_{n-1}\Big(\sinh(n+3/2)\zeta_1\sinh(n-1/2)\zeta_2 - \sinh(n+3/2)\zeta_2\sinh(n-1/2)\zeta_1\Big) \\
& - B^{(1)}_{n-1}\Big(\sinh(n+3/2)\zeta_1\cosh(n-1/2)\zeta_2 - \sinh(n+3/2)\zeta_2\cosh(n-1/2)\zeta_1\Big)\Bigg] \\
& \times \frac{1}{\sinh(n+3/2)(\zeta_1-\zeta_2)}
\end{aligned}
$$

So as long as I did not make any lasting mistakes, we can write the recursion relation for $B^{(1)}_{n-1}$ in terms of two new G factors slightly different from Eq. 10.107

$$1 - \tilde{G}^{(2)}_n = \frac{n}{n+1}\frac{-\sinh(n+3/2)\zeta_1\sinh(n-1/2)\zeta_2 + \sinh(n+3/2)\zeta_2\sinh(n-1/2)\zeta_1}{\sinh(n+3/2)(\zeta_1-\zeta_2)} \tag{10.120}$$

$$1 - \tilde{G}^{(1)}_n = \frac{n}{n+1}\frac{-\sinh(n+3/2)\zeta_1\cosh(n-1/2)\zeta_2 + \sinh(n+3/2)\zeta_2\cosh(n-1/2)\zeta_1}{\sinh(n+3/2)(\zeta_1-\zeta_2)} \tag{10.121}$$

$$B^{(1)}_{n+1} - \tilde{c}(n) = B^{(1)}_n + \left(B^{(2)}_{n-1} - B^{(2)}_n\right)\left(1 - \tilde{G}^{(2)}_n\right) + \left(B^{(1)}_{n-1} - B^{(1)}_n\right)\left(1 - \tilde{G}^{(1)}_n\right) \tag{10.122}$$

$$= \tilde{G}^{(1)}_n B^{(1)}_n + \left(1 - \tilde{G}^{(1)}_n\right)B^{(1)}_{n-1} + \left(1 - \tilde{G}^{(2)}_n\right)\left(B^{(2)}_{n-1} - B^{(2)}_n\right) \tag{10.123}$$

The last step is to combine this with the recursion relation for $B^{(2)}_{n+1}$ and determine $B^{(2)}_0$ and $B^{(1)}_0$ from the need for $\lim_{n\to\infty} B^{(1,2)}_n = 0$. We can define the vector equation

$$\mathbf{B}_{n+1} = \mathbf{G}_n \cdot \mathbf{B}_n + (\mathbf{1} - \mathbf{G}_n)\cdot\mathbf{B}_{n-1} + \mathbf{F}_n \tag{10.124}$$

where

$$\mathbf{B}_n \equiv \begin{pmatrix} B^{(1)}_n \\ B^{(2)}_n \end{pmatrix} \tag{10.125}$$

$$\mathbf{G}_n \equiv \begin{pmatrix} \tilde{G}_n^{(1)} & -(1-\tilde{G}_n^{(2)}) \\ -(1-G_n^{(1)}) & G_n^{(2)} \end{pmatrix} \tag{10.126}$$

and

$$\mathbf{F}_n \equiv \begin{pmatrix} \tilde{c}_n \\ bc_n \end{pmatrix} \tag{10.127}$$

This expression can be solved in the same way as the homodimer case. Making the definition $\mathbf{H}_n = \mathbf{B}_{n+1} - \mathbf{B}_0$ and plugging in to the vector recursion relation,

$$\mathbf{H}_n + \cancel{\mathbf{B}_0} = \mathbf{G}_n \cdot \mathbf{H}_{n-1} + \cancel{\mathbf{G}_n \cdot \mathbf{B}_0} + \mathbf{H}_{n-2} + \cancel{\mathbf{B}_0} - \mathbf{G}_n \cdot \mathbf{H}_{n-2} - \cancel{\mathbf{G}_n \cdot \mathbf{B}_0} + \mathbf{F}_n \tag{10.128}$$

$$\mathbf{H}_n = \mathbf{G}_n \cdot \mathbf{H}_{n-1} + (\mathbf{1} - \mathbf{G}_n) \cdot \mathbf{H}_{n-2} + \mathbf{F}_n \tag{10.129}$$

which defines B_0 in the limit

$$\lim_{n\to\infty} \mathbf{H}_n = \cancel{\mathbf{B}_n}^{0} - \mathbf{B}_0 \tag{10.130}$$

starting with the relations

$$\mathbf{H}_0 = \mathbf{F}_0 \tag{10.131}$$

$$\mathbf{H}_1 = \mathbf{G}_1 \cdot \mathbf{F}_0 + \mathbf{F}_1 \tag{10.132}$$

Average surface temperature

Because we have solved the heat diffusion equation outside the spheres, we must average the temperature at the sphere surface in order to define sphere temperatures. This seems reasonable since the metallic spheres have heat conductivity much greater then the surroundings.

The average surface temperature in our nondimentionalized units is therefore

$$\overline{\theta}_{1,2} = \frac{1}{A_{1,2}} \int_{S_{1,2}} \theta \, \mathrm{d}S = \frac{1}{A_{1,2}} \int_0^{\pi} \int_0^{2\pi} \theta \, h_\beta h_\phi \, \mathrm{d}\phi \mathrm{d}\beta \tag{10.133}$$

$$= \frac{1}{A_{1,2}} \int_0^{\pi} \int_0^{2\pi} \frac{\theta c^2 \sin\beta}{(\cosh\zeta_{1,2} - \cos\beta)^2} \, \mathrm{d}\phi \mathrm{d}\beta \tag{10.134}$$

$$= \frac{2\pi c^2}{A_{1,2}} \int_0^{\pi} \frac{\theta \sin\beta}{(\cosh\zeta_{1,2} - \cos\beta)^2} \, \mathrm{d}\beta \tag{10.135}$$

$$= \frac{2\pi c^2}{A_{1,2}} \sum_{m=0}^{\infty} \left[B_m^{(1)} \sinh(m+1/2)\zeta + B_m^{(2)} \cosh(m+1/2)\zeta \right] \tag{10.136}$$

$$\times \int_0^{\pi} \frac{\sin\beta P_m(\cos\beta)}{(\cosh\zeta_{1,2} - \cos\beta)^{3/2}} \, \mathrm{d}\beta \tag{10.137}$$

In order to solve the integral

$$I = \int_0^{\pi} \frac{\sin\beta P_m(\cos\beta)}{(\cosh\zeta_{1,2} - \cos\beta)^{3/2}} \mathrm{d}\beta \tag{10.138}$$

we can employ the derivative

$$\frac{\partial}{\partial\zeta_{1,2}} \frac{\sin\beta}{\sqrt{\cosh\zeta_{1,2} - \cos\beta}} = \frac{-\sinh\zeta_{1,2}\sin\beta}{2(\cosh\zeta_{1,2} - \cos\beta)^{3/2}} \tag{10.139}$$

the integral then takes the form

$$I = \frac{-2}{\sinh\zeta_{1,2}} \frac{\partial}{\partial\zeta_{1,2}} \int_0^{\pi} \frac{\sin\beta P_m(\cos\beta)}{\sqrt{\cosh\zeta_{1,2} - \cos\beta}} \mathrm{d}\beta \tag{10.140}$$

We can then change the integration variable to

$$x = \cos\beta \tag{10.141}$$

$$\mathrm{d}x = -\sin\beta \mathrm{d}\beta \tag{10.142}$$

yielding

$$I = \frac{-2}{\sinh\zeta_{1,2}} \frac{\partial}{\partial\zeta_{1,2}} \int_{-1}^{1} \frac{P_m(x)}{\sqrt{\cosh\zeta_{1,2} - x}} \mathrm{d}x \tag{10.143}$$

At this point, we can use

$$\int_{-1}^{1} \frac{P_m(x)}{\sqrt{\cosh\zeta - x}} \mathrm{d}x = \frac{2\sqrt{2}}{2m+1} e^{-(m+1/2)|\zeta|} \tag{10.144}$$

to compute the integral

$$I = \frac{-2}{\sinh\zeta_{1,2}} \frac{\sqrt{2}}{m+1/2} \frac{\partial}{\partial\zeta_{1,2}} e^{-(m+1/2)|\zeta_{1,2}|} \tag{10.145}$$

$$= \frac{2\sqrt{2}}{\sinh\zeta_{1,2}} e^{-(m+1/2)|\zeta_{1,2}|} \left\{\times(-1) \text{ if } \zeta_{1,2} < 0\right\} \tag{10.146}$$

$$= \frac{2\sqrt{2}}{\sinh|\zeta_{1,2}|} e^{-(m+1/2)|\zeta_{1,2}|} \tag{10.147}$$

where the conditional -1 comes from the derivative of the absolute value in the exponential. This allows us to write the average surface temperature as

$$\overline{\theta}_{1,2} = \frac{2\pi c^2}{A_{1,2}} \frac{2\sqrt{2}}{\sinh|\zeta_{1,2}|} \sum_{m=0}^{\infty} \left[B_m^{(1)} \sinh(m+1/2)\zeta_{1,2} + B_m^{(2)} \cosh(m+1/2)\zeta_{1,2}\right] e^{-(m+1/2)|\zeta_{1,2}|} \quad \blacksquare \tag{10.148}$$

I should try and take the Kang limit of this expression and make sure it matches up.

$$\lim_{\text{Kang}} \overline{\theta}_{1,2} = \frac{2\pi(\sinh\zeta_0)^{\not 2}}{4\pi} \frac{2\sqrt{2}}{\cancel{\sinh\zeta_0}} \sum_{m=0}^{\infty} B_m^{(2)} \cosh(m+1/2)\zeta_0 e^{-(m+1/2)\zeta_0} \tag{10.149}$$

$$= \sqrt{2}\sinh\zeta_0 \sum_{m=0}^{\infty} B_m^{(2)} \cosh(m+1/2)\zeta_0 e^{-(m+1/2)\zeta_0} \tag{10.150}$$

$$= \sqrt{2}\sinh\zeta_0 \sum_{m=0}^{\infty} B_m^{(2)} \frac{e^{(m+1/2)\zeta_0} + e^{-(m+1/2)\zeta_0}}{2} e^{-(m+1/2)\zeta_0} \tag{10.151}$$

$$= \frac{\sinh\zeta_0}{\sqrt{2}} \sum_{m=0}^{\infty} B_m^{(2)} [1 + e^{-(2m+1)\zeta_0}] \quad \blacksquare \tag{10.152}$$

BIBLIOGRAPHY

[1] Ernst Abbe. Beiträge zur theorie des mikroskops und der mikroskopischen wahrnehmung. *Mikroskop. Anat.*, 9:413–418, 1873.

[2] Subhasis Adhikari, Patrick Spaeth, Ashish Kar, Martin Dieter Baaske, Saumyakanti Khatua, and Michel Orrit. Photothermal microscopy: Imaging the optical absorption of single nanoparticles and single molecules. *ACS Nano*, 2020.

[3] Gleb M. Akselrod, Christos Argyropoulos, Thang B. Hoang, Cristian Ciracì, Chao Fang, Jiani Huang, David R. Smith, and Maiken H Mikkelsen. Probing the mechanisms of large purcell enhancement in plasmonic nanoantennas. *Nat. Photonics*, 8(11):835–840, 2014.

[4] R.S. Alassar and B.J. Alminshawy. Heat conduction from two spheres. *AIChE J*, 56(9):2248–2256, 2010.

[5] W. Patrick Ambrose, Peter M. Goodwin, James H. Jett, Alan Van Orden, James H. Werner, and Richard A. Keller. Single molecule fluorescence spectroscopy at ambient temperature. *Chem. Rev.*, 99(10):2929–2956, 1999.

[6] Andre Anda, Luca De Vico, Thorsten Hansen, and Darius Abramavicius. Absorption and fluorescence lineshape theory for polynomial potentials. *J. Chem. Theory Comput*, 12(12):5979–5989, 2016.

[7] Pascal Anger, Palash Bharadwaj, and Lukas Novotny. Enhancement and quenching of single-molecule fluorescence. *Phys. Rev. Lett.*, 96(11):113002, 2006.

[8] Jeffrey N. Anker, W. Paige Hall, Olga Lyandres, Nilam C. Shah, Jing Zhao, and Richard P. Van Duyne. Biosensing with plasmonic nanosensors. In *Nanoscience and Technology: A Collection of Reviews from Nature Journals*, pages 308–319. World Scientific, 2010.

[9] Ciceron Ayala-Orozco, Jun G. Liu, Mark W. Knight, Yumin Wang, Jared K. Day, Peter Nordlander, and Naomi J. Halas. Fluorescence enhancement of molecules inside a gold nanomatryoshka. *Nano Lett.*, 14(5):2926–2933, 2014.

[10] Guillaume Baffou and Romain Quidant. Thermo-plasmonics: using metallic nanostructures as nano-sources of heat. *Laser Photonics Rev.*, 7(2):171–187, 2013.

[11] Christopher L. Baldwin, Nicholas W. Bigelow, and David J. Masiello. Thermal signatures of plasmonic fano interferences: Toward the achievement of nanolocalized temperature manipulation. *J. Phys. Chem. Lett.*, 5(8):1347–1354, 2014.

[12] JR Barnes, R.J. Stephenson, M.E. Welland, C. Gerber, and J.K. Gimzewski. Photothermal spectroscopy with femtojoule sensitivity using a micromechanical device. *Nature*, 372(6501):79–81, 1994.

[13] J.R. Barnes, R.J. Stephenson, C.N. Woodburn, S.J. Oshea, M.E. Welland, T. Rayment, J.K. Gimzewski, and C. Gerber. A femtojoule calorimeter using micromechanical sensors. *Rev. Sci. Instrum.*, 65(12):3793–3798, 1994.

[14] Stéphane Berciaud, Laurent Cognet, Gerhard A. Blab, and Brahim Lounis. Photothermal heterodyne imaging of individual nonfluorescent nanoclusters and nanocrystals. *Phys. Rev. Lett.*, 93(25):257402, 2004.

[15] Stéphane Berciaud, Laurent Cognet, and Brahim Lounis. Photothermal absorption spectroscopy of individual semiconductor nanocrystals. *Nano Lett.*, 5(11):2160–2163, 2005.

[16] Stéphane Berciaud, Laurent Cognet, Philippe Poulin, R Bruce Weisman, and Brahim Lounis. Absorption spectroscopy of individual single-walled carbon nanotubes. *Nano Lett.*, 7(5):1203–1207, 2007.

[17] Stéphane Berciaud, Laurent Cognet, Philippe Tamarat, and Brahim Lounis. Observation of intrinsic size effects in the optical response of individual gold nanoparticles. *Nano Lett.*, 5(3):515–518, 2005.

[18] Stéphane Berciaud, David Lasne, Gerhard A. Blab, Laurent Cognet, and Brahim Lounis. Photothermal heterodyne imaging of individual metallic nanoparticles: Theory versus experiment. *Physical Review B*, 73(4):045424, 2006.

[19] Eric Betzig, George H. Patterson, Rachid Sougrat, O. Wolf Lindwasser, Scott Olenych, Juan S. Bonifacino, Michael W. Davidson, Jennifer Lippincott-Schwartz, and Harald F. Hess. Imaging intracellular fluorescent proteins at nanometer resolution. *Science*, 313(5793):1642–1645, 2006.

[20] Palash Bharadwaj and Lukas Novotny. Spectral dependence of single molecule fluorescence enhancement. *Optics Express*, 15(21):14266–14274, 2007.

[21] Ujjal Bhattacharjee, Claire A. West, Seyyed Ali Hosseini Jebeli, Harrison J. Goldwyn, Xiang-Tian Kong, Zhongwei Hu, Elliot K. Beutler, Wei-Shun Chang, Katherine A. Willets, Stephan Link, and David J. Masiello. Active far-field control of the thermal near-field via plasmon hybridization. *ACS Nano*, 13(8):9655–9663, 2019.

[22] Connor R. Bilchak and Zahra Fakhraai. *unpublished*.

[23] Julie Biteen and Katherine A. Willets. Introduction: Super-resolution and single-molecule imaging. *Chem. Rev.*, 117(11):7241–7243, 2017.

[24] Karole L. Blythe and Katherine A. Willets. Super-resolution imaging of fluorophore-labeled dna bound to gold nanoparticles: A single-molecule, single-particle approach. *J. Phys. Chem. C*, 120(2):803–815, 2016.

[25] Craig F. Bohren and Donald R. Huffman. *Absorption and scattering of light by small particles*. John Wiley & Sons, 2008.

[26] Robert Charles Boutelle, Daniel Neuhauser, and Shimon Weiss. Far-field super-resolution detection of plasmonic near-fields. *ACS Nano*, 10(8):7955–7962, 2016.

[27] David Boyer, Philippe Tamarat, Abdelhamid Maali, Brahim Lounis, and Michel Orrit. Photothermal imaging of nanometer-sized metal particles among scatterers. *Science*, 297(5584):1160–1163, 2002.

[28] Alexandre G. Brolo. Plasmonics for future biosensors. *Nat. Photonics*, 6(11):709–713, 2012.

[29] Yi-Yu Cai, Jun G. Liu, Lawrence J. Tauzin, Da Huang, Eric Sung, Hui Zhang, Anneli Joplin, Wei-Shun Chang, Peter Nordlander, and Stephan Link. Photoluminescence of gold nanorods: Purcell effect enhanced emission from hot carriers. *ACS Nano*, 12(2):976–985, 2018.

[30] Jon P. Camden, Jon A. Dieringer, Yingmin Wang, David J. Masiello, Lawrence D. Marks, George C. Schatz, and Richard P. Van Duyne. Probing the structure of single-molecule surface-enhanced Raman scattering hot spots. *J. Am. Chem. Soc.*, 130:12616, 2008.

[31] Jon P. Camden, Jon A. Dieringer, Jing Zhao, and Richard P. Van Duyne. Controlled plasmonic nanostructures for surface-enhanced spectroscopy and sensing. *Accounts of chemical research*, 41(12):1653–1661, 2008.

[32] Michele Celebrano, Philipp Kukura, Alois Renn, and Vahid Sandoghdar. Single-molecule imaging by optical absorption. *Nat. Photonics*, 5(2):95–98, 2011.

[33] R.R. Chance, A. Prock, and R. Silbey. Molecular fluorescence and energy transfer near interfaces. *Adv. Chem. Phys*, 37(1):65, 1978.

[34] Wei-Shun Chang and Stephan Link. Enhancing the sensitivity of single-particle photothermal imaging with thermotropic liquid crystals. *J. Phys. Chem. Lett.*, 3(10):1393–1399, 2012.

[35] Weilun Chao, Bruce D. Harteneck, J. Alexander Liddle, Erik H. Anderson, and David T. Attwood. Soft x-ray microscopy at a spatial resolution better than 15 nm. *Nature*, 435(7046):1210–1213, 2005.

[36] Charles Cherqui, Nicholas W. Bigelow, Alex Vaschillo, Harrison Goldwyn, and David J. Masiello. Combined tight-binding and numerical electrodynamics understanding of the STEM/EELS magneto-optical responses of aromatic plasmon-supporting metal oligomers. *ACS Photonics*, 1:1013–1024, 2014.

[37] Charles Cherqui, Marc R. Bourgeois, Danqing Wang, and George C. Schatz. Plasmonic surface lattice resonances: Theory and computation. *Accounts of chemical research*, 52(9):2548–2558, 2019.

[38] Charles Cherqui, Guoliang Li, Jacob A. Busche, Steven C. Quillin, Jon P. Camden, and David J. Masiello. Multipolar nanocube plasmon mode-mixing in finite substrates. *J. Chem. Phys. Lett.*, 9(3):504–512, 2018.

[39] Charles Cherqui, Niket Thakkar, Guoliang Li, Jon P. Camden, and David J. Masiello. Characterizing localized surface plasmons using electron energy-loss spectroscopy. *Annu. Rev. Phys. Chem.*, 67:331–57, 05 2016.

[40] Charles Cherqui, Yueying Wu, Guoliang Li, Steven C. Quillin, Jacob A. Busche, Niket Thakkar, Claire A. West, Nicholas P. Montoni, P Rack, Jon P. Camden, et al. Stem/eels imaging of magnetic hybridization in symmetric and symmetry-broken plasmon oligomer dimers and all-magnetic fano interference. *Nano Lett.*, 16(10):6668–6676, 2016.

[41] Miao-Hsuan Chien, Mario Brameshuber, Benedikt K. Rossboth, Gerhard J. Schütz, and Silvan Schmid. Single-molecule optical absorption imaging by nanomechanical photothermal sensing. *Proc. Natl. Acad. Sci. U.S.A.*, 115(44):11150–11155, 2018.

[42] Tyler J. Chozinski, Lauren A. Gagnon, and Joshua C Vaughan. Twinkle, twinkle little star: Photoswitchable fluorophores for super-resolution imaging. *FEBS Lett.*, 588(19):3603–3612, 2014.

[43] H.Y. Chung, P.T. Leung, and D.P. Tsai. Dynamic modifications of polarizability for large metallic spheroidal nanoshells. *J. Chem. Phys.*, 131(12):124122, 2009.

[44] Dana Cialla, Anne März, René Böhme, Frank Theil, Karina Weber, Michael Schmitt, and Jürgen Popp. Surface-enhanced raman spectroscopy (sers): progress and trends. *Anal. Bioanal. Chem.*, 403(1):27–54, 2012.

[45] Laurent Cognet, Catherine Tardin, David Boyer, Daniel Choquet, Philippe Tamarat, and Brahim Lounis. Single metallic nanoparticle imaging for protein detection in cells. *Proc. Natl. Acad. Sci. U.S.A.*, 100(20):11350–11355, 2003.

[46] Guoqiang Cui and M.G. Raymer. Emission spectra and quantum efficiency of single-photon sources in the cavity-qed strong-coupling regime. *Phys. Rev. A*, 73(5):053807, 2006.

[47] Alberto G. Curto, Giorgio Volpe, Tim H. Taminiau, Mark P. Kreuzer, Romain Quidant, and Niek F. van Hulst. Unidirectional emission of a quantum dot coupled to a nanoantenna. *Science*, 329(5994):930–933, 2010.

[48] Beatriz E. de Cominges, Manuel M. Piñeiro, Laura Mosteiro, Teresa P. Iglesias, Jose L. Legido, and María I. Paz Andrade. Temperature dependence of thermophysical properties of hexane+ 1-hexanol. *J. Chem. Eng. Data*, 46(5):1206–1210, 2001.

[49] Hendrik Deschout, Francesca Cella Zanacchi, Michael Mlodzianoski, Alberto Diaspro, Joerg Bewersdorf, Samuel T. Hess, and Kevin Braeckmans. Precisely and accurately localizing single emitters in fluorescence microscopy. *Nat. Methods*, 11(3):253, 2014.

[50] Velauthapillai Dhayalan and Jakob J. Stamnes. Focusing of electric-dipole waves in the debye and kirchhoff approximations. *Pure Appl. Opt. Europ. Opt. Soc. P. A.*, 6(3):347, 1997.

[51] Tina X. Ding, Lei Hou, Harmen van der Meer, A. Paul Alivisatos, and Michel Orrit. Hundreds-fold sensitivity enhancement of photothermal microscopy in near-critical xenon. *J. Phys. Chem. Lett.*, 7(13):2524–2529, 2016.

[52] Gonçalo Doria, João Conde, Bruno Veigas, Leticia Giestas, Carina Almeida, Maria Assunção, João Rosa, and Pedro V Baptista. Noble metal nanoparticles for biosensing applications. *Sensors*, 12(2):1657–1687, 2012.

[53] Bruce T. Draine and Piotr J. Flatau. Discrete-dipole approximation for scattering calculations. *Josa a*, 11(4):1491–1499, 1994.

[54] Ying Fang, Wei-Shun Chang, Britain Willingham, Pattanawit Swanglap, Sergio Dominguez-Medina, and Stephan Link. Plasmon emission quantum yield of single gold nanorods as a function of aspect ratio. *ACS Nano*, 6(8):7177–7184, 2012.

[55] Ugo Fano. Effects of configuration interaction on intensities and phase shifts. *Phys. Rev.*, 124(6):1866, 1961.

[56] Marta Fernández-Suárez and Alice Y Ting. Fluorescent probes for super-resolution imaging in living cells. *Nat. Rev. Mol. Cell Biol.*, 9(12):929, 2008.

[57] Jessica D. Flynn, Beth L. Haas, and Julie S. Biteen. Plasmon-enhanced fluorescence from single proteins in living bacteria. *J. Phys. Chem. C*, 120(37):20512–20517, 2015.

[58] Bing Fu, Jessica D. Flynn, Benjamin P. Isaacoff, David J. Rowland, and Julie S. Biteen. Super-resolving the distance-dependent plasmon-enhanced fluorescence of single dye and fluorescent protein molecules. *J. Phys. Chem.*

[59] Bing Fu, Benjamin P. Isaacoff, and Julie S. Biteen. Super-resolving the actual position of single fluorescent molecules coupled to a plasmonic nanoantenna. *ACS Nano*, 11(9):8978–8987, 2017.

[60] Bing Fu, Benjamin P. Isaacoff, and Julie S. Biteen. Super-resolving the actual position of single fluorescent molecules coupled to a plasmonic nanoantenna. *ACS Nano*, 11(9):8978–8987, 2017.

[61] A. Gaiduk, M. Yorulmaz, P.V. Ruijgrok, and M. Orrit. Room-temperature detection of a single molecules absorption by photothermal contrast. *Science*, 330(6002):353–356, 2010.

[62] Alexander Gaiduk, Paul V. Ruijgrok, Mustafa Yorulmaz, and Michel Orrit. Detection limits in photothermal microscopy. *Chemical Science*, 1(3):343–350, 2010.

[63] Howard Gest. The discovery of microorganisms by robert hooke and antoni van leeuwenhoek, fellows of the royal society. *Notes Rec.*, 58(2):187–201, 2004.

[64] Harrison J. Goldwyn, Kevin C. Smith, Jacob A. Busche, and David J. Masiello. Mislocalization in plasmon-enhanced single-molecule fluorescence microscopy as a dynamical young's interferometer. *ACS Photonics*, 5(8):3141–3151, 2018.

[65] Joseph W Goodman. *Introduction to Fourier optics*. Roberts and Company Publishers, 2005.

[66] Amanda J. Haes, Christy L. Haynes, Adam D. McFarland, George C. Schatz, Richard P. Van Duyne, and Shengli Zou. Plasmonic materials for surface-enhanced sensing and spectroscopy. *MRS bulletin*, 30(5):368–375, 2005.

[67] Charles W. Heaps and George C. Schatz. Modeling super-resolution sers using a t-matrix method to elucidate molecule-nanoparticle coupling and the origins of localization errors. *J. Chem. Phys.*, 146(22):224201, 2017.

[68] Stefan W. Hell and Jan Wichmann. Breaking the diffraction resolution limit by stimulated emission: Stimulated-emission-depletion fluorescence microscopy. *Opt. Lett.*, 19(11):780–782, 1994.

[69] Samuel T. Hess, Thanu P.K. Girirajan, and Michael D. Mason. Ultra-high resolution imaging by fluorescence photoactivation localization microscopy. *Biophys. J.*, 91(11):4258–4272, 2006.

[70] Kevin D Heylman, Niket Thakkar, Erik H Horak, Steven C Quillin, Charles Cherqui, Kassandra A Knapper, David J Masiello, and Randall H Goldsmith. Optical microresonators as single-particle absorption spectrometers. *Nat. Photonics*, 10(12):788–795, 2016.

[71] Thanh Xuan Hoang, Yubo Duan, Xudong Chen, and George Barbastathis. Focusing and imaging in microsphere-based microscopy. *Opt. Express*, 23(9):12337–53, May 2015.

[72] Ulrich Hohenester. Simulating electron energy loss spectroscopy with the mnpbem toolbox. *Computer Physics Communications*, 185(3):1177–1187, 2014.

[73] Ulrich Hohenester and Andreas Trügler. Mnpbem–a matlab toolbox for the simulation of plasmonic nanoparticles. *Comput. Phys. Commun.*, 183(2):370–381, 2012.

[74] Phil Holzmeister, Enrico Pibiri, Jürgen J. Schmied, Tapasi Sen, Guillermo P. Acuna, and Philip Tinnefeld. Quantum yield and excitation rate of single molecules close to metallic nanostructures. *Nature Comm.*, 5:5356, 2014.

[75] R. Hooke. *Micrographia: or some Physiological Descriptions of Minute Bodies made by Magnifying Glasses with Observations and Inquiries thereupon*. Jo. Martyn and Ja. Allestry, Printers to the Royal Society, London, 1665.

[76] Bo Huang, Mark Bates, and Xiaowei Zhuang. Super-resolution fluorescence microscopy. *Annu. Rev. Biochem.*, 78:993–1016, 2009.

[77] Jiaqing Huang, Kristyn Gumpper, Yuejie Chi, Mingzhai Sun, and Jianjie Ma. Fast two-dimensional super-resolution image reconstruction algorithm for ultra-high emitter density. *Opt. Lett.*, 40(13):2989–2992, 2015.

[78] Christian G. Hübner, Alois Renn, Indrek Renge, and Urs P. Wild. Direct observation of the triplet lifetime quenching of single dye molecules by molecular oxygen. *J. Chem. Phys.*, 115(21):9619–9622, 2001.

[79] Benjamin P. Isaacoff, Yilai Li, Stephen A. Lee, and Julie S. Biteen. Small-labs: Measuring single-molecule intensity and position in obscuring backgrounds. *Biophys. J.*, 116(6):975–982, 2019.

[80] John David Jackson. *Classical electrodynamics*. John Wiley & Sons, 2007.

[81] Peter B. Johnson and R.W. Christy. Optical constants of the noble metals. *Phys. Rev. B*, 6(12):4370, 1972.

[82] Anneli Joplin, Wei-Shun Chang, and Stephan Link. Imaging and spectroscopy of single metal nanostructure absorption. *Langmuir*, 34(13):3775–3786, 2017.

[83] Anneli Joplin, Seyyed Ali Hosseini Jebeli, Eric Sung, Nathan Diemler, Patrick J Straney, Mustafa Yorulmaz, Wei-Shun Chang, Jill E Millstone, and Stephan Link. Correlated absorption and scattering spectroscopy of individual platinum-decorated gold nanorods reveals strong excitation enhancement in the nonplasmonic metal. *ACS Nano*, 11(12):12346–12357, 2017.

[84] Saeed Jafari Kang, Esmaeil Dehdashti, and Hassan Masoud. Conduction heat transfer from oblate spheroids and bispheres. *Int. J. Heat Mass Transf.*, 139:115–120, 2019.

[85] Richard A. Keller, W. Patrick Ambrose, Peter M. Goodwin, James H. Jett, John C. Martin, and Ming Wu. Single-molecule fluorescence analysis in solution. *Appl. Spectrosc.*, 50(7):12A–32A, 1996.

[86] Saumyakanti Khatua, Pedro M..R.. Paulo, Haifeng Yuan, Ankur Gupta, Peter Zijlstra, and Michel Orrit. Resonant plasmonic enhancement of single-molecule fluorescence by individual gold nanorods. *ACS Nano*, 8(5):4440–4449, 2014.

[87] Anika Kinkhabwala, Zongfu Yu, Shanhui Fan, Yuri Avlasevich, Klaus Müllen, and WE Moerner. Large single-molecule fluorescence enhancements produced by a bowtie nanoantenna. *Nat. Photonics*, 3(11):654, 2009.

[88] Kassandra A. Knapper, Kevin D. Heylman, Erik H. Horak, and Randall H. Goldsmith. Chip-scale fabrication of high-q all-glass toroidal microresonators for single-particle label-free imaging. *Adv. Mater.*, 28(15):2945–2950, 2016.

[89] Katrin Kneipp, Yang Wang, Harald Kneipp, Lev T. Perelman, Irving Itzkan, Ramachandra R. Dasari, and Michael S. Feld. Single molecule detection using surface-enhanced raman scattering (sers). *Phys. Rev. Lett.*, 78(9):1667, 1997.

[90] Daniel Kraemer, Bed Poudel, Hsien-Ping Feng, J. Christopher Caylor, Bo Yu, Xiao Yan, Yi Ma, Xiaowei Wang, Dezhi Wang, Andrew Muto, Kenneth McEnaney, Matteo Chiesa, Zhifeng Ren, and Gang Chen. High-performance flat-panel solar thermoelectric generators with high thermal concentration. *Nat. Materials*, 10, 2011.

[91] Philipp Kukura, Michele Celebrano, Alois Renn, and Vahid Sandoghdar. Single-molecule sensitivity in optical absorption at room temperature. *J. Phys. Chem. Lett.*, 1(23):3323–3327, 2010.

[92] Karl S. Kunz and Raymond J. Luebbers. *The finite difference time domain method for electromagnetics*. CRC press, 1993.

[93] Tom Larsen, Silvan Schmid, Leif Grönberg, AO Niskanen, Juha Hassel, Søren Dohn, and Anja Boisen. Ultrasensitive string-based temperature sensors. *Appl. Phys. Lett.*, 98(12):121901, 2011.

[94] Tom Larsen, Silvan Schmid, Luis G Villanueva, and Anja Boisen. Photothermal analysis of individual nanoparticulate samples using micromechanical resonators. *ACS Nano*, 7(7):6188–6193, 2013.

[95] Stephen A. Lee and Julie S. Biteen. Interplay of nanoparticle resonance frequency and array surface coverage in live-cell plasmon-enhanced single-molecule imaging. *J. Phys. Chem. C*, 122(10):5705–5709, 2018.

[96] Stephen A. Lee and Julie S. Biteen. Spectral reshaping of single dye molecules coupled to single plasmonic nanoparticles. *J. Phys. Chem. Lett.*, 10(19):5764–5769, 2019.

[97] Haixu Leng, Brian Szychowski, Marie-Christine Daniel, and Matthew Pelton. Strong coupling and induced transparency at room temperature with single quantum dots and gap plasmons. *Nature Comm.*, 9(1):1–7, 2018.

[98] Ran Li, Marc R. Bourgeois, Charles Cherqui, Jun Guan, Danqing Wang, Jingtian Hu, Richard D. Schaller, George C. Schatz, and Teri W. Odom. Hierarchical hybridization in plasmonic honeycomb lattices. *Nano Lett.*, 19(9):6435–6441, 2019.

[99] Kangmook Lim, Chad Ropp, Sabyasachi Barik, John Fourkas, Benjamin Shapiro, and Edo Waks. Nanostructure-induced distortion in single-emitter microscopy. *Nano Lett.*, 16(9):5415–5419, 2016.

[100] Stephan Link and Mostafa A. El-Sayed. Spectral properties and relaxation dynamics of surface plasmon electronic oscillations in gold and silver nanodots and nanorods. *J. Phys. Chem. B*, 103(40):8410–8426, 1999.

[101] Zhe Liu, Luke D. Lavis, and Eric Betzig. Imaging live-cell dynamics and structure at the single-molecule level. *Mol. Cell*, 58(4):644–659, 2015.

[102] David L. Mack, Emiliano Cortés, Vincenzo Giannini, Peter Török, Tyler Roschuk, and Stefan A. Maier. Decoupling absorption and emission processes in super-resolution localization of emitters in a plasmonic hotspot. *Nat. Commun.*, 8:14513, 2017.

[103] David J. Masiello and George C. Schatz. Many-body theory of surface-enhanced Raman scattering. *Phys. Rev. A*, 78:042505, 2008.

[104] M. Meier and A. Wokaun. Enhanced fields on large metal particles: dynamic depolarization. *Optics Lett.*, 8(11):581–583, 1983.

[105] Masafumi Minoshima and Kazuya Kikuchi. Photostable and photoswitching fluorescent dyes for super-resolution imaging. *J. Biol. Inorg. Chem.*, 22(5):639–652, 2017.

[106] Robert J. Moerland, Tim H. Taminiau, Lukas Novotny, Niek F. Van Hulst, and Laurens Kuipers. Reversible polarization control of single photon emission. *Nano Lett.*, 8(2):606–610, 2008.

[107] W.E. Moerner and David P. Fromm. Methods of single-molecule fluorescence spectroscopy and microscopy. *Rev. Sci. Instrum.*, 74(8):3597–3619, 2003.

[108] William E. Moerner and Lothar Kador. Optical detection and spectroscopy of single molecules in a solid. *Phys. Rev. Lett.*, 62(21):2535, 1989.

[109] William E. Moerner and Michel Orrit. Illuminating single molecules in condensed matter. *Science*, 283(5408):1670–1676, 1999.

[110] Nicholas P. Montoni, Steven C. Quillin, Charles Cherqui, and David J. Masiello. Tunable spectral ordering of magnetic plasmon resonances in noble metal nanoclusters. *ACS Photonics*, 5(8):3272–3281, 2018.

[111] Alexander Moroz. Depolarization field of spheroidal particles. *J. Opt. Soc. Am. B*, 26(3):517–527, 2009.

[112] Martin Moskovits. Surface-enhanced spectroscopy. *Rev. Mod. Phys.*, 57(3):783, 1985.

[113] Shaul Mukamel. *Principles of nonlinear optical spectroscopy*. Number 6. Oxford University Press on Demand, 1999.

[114] George Ni, Gabriel Li, Svetlana V. Boriskina, Hongxia Li, Weilin Yang, TieJun Zhang, and Gang Chen. Steam generation under one sun enabled by a floating structure with thermal concentration. *Nat. Energy*, 1(9):16126, 2016.

[115] Shuming Nie and Steven Emory. Probing single molecules and single nanoparticles by surface-enhanced Raman scattering. *Science*, 275:1102, 1997.

[116] Shuming Nie and Steven R. Emory. Probing single molecules and single nanoparticles by surface-enhanced raman scattering. *Science*, 275(5303):1102–1106, 1997.

[117] Lukas Novotny and Bert Hecht, editors. *Principles of Nano-Optics*. Cambridge University Press, Cambridge, 2006.

[118] Lukas Novotny and Niek Van Hulst. Antennas for light. *Nat. Photonics*, 5(2):83–90, 2011.

[119] Vasilis Ntziachristos. Going deeper than microscopy: the optical imaging frontier in biology. *Nature methods*, 7(8):603–614, 2010.

[120] Hiroshi Ono and Kazuaki Shibata. Simple determination of thermal and thermo-optical constants of liquid crystals by means of a photothermal self-diffracting technique. *Jpn. J. Appl. Phys.*, 42(1R):186, 2003.

[121] Michel Orrit and J Bernard. Single pentacene molecules detected by fluorescence excitation in a p-terphenyl crystal. *Phys. Rev. Lett.*, 65(21):2716, 1990.

[122] Ekmel Ozbay. Plasmonics: merging photonics and electronics at nanoscale dimensions. *Science*, 311(5758):189–193, 2006.

[123] George Patterson, Michael Davidson, Suliana Manley, and Jennifer Lippincott-Schwartz. Superresolution imaging using single-molecule localization. *Annu. Rev. Phys. Chem.*, 61:345–367, 2010.

[124] Matthew Pelton. Modified spontaneous emission in nanophotonic structures. *Nat. Photonics*, 9(7):427–435, 2015.

[125] Emil Prodan, Corey Radloff, Naomi J. Halas, and Peter Nordlander. A hybridization model for the plasmon response of complex nanostructures. *Science*, 302(5644):419–422, 2003.

[126] H.C. Purcell, Edward M .and Torrey and Robert V. Pound. Resonance absorption by nuclear magnetic moments in a solid. *Phys. Rev.*, 69(1-2):37, 1946.

[127] Steven C. Quillin, Charles Cherqui, Nicholas P. Montoni, Guoliang Li, Jon P. Camden, and David J. Masiello. Imaging plasmon hybridization in metal nanoparticle aggregates with electron energy-loss spectroscopy. *J. Phys. Chem. C*, 120(37):20852–20859, 2016.

[128] Mario Raab, Carolin Vietz, Fernando Daniel Stefani, Guillermo Pedro Acuna, and Philip Tinnefeld. Shifting molecular localization by plasmonic coupling in a single-molecule mirage. *Nat. Commun.*, 8:13966, 2017.

[129] Emily J. Rabe, Harrison J. Goldwyn, Doyk Hwang, David J. Masiello, and Cody W. Schlenker. Intermolecular hydrogen bonding tunes vibronic coupling in heptazine complexes. *J. Phys. Chem. C*.

[130] Lord Rayleigh. On the theory of optical images, with special reference to the microscope. *Philos. Mag.*, 42:167–195, 1896.

[131] Ludwig Reimer. *Scanning electron microscopy: physics of image formation and microanalysis*. IOP Publishing, 2000.

[132] Mengxin Ren, Mo Chen, Wei Wu, Lihui Zhang, Junku Liu, Biao Pi, Xinzheng Zhang, Qunqing Li, Shoushan Fan, and Jingjun Xu. Linearly polarized light emission from quantum dots with plasmonic nanoantenna arrays. *Nano Lett.*, 15(5):2951–2957, 2015.

[133] Alois Renn, Johannes Seelig, and Vahid Sandoghdar. Oxygen-dependent photochemistry of fluorescent dyes studied at the single molecule level. *Mol. Phys.*, 104(3):409–414, 2006.

[134] Malte Renz. Fluorescence microscopy–a historical and technical perspective. *Cytom. A*, 83(9):767–779, 2013.

[135] M. Ringler, A. Schwemer, M. Wunderlich, A. Nichtl, K. Kürzinger, T.A. Klar, and J. Feldmann. Shaping emission spectra of fluorescent molecules with single plasmonic nanoresonators. *Physical review Lett.*, 100(20):203002, 2008.

[136] Chad Ropp, Zachary Cummins, Sanghee Nah, John T. Fourkas, Benjamin Shapiro, and Edo Waks. Nanoscale probing of image-dipole interactions in a metallic nanostructure. *Nat. Commun.*, 6:6558, 2015.

[137] Michael J. Rust, Mark Bates, and Xiaowei Zhuang. Sub-diffraction-limit imaging by stochastic optical reconstruction microscopy (storm). *Nat. Methods*, 3(10):793, 2006.

[138] Steffen J. Sahl and W.E. Moerner. Super-resolution fluorescence imaging with single molecules. *Curr. Opin. Struct. Biol.*, 23(5):778–787, 2013.

[139] George C. Schatz and Richard P. Van Duyne. Electromagnetic mechanism of surface-enhanced spectroscopy, 2002.

[140] Marlan O. Scully and M. Suhail Zubairy. *Quantum optics*. American Association of Physics Teachers, 1999.

[141] Markus Selmke, Marco Braun, and Frank Cichos. Gaussian beam photothermal single particle microscopy. *J. Opt. Soc. Am. A*, 29(10):2237–2241, 2012.

[142] Markus Selmke, Marco Braun, and Frank Cichos. Nano-lens diffraction around a single heated nano particle. *Opt. Express*, 20(7):8055–8070, Mar 2012.

[143] Markus Selmke, Marco Braun, and Frank Cichos. Photothermal single-particle microscopy: Detection of a nanolens. *ACS Nano*, 6(3):2741–2749, 2012.

[144] Alexey Sharonov and Robin M Hochstrasser. Wide-field subdiffraction imaging by accumulated binding of diffusing probes. *Proc. Natl. Acad. Sci. U.S.A.*, 103(50):18911–18916, 2006.

[145] Timur Shegai, Zhipeng Li, Tali Dadosh, Zhenyu Zhang, Hongxing Xu, and Gilad Haran. Managing light polarization via plasmon–molecule interactions within an asymmetric metal nanoparticle trimer. *Proc. Natl. Acad. Sci. U.S.A.*, 105(43):16448–16453, 2008.

[146] Zhonghong Shi, Xiaorui Tian, Zhangzeng Luo, Rongchen Huang, Lijun Wu, and Qiang Li. Photothermal imaging of individual nano-object with large scattering cross section. *The Journal of Physical Chemistry A*, 2020.

[147] Carsten Sönnichsen and A Paul Alivisatos. Gold nanorods as novel nonbleaching plasmon-based orientation sensors for polarized single-particle microscopy. *Nano Lett.*, 5(2):301–304, 2005.

[148] T.and Wilk T. Sönnichsen, C.and Franzl, Gero von Plessen, J. Feldmann, O.V. Wilson, and Paul Mulvaney. Drastic reduction of plasmon damping in gold nanorods. *Phys. Rev. Lett.*, 88(7):077402, 2002.

[149] Paul L. Stiles, Jon A. Dieringer, Nilam C. Shah, and Richard P. Van Duyne. Surface-enhanced raman spectroscopy. *Annu. Rev. Anal. Chem.*, 1:601–626, 2008.

[150] Liang Su, Haifeng Yuan, Gang Lu, Susana Rocha, Michel Orrit, Johan Hofkens, and Hiroshi Uji-i. Super-resolution localization and defocused fluorescence microscopy on resonantly coupled single-molecule, single-nanorod hybrids. *ACS Nano*, 10(2):2455–2466, 2016.

[151] Liang Su, Haifeng Yuan, Gang Lu, Susana Rocha, Michel Orrit, Johan Hofkens, and Hiroshi Uji-i. Super-resolution localization and defocused fluorescence microscopy on resonantly coupled single-molecule, single-nanorod hybrids. *ACS Nano*, 10(2):2455–2466, 2016.

[152] Orazio Svelto and David C. Hanna. *Principles of lasers*, volume 1. Springer, 2010.

[153] T.H. Taminiau, F.D. Stefani, Franciscus B. Segerink, and N.F. Van Hulst. Optical antennas direct single-molecule emission. *Nat. Photonics*, 2(4):234–237, 2008.

[154] Tim H. Taminiau, Fernando D. Stefani, and Niek F. van Hulst. Enhanced directional excitation and emission of single emitters by a nano-optical yagi-uda antenna. *Opt. Express*, 16(14):10858–10866, 2008.

[155] Niket Thakkar, Charles Cherqui, and David J. Masiello. Quantum beats from entangled localized surface plasmons. *ACS Photonics*, 2(1):157–164, 2015.

[156] Niket Thakkar, Morgan T. Rea, Kevin C. Smith, Kevin D. Heylman, Steven C. Quillin, Kassandra A. Knapper, Erik H. Horak, David J. Masiello, and Randall H. Goldsmith. Sculpting fano resonances to control photonic-plasmonic hybridization. *Nano Lett.*, 17(11):6927–6934, 2017.

[157] Pierre Thibault, Martin Dierolf, Andreas Menzel, Oliver Bunk, Christian David, and Franz Pfeiffer. High-resolution scanning x-ray diffraction microscopy. *Science*, 321(5887):379–382, 2008.

[158] Manabu Tokeshi, Marika Uchida, Akihide Hibara, Tsuguo Sawada, and Takehiko Kitamori. Determination of subyoctomole amounts of nonfluorescent molecules using a thermal lens microscope: subsingle-molecule determination. *Appl. Spectrosc.*, 73(9):2112–2116, 2001.

[159] Esther Wertz, Benjamin P. Isaacoff, Jessica D. Flynn, and Julie S. Biteen. Single-molecule super-resolution microscopy reveals how light couples to a plasmonic nanoantenna on the nanometer scale. *Nano Lett.*, 15(4):2662–2670, 2015.

[160] Esther A. Wertz, Benjamin P. Isaacoff, and Julie S. Biteen. Wavelength-dependent super-resolution images of dye molecules coupled to plasmonic nanotriangles. *ACS Photonics*, 3(10):1733–1740, 2016.

[161] Katherine A. Willets and Richard P. Van Duyne. Localized surface plasmon resonance spectroscopy and sensing. *Annu. Rev. Phys. Chem.*, 58:267–297, 2007.

[162] Katherine A. Willets, Andrew J. Wilson, Vignesh Sundaresan, and Padmanabh B. Joshi. Super-resolution imaging and plasmonics. *Chem. Rev.*, 117(11):7538–7582, 2017.

[163] Emil Wolf. Electromagnetic diffraction in optical systems - i. an integral representation of the image field. *Proc. R. Soc. Lond. A*, 253(1274):349–357, 1959.

[164] Ravindra Kumar Yadav, Marc R. Bourgeois, Charles Cherqui, Xitlali G. Juarez, Weijia Wang, Teri W. Odom, George C. Schatz, and Jaydeep Kumar Basu. Room temperature weak-to-strong coupling and the emergence of collective emission from quantum dots coupled to plasmonic arrays. *ACS Nano*, 2020.

[165] Shoko Yamada, Silvan Schmid, Tom Larsen, Ole Hansen, and Anja Boisen. Photothermal infrared spectroscopy of airborne samples with mechanical string resonators. *Appl. Spectrosc.*, 85(21):10531–10535, 2013.

[166] Mustafa Yorulmaz, Anneli Hoggard, Hangqi Zhao, Fangfang Wen, Wei-Shun Chang, Naomi J Halas, Peter Nordlander, and Stephan Link. Absorption spectroscopy of an individual fano cluster. *Nano Lett.*, 16(10):6497–6503, 2016.

[167] Mustafa Yorulmaz, Sara Nizzero, Anneli Hoggard, Lin-Yung Wang, Yi-Yu Cai, Man-Nung Su, Wei-Shun Chang, and Stephan Link. Single-particle absorption spectroscopy by photothermal contrast. *Nano Letters*, 15(5):3041–3047, 2015.

[168] Haifeng Yuan, Saumyakanti Khatua, Peter Zijlstra, Mustafa Yorulmaz, and Michel Orrit. Thousand-fold enhancement of single-molecule fluorescence near a single gold nanorod. *Angewandte Chemie*, 125(4):1255–1259, 2013.

[169] Qinsi Zheng, Steffen Jockusch, Zhou Zhou, and Scott C. Blanchard. The contribution of reactive oxygen species to the photobleaching of organic fluorophores. *Photochem. Photobiol.*, 90(2):448–454, 2014.

[170] Tiancheng Zuo, Harrison J. Goldwyn, Benjamin P. Isaacoff, David J. Masiello, and Julie S. Biteen. Rotation of single-molecule emission polarization by plasmonic nanorods. *The Journal of Physical Chemistry Letters*, 10(17):5047–5054, 2019.

VITA

Harrison J. Goldwyn

311D Bagley Hall, Department of Chemistry
University of Washington, Seattle, WA 98105

github.com/theomnipanda
goldwyn@uw.edu
805-443-2985

SUMMARY OF QUALIFICATIONS

- Analysis of the performance and predictive power of mathematical and machine learning models.
  - Predicting nanoscale electrodynamics at low computational cost.
  - Machine learning on spatiotemporal covariates derived from neural-networks (scikit-learn).
  - Uncertainty quantification through Bayesian probability theory.
- Implementation of models into scientific Python software to contemporary standards.
  - Leveraged existing Natural Language Processing code base to address questions in materials science.
  - Version control, testing, and collaborative software development through GitHub.
- Lead collaborations in joint theoretical+experimental science from predictions to publication.

RELEVANT EXPERIENCE

- **Research Intern, Independent Contractor** Summer 2019 & Feb. 2020 - Dec. 2020
  Institute for Disease Modeling *Bellevue, WA*
  - Improved resilience of measles transmission models to variation in data reporting.
  - Cleaned and queried large geospatial datasets for prediction of health-care access.
  - Built predictive regression models on neural network processed satellite imagery.

- **Graduate Research Assistant** 2015 - 2020
  University of Washington *Seattle, WA*
  - Constructed reduced-order mathematical models of electromagnetically interacting nanoscale objects and light propagation for Super-Resolution microscopy.
  - Led collaborative writing and publication of peer-reviewed research articles.
  - Written and maintained cross-platform software for numerical simulation, analysis, and visualization.

- **DIRECT Trainee (Data Intensive Research Enabling Clean Technologies)** Winter-Spring 2019
  Clean Energy Institute, UW *Seattle, WA*
  - Project 2: github.com/metromojo/Route_Dynamics
    Designed and developed the physics-based backend for a geospatial python package predicting battery degradation on King County Metro hybrid-electric buses.
  - Project 1: github.com/paper-parser/paper-parser
    Designed and co-developed a natural language processing (NLP) python package for academic articles.

EDUCATION

- **Ph.D. Physical Chemistry, Data Science Option (GPA: 3.69)** 2015 - 2020
  University of Washington *Seattle, WA*

  Relevant Coursework;
  - Data Science Capstone
  - Data Science Methods for Clean Energy Research
  - Software Engineering for Molecular Data Scientists

- **B.Sc. Physics (GPA: 3.61)** 2010 - 2014
  University of California, Santa Barbara *Santa Barbara, CA*

PEER REVIEWED PUBLICATIONS

8. **H.J. Goldwyn**, T.C. Zuo, J. Biteen, D.J. Masiello, *Resolution of the Plasmon-Induced Mislocalization Problem by Coupled-Dipole Image Model*. In preparation.
7. **H.J. Goldwyn**, S. Link, D.J. Masiello, *Resolving Resonance Effects in the Theory of Photothermal Imaging*. In preparation.

6. R. Baiyasi, **H.J. Goldwyn**, L. McCarthy, C. West, D.J. Masiello, S. Link, C. Landes, *Coupled-dipole models reveal the role of nanoantenna geometry in tunable optical dichroism.* In preparation.
5. E.J. Rabe*****, **H.J. Goldwyn***, X. Huang, A.L. Sobolewski, W. Domcke, D.J. Masiello, C.W. Schlenker, *Using Time-Resolved Photoluminescence to Understand the Excited-State Hydrogen-Bonded Complexes of Heptazine.* J. Phys. Chem. B (2020). ***equal contribution**.
4. T.C. Zuo*****, **H.J. Goldwyn***, B.P. Isaacoff, D. J. Masiello, J. Biteen, *Rotation of Single-Molecule Emission Polarization by Plasmonic Nanorods.* J. Phys. Chem. Lett. (2019). ***equal contribution**.
3. U. Bhattacharjee*****, C.A. West*****, S.A.H. Jebeli*****, **H.J. Goldwyn**, X.T. Kong, Z. Hu, E.K. Beutler, K.A. Willets, S. Link, D.J. Masiello, *Active Binary Control of the Thermal Near Field* via *Plasmon Hybridization.* ACS Nano (2019). *****equal contribution.
2. **H.J. Goldwyn**, K.C. Smith, J.A. Busche, D.J. Masiello, *Mislocalization in Plasmon-Enhanced Single-Molecule Fluorescence Microscopy as a Dynamical Youngs Interferometer.* ACS Photonics (2018).
1. C. Cherqui, N.W. Bigelow, A. Vaschillo, **H.J. Goldwyn**, D.J. Masiello, *A Combined Tight-Binding and Numerical Electrodynamics Understanding of the STEM/EELS Magneto-Optical Responses of Aromatic Plasmon-Supporting Metal Oligomers.* ACS Photonics (2014).

PRESENTATIONS

Contributed Talks

- **American Chemical Society National Meeting 258**, San Diego, CA — Aug. 26, 2019
  Resolving Mislocalization in Plasmon-Enhanced Single-Molecule Microscopy
- **American Chemical Society National Meeting 255**, New Orleans, LA — Mar. 18, 2018
  Understanding Mislocalization Error in Plasmon Enhanced Super-Resolution Fluorescence Microscopy

Posters

- **ORCAS International Conference on Energy Conversion & Storage** — Sep. 6, 2018
  Mathematical Model for Photothermal Imaging of Nanoparticle Aggregates: Deducing Local Temperature from Far-Field Measurement
- **Gordon Research Conference on Noble Metal Nanoparticles** — Jun. 17-22, 2018
  Nanoscale Temperature Manipulation via Plasmonic Fano Interferences

AWARDS

- George H. Hitchings Endowed Scholarship, 2015.
- NSF Research Experience for Undergraduates (REU) in Masiello Group at UW Seattle, 2013.
- Summer Undergraduate Research Experience in Synthetic Biology, 2012.

TEACHING

At the university level I have served as a Teaching Assistant for;

- Physical Chemistry Lab
- Graduate Thermodynamics
- Computational Data Analysis
- General Chemistry (5 quarters)

all as a graduate student at UW. During my undergrad, I TA'ed an intro physics class for engineers, was employed by the UCSB physics department to tutor, and ran an independent tutoring company for young undergrads.